

Science and Technology of Nuclear Installations

Advanced Reactor Concepts and Fuel Cycle Technologies

Guest Editors: Hangbok Choi and Wei Shen





Advanced Reactor Concepts and Fuel Cycle Technologies

Science and Technology of Nuclear Installations

Advanced Reactor Concepts and Fuel Cycle Technologies

Guest Editors: Hangbok Choi and Wei Shen



Copyright © 2013 Hindawi Publishing Corporation. All rights reserved.

This is a special issue published in “Science and Technology of Nuclear Installations.” All articles are open access articles distributed under the Creative Commons Attribution License, which permits unrestricted use, distribution, and reproduction in any medium, provided the original work is properly cited.

Editorial Board

Nusret Aksan, Switzerland
A. C. M. Alvim, Brazil
Won Pil Baek, Korea
Stephen M. Bajorek, USA
George Bakos, Greece
Jozsef Banati, Sweden
Ricardo Barros, Brazil
Anis Bousbia Salah, Belgium
Giovanni B. Bruna, France
Nikola Čavlina, Croatia
Xu Cheng, China
Leon Cizelj, Slovenia
Alejandro Clausse, Argentina
Francesco D' Auria, Italy
Marcos P. de Abreu, Brazil
Giovanni Dell'Orco, France
Juan Carlos Ferreri, Argentina
Nikolay Fil, Russia
Cesare Frepoli, USA
Giorgio Galassi, Italy
Regina Galetti, Brazil

Michel Giot, Belgium
Valerio Giusti, Italy
Horst Glaeser, Germany
Satish Kumar Gupta, India
Ali Hainoun, Syria
Keith E. Holbert, USA
Kostadin Ivanov, USA
Y. Kadi, Republic of Korea
Ahmed Khedr, Egypt
Tomasz Kozłowski, USA
Tomoaki Kunugi, Japan
Mike Kuznetsov, Germany
H.-Y. Lee, Republic of Korea
B. Limmeechokchai, Thailand
Jiri Macek, Czech Republic
Annalisa Manera, USA
Borut Mavko, Slovenia
Oleg Melikhov, Russia
Rafael Miró, Spain
Josef Misak, Czech Republic
Rahim Nabbi, Germany

Manmohan Pandey, India
Yuriy Parfenov, Russia
Yves Pontillon, France
Nik Popov, Canada
Piero Ravetto, Italy
Francesc Reventos, Spain
Enrico Sartori, France
Carlo Sborchia, France
Massimo Sepielli, Italy
Arkady Serikov, Germany
James F. Stubbins, USA
Iztok Tiselj, Slovenia
Rizwan Uddin, USA
Eugenijus Upuras, Lithuania
Richard Wright, Norway
Chao Xu, China
X. George Xu, USA
Yanko Yanev, Bulgaria
Zhiwei Zhou, China
Enrico Zio, Italy
Massimo Zucchetti, Italy

Contents

Advanced Reactor Concepts and Fuel Cycle Technologies, Hangbok Choi and Wei Shen
Volume 2013, Article ID 185640, 1 page

Design Concept of Advanced Sodium-Cooled Fast Reactor and Related R&D in Korea, Yeong-il Kim, Yong Bum Lee, Chan Bock Lee, Jinwook Chang, and Chiwoong Choi
Volume 2013, Article ID 290362, 18 pages

Modeling Forced Flow Chemical Vapor Infiltration Fabrication of SiC-SiC Composites for Advanced Nuclear Reactors, Christian P. Deck, H. E. Khalifa, B. Sammulu, and C. A. Back
Volume 2013, Article ID 127676, 10 pages

A Compact Gas-Cooled Fast Reactor with an Ultra-Long Fuel Cycle, Hangbok Choi, Robert W. Schleicher, and Puja Gupta
Volume 2013, Article ID 618707, 10 pages

Multiphysics Model Development and the Core Analysis for In Situ Breeding and Burning Reactor, Shengyi Si
Volume 2013, Article ID 154706, 14 pages

Moderating Material to Compensate the Drawback of High Minor Actinide Containing Transmutation Fuel on the Feedback Effects in SFR Cores, Bruno Merk
Volume 2013, Article ID 172518, 10 pages

Current Status of Pyroprocessing Development at KAERI, Hansoo Lee, Geun-IL Park, Jae-Won Lee, Kweon-Ho Kang, Jin-Mok Hur, Jeong-Guk Kim, Seungwoo Paek, In-Tae Kim, and IL-Je Cho
Volume 2013, Article ID 343492, 11 pages

Improvement of Core Performance by Introduction of Moderators in a Blanket Region of Fast Reactors, Toshio Wakabayashi
Volume 2013, Article ID 879634, 7 pages

Simulation Strategy for the Evaluation of Neutronic Properties of a Canadian SCWR Fuel Channel, G. Harrisson and G. Marleau
Volume 2013, Article ID 352757, 10 pages

Study of Thorium-Plutonium Fuel for Possible Operating Cycle Extension in PWRs, Klara Insulander Björk, Cheuk Wah Lau, Henrik Nylén, and Urban Sandberg
Volume 2013, Article ID 867561, 8 pages

Economic Evaluation on the MOX Fuel in the Closed Fuel Cycle, Youqi Zheng, Hongchun Wu, Liangzhi Cao, and Shizhuang Jia
Volume 2012, Article ID 698019, 9 pages

Editorial

Advanced Reactor Concepts and Fuel Cycle Technologies

Hangbok Choi¹ and Wei Shen²

¹ *General Atomics, 3550 General Atomics Court, San Diego, CA 92121-1122, USA*

² *Canadian Nuclear Safety Commission, 280 Slater Street, Ottawa, ON, Canada K1P 5S9*

Correspondence should be addressed to Hangbok Choi; h.choi@ga.com

Received 7 April 2013; Accepted 7 April 2013

Copyright © 2013 H. Choi and W. Shen. This is an open access article distributed under the Creative Commons Attribution License, which permits unrestricted use, distribution, and reproduction in any medium, provided the original work is properly cited.

Nuclear power is an abundant source with zero CO₂ output, and expanded fission power is an attractive option especially in growing countries. Various reactor concepts are being studied to comply with requirements of future nuclear fuel cycle such as safety, sustainability, cost-effectiveness, and proliferation risk reduction. These generation IV reactor concepts include both thermal and fast reactors and are being developed in conjunction with advanced reprocessing technology. In addition, beyond-generation IV type reactors are being developed, which mitigate the concern on the nuclear waste issue by adopting very high-burnup fuel and long-life core. Considering movement towards future nuclear cycle, we have collected papers which cover the topical areas of new activities in advanced reactors and fuel cycle technologies and published these in this special issue on advanced reactor concepts and fuel cycle technologies.

This special issue contains 10 research articles, including seven papers on advanced reactor concepts. The advanced reactor concept covers sodium-cooled fast reactor (SFR), gas-cooled fast reactor (GFR), supercritical water reactor (SCWR), and pressurized water reactor (PWR). The research topics include an advanced Korean SFR system design and analysis, improvement of Japanese SFR core performance by moderators in the blanket region, use of moderating materials to compensate the drawback of minor actinide containing transmutation fuel in European fast reactors, a multi-physics modeling technique for in situ breeding and burning reactors, an ultralong fuel cycle compact GFR system design and analysis, a simulation strategy for the evaluation of neutronic properties of a Canadian SCWR fuel channel, and a thorium-plutonium fuel cycle for operating cycle extension of a PWR. The special issue also includes research results

on the modeling forced-flow chemical vapor infiltration for fabrication of SiC-SiC composite materials, development of inactive demonstration facility for a proliferation-resistant pyroprocessing technology, and the economic analysis of a closed fuel cycle.

*Hangbok Choi
Wei Shen*

Review Article

Design Concept of Advanced Sodium-Cooled Fast Reactor and Related R&D in Korea

Yeong-il Kim, Yong Bum Lee, Chan Bock Lee, Jinwook Chang, and Chiwoong Choi

Korean Atomic Energy Research Institute (KAERI), 989-111 Daedeok-Daero, Yuseong-Gu, Daejeon 305-353, Republic of Korea

Correspondence should be addressed to Chiwoong Choi; cwchoi@kaeri.re.kr

Received 28 September 2012; Revised 16 February 2013; Accepted 26 February 2013

Academic Editor: Wei Shen

Copyright © 2013 Yeong-il Kim et al. This is an open access article distributed under the Creative Commons Attribution License, which permits unrestricted use, distribution, and reproduction in any medium, provided the original work is properly cited.

Korea imports about 97% of its energy resources due to a lack of available energy resources. In this status, the role of nuclear power in electricity generation is expected to become more important in future years. In particular, a fast reactor system is one of the most promising reactor types for electricity generation, because it can utilize efficiently uranium resources and reduce radioactive waste. Acknowledging the importance of a fast reactor in a future energy policy, the long-term advanced SFR development plan was authorized by KAEC in 2008 and updated in 2011 which will be carried out toward the construction of an advanced SFR prototype plant by 2028. Based upon the experiences gained during the development of the conceptual designs for KALIMER, KAERI recently developed advanced sodium-cooled fast reactor (SFR) design concepts of TRU burner that can better meet the generation IV technology goals. The current status of nuclear power and SFR design technology development program in Korea will be discussed. The developments of design concepts including core, fuel, fluid system, mechanical structure, and safety evaluation have been performed. In addition, the advanced SFR technologies necessary for its commercialization and the basic key technologies have been developed including a large-scale sodium thermal-hydraulic test facility, super-critical Brayton cycle system, under-sodium viewing techniques, metal fuel development, and developments of codes, and validations are described as R&D activities.

1. Introduction

In Korea, electricity demand has increased by about eleven times since 1980 with an average annual growth rate of 8.7% mainly due to economic growth. The anticipated average annual growth rate is estimated to be 2.2% during the period of 2010 to 2024, as shown in Figure 1 [1]. However, the available energy resources are extremely limited in Korea: no domestic crude oil, little natural gas, and limited sites for hydro power. Consequently, about 97% of energy resources come from abroad. Nuclear power plants currently generate about 40% of the total electricity, and the role of nuclear power plants in electricity generation in Korea is expected to become more important in the years to come due to Korea's lack of natural resources. The significance of nuclear power will become even greater, considering its practical potential in coping with the emission control of green-house gases. This heavy dependence on nuclear power eventually raise the issues of an efficient utilization of uranium resources, which

Korea presently imports from abroad, and of a spent fuel storage [2].

From the viewpoint that a sodium-cooled fast reactor (SFR) has the potential of an enhanced safety by utilizing inherent safety characteristics, transuranics (TRU) reduction, and resolving the spent fuel storage problems through a proliferation-resistant actinide recycling, an SFR is sure to be the most promising nuclear power option.

The Korean Atomic Energy Research Institute (KAERI) has been developing SFR design technologies since 1997 under a National Nuclear R&D Program. The goals of the SFR design technology development project are to secure strategic key technologies and develop the conceptual design of an SFR which are necessary for an efficient utilization of uranium resources and a reduction of a high level waste volume. The SFR design technology development project has been carried out as follows. From 2002 to 2005, the preliminary design concept for KALIMER-600 was developed [3]. The basic key technologies were developed according to a power level

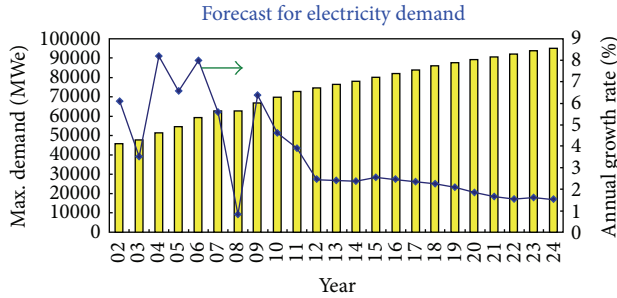


FIGURE 1: Forecast for electricity demand.

increase based on the KALIMER-150 design concepts and the advanced concepts such as a nuclear proliferation resistant core, a simplification of an IHTS pipeline and reactor structures, have been developed. The experimental data were secured through basic experiments such as a verification experiment for the computational models and sodium detection experiments. The basic key computer codes and methodologies have been continuously improved, and additional ones have been developed as necessary. Recently, the long-term advanced SFR R&D plan has been set up again aiming at the construction of an advanced SFR prototype reactor in 2028.

2. Design Concept of the Demonstration Reactor

2.1. Top-Tier Design Requirements. The KALIMER-600 design served as a starting point for developing a new advanced design which is equipped with advanced design concepts and features. Various advanced design concepts have been proposed and evaluated against the design requirements which were established to satisfy the Gen IV technology goals.

The top-tier design requirements of a 600 MWe TRU burner are categorized by three criteria: general design requirements, safety and investment protection, and plant performance and economy. Details of these design requirements are given in Table 1. These requirements reflect the design policies, especially emphasizing proliferation resistance, safety assurance, and metal fuel performance, and form the basis for developing the detailed system design requirements for key NSSS concepts.

2.2. Core Design. A conceptual core design for demonstrating TRU burning has been developed. The main objectives are to test and demonstrate the TRU fuel, operate a large sized (1,500 MWth) SFR, and show the TRU burning capability of a commercial burner reactor [4]. It is scheduled to use uranium fuel for the initial core due to the uncertainty of the demonstration of TRU fuel. The LTRU core fuel from a light water reactor (LWR) spent fuel and MTRU core fuel, which consists of LMR spent fuel and self-recycled fuel, will be used progressively, and thus three cores a uranium core, LTRU core, and MTRU core were designed.

TABLE 1: Summary of top-tier design requirements of an SFR demonstration plant.

General design	
Reactor type:	pool type
Plant size:	600 MWe
Plant design lifetime:	60 years
Design basis earthquakes (SSE):	0.3 g
Initial core:	U-Zr metal fuel
Reloading core:	U-TRU-Zr metal fuel
Safety and investment protection	
Design simplification	
Negative power reactivity coefficient	
CDF	$< 10^{-6}/\text{reactor} \cdot \text{yr}$
No fuel-cladding liquid phase propagation during DBEs	
Diversified core shutdown mechanism	
Reliable and diversified decay heat removal	
Accommodating unprotected ATWS events without any operator's action	
Large radioactivity release	$< 10^{-7}/\text{reactor} \cdot \text{yr}$
3 days grace time w/o any operator's action for design basis events	
Performance and economy	
Plant thermal efficiency: net	$> 38\%$
Plant availability	$\geq 70\%$
Refueling interval: U-Zr initial core	≥ 6 months
TRU burner core	≥ 11 months
Spent fuel storage capacity in RV	≥ 1.5 cycle discharge
100% off-site load rejection w/o a plant trip	
Safety grade diesel generator	

The core functions are given in Table 2. Every core was designed maintaining the same core dimension of the TRU core. Figure 2 shows the layout of the 600 MWe-rated uranium core. As shown in Figure 2, the core consists of two fuel regions. It consists of 151 fuel assemblies in the inner core and 174 fuel assemblies in the outer core. The fissile enrichments of the inner/outer cores for the radial power control are 15 and 20 wt.%, in which the enrichment of 20 wt.% is the maximum allowable enrichment in the commercial market for the uranium core. The hexagonal fuel assembly consists of 271 rods within a duct wrapper. The outer diameter of a rod is 7.4 mm. The core configuration is a radial homogeneous one that incorporates annular rings with a region-wise enrichment variation. The active core height was adjusted to make the enrichment of the outer core 20 wt.%, and the adjusted height is 85 cm. Table 3 shows a summary of the core performance analysis results, obtained with the equilibrium cycle analysis. The burnup reactivity swing for the uranium core was estimated to be 1,698 pcm.

TABLE 2: Core function for TRU burning.

U core	Trans core	LTRU core	Trans core	MTRU core
Pure U core equilibrium		LWR-TRU equilibrium		Pure TRU core equilibrium (MTRU fuel equilibrium)
Open fuel cycle	U/LWR-TRU transition cycle	Open fuel cycle	Transition core to final TRU core	FOAK role start
LWR-TRU (LTRU) fuel demonstration	Open fuel cycle	LWR-TRU and self TRU mixed (MTRU) fuel demonstration	Beginning of self cycle	
LTRU test zone install				

TABLE 3: Core performance of demonstration cores.

	Uranium core	LTRU core	MTRU core
Charged fuel enrichment (U, TRU) (wt.%) (inner/outer core)	15.0/20.0	19.2/24.8	21.5/28.8
Conversion ratio (Fissile/TRU)	0.54/–	0.80/0.71	0.81/0.64
Burnup reactivity swing (pcm)	1,698	2,588	2,945
Cycle length (EFPD)	255	365	365
Avg. discharged burnup (MWD/kg) (inner/outer core)	51.8/42.4	83.4/76.0	79.5/81.9
Peak fast neutron fluence ($\times 10^{23}$ n/cm ²)	1.92	3.23	3.12
Power peaking factor (BOEC/EOEC)	1.480/1.53	1.50/1.44	1.57/1.50
TRU consumption rate (kg/cycle)	–	145.9	184.9
Sodium void worth (EOEC, \$)	–0.22	7.70	7.03
Doppler coefficient (pcm/°C)	$-1172.7T^{-1.122}$	$-1012.4T^{-1.152}$	$-911.0T^{-1.149}$
Axial expansion coefficient (pcm/°C)	–0.140	–0.217	–0.268
Radial expansion coefficient (pcm/°C)	–0.780	–0.949	–0.980
Sodium density coefficient (pcm/°C)	0.076	0.717	0.627

The LTRU core was designed next to the uranium core. The core uses the spent fuel from the LWR and adapts a once-through cycle option. Radial and axial power distributions were flattened through searching enrichment ratios between the inner and outer cores to minimize power peaking. When the TRU enrichments of the inner and outer core regions reach 19.2 wt.% and 24.8 wt.%, the power peaking factors were estimated to be 1.50 at the beginning of equilibrium cycle (BOEC) and 1.44 at the end of the equilibrium cycle (EOEC), and these values are well below 1.60 of the predetermined design limit.

The MTRU core uses a mixed TRU fuel with LWR spent fuel and self-recycled fuel. In the MTRU core design, reflector assemblies were introduced in the central region of the core to reduce the increased sodium void worth. The TRU consumption rate was estimated to be 185 kg/cycle, and the burnup reactivity swing, 2,945 pcm.

A demonstration core was selected after a series of core designs, ranging from the U core to the LTRU and MTRU cores. A special effort to increase the discharge burnup was made due to a relatively low discharge burnup in the U core. As shown in Table 4, five candidates including the first one as the reference were applied and analyzed. Candidates 1, 2, and 3 had the same core height but a different fuel loading cycle to simplify core modification from U core to TRU core without any geometry changes in structure. However, these modifications could not improve the discharge burnup effectively in the U core as well as sodium void reactivity also increased in the LTRU and MTRU cores, as shown in Figure 3.

TABLE 4: Parameters of candidate cores.

Core candidate	1	2	3	4	5
U core height (cm)	85	85	85	95	106
TRU core height (cm)	85	85	85	85	85
Fuel diameter (mm)	7.4	7.4	7.4	7.4	7.0
Fuel batch cycle (inner/outer core)	3/3	4/3	4/4	3/3	3/3

As alternate approaches, candidates 4 and 5 were suggested by changing the active core heights and a fuel pin diameter for the same purpose, even though modification of the core structure was required. Candidates 4 and 5 had an improved discharge burnup compared with candidates 1, 2, and 3 in the U core, but higher sodium void reactivity relatively than that of candidates 1 and 2 in the MTRU core. Therefore, candidate 1 was selected even though this core showed a lower discharge burnup than that of candidates 4 and 5 because it revealed the best performance from U core to TRU core in the safety aspect between candidates 1, 2, and 3 and could keep the same core dimension.

2.3. Fuel Design. The probability of cladding failure or damage during the steady state and transient conditions must be evaluated by appropriate predictive codes. To prevent a metallic fuel rod failure in a fast reactor, it is required to evaluate the design limits such as (1) cladding strain and cumulative damage fraction (CDF), (2) fuel melting, and (3) eutectic melting.

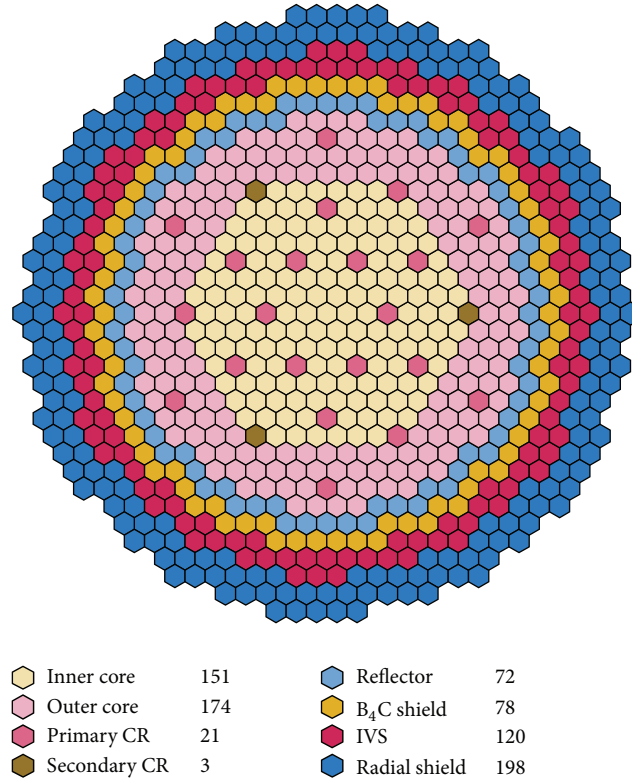


FIGURE 2: Layout of uranium core (600 MWe).

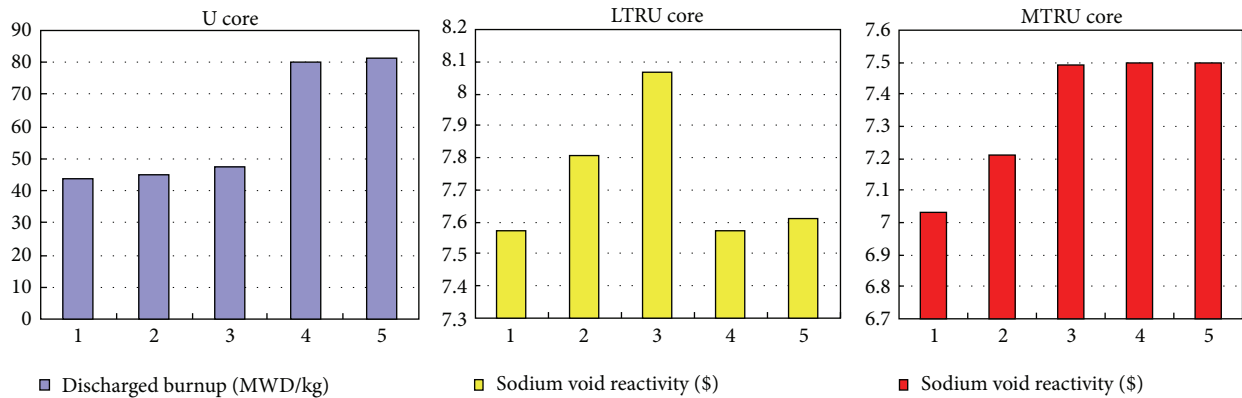


FIGURE 3: Core performance comparison.

The design requirement for cladding is assumed to be 1% of the thermal creep strain and 0.05 of CDF. The cladding strain limit and CDF limit for metal fuel were evaluated by the MACSIS code. These limits depend on the plenum-to-fuel ratio, cladding thickness/temperature, and burnup.

If the cladding temperature becomes higher than 625°C, it was estimated that the HT9 cladding was not conservative enough to satisfy the CDF limit because the creep rupture strength was too low at a higher temperature. If the cladding temperature becomes higher than 645°C, it was estimated that the HT9M cladding satisfied the CDF limit by establishing the optimum design parameters. Therefore, 625 and

645°C are conservatively selected as the peak clad temperature for the HT9 and HT9M, respectively.

Figure 4 shows the calculation results of the CDF limits according to the plenum-to-fuel ratio, cladding temperature, and burnup. If the plenum-to-fuel ratio was enlarged, it was estimated that the HT9M cladding satisfied the CDF limit at the discharge burnup goal.

Radiation damage to the cladding by fast neutrons can result in swelling and a ductility reduction of the cladding. HT9 and HT9M cladding are very tolerant to fast neutron irradiation owing to their lattice structure of body centered cubic (BCC). HT9 cladding is known to show very low

swelling and maintain its mechanical integrity up to 4.0×10^{23} n/cm². The peak fast neutron fluence of the cladding shown in Table 3 is below 4.0×10^{23} n/cm².

The fuel melting temperature limits of 955 and 1200°C are used for U-TRU-Zr and U-Zr fuel, respectively. It was estimated that the metallic fuel had a sufficient margin to the slug melting temperature. However, the fuel surface temperature to avoid eutectic melting is limited to 650 and 720°C for U-TRU-Zr and U-Zr, respectively. It was calculated that there is a sufficient margin for U-Zr. However, the power-to-eutectic limit was decreased to about 350 W/cm for U-TRU-Zr. This result showed that the concept of a barrier cladding may be necessary for preventing the eutectic melting, in the case of U-TRU-Zr.

2.4. Fluid System Design. The fluid system has been designed to ensure the safety goal of the Gen IV reactor system and enhance the economics through a tradeoff study between various proposed design candidates based on proven technologies [5]. The fluid transport system is composed of a heat transport system and safety system.

The heat transport system consists of a primary heat transport system (PHTS), intermediate heat transport system (IHTS), and power conversion system (PCS). The Decay Heat Removal System (DHRS) is employed as one of the safety design features to remove the decay heat of the reactor core after the reactor shutdown when the normal heat transport path is unavailable.

The PHTS is a pool type in which all the primary components and primary sodium are within a reactor vessel to prevent primary sodium from leaking outside of the containment, as shown in Figure 5. Two PHTS pumps and four intermediate heat exchangers (IHXs) are immersed in the sodium pool inside a reactor vessel, and their arrangement is presented in Figure 6. The PHTS pump is a centrifugal type mechanical pump with a capacity of 290.3 m³/min. The IHX is a counter flow shell and tube types (TEMA type S) with a vertical orientation inside the reactor vessel where PHTS sodium flows through the shell side and IHTS sodium flows through the tube side. The schematic design concepts of the PHTS pump and IHX are shown in Figure 7. The core inlet and outlet temperatures are 365°C and 510°C, respectively.

The IHTS is two loops, and two IHXs are connected to one steam generator and one IHTS pump in each loop as shown in Figure 6. An IHTS pump is a centrifugal type with a capacity of 209.8 m³/min and is located in each cold leg. A steam generator is a helical tube type with a thermal capacity of 776.7 MWt, and its schematic design concepts are shown in Figure 7. The IHTS sodium flows downward through the shell side while the water/steam goes up through the tube side. Steam temperature and pressure at a 100% normal operating condition are 471.2°C and 17.8 MPa, respectively. The cold leg of the IHTS piping is a bottom up U-shape with sufficient height to prevent sodium-water reaction products from reaching the IHX in case of a steam generator tube failure. Also, the IHTS piping is arranged to enhance the natural circulation capability in IHTS pump trip case.

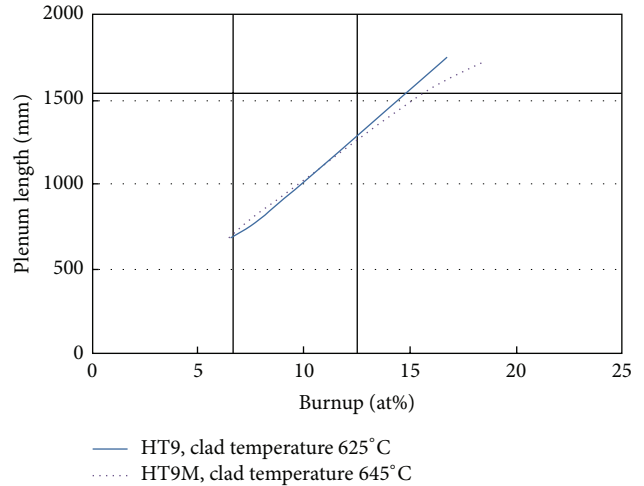


FIGURE 4: CDF limits according to plenum-to-fuel ratio, cladding temperature, and burnup.

The PCS employs a superheated steam Rankine cycle. The normal operating condition at 100% power is shown in Figure 8. It was determined in such a way to minimize the total heat transfer area of IHX and steam generator and maximize the plant efficiency.

The DHRS is composed of two passive decay heat removal circuits (PDRCs) and two active decay heat removal circuits (ADRCs). It was designed to have the sufficient capacity to remove the decay heat in all design bases events by incorporating the principles of redundancy and independency. The heat removal capacity of each loop is 9 MWt. The PDRC is a safety-grade passive system which is comprised of two independent loops with a decay heat exchanger (DHX) immersed in a hot pool region and a natural-draft sodium-to-air heat exchanger (AHX) located in the upper region of the reactor building for each loop. It is operated based on the natural circulation by density and the elevation difference between the DHX and AHX. The ADRC is a safety-grade active system, which is comprised of two independent loops with a DHX, a forced-draft sodium-to-air heat exchanger (FDHX), an electromagnetic pump, and an FDHX blower for each loop. The electromagnetic pump and FDHX blower derive the sodium circulation in the loop and the air flow in the shell side of FDHX, respectively. Because the ADRC can also be operated in natural convection mode against a loss of power supply, the heat transferred to the DHRS can be finally dissipated to the atmosphere through AHXs and FDHXs by the natural convection mechanism of sodium and air. Figure 9 shows the design concepts of heat exchangers.

2.5. Mechanical Structure Design. The reactor enclosure system is composed of double vessels (reactor vessel and guard vessel) and a thick flat plate of the reactor head. Figure 10 shows the configuration of the conceptually designed reactor steam supply system. In this design, the reactor vessel size is 12 m in diameter and 16.5 m in height. IHTS main piping is 144 m long per loop system. Figure 10 shows the top view of

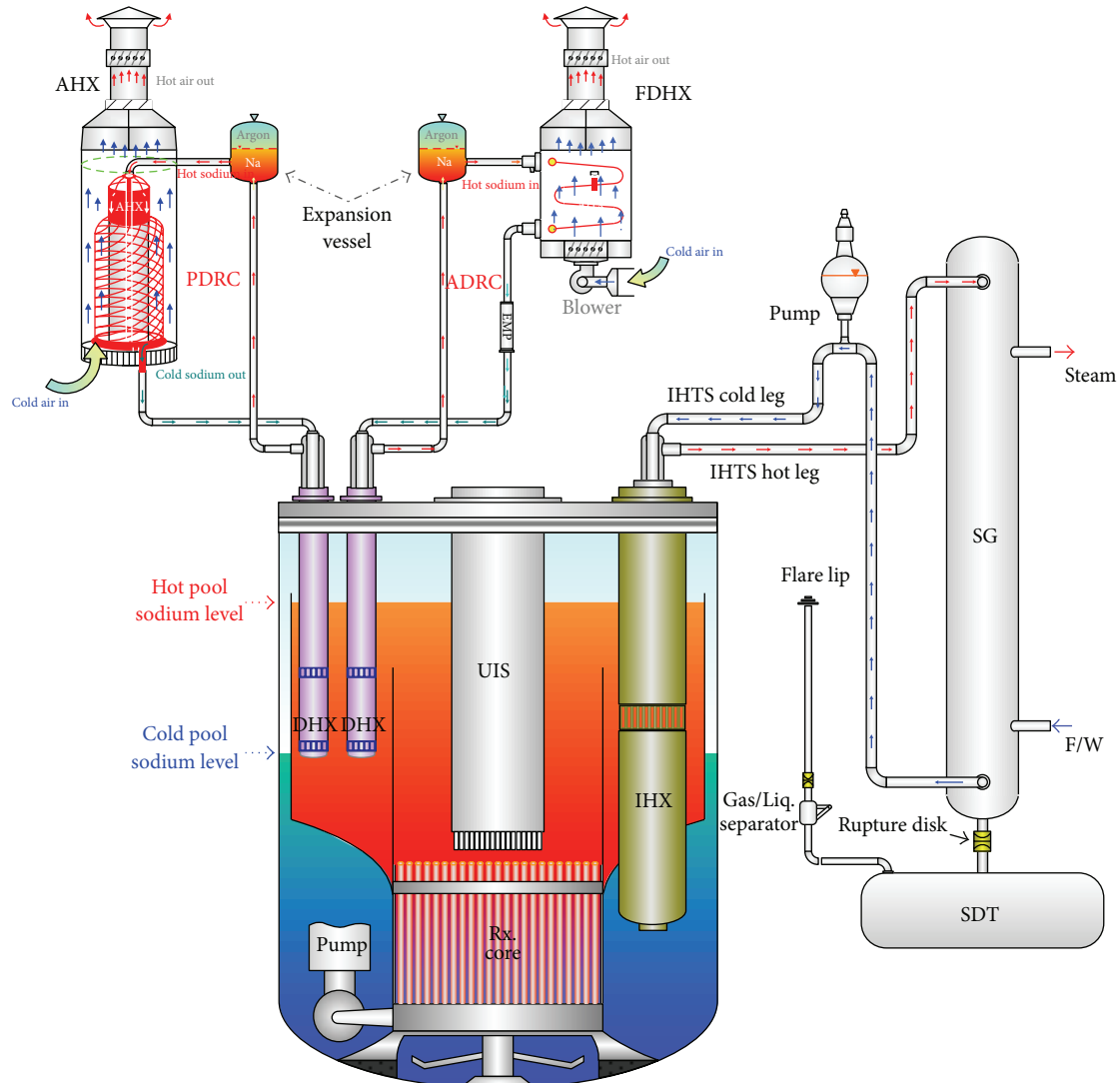


FIGURE 5: Configuration of the heat transport system.

the arrangements of the main components and IHTS piping including the decay heat removal system.

The reactor system is supported by a skirt type support structure which joints the reactor head and the reactor vessel by bolts. This will provide access holes for in-service inspection devices to inspect the reactor and guard vessels. The core support structure is a detached skirt type structure which has no welds between the core support structure and reactor vessel bottom head. This is just put on the flange forged with a reactor vessel bottom head to allow a free thermal expansion.

2.6. Safety Analysis. The TOP, LOF, LOHS, primary pipe break, and reactor vessel leak event are analyzed using the MARS-LMR code. The ANS-79 model is used for a core decay power after a reactor scram. AHX dampers are assumed to open at 5 seconds after a reactor trip. The isolation time of the SG feed water line is assumed to be the same as the pump trip time. Two independent PDRCs and one ADRC are assumed to be available by applying a single failure criterion.

The TOP accident was assumed to be initiated due to a control rod withdrawal by the drive motor failure. The TOP accident is initiated at 10 seconds, and a positive reactivity is inserted by the amount of 30¢ during 15 seconds. The reactor trip occurred at 22.73 seconds by a high power/flow trip. The power peaks after the initiation of rod withdrawal, it decreases drastically due to the reactor trip, and the cladding temperature in the reactor core shows the highest value. The peak cladding temperature was calculated at 580.93°C which was lower than the limit value. Figures 11(a) and 11(b) show behavior of the core inlet temperature and total heat balance in the plant, respectively. The AHX heat removal exceeds the core power after 4400 seconds, and the core outlet temperature decreases continuously. In conclusion, PHTS and the fuel temperature meet all safety criteria for the TOP accident.

The LOF means the loss of core cooling capability due to a pumping failure of the primary pumps. The imbalance between the reactor power and primary flow rate is a main

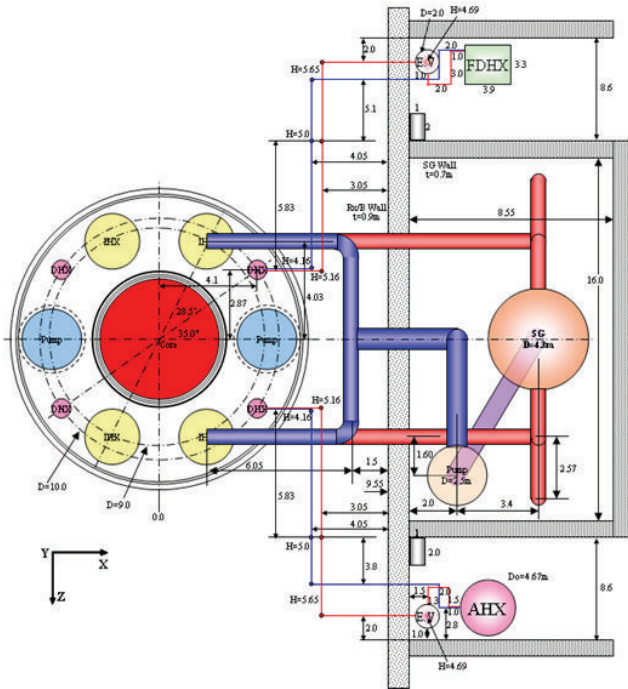


FIGURE 6: The arrangement of PHTS and IHTS.

safety concern in the LOF event. To prevent the occurrence of the severe imbalance between power and flow, the DFR is designed so as far the reactor to be tripped by a high power/flow trip. Figure 12 shows the coolant temperature behaviors during the LOF accident. In this simulation, all primary pumps are tripped at 10 seconds. The reactor scram occurs at 16.9 seconds, and the reactor power and flow rate decrease. The power decreases drastically due to the reactor trip, and the cladding temperature in the reactor core then shows the highest value. The peak cladding temperature was calculated at 624.27°C. The temperature is evaluated to meet the safety criteria.

The LOHS accident was assumed to occur from an initiated steam generator feedwater isolation. IHTS pumps and PHTS pumps are also stopped with the assumption that the loss of offsite power occurred at 5 seconds after the reactor trip. Therefore, the residual heat removal is achieved only by the evaporation of water in SG tubes and by the SHRS after the accident. In this simulation, a loss of feedwater to SG is assumed to occur at 10 seconds. The reactor was tripped at 58.77 seconds by an abnormal rise of the IHX inlet temperature after the accident. The reactor trip occurs late unlike other accidents. Figure 13 shows the coolant temperature behaviors during the LOHS accident. After the pump trip, the coolant temperatures go up rapidly and the maximum coolant temperature is calculated as around approximately 513.56°C. The temperature meets the safety criteria.

Coolant flows into the inlet plenum from four pipes which are connected with two PHTS pumps. The primary pipe break accident is occurred by a pipe break for one of the pipes. The flow through the broken pipe is discharged into the cold pool, and some of the low temperature sodium flowing

through an intact pipe into the inlet plenum is released into the pool. Essentially, this event is similar to an LOF accident. The accident occurs at 10 seconds as shown in Figure 14. The initial temperature increases due to the decrease of sodium flux into the reactor core. In this simulation, the peak coolant temperature was calculated at 579.23°C. The temperature is lower than the limit value.

A reactor-vessel-leak accident is a typical accident of a sodium leak at the PHTS boundary. It mainly affects the level of sodium in the PHTS. To analyze the damage of the reactor vessel leak accidents, the leak was assumed to occur at the bottom of the reactor vessel, conservatively, and the leak size was assumed to be 10 cm² in size.

Figure 15 shows the coolant temperature behaviors during the reactor vessel leak. The accident occurred at 10 seconds. The reactor trip occurred at 884.47 seconds. It is detected by the low liquid level from the reactor vessel leak. After the reactor trip, the flow behavior is similar to the loss of flow. The highest cladding temperature was calculated at 609°C. The peak cladding temperature satisfies the safety criteria.

The consequence of the blockage formation in a drive fuel assembly was deliberately analyzed with a subchannel analysis code, MATRA-LMR/FB, for the demonstration reactor. It was applied to the analysis of flow blockage accidents postulated in a conceptual design of the demonstration reactor with 3 types of core designs, that is, uranium, L-TRU, and M-TRU cores. The analysis was performed for a hot fuel subassembly. The blockage size and radial channel blockage position in the subassembly were the main parameters taken into account in the analysis. The three radial positions examined in the analysis were the center, the middle between the subassembly center and the duct wall, and the edge of the subassembly.

Figure 16 summarizes the analysis results. The design basis event, that is, 6 subchannel blockage was ensured to satisfy the safety limits. The cases for the 24 and 54 subchannel blockages, however, could not meet the peak cladding temperature limit. Although a sufficient margin of more than approximately 150°C might be obtained against sodium boiling, fuel melting was threatened for the 54 subchannel blockage.

3. R&D Activities

3.1. Large-Scale Sodium Thermal-Hydraulic Test Facilities. According to the long-term SFR development plan approved by the Korean government, a specific design approval of the prototype SFR will be obtained by 2020, and its construction is scheduled to be completed by 2028. To support this program plan, a large-scale sodium thermal-hydraulic test program called STELLA (sodium test loop for safety simulation and assessment) is recently being progressed by KAERI.

The reference design of the program is the Korean prototype SFR which employs highly reliable safety-grade decay heat removal systems. Since a reliable decay heat removal is one of the most important issues of nuclear safety, the performance of a decay heat removal system should be verified using a large-scale test facility. To this end, the first test facility

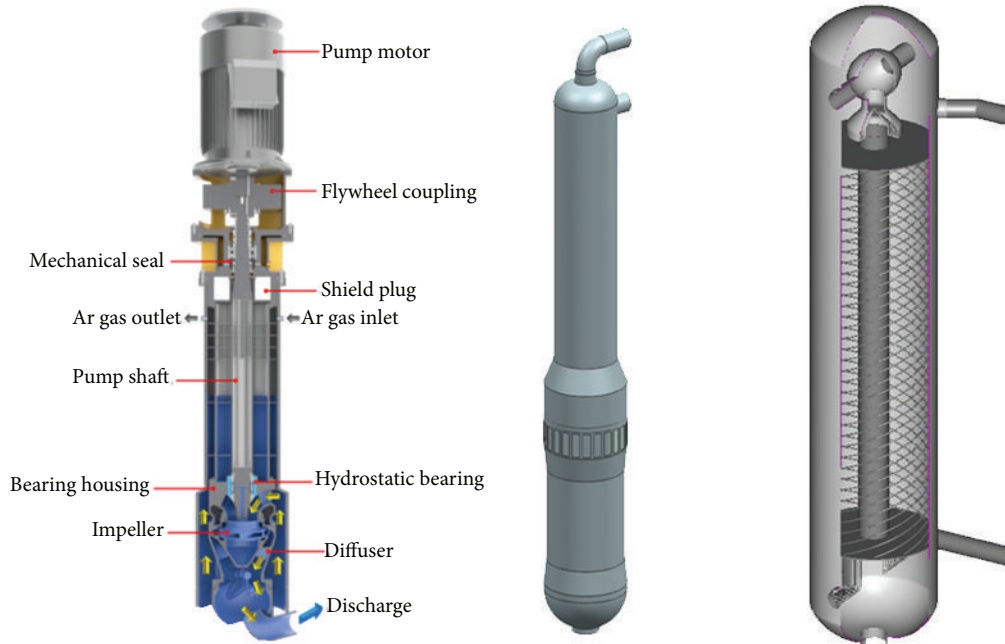


FIGURE 7: Schematic design concepts of main component in heat transport system.

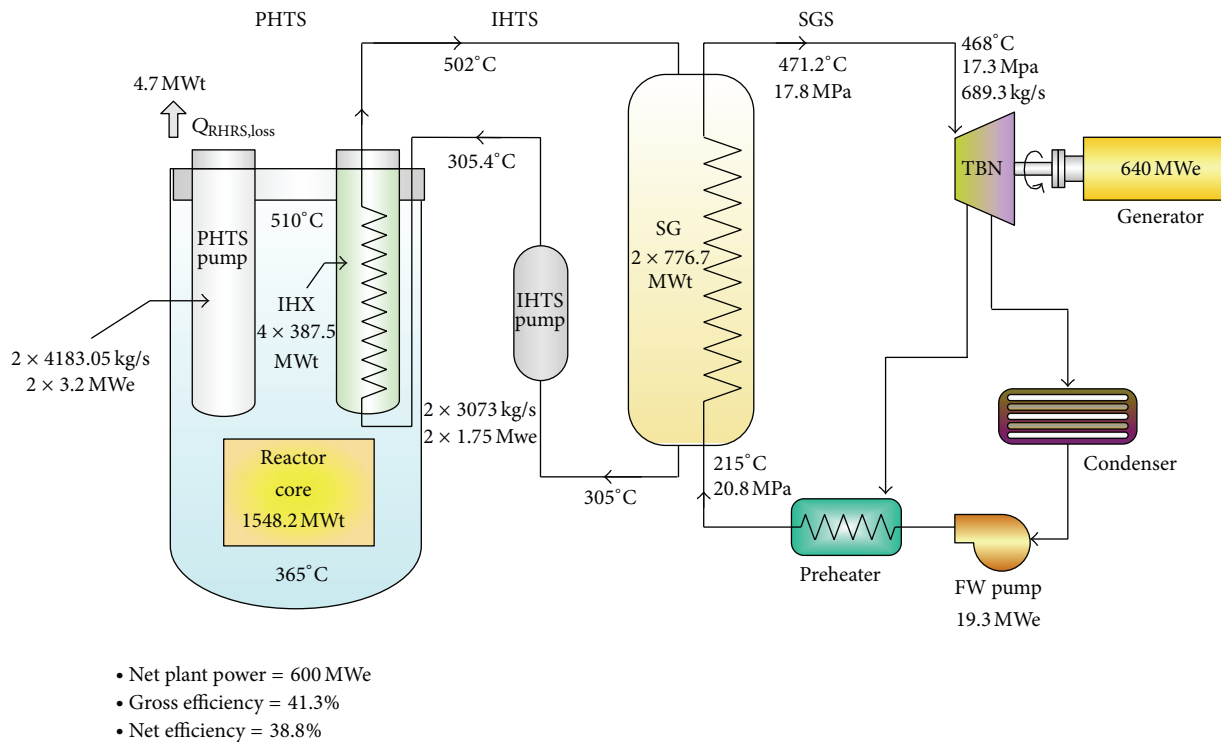


FIGURE 8: Heat balance at 100% power operating condition.

of the STELLA program (hereafter called STELLA-1) was completed which is to be used for demonstrating the thermal-hydraulic performance of major sodium components such as heat exchangers and a mechanical sodium pump and their design code V&V.

The second step of an integral effect test loop, called STELLA-2, will be constructed to demonstrate the plant safety and support the design approval for the prototype reactor. Starting with the conceptual design of the prototype reactor, the basic and detailed design of the test facility

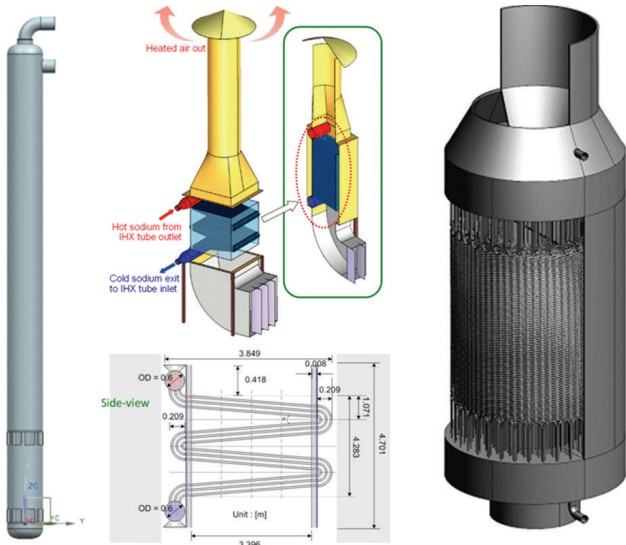


FIGURE 9: Heat exchanger design concepts of DHRS.

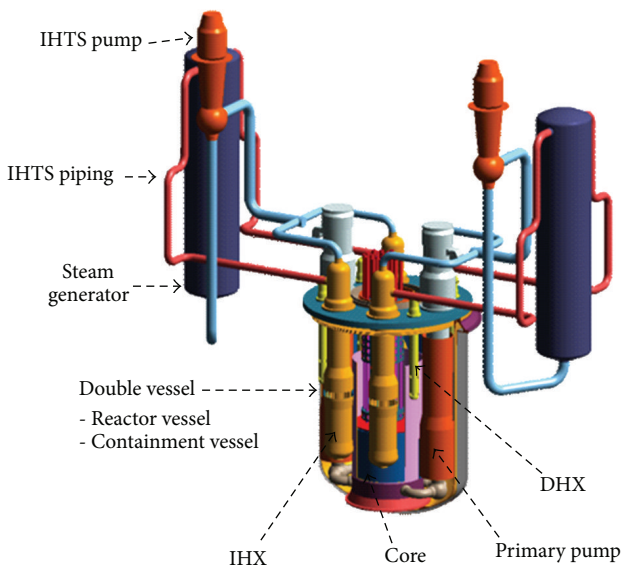


FIGURE 10: Reactor structure, system, and components.

reflecting the prototype design concept will be performed on the basis of design requirements subject to the prototype reactor. The facility is scheduled to be installed by the end of 2016. The main experiments including the start-up tests will commence in 2017. The STELLA program finally aims the integral effect test to support a specific design approval for a Korean prototype SFR.

STELLA-1 consists of a main test loop, a sodium purification system, and a gas supply and related auxiliary systems. The main components of this facility are a sodium-to-sodium heat exchanger, sodium-to-air heat exchanger, mechanical sodium pump, loop heaters, cold trap, plugging meter, electromagnetic pumps, flow meters, and a sodium storage tank. The general arrangement of the STELLA-1 facility is shown in Figure 17.

The designed maximum temperature of the facility is 600°C, and the designed power capacity of the main heat exchangers, such as sodium-to-sodium and sodium-to-air heat exchanger, are 1 MWt. The maximum electric power into the facility is around 2.5 MWt, and the nominal liquid sodium flow rate supplying the test heat exchangers is designed to be less than 10 kg/sec. During the mechanical pump test, more than 120 kg/sec of liquid sodium circulates along 10-inch diameter pipes.

At the first step of the demonstration of the design characteristics and system performance, separate effect tests for assessing the performance of heat exchangers and the mechanical sodium pump have been planned. The sodium-to-sodium heat exchanger tests are performed to investigate the rate of heat transfer through the tube wall by hot and cold sodium loop operation. In the sodium-to-air heat exchanger tests, the heat transfer performance from liquid sodium flow inside the tubes to the air flow is investigated by cooling the external tube surface with ambient air. To evaluate the heat removal capability in passive mode, a natural circulation flow inside sodium loop piping is also investigated using a bypass of the electromagnetic pump. The PHTS pump test loop consists of a reservoir, pipes, valves, and a vertical pump unit. This loop is equipped with various sensors for measuring the flow rate, temperature, liquid sodium level, and so forth. The main test loop is designed to simulate the transient operation mode using a flywheel as well as normal operation mode.

3.2. S-CO₂ Brayton Cycle System. The S-CO₂ Brayton cycle energy conversion option has many advantages such as excellent thermal efficiency and compactness of its equipment, for example, small turbo machinery and heat exchangers. Furthermore, by coupling the system to the SFR, the safety of the SFR could be enhanced by an elimination of the sodium-water reaction. To adopt the S-CO₂ Brayton cycle to the SFR, several R&D activities were done, such as the system design, operational strategy, Na-CO₂ reaction, and heat exchanger development.

In the system design, a design concept of an S-CO₂ Brayton cycle coupled with a KALIMER-600 was developed, and the system operational strategy was developed to evaluate the operating conditions at various power levels. When changing the system flow rate to vary the system power level, a pressure imbalance occurs from the difference of turbine and compressors design characteristics. To resolve the pressure imbalance, a clutch and throttle valve design concept was introduced and a system transient analysis was done by the use of the MMS-LMR commercial code.

For the enhancement of system performance by decreasing the pressure loss in a high and low temperature recuperator, a new design concept of heat exchanger was proposed by the application of an airfoil type fin to S-CO₂ flow path. For the new model, three-dimensional numerical analysis was performed to investigate the heat transfer and pressure drop characteristics of supercritical CO₂ flow using the commercial CFD code, Fluent 6.3. From the simulation results, the total heat transfer rate per unit volume was almost the same with a zigzag channel PCHE and the pressure drop was

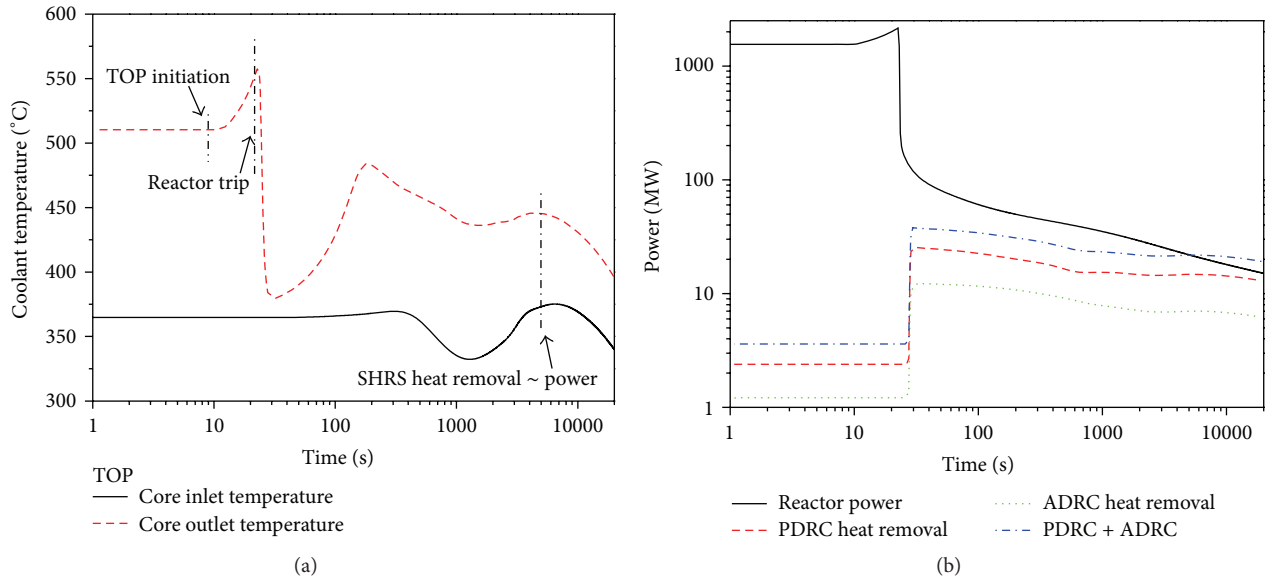


FIGURE 11: Predicted transient behaviors for TOP event.

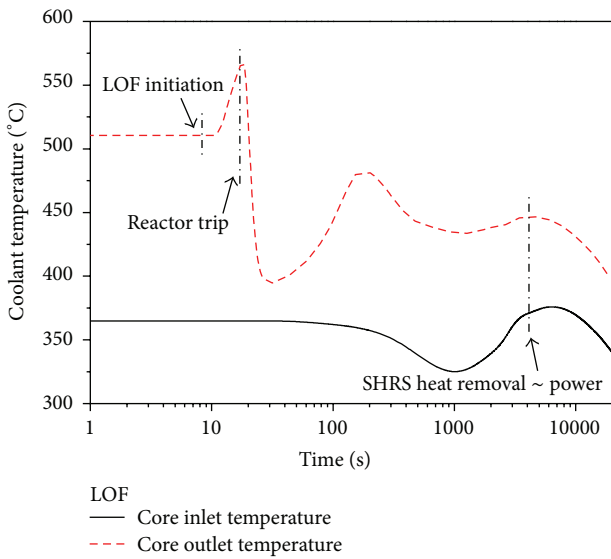


FIGURE 12: Coolant temperature behaviors for LOF event.

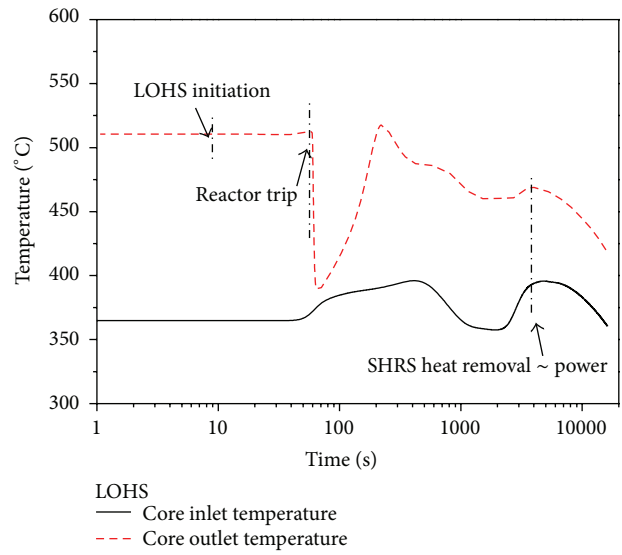


FIGURE 13: Coolant temperature behaviors for LOHS event.

reduced to one-twentieth of that in the zigzag channel PCHE by suppressing the generation of a separated flow owing to the streamlined shape of the airfoil fins [6].

To test the performances of the new design, a model heat exchanger was fabricated as shown in Figure 18 and installed in the test facility in Figure 19. The test facility is composed of a storage tank, an electromagnetic pump, an electromagnetic flow meter, an expansion tank, a heat exchanger test section, a liquid sodium line, and a cover gas line used for the charging and returning the sodium. There are two emersion heaters inside of an expansion tank as a 4 kW heat source, 2 kW each. The storage tank has a capacity of 10 liters with a cylindrical shape. An EM pump is installed vertically upright to prevent trapping the cover gas inside the pump. The material of every

component and piping is stainless steel 316 L, and only the cover gas lines are stainless steel 304. The total charged amount of sodium in the storage tank is 8 liters, and 5~6 liters of sodium were used for the experiment.

From the test results, the pressure loss was one-fifth of that of a zigzag channel which comes from the fact that the streamlined shape of airfoil fins also suppresses the generation of a separated flow. Thus, the airfoil shape fin model resulted in a much smaller pressure drop than observed in the zigzag PCHE. However, the smaller pressure loss in the experimental results than the numerical results seems to come from the uncertainties of manufacturing and fabrication but the heat transfer rate is almost similar to the numerical simulation results [7].

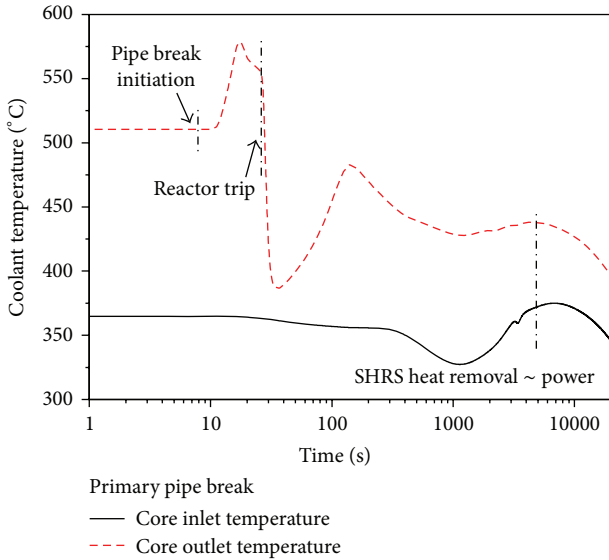


FIGURE 14: Coolant temperature behaviors for pipe break event.

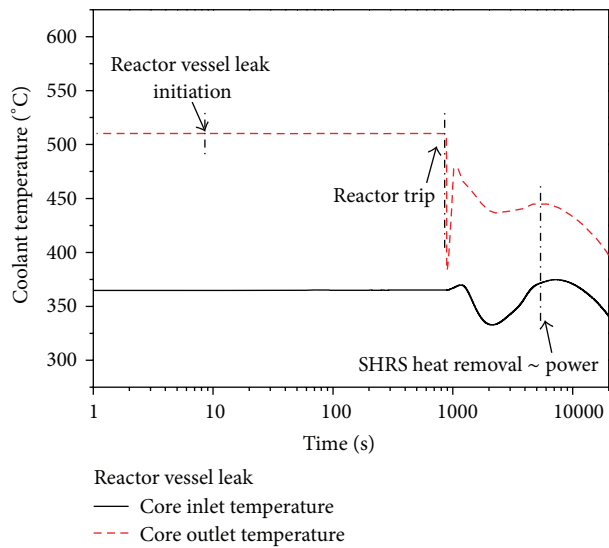


FIGURE 15: Coolant temperature behaviors for vessel leak event.

Even though the S-CO₂ Brayton cycle has many advantages, there still exists a possibility of CO₂ leakage into liquid sodium from a pressure boundary failure. The pressure boundary failure can raise technical issues such as structural integrity from the blow down of high pressure CO₂ gas into a liquid sodium space with a significant chemical reaction and the introduction of solid reaction products into the primary coolant system, which could result in the plugging of narrow flow channels.

To quantify the reaction rate for various sodium temperatures and determine the detailed kinetic parameters coupled with a mass diffusion process, a two zone model was proposed and experimental work on a surface reaction test was carried out to decide the value of the E_a/R values of Figure 20. From

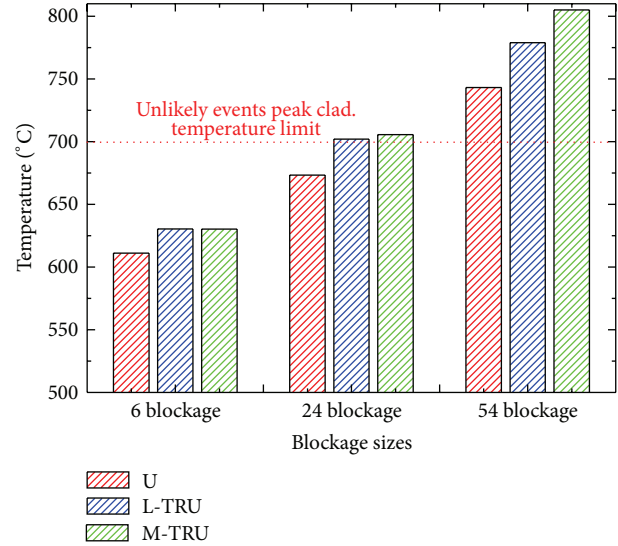


FIGURE 16: Outlet temperatures for subassembly with flow blockage.

the test results, it was found that the reaction kinetics over a sodium temperature range of 300°C to 500°C depends heavily on temperature but is not sensitive to a mass transfer effect, and it was also found that the two zone model with a 460°C threshold temperature is valid for the temperature range of a sodium fast reactor [8]. Furthermore, we need to investigate the ingress of a CO/CO₂ mixture gas into the primary coolant path and the resulting induction of a potential CO₂ void transport to the reactor core as a critical issue. The potential introduction of solid particles into the primary coolant system would also lead to a risk of plugging in narrow in-core fuel assembly channels, very narrow sections of PCHes, and so forth. Particle formation makes adequate purification systems necessary; such systems should be equipped with high-performance filters to eliminate particles and control the quantity of solid reaction products. This design feature only needs to be considered for a supercritical CO₂ system. Therefore, highly reliable detection systems are required for mitigating the CO₂ ingress event and should include several complementary devices accommodating various local conditions to cope with a sodium-CO₂ interaction [9].

3.3. Under-Sodium Viewing Technique. The ultrasonic waveguide sensor modules have been developed for potential application to under-sodium viewing of in-vessel structures in opaque liquid metal sodium. The sensor modules have a slender structure so that they can be inserted into the ISI access ports in the rotating plug. Two prototype ultrasonic waveguide sensor modules were designed and fabricated for the basic performance tests in water. One is single waveguide sensor module and the other is the dual waveguide sensor module.

The single waveguide sensor module was designed and developed for the under-sodium viewing and ranging using one channel waveguide sensor. The dual waveguide sensor module was designed and developed for the detection and

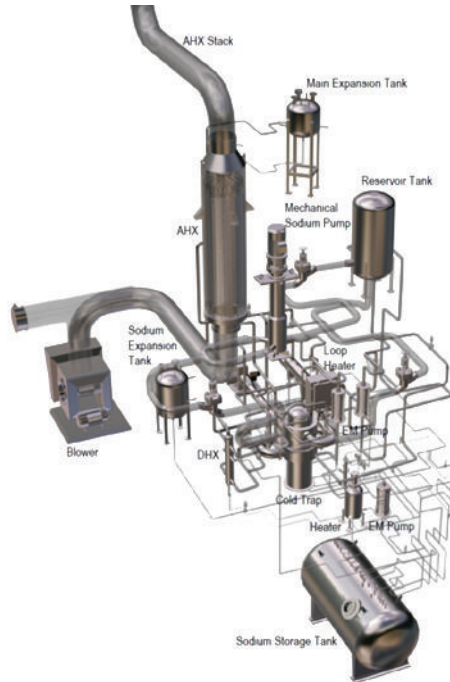


FIGURE 17: Current images of general arrangement for STELLA-1 facility.

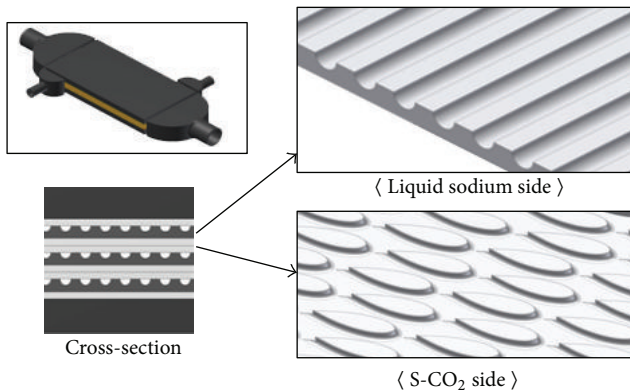


FIGURE 18: Shape of heat exchanger plates.

identification of the loose parts by the double rotation scanning of two channel waveguide sensors.

The 13 m long H-beam frame structure was designed and constructed to install the 10 m long prototype ultrasonic waveguide sensor modules in a vertical state. The prototype ultrasonic waveguide sensor modules are comprised of an ultrasonic waveguide sensor, the multistage cylindrical guide tubes, and an upper head unit. In the upper head unit, the stepping motors are installed for the rotation and vertical movement of the ultrasonic waveguide sensor.

The experimental facility is composed of a 13 m long H-beam frame, an XYZ scanner, a scanner driving module, and an ultrasonic C-scan system. Also the under-sodium inspection software program (US-MultiView) has been developed for control of the ultrasonic waveguide sensor modules and

the C-scan imaging visualization using a LabVIEW graphical programming language. The visualization imaging resolution using the 10 m long single waveguide sensor module was evaluated by a C-scan test of various targets in water. The test targets are a reactor core mockup, loose part pins, and surface slit flaws on the block. The reactor core mockup and loose part pins were clearly identified and resolved in the image, as shown in Figure 21. It was shown that a spatial resolution of the C-scan image for the detection of surface slits is about 0.8 mm.

The novel under-sodium ultrasonic waveguide sensor module has been developed for actual application in sodium. The under-sodium ultrasonic waveguide sensor where a beryllium (Be) and a nickel (Ni) are coated on the SS304 waveguide plate is suggested for the effective generation of a leaky wave in liquid sodium. The inside surface of the radiating end section of the 1.5 mm thick waveguide plate was coated with 0.25 mm thick beryllium to decrease the angle of the radiation beam and make a well-developed beam profile in sodium. The outer surface of the radiating end section was coated with 0.1 mm thick nickel and micropolished to obtain a surface roughness within $0.02 \mu\text{m}$ such that the sodium wetting was greatly enhanced.

The sodium experimental facility has been designed and constructed to demonstrate the performance of an under-sodium ultrasonic waveguide sensor module in a sodium environment condition. The sodium test facility consists of an open-type sodium test tank, a sodium storage tank, a glove box system with an antichamber, an electrical heater and control unit, and an argon circulation and cooling system. The sensitivity of the under-sodium waveguide sensor module is

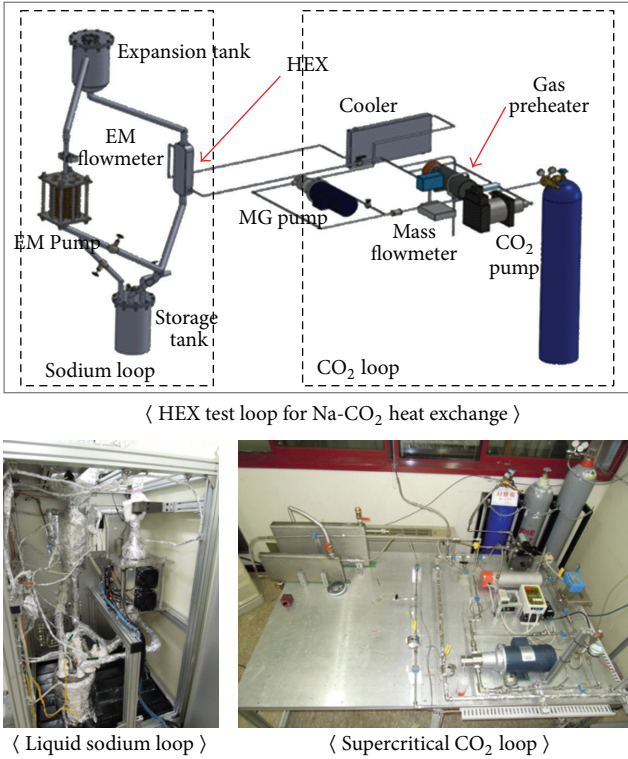


FIGURE 19: Test facility of sodium-CO₂ heat exchanger.

evaluated by a measurement of the received ultrasonic signal from a flat reflector in sodium.

Figure 22(a) shows the under-sodium C-scan test, and Figure 22(b) shows the typical ultrasonic pulse-echo signal which has the initial pulse, the reflection signal from the end section of an under-sodium waveguide sensor, and the reflection signal from the test target in sodium (250°C). The signal-to-noise (S/N) ratio of the reflection echo signal from the test target in sodium was measured as the level of 10 dB. The visualization performance tests of the 10 m long under-sodium waveguide sensor module have been carried out by a C-scan test in sodium. The test target is the SS304 block in which SFR character with 2 mm slits was engraved. As shown in Figure 22(c), the “SFR” character was clearly identified and resolved in the C-scan image.

3.4. Metal Fuel Development. Metallic fuels, such as the U-Pu-Zr alloys, have been considered as a nuclear fuel for a sodium-cooled fast reactor (SFR) related to the closed fuel cycle for managing minor actinides and reducing the amount of highly radioactive spent nuclear fuels since the 1980s. Metallic fuels fit well with such a concept owing to their high thermal conductivity, high thermal expansion, compatibility with a pyrometallurgical reprocessing scheme, and their demonstrated fabrication at the engineering scale in a remote hot cell environment [10]. A previous attempt at casting metallic fuels with americium using an injection casting furnace that had fabricated hundreds of U-Pu-Zr fuels for EBR-II resulted in a significant volatile loss of elemental

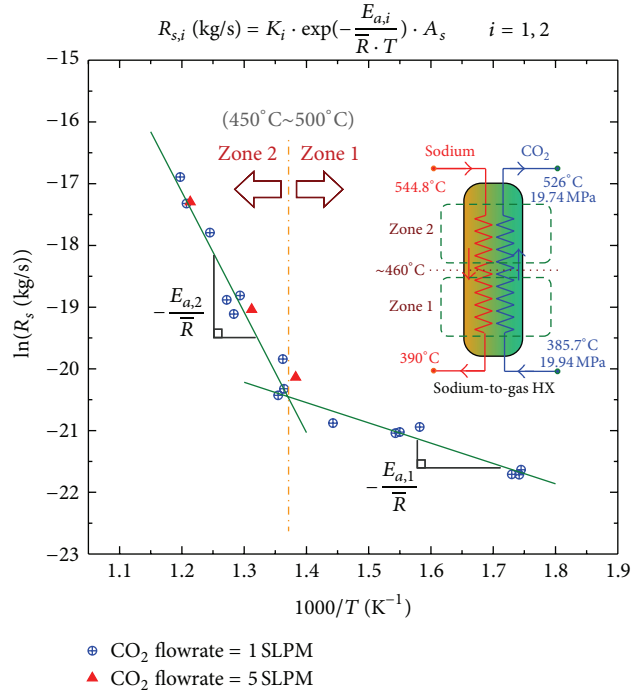


FIGURE 20: Na-CO₂ chemical interaction model.

TABLE 5: Material balance after casting of U-10 wt.% Zr-5 wt.% RE fuel slugs.

	Melting/casting part	Weight (g)	Fraction (%)
Before casting	Crucible	2,461.3	100
After casting	Crucible	122.4	5.0
After casting	Mold	2,331.7	92.7
Fuel loss		7.2	0.3

americium during the process [11]. The reference fuel for the Korean sodium-cooled fast reactor (SFR) being developed by the Korean Atomic Energy Research Institute (KAERI) is a metallic alloy. To increase the productivity and efficiency of the fuel fabrication process, waste streams must be minimized and fuel losses quantified and reduced to lower levels.

U-Zr alloy system fuel slugs were fabricated by a gravity casting method, as shown in Figure 23 [12]. After casting a considerable number of fuel slugs in the casting furnaces, the fuel loss in the melting chamber, the crucible, and the molds have been evaluated quantitatively. The elemental lumps of depleted uranium (DU), zirconium, and RE (Nd 53%, Ce 25%, Pr 16%, La 6%) were used to fabricate U-10 wt.% Zr-5 wt.% RE alloy fuel slugs. The material balance in the crucible assembly and the mold assembly after melting and casting of fuel slugs are shown in Table 5. A considerable amount of dross and melt residue remained in the crucible after melting and casting; however, most charged materials were recovered after melting and casting of the fuel slugs. The mass fraction of fuel loss relative to the charge amount after the fabrication of U-10 wt.% Zr-5 wt.% RE fuel slugs was low, about 0.3%. Based on these results, there is a high level of confidence that RE losses will be effectively controlled.

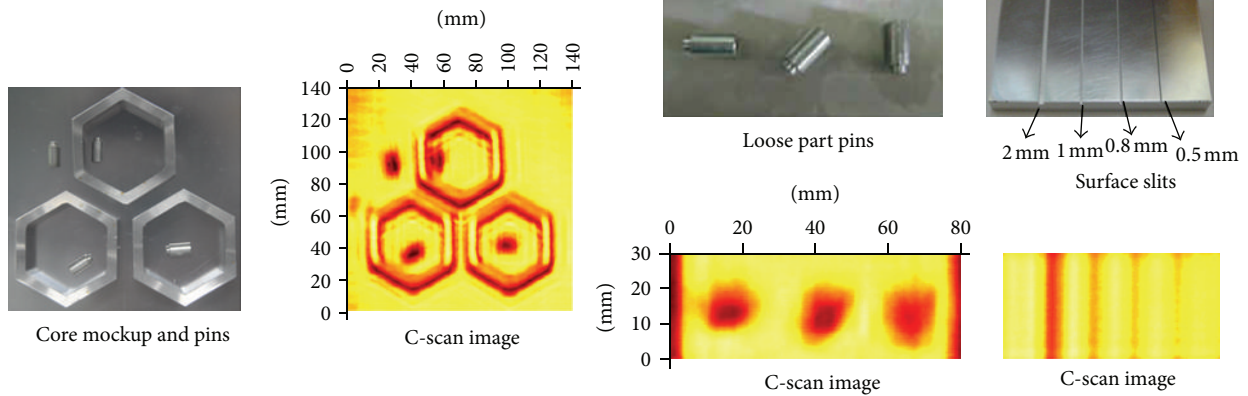


FIGURE 21: C-scan performance test results of reactor core mockup, loose parts and slits by the 10 m long ultrasonic waveguide sensor module.

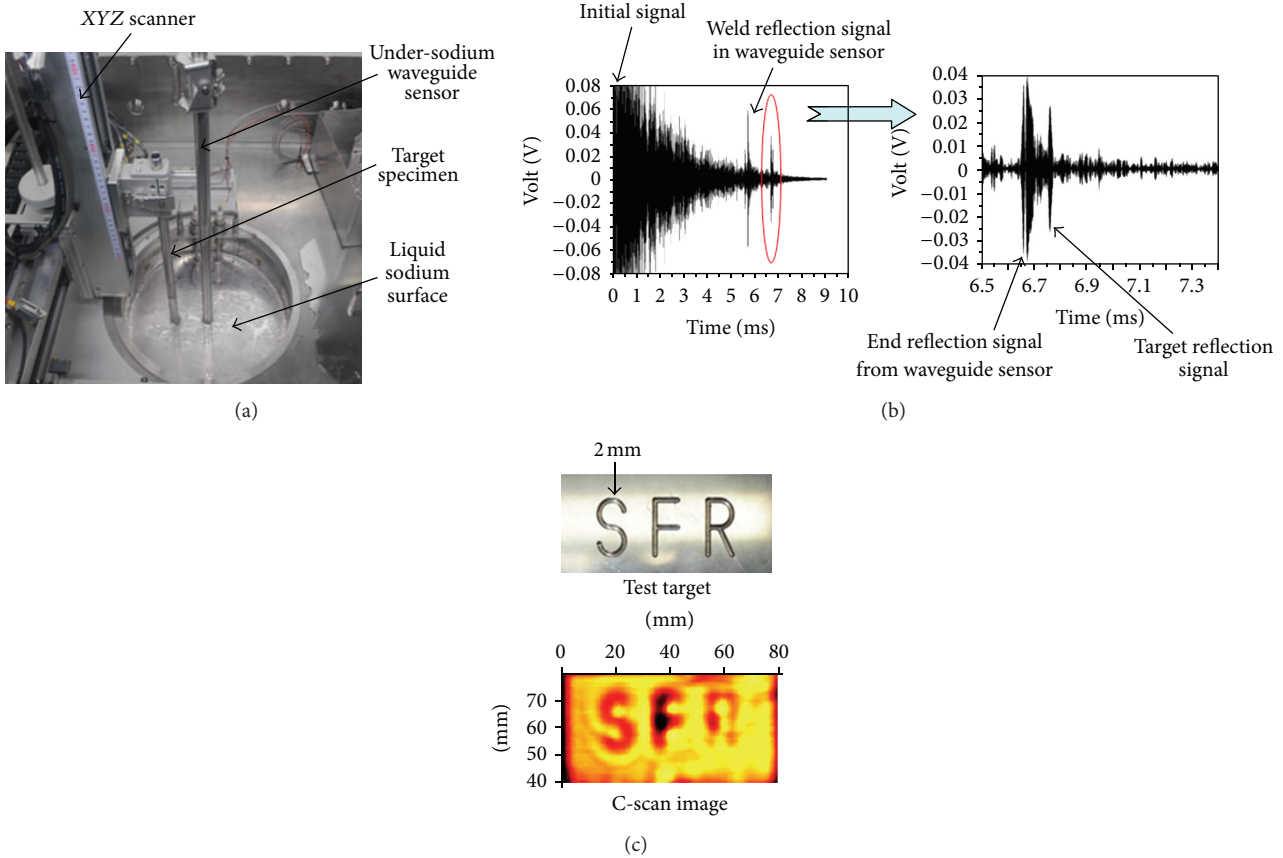


FIGURE 22: Basic performance tests of 10 m long under-sodium ultrasonic waveguide sensor in sodium.

HT9 cladding tubes were preliminary fabricated in cooperation with the steel tube making companies. The HT9 cladding tubes were examined by optical microscopy and TEM (transmission electron microscopy). The microstructure of the cladding tube was martensite + delta ferrite. Tensile tests were carried out at room temperature to 700°C. The HT9 cladding tube had yield and tensile strengths similar to the data in the literature. A burst test was performed by

pumping gas up to a burst of a 200 mm long section tube. The pressurization speed was 14 MPa/min. Burst tests were performed at room temperature to 688°C. The ultimate hoop stresses of the HT9 cladding tubes were 1135 MPa and 487 MPa at room temperature and 688°C, respectively. Tube creep tests were also carried out at 650°C. The HT9 cladding tube had creep rupture strength similar to the data in the literature (Figure 24). The tube fabrication process also is being

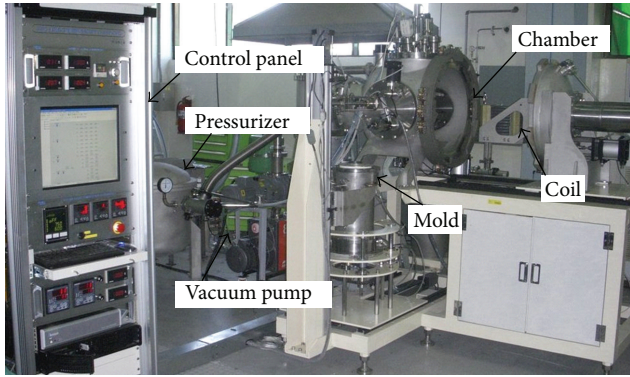


FIGURE 23: Low pressure gravity casting system.

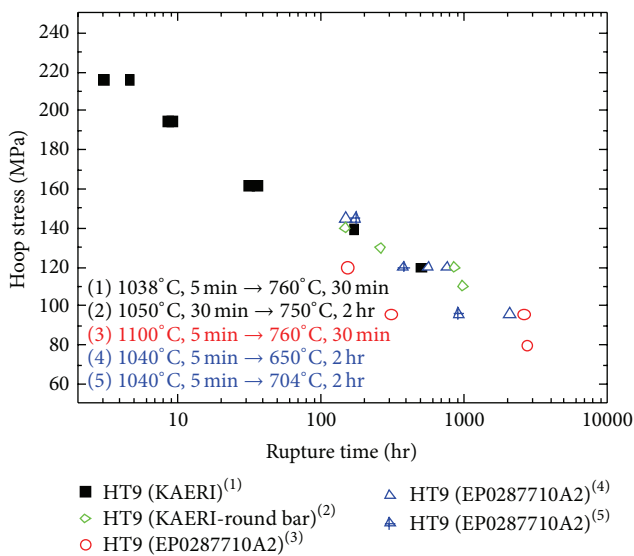


FIGURE 24: HT9 cladding tubes.

developed to improve the characteristics of the cladding tube. The HT9 cladding tube will be fabricated with an optimized fabrication process in 2013.

One of the factors that may limit burnup in metal alloy fuel is cladding wastage due to the reaction of fuel constituents and fission products with the cladding (FCCI—fuel cladding chemical interaction). To resolve this issue, diffusion couple tests were carried out by inserting barrier materials such as Zr, Nb, Ti, Mo, Ta, V, and Cr between the fuel slug and cladding. Among these barriers, V and Cr exhibited the most promising performance (Figure 25). After scoping various coating methods, Cr electroplating has been selected as one of the probable candidates because it is cost effective and easily applicable to a smaller tube geometry. To demonstrate barrier tube technology, 20 μm of Cr has uniformly plated at the inner surface of the 9Cr-2W FMS tube having 4.6 mm inner diameter and 170 mm length (Figure 25). However, it was revealed that when plating conventional condition, numerous cracks generated during the plating which acts as the diffusion path for the fuel component during the diffusion couple test. Research has focused to reduce such crack to

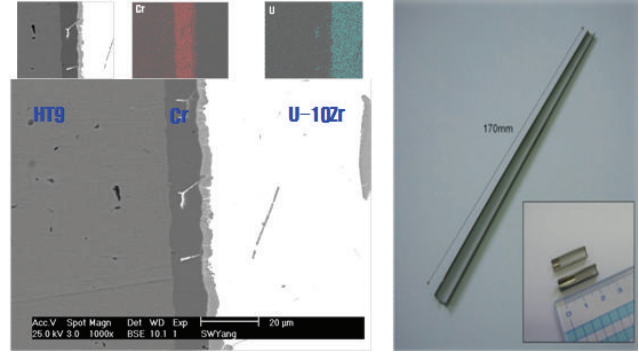


FIGURE 25: Diffusion couple test and Cr-plated barrier cladding prototype.

enhance the Cr barrier performance. A diffusion couple test showed excellent results when compared to conventional Cr plating.

The irradiation test of U-Zr-(Ce) metal fuel in HANARO was done from 2010 to 2012. HANARO is an experimental thermal reactor using water coolant. Therefore, the temperature and fission density of a fast reactor fuel were simulated, while the fast neutron flux of HANARO is much lower than fast reactor. The composition of the fuel slug is U-10% Zr-(0, 6 Ce). Its objective is to irradiate U-Zr-Ce fuel up to 3 at.%. It is also intended to identify the characteristics of the Cr barrier which is being developed to suppress a eutectic reaction between the metal fuel and cladding. The composition of the fuel slug is U-10% Zr-(0, 6 Ce). Figure 26 shows the irradiation capsule schematic diagram and coolant channel cross-section. Figure 26 also shows the irradiation history of HANARO metal fuel. The average burnup of metal fuel was about 3 at.%. The as-run linear heat rate was 240 W/cm at BOC, and decreased to 220 W/cm at EOC. The as-run analysis shows that the experiment reached an average 2.73 at.% burnup at the completion of the irradiation test. It was estimated that the maximum burnup goal was satisfied.

Postirradiation examination of the irradiated capsule and fuels is being carried out in a hot cell from 2012. Representative destructive tests are to measure or observe the fuel burnup, microstructure, fission gas release, and constituent redistribution. Nondestructive test such as gamma scans was carried out for the five rodlets. A destructive test such as the measurement of the fission gas release and a microstructure analysis is being carried out.

3.5. Development of Codes and Validations

3.5.1. Reactor Physics Experiment for TRU Burner. KAERI has been collaborating with IPPE for validating the reactor core design code system (TRANSX/TWODANT/REBUS-3), in which the self-shielded fine-group (150 groups) cross-sections are generated by TRANSX [13], and the region-wise spectrums from TWODANT [14] are subsequently used to collapse the cross sections in TRANSX. The resulting few-group (25 groups) cross sections are used for the whole core depletion calculation by REBUS-3 [15].

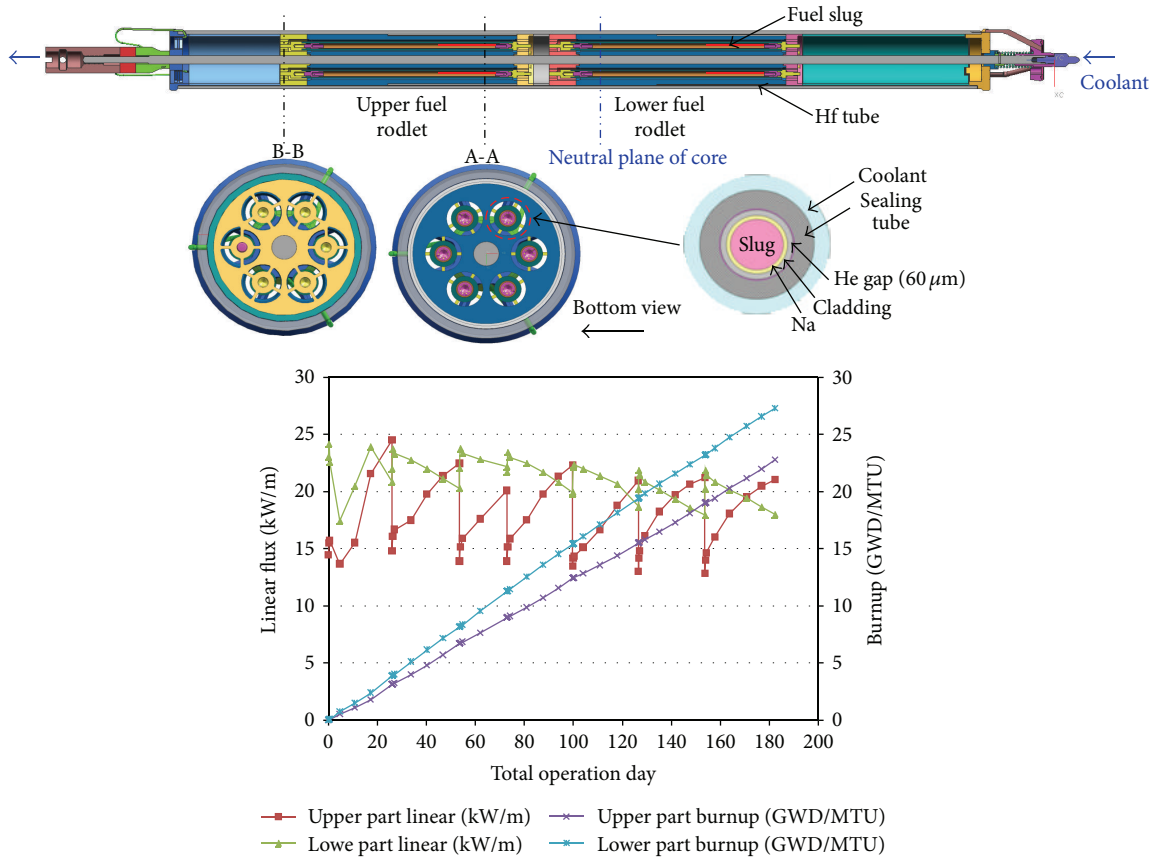


FIGURE 26: Irradiation test in HANARO.

Four critical assemblies had been constructed in BFS-1 or BFS-2 facilities, called BFS-73-1, -75-1, -76-1A, and -109-2A. The first two critical assemblies represent the early phase of the KALIMER-150 core design in the late 1990's which is a metal uranium fuel (U-10Zr) loaded sodium cooled fast reactor. The BFS-76-1A stands for the recent TRU burner core which is characterized by a core without a blanket, a low conversion ratio core, a high burnup reactivity swing, and the consequent deep insertion of a primary control rod at BOEC. Also, the BFS-109-2A demonstrates the initial uranium core, in which the metal uranium fuel is loaded without radial and axial blankets. The recent experimental work of BFS-109-2A will be finished at the end of this year (2013), and the analysis of BFS-109-2A will be finalized at 2014.

3.5.2. System Transients Analysis Code. For a successful design and analysis of a sodium-cooled fast reactor (SFR), it is necessary to have a reliable and well-proven system analysis code. To achieve this purpose, KAERI has been enhancing the modeling capability of the MARS code by adding the SFR-specific thermal-hydraulic models and reactivity feedback models. This effort resulted in the development of the MARS-LMR code. Before using the MARS-LMR code in wide applications, it is necessary to verify and validate the code models through analyses for appropriate experimental data

or analytical results. The reference design of an SFR, which is being developed in Korea, is a pool-type design. In a pool-type SFR, all the main components of the primary heat transport system are arranged in two big sodium volumes: a hot pool and a cold pool. During the transients in a pool-type SFR, the thermal-hydraulic phenomena in the pools become highly complex due to the formation of mixing, stratification and existence of buoyancy force. Therefore, it is necessary to have flexible modeling including a multidimensional approach to enhance the accuracy of a safety evaluation.

Recently, KAERI evaluated the capability of multidimensional modeling for large pools using available test data. One of the important data sets suitable for this evaluation was provided from phenix end-of-life (EOL) natural circulation tests. In the MARS-LMR modeling, the hot pool region from the core outlet to the inlet of IHXs has been divided into 8 axial nodes, 4 radial nodes, and 6 azimuthal nodes, as shown in Figure 27. Further, the cold pool region has been modeled with 12 axial nodes, 1 radial node, and 9 azimuthal nodes. The remarkable results of this multidimensional pool modeling are compared with one-dimensional modeling in Figure 28. It was found that the overpredicted core outlet temperature with a one-dimensional approach is diminished in the multidimensional calculation. This result indicated that the multidimensional effect in the pool behaviors is important in a pool-type SFR.

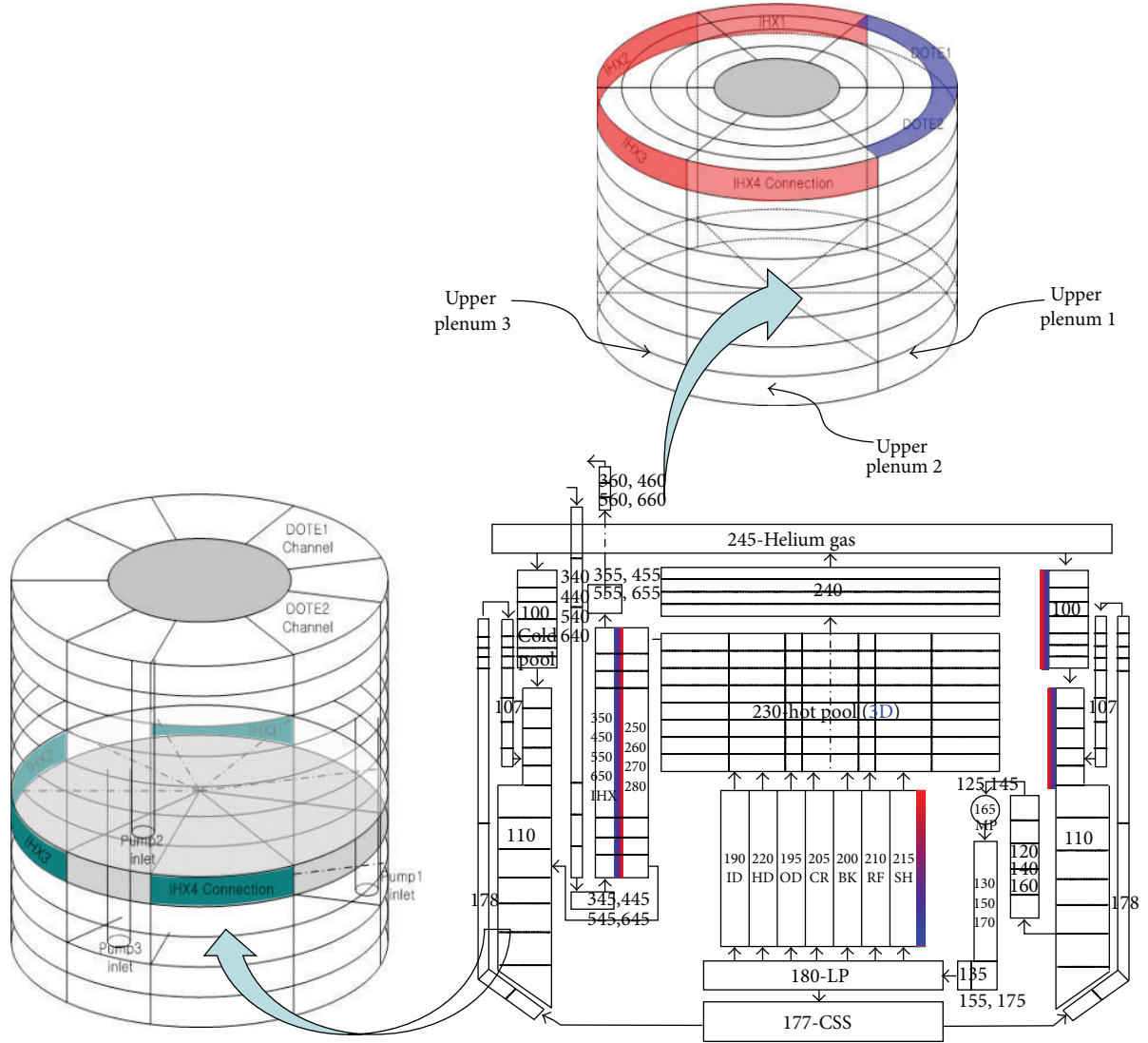


FIGURE 27: Nodalization of phenix for MARS-LMR simulation.

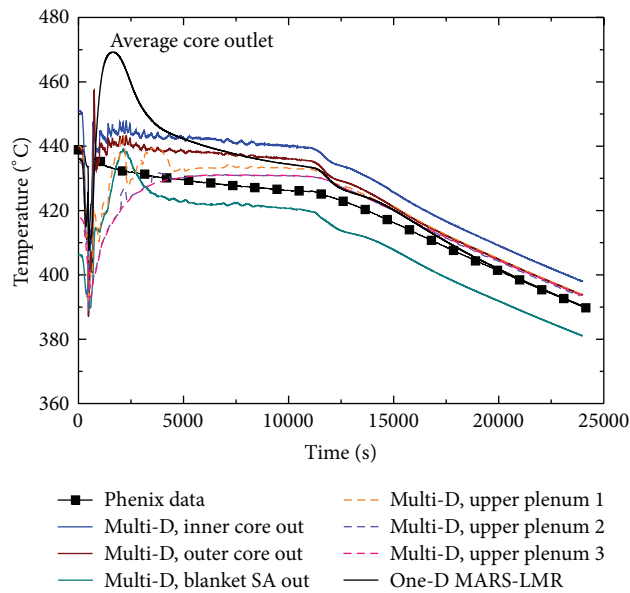


FIGURE 28: Predicted core outlet temperature.

4. Summary

In Korea, most energy resource supplies depend on imports because the available energy resources are extremely limited. Therefore, the portion of nuclear power in electricity generation is expected to be continuously increased in the years to come in achieving energy self-reliance. A fast reactor is the most promising future nuclear power plant because of efficient usage of uranium and reduction of radioactive waste. In particular, a sodium cooled Fast reactor (SFR) has been focused as a new generation of nuclear power plants in Korea.

Since 1977, the basic key technology development for an SFR has been continued, and the design concepts of KALIMER-150 and KARIMER-600 have been successfully achieved. In 2008, KAEC approved a long-term advanced SFR R&D plan which aims at the construction of an Advanced SFR prototype plant by 2028 in association with the pyroprocess technology development. To support this R&D plan, KAERI has been focusing on the development of an advanced design concept of a burner reactor, which satisfies the future goals of safety, economics, sustainability, and proliferation resistance. In addition, R&D activities have been worked to achieve a safe and reliable advanced SFR design, such as large scale sodium thermal-hydraulic test facilities, a supercritical CO₂ Brayton cycle system, an under-sodium viewing technique, metal fuel, and a safety analysis code.

Acknowledgment

This work was supported by Nuclear Research & Development Program of the National Research Foundation Grant funded by the Ministry of Education, Science and Technology in Korea.

References

- [1] "The 5th basic plan for long term," Electricity Supply and Demand (2010–2024) 2010-490, Ministry of Knowledge Economy, 2010.
- [2] D. H. Hahn, "Status of the fast reactor technology development program in Korea," in *Proceedings of the 40th Technical Working Group on Fast Reactors Meeting (TWG-FR '07)*, Tsuruga, Japan, May 2007.
- [3] D. Hahn et al., "KALIMER-600 conceptual design report," KAERI/TR-3381/2007, Korea Atomic Energy Research Institute, Daejeon, Korea, 2007.
- [4] H. Song, S. J. Kim, H. Y. Jeong, and Y. I. Kim, "Design studies on a large-scale sodium-cooled tru burner," in *Proceedings of the International Conference on Advances in Nuclear Power Plants (ICAPP '08)*, pp. 450–457, June 2008.
- [5] IAEA, Fast Reactor Database 2006 Update, IAEA-TECDOC-1531, 2006.
- [6] D. E. Kim, M. H. Kim, J. E. Cha, and S. O. Kim, "Numerical investigation on thermal-hydraulic performance of new printed circuit heat exchanger model," *Nuclear Engineering and Design*, vol. 238, no. 12, pp. 3269–3276, 2008.
- [7] J. E. Cha et al., "Report on the design concepts of Na/CO₂ heat exchangers," Gen IV International Forum Report SFR/CDBOP/2011/015, 2011.
- [8] J.-H. Eoh, H. C. No, Y. H. Yoo, and S. O. Kim, "Sodium-CO₂ interaction in a supercritical CO₂ power conversion system coupled with a sodium fast reactor," *Nuclear Technology*, vol. 173, no. 2, pp. 99–114, 2011.
- [9] J. H. Eoh, H. C. No, Y. H. Yoo, J. Y. Jeong, J. M. Kim, and S. O. Kim, "Wastage and self-plugging by a potential CO₂ ingress in a supercritical CO₂ power conversion system of an SFR," *Journal of Nuclear Science and Technology*, vol. 47, no. 11, pp. 1023–1036, 2010.
- [10] Y. I. Chang, "Technical rationale for metal fuel in fast reactor," *Nuclear Engineering and Technology*, vol. 39, no. 3, 2007.
- [11] C. L. Trybus, "Injection casting of U-Zr-Mn, surrogate alloy for U-Pu-Zr-Am-Np," *Journal of Nuclear Materials*, vol. 224, p. 305, 1995.
- [12] C. T. Lee et al., "Casting technology development for SFR metallic fuel," in *Proceedings of Global-2009*, Paris, France, September 2009.
- [13] R. E. Macfarlane, "TRANSX 2: a code for interfacing MATXS cross-section libraries to nuclear transport codes," LA-12312-MS, 1992.
- [14] R. E. Alcouffe et al., "DANTSYS: a diffusion accelerated neutral particle transport code system," LA-12969-M, 1995.
- [15] B. J. Toppel, "A user's guide for the REBUS-3 fuel cycle analysis capability," ANL-83-2, 1983.

Research Article

Modeling Forced Flow Chemical Vapor Infiltration Fabrication of SiC-SiC Composites for Advanced Nuclear Reactors

Christian P. Deck, H. E. Khalifa, B. Sammuli, and C. A. Back

General Atomics, P.O. Box 85608, San Diego, CA 92186-5608, USA

Correspondence should be addressed to Christian P. Deck; christian.deck@ga.com

Received 21 November 2012; Accepted 5 February 2013

Academic Editor: Hangbok Choi

Copyright © 2013 Christian P. Deck et al. This is an open access article distributed under the Creative Commons Attribution License, which permits unrestricted use, distribution, and reproduction in any medium, provided the original work is properly cited.

Silicon carbide fiber/silicon carbide matrix (SiC-SiC) composites exhibit remarkable material properties, including high temperature strength and stability under irradiation. These qualities have made SiC-SiC composites extremely desirable for use in advanced nuclear reactor concepts, where higher operating temperatures and longer lives require performance improvements over conventional metal alloys. However, fabrication efficiency advances need to be achieved. SiC composites are typically produced using chemical vapor infiltration (CVI), where gas phase precursors flow into the fiber preform and react to form a solid SiC matrix. Forced flow CVI utilizes a pressure gradient to more effectively transport reactants into the composite, reducing fabrication time. The fabrication parameters must be well understood to ensure that the resulting composite has a high density and good performance. To help optimize this process, a computer model was developed. This model simulates the transport of the SiC precursors, the deposition of SiC matrix on the fiber surfaces, and the effects of byproducts on the process. Critical process parameters, such as the temperature and reactant concentration, were simulated to identify infiltration conditions which maximize composite density while minimizing the fabrication time.

1. Introduction

Advanced nuclear reactor concepts promise significant improvements over current technology, including increased efficiency, higher fuel burn-up, and longer core life. However, these features put increasing demands on the performance of fuel cladding and other reactor components, and materials must be developed for these reactors that are both resistant to high levels of irradiation damage and offer accident tolerant behavior. Silicon carbide fiber/silicon carbide matrix (SiC-SiC) composites offer many desirable properties, and are being considered for use in advanced nuclear reactor designs, such as the General Atomics Energy Multiplier Module (EM²) concept. Experiments on monolithic silicon carbide have shown that it maintains excellent mechanical performance in harsh, high temperature, and high irradiation rate environments, but its low toughness limits its application [1–3]. High purity and high quality SiC fiber-reinforced composites have shown similar performance under harsh

conditions but offer improved toughness to address this limitation. In these composites, a silicon carbide matrix is deposited within a preform composed of high purity, near-stoichiometric silicon carbide fibers, such as Tyranno-SA fibers (Ube Industries, Ube, Japan) or Hi-Nicalon type S fibers (Nippon Carbon Co., Ltd., Tokyo, Japan). The performance of these composites has the potential to enable the development and construction of high temperature, long-life advanced reactor concepts.

Several techniques have been developed to fabricate SiC matrix composite materials, including melt infiltration, polymer infiltration and pyrolysis, and chemical vapor infiltration (CVI) [4–6]. However, in order to achieve good irradiation resistance, very high purity material is required, and CVI is the most reliable approach to produce a sufficiently pure matrix for nuclear applications. In CVI, a silicon carbide precursor (or precursors) is introduced into a high temperature chamber in the gas phase. This is commonly done under vacuum, and the precursors are allowed to diffuse

into the preform and chemically react, forming a silicon carbide matrix within the sample. The most commonly used precursor is methyltrichlorosilane (CH_3SiCl_3), which is mixed with hydrogen and decomposes to form silicon carbide according to (1) [1]



While CVI produces a very high purity matrix, the deposition process is dependent on the diffusion of reactants into the fiber preform, and a slow reaction rate can be desirable to ensure uniform transport of reactants throughout the fiber preform. The reaction rate can be controlled through selection of the deposition parameters; for example, higher process temperatures generally lead to more rapid reaction and higher deposition rates. Uniform matrix deposition is essential to achieve high composite density and good material properties, but by slowing the reaction rate, the fabrication process may require long infiltration times. For fiber-reinforced composite materials, small voids between fibers within the tows are vulnerable to being closed off by matrix deposits on the tow surface. Because of this, density uniformity is especially important for thicker samples, and reduced density can lead to reduced material performance. Often, a density gradient will exist in the composite, where the densest regions are located near the surface (where the precursors first reach the composite), and the least dense areas are located towards the center, especially inside fiber tows. A schematic of this conventional CVI is shown in Figure 1(a).

Several approaches to reduce fabrication time have been reported in the literature. Two of the more promising routes are thermal gradient chemical vapor infiltration and pressure gradient chemical vapor infiltration (also called forced flow CVI). In thermal gradient CVI, modifications to both the CVI chamber and fixtures are designed to establish a temperature gradient in the opposite direction of the diffusion-related reactant concentration gradient. This allows for faster reaction rates near the center of the composite, which helps offset the reduction in precursor concentration, and reduces the overall infiltration time needed to make the composite. In forced flow CVI (FFCVI), a pressure gradient is established to enhance reactant transport into the fiber preform (compared to transport via diffusion only). By improving transport of reactants into the preform, the depletion of the precursors is reduced, and conditions allowing for faster deposition rates can be used while still achieving acceptable final composite densities. However, this approach must be carefully controlled, as variations in pressure in different regions of the composite can have detrimental effects on the matrix infiltration uniformity. In addition, it is necessary to hold the sample in more complicated fixtures to direct the flow of reactants (Figure 1(b)).

In order to help understand the effects of different parameters on the composite infiltration process, the diffusion and chemical reaction of the precursors can be modeled. Several approaches have been reported in the literature, including modeling chemical compositions of the gas and solid phases [7], modeling diffusion through a fibrous preform [8], and

simulating precursor concentrations on a sample in a typical reactor [9]. These models can be used to consider the effects of different reaction parameters, although the trends predicted by some models have not always been consistent with experimentally observed results, and simplified models cannot account for all the phenomena occurring during deposition.

In this work, SiC-SiC composites were fabricated by chemical vapor infiltration, and an empirical model was developed to simulate forced-flow CVI. This work expands on a model which we had previously developed [10] to simulate the infiltration process at the fiber scale ($\sim 10\text{--}100\ \mu\text{m}$). In these current results, the effects of forced flow are included in the simulation. The infiltration simulated by the model was qualitatively similar to that observed in the experiments, and the effects of different fabrication parameters were investigated.

2. Sample Fabrication and Characterization

SiC matrix composites were fabricated under a range of conditions, including forced flow CVI and conventional CVI (with no pressure gradient). Various composite geometries can be fabricated; however, for most of this work, the material was produced as larger planar sheets that were then cut into samples appropriate for different characterization techniques.

The sample fabrication process has been described previously [10]. Briefly, SiC fiber fabric is cut to shape and stacked to achieve a nominally 1 mm thick preform of $\sim 35\%$ fiber volume fraction. This fiber preform is then processed under vacuum and at elevated temperatures ($900\text{--}1100^\circ\text{C}$) to form a composite using chemical vapor infiltration. This infiltration process is used to first deposit a thin pyrolytic carbon interface layer over the fibers and then infiltrate the SiC matrix. The silicon carbide matrix was deposited from a dilute reactant mixture composed of methyltrichlorosilane (MTS) evaporated into a hydrogen flow.

Samples were infiltrated using both conventional (isobaric) CVI and forced flow CVI, and all samples were weighed prior to infiltration and at regular intervals during infiltration to monitor weight gain as a function of processing time. Forced flow samples were processed until the pressure differential through the sample increased approximately tenfold from the starting pressure drop, which varied with the fiber preform size and structure. Depending on the deposition conditions, this process took up to 3 days. In order to allow a more direct comparison, the durations of the conventional CVI runs were selected to yield samples with similar densities to the forced flow samples, and these runs took significantly longer than the forced flow runs. The relative sample density was calculated from the measured sample volume and mass and was compared to the maximum theoretical density of $3.2\ \text{g/cm}^3$ for SiC fiber-reinforced samples.

3. Modeling SiC Matrix Infiltration

In order to help optimize infiltration process parameters, a two-dimensional computer simulation was developed to

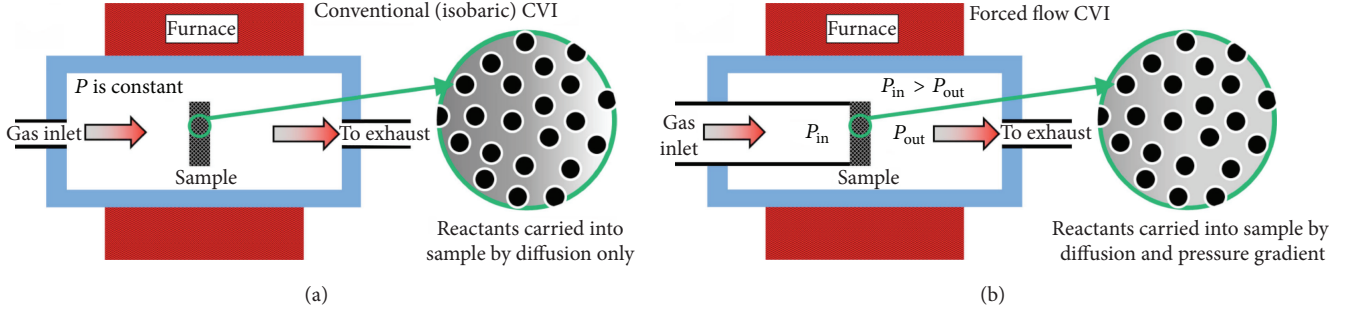


FIGURE 1: (a) Schematic of conventional (isobaric) CVI and (b) schematic of forced flow or pressure gradient CVI.

model the effects of different deposition conditions on the infiltration process. To accurately simulate the matrix infiltration process, the transport of the reactants through the fiber preform must be followed. However, due to the size of the fibers (7–10 μm diameter), a system including several fibers would be much too large (approximately 100 μm) to practically model and track the motions of individual reactant molecules. Typical Knudsen numbers ($\text{Kn} = \text{mean free path } \lambda, \text{ divided by characteristic length } L$) for deposition conditions are also too large ($\lambda/L \gg 1$) to use standard computational fluid flow codes to model the infiltration. In order to address these restrictions and accommodate the larger system size, the model uses a direct simulation Monte Carlo (DSMC) solver with the OpenFOAM toolbox.

With the DSMC approach, statistically representative parcels are tracked, rather than individual molecules, and each parcel contains many particles. During the simulation of conventional (isobaric) infiltration, the initial velocity of each parcel is obtained from a thermal velocity distribution function. In the simulation of forced flow infiltration, a net velocity is applied to the parcels in the model, with this velocity representing the effect of a pressure gradient on the reactant gas flow. In both cases, the subsequent motions of the parcels are tracked ballistically, accounting for collisions with walls and other particles.

In addition to tracking the motion of different parcels, the DSMC solver also tracks the reaction of MTS on surfaces to produce SiC. The general growth rate equation used in the model is $G = S_{\text{MTS}} F_{\text{MTS}}$, where G is the growth rate, S_{MTS} is the sticking coefficient, or probability that MTS will react to form silicon carbide on a surface, and F_{MTS} is the flux of MTS on that surface. The sticking coefficient of MTS is given by $S_{\text{MTS}}^0 = A \exp(-E_{a\text{MTS}}/RT) \sqrt{P_{\text{H}_2}}$, where P_{H_2} is the partial pressure of hydrogen in the system, $E_{a\text{MTS}}$ is the activation energy for MTS decomposition, R is the natural gas constant, T is the temperature, and A is a constant [11]. This SiC deposition is modeled by depleting the number of MTS particles in each parcel in contact with a surface. The simulation also accounts for the presence of HCl byproducts, which have been shown both experimentally and in other models to inhibit the deposition process [11–14]. HCl can occupy surface sites, and the probability of MTS conversion to silicon carbide is reduced by $1 - \theta/\theta_m$, in proportion to the surface area covered by adsorbed HCl (θ/θ_m).

As MTS decomposes on the surface to form SiC, γ is the fraction of HCl that remains on the surface, and the HCl adsorption rate is given by (2), where S_{HCl}^0 is the sticking coefficient of HCl on the surface and F_{HCl} is the flux of HCl particles on the surface:

$$\frac{d\theta}{dt} = (S_{\text{MTS}}^0 \gamma F_{\text{MTS}} + S_{\text{HCl}}^0 F_{\text{HCl}}) \left(1 - \frac{\theta}{\theta_m}\right). \quad (2)$$

HCl will also desorb from the surface according to $d\theta/dt = -\nu \theta \exp(-E_{a\text{HCl}}/RT)$, where $E_{a\text{HCl}}$ is the activation energy for the desorption of HCl and ν is a rate constant. The steady state growth rate is given by (3), where C is a constant:

$$G = \frac{S_{\text{MTS}}^0 F_{\text{MTS}} C}{1 + (\gamma S_{\text{MTS}}^0 F_{\text{MTS}} + S_{\text{HCl}}^0 F_{\text{HCl}}) / \theta_m \nu \exp(-E_{a\text{HCl}}/RT)}. \quad (3)$$

In this equation, the activation energies are taken from the literature, with $E_{a\text{MTS}} = 188 \text{ kJ/mol}$ [12] and $E_{a\text{HCl}} = 268 \text{ kJ/mol}$ [13]. SiC deposition experiments were performed across a range of different process conditions, and coating rates were measured and compared to the simulation in order to empirically fit values for the MTS and HCl sticking coefficients and γ . For each collision between a given parcel and a surface, the modified DSMC solver uses the growth rate equation to determine the amount of MTS that reacts to form SiC. The solver also tracks the HCl generated by the MTS decomposition, of which a fraction remains on the surface (given by γ), and the remainder is added to the parcel. The solver represents the deposited SiC by adding elements to fiber surfaces upon which SiC has been deposited, increasing the fiber diameter and reducing the open pore volume.

4. Results and Discussion

4.1. Forced Flow Chemical Vapor Infiltration. Forced flow chemical vapor infiltration offers a means to increase transport of reactants through the fiber preform during the matrix infiltration process. As a result, process conditions that allow for more rapid deposition can be used, such as higher temperatures and MTS partial pressures. This can reduce process time, while the pressure gradient helps ensure matrix deposition uniformity.

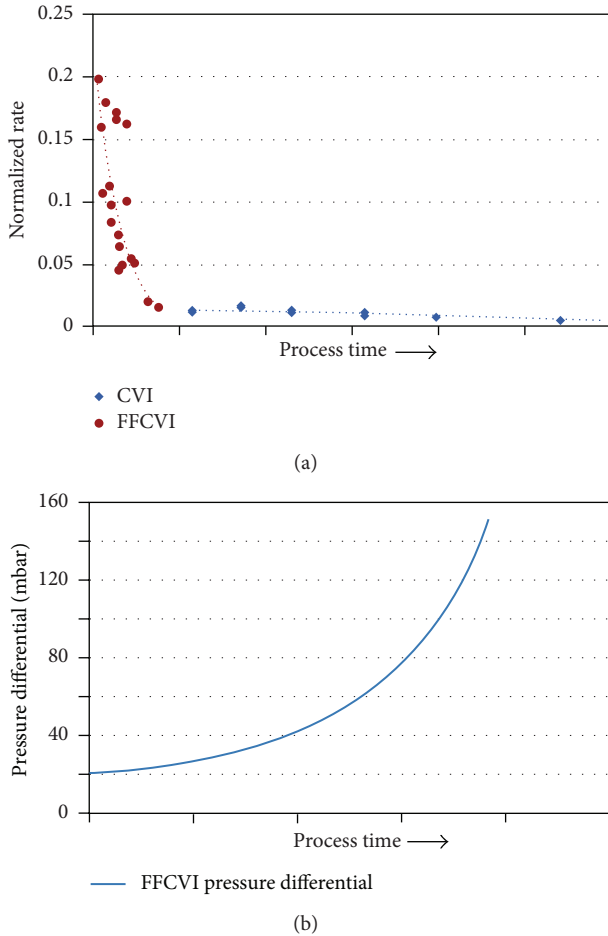


FIGURE 2: (a) Plot of normalized rate of mass gain as a function of process time for conventional CVI and FFCVI and (b) plot of increasing pressure differential across sample observed during FFCVI.

The infiltration process was interrupted at several intervals in order to measure the mass gain of the samples and remove portions for characterization. It was found that the infiltration process could be started and stopped in this manner without causing discontinuities in the matrix. Figure 2(a) shows a typical rate of mass gain for conventional CVI and forced flow CVI. Also plotted is the pressure differential between the inlet and exhaust sides of the sample in the forced flow case (Figure 2(b)). As a result of the improved reactant transport into the sample during FFCVI, higher deposition rates can be used while still achieving reasonable infiltration uniformity.

For both FFCVI and isobaric CVI, the rate of mass gain typically starts out high, and then drops as the infiltration process continues. The amount of SiC deposited on the samples is a function of CVI conditions but also of the available surface area of the substrate. Initially, the fiber preform has a very high surface area, and consequently, a high rate of mass gain is observed. However, as the matrix fills in the voids within the preform, some regions become closed off, trapping voids within the sample. This reduces the available surface area as well as the rate of mass gain.

In conventional CVI, very low deposition rates are used to allow sufficient reactant diffusion into the preform. The added pressure gradient in FFCVI allows for higher deposition rates to be achieved while maintaining uniformity through the sample. If process conditions are changed in a conventional CVI process to achieve deposition rates comparable to FFCVI, a significant SiC deposition gradient develops from the surface of the sample (the surface exposed to the reactant flow) towards the center of the sample (Figure 3(a)). The gradient is much reduced when a forced flow configuration is used to achieve similar deposition rates (Figures 3(b) and 3(c)).

In both conventional and forced flow CVI, the rate of mass gain drops with time, as pores are closed off and the available surface area for deposition is reduced. In conventional CVI, the reactants are flowing around the sample, so SiC deposition on the sample and this eventual pore closure do not affect the process pressure. However, in forced flow CVI, all reactants are forced to flow through the sample, and as the open porosity begins to be filled or closed off, the pathways for gas flow are reduced, and the pressure differential across the samples increases. This pressure difference increases rapidly towards the end of the process and can result in the upstream side of the sample seeing significantly higher pressures than the exhaust. As the deposition rate can be strongly dependent on reactant partial pressures, this increasing pressure differential can lead to nonuniform deposition (Figure 4). This can result in excess SiC build-up on the inlet side of the composite and can also result in deposition conditions that produce nonstoichiometric, silicon-rich SiC.

4.2. Simulation of SiC Matrix Deposition. Although forced flow CVI can be used to potentially provide increased deposition rates, the conditions must be understood to ensure uniform infiltration. To more rapidly investigate the effects of various process parameters and sample geometries on the fabrication process, a computer model was used to simulate SiC infiltration into an idealized fiber arrangement. The influence of different process parameters was explored in the context of the maximum simulated composite density achieved and the infiltration duration required to reach that density. The end of the simulation was defined as the time at which the reactant transport pathways to the inside fibers became completely blocked off; after this point, any additional deposition would occur only on the surface, and the composite density and pore volume would no longer change.

Prior to the start of infiltration, the structure of the composite consists of bundles or tows of hundreds or thousands of SiC fibers, and these tows are woven into the desired macroscopic component geometry. The simulation developed in this work focuses on the deposition at the microscale, and the geometry and boundary conditions were selected to provide an approximation of an actual fiber bundle. Although transport of reactants within the CVD chamber and between adjacent tows (on the macroscopic scale) is also important to the overall composite uniformity, running the simulation

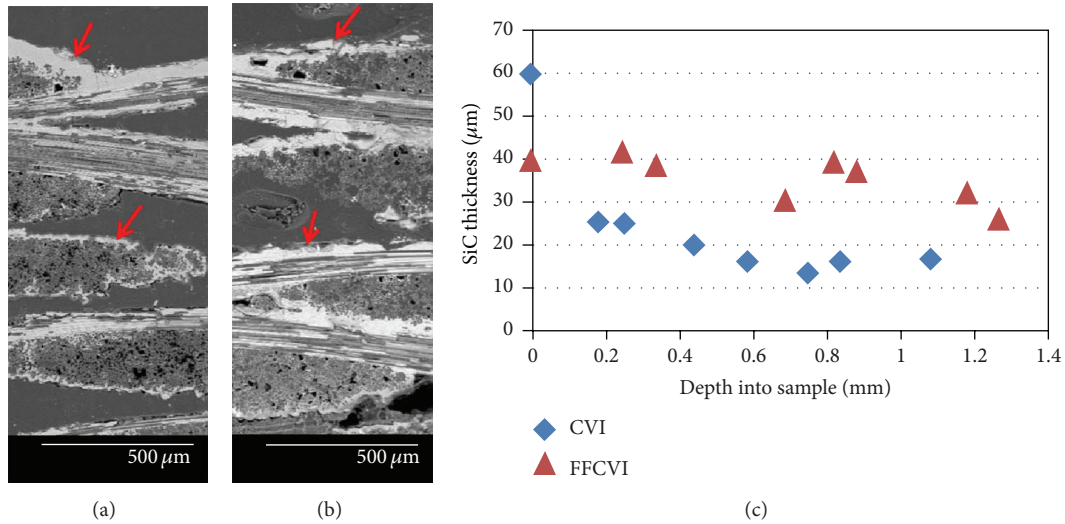


FIGURE 3: (a) Cross-section of fiber preform partially infiltrated with higher rate isobaric CVI, (b) cross-section of fiber preform partially infiltrated with forced flow CVI, and (c) SiC deposit thickness as a function of depth into the sample for CVI and FFCVI.

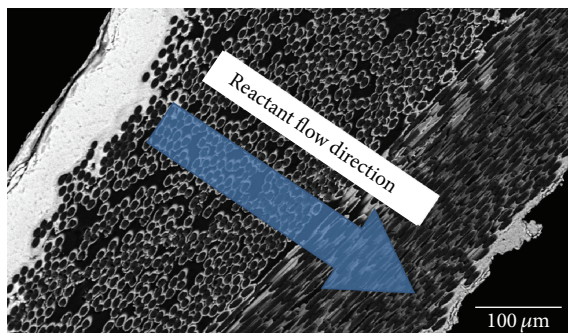


FIGURE 4: SiC build-up on the upstream side of the sample caused by increasing reactant pressure and varying deposition conditions on the upstream side of the sample during FFCVI.

at this scale would be too computationally intensive to be practical.

Infiltration into the fiber tows was simulated with a narrow column of fiber cross-sections. Fiber spacing was kept constant, although the simulation approach could also be used to model a more realistic system or randomly arranged fibers. The fiber tows used in these composites have elliptical cross-sections, and the column of fibers used in the simulation represents approximately half the yarn minor axis, as shown in Figure 5. Reactant gases were introduced from one side, and a net velocity could be applied to the reactants to simulate forced flow conditions. The boundary conditions used for the other sides of the system are shown in Figure 5(c).

With the empirically determined reactant sticking coefficients, the simulated SiC infiltration is qualitatively similar to the experimentally observed deposition gradient, as shown in Figure 5(d). For this comparison, the coating thickness was measured as a function of position within the fiber bundle, and the model reproduced the variation in coating thickness away from the tow surface that was observed in

the actual sample. The simulation was then used to model the infiltration for both isobaric and forced flow conditions and to investigate the effects of different coating parameters on the deposition process. Certain parameters (including temperature, pressure, and MTS concentration) were varied within ranges that coincided with the typical conditions used in the experiments.

4.2.1. Reactant Velocity Effects. In the model, reactants can be introduced with a net velocity which can be set for different forced flow conditions or reduced to zero to represent isobaric (conventional) CVI. At very low velocities, reactant transport into the fiber preform occurs due to diffusion. If this transport is slow relative to the reaction rate of the precursors, SiC will be deposited towards the outer surface of the sample, and a large deposition gradient will lead to a composite with low final density and high internal porosity. Slow deposition rates are needed to achieve higher final composite densities.

If the reactants have a positive net velocity, this provides additional means to facilitate their transport into the fiber preform. At moderate velocities, the time scale for transport through the sample is comparable to the reaction rate of the precursors, and deposition uniformity is improved. This allows a faster reaction rate to be used which reduces composite fabrication time while maintaining improved uniformity. However, the simulation indicated that if the reactant velocities are very high, transport through the fiber preform can be too fast, and the short residence time can reduce the deposition uniformity. This effect could be exaggerated in our simulation, as the system volume is very small relative to an actual sample (which would be thicker and contain many thousands of fibers). Thus, a given velocity in the model could be sufficient to transport the precursors out of the system before they can completely react, whereas in an actual sample, these unreacted precursors would react and deposit elsewhere.

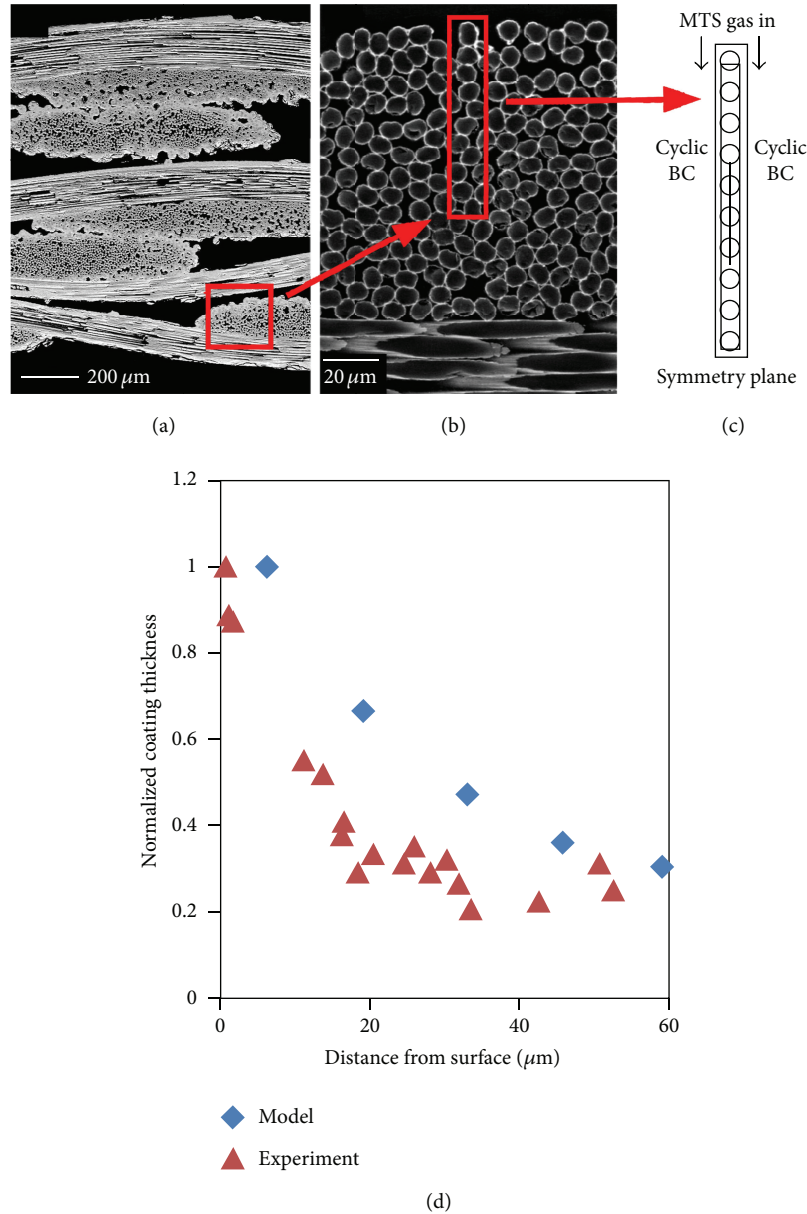


FIGURE 5: (a) Cross-section of stacked fabric layers, (b) cross-section of fiber bundle, (c) model geometry showing MTS introduction and boundary conditions, and (d) comparison between simulated and experimentally observed SiC deposition gradients into the fiber preform.

To examine the influence of reactant velocity, the model was run with zero, moderate, and fast reactant velocities. The precursor partial pressure was held constant, and infiltration was simulated at two different SiC deposition temperatures (900°C and 1100°C). These temperatures are in the range of infiltration temperatures commonly reported in the literature [5]. Reactant velocity was found to have a significant effect on the deposition uniformity and the corresponding final composite relative density. For both slow and moderate reactant velocities, similar deposition was seen at the surface. However, the improved reactant transport achieved by forced flow CVI was apparent in the simulated deposition inside the fiber preform. Moderate velocities (which could be obtained under appropriate FFCVI conditions) provided the highest

relative density and most uniform infiltration, as shown in Figure 6(a). The effects of reactant velocity were similar for both temperatures modeled (Figure 6(b)).

4.2.2. Reactant Concentration Effects. The reactant partial pressure also plays an important role in the infiltration process. The MTS flux at the fiber surface is proportional to the MTS partial pressure, and the growth rate increases with the increasing flux (according to (3)). In the model, the reactant concentration is varied by setting the MTS partial pressure (a function of the MTS concentration and the overall pressure). Unlike isobaric infiltration, in FFCVI, the overall pressure cannot be simply controlled. Typically, the downstream pressure is fixed, but unless a bypass is used,

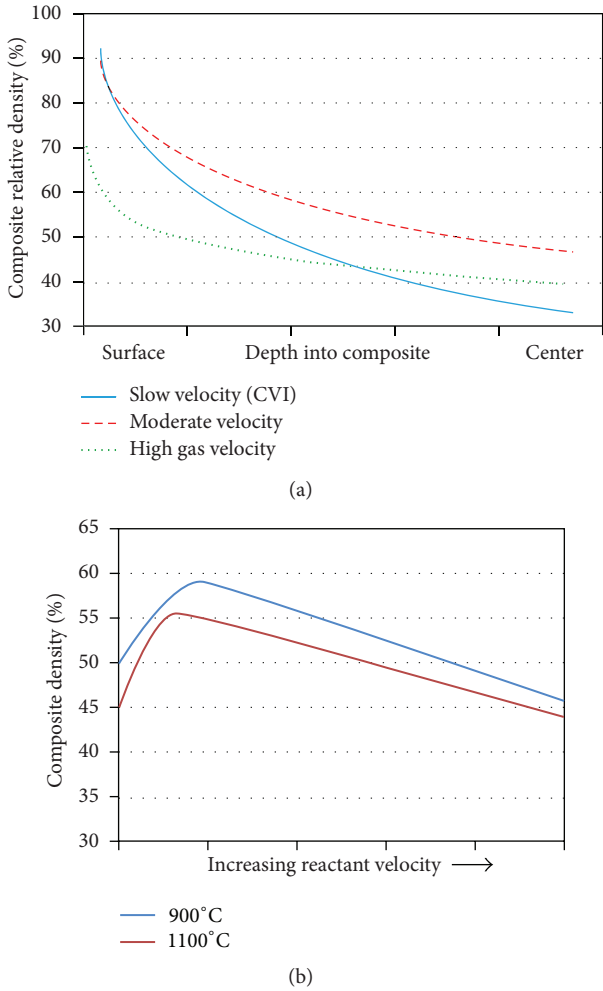


FIGURE 6: (a) Simulated deposition gradient for varying reactant velocities and (b) variation in simulated composite density as a function of temperature and reactant velocity.

the upstream pressure increases as the transport pathways through the fiber preform close during infiltration. As the process pressure then varies as a function of time and position within the sample, control over the reactant concentration becomes the means by which the reactant partial pressure can be set.

Simulations and experiments were carried out over a range of MTS concentrations, with temperature and reactant velocity held constant. For low MTS concentrations, SiC deposition can be limited by reactant availability. With increasing reactant concentration, the reaction becomes limited by surface site availability, and the deposition rate is no longer strongly influenced by reactant concentration. Both the simulation and experimental results show this effect, and the infiltration process becomes less sensitive to the MTS partial pressure at high MTS concentrations. The simulated infiltration as a function of depth into the composite is shown in Figure 7(a), and for moderate and higher MTS concentrations, there is a minimal effect on the infiltration.

Model results were also compared with experimental results for a range of MTS partial pressures (Figure 7(c)). These experiments were carried out in both CVI and FFCVI conditions, and the infiltration duration was limited (which limited the densities that could be achieved). At higher MTS partial pressures, there was good agreement between the simulated and experimental densities, but at lower partial pressures, the experimental densities were much lower than the simulation. This is likely caused by reactant depletion in the experiment before the precursors reach the fiber preform. Precursors can react on other surfaces inside the furnace, and with very low reactant partial pressures, this can deplete the reactant concentration enough to impact the sample density achieved. At higher reactant partial pressures, the relative amount of depletion is greatly reduced, and in the simulation, the reactants are introduced directly at the fiber preform surface, so the depletion in other regions of the furnace is not considered.

4.2.3. Fiber Spacing Effects. The final parameter modeled in this work is the average fiber spacing in the preform. This variable is governed by the fiber architecture and sample preparation and is unlike reactant pressure or velocity, in that it cannot be set during the actual infiltration. However, the same simulation can be used to model the effects of different fiber spacing by increasing the system size. Coupled with the cyclic boundary conditions, this effectively increases the width of the gaps between adjacent fibers, which allows for more infiltration to occur before the reactant pathways become blocked.

In this study, the width of the simulated system was increased from 15 to 30 μm . This effectively tripled the gap between adjacent fibers from a 7.5 μm gap to a 22.5 μm gap. More SiC deposition is required before these larger reactant transport pathways are closed off. As a result, prolonged infiltration is required for this closure to occur, and a 3.1x increase in processing time was observed in the simulation. This is roughly proportional to the 3x increase in gap width used in this study. While increased fabrication time is not desirable in terms of rapid processing, if this is accompanied by an increase in composite density and performance, then these gains could offset the long infiltration required. At the end of infiltration, the simulated composite with the larger gap spacing showed an increase of 57% and 39% in density compared to the narrow gap model for the 900°C and 1100°C simulations, respectively (Figure 8).

Composite density has been shown to have a very significant effect on mechanical and thermal performance, and careful control of the average fiber spacing within the composite could be a means to optimize the tradeoff between fabrication time and improved material properties. However, in increasing the average gap between fibers, the overall fiber volume fraction of fibers in the composite is reduced as well. Maintaining a sufficient fiber loading in the composite is essential to obtain increased fracture toughness and more graceful failure characteristic of a composite, so any adjustments to the fiber architecture would need to be evaluated in the context of composite behavior as well.

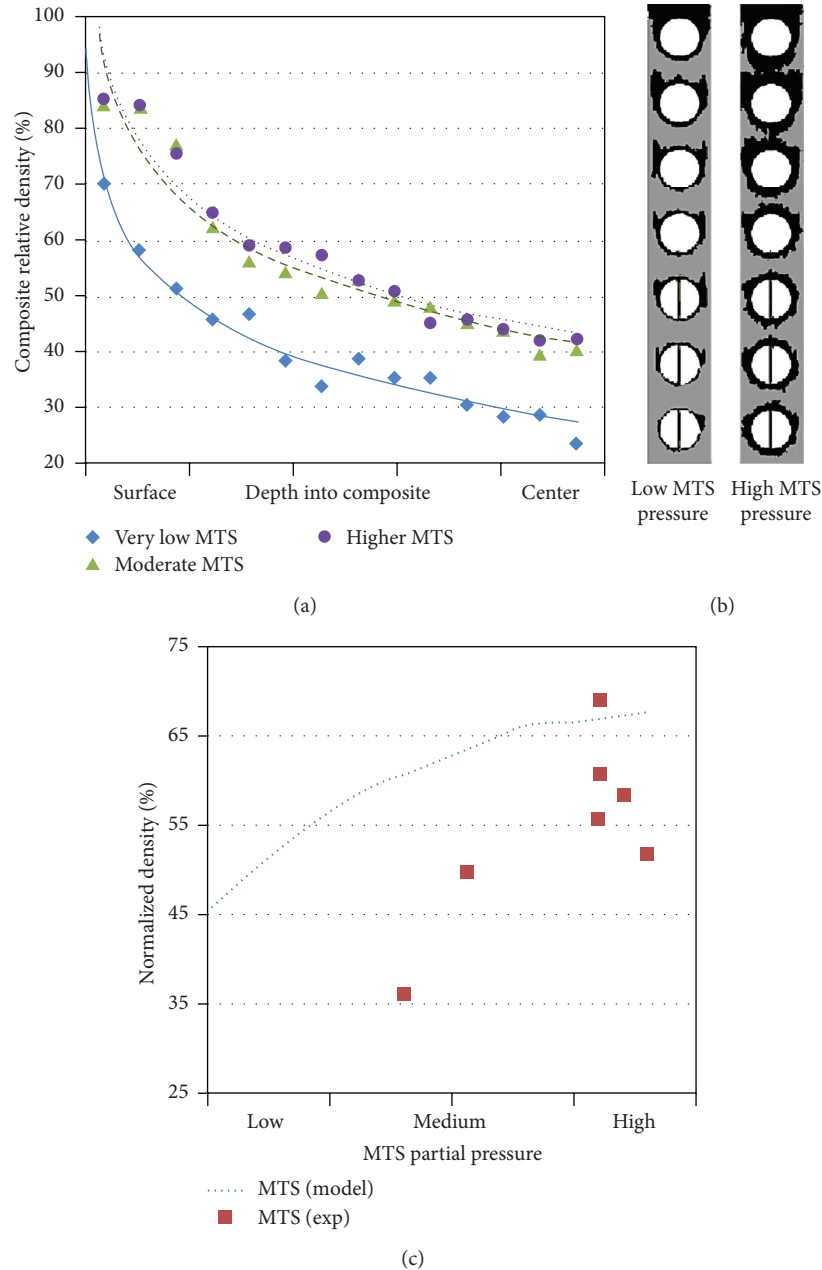


FIGURE 7: (a) Simulated deposition gradient for varying MTS partial pressures, (b) simulated infiltration for low and high MTS partial pressures, where black indicates deposited SiC matrix, and (c) comparison between simulation and experimental results for MTS concentration effects on density.

Simulations of the SiC infiltration process have also been performed by other groups and trends that are consistent with the results of this work have been reported. Roman et al. [15, 16] developed an extensive model of the reaction and deposition process for forced flow CVI and observed similar trends with increasing precursor velocity through the sample. In that work, reactant introduction was given as a volumetric flow, rather than a net velocity, and this makes it difficult to make an exact comparison with this work. However, in both that model and ours, increasing reactant flow from very low to moderate velocities resulted in reduced processing time and increased density and matrix uniformities (Figure 9).

5. Conclusions

SiC-SiC composites exhibit many properties that could make them very desirable for use in advanced nuclear reactor concepts, including strength at high temperatures and exceptional stability under irradiation. However, one of the challenges that must be overcome before these materials are widely adopted is the time-consuming and expensive fabrication process required to produce very high purity material. Forced flow CVI is a modification to the conventional isobaric infiltration process, which allows for increased densification rates while maintaining infiltration

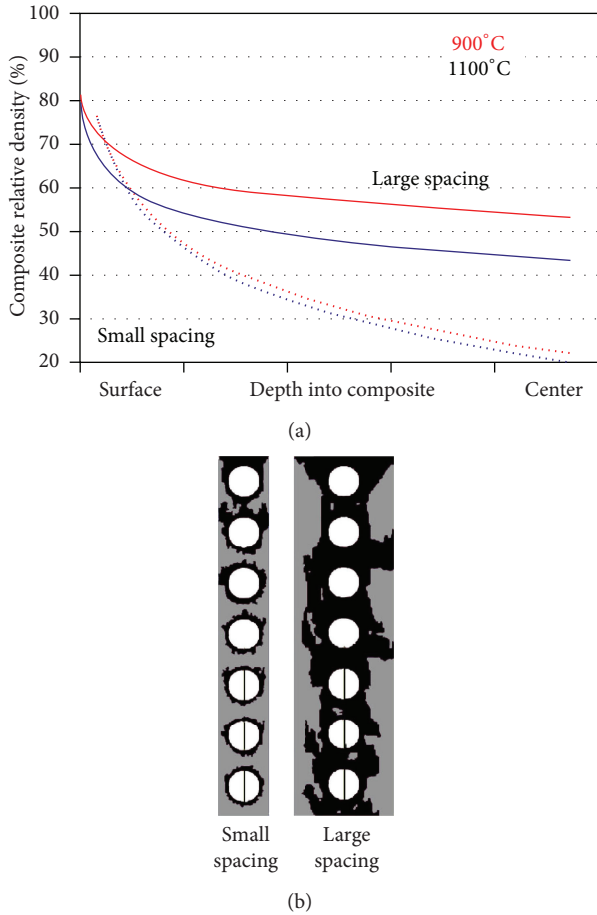


FIGURE 8: (a) Simulated deposition gradient for varying fiber spacings and temperatures, (b) simulated infiltration for small and large fiber spacing, where black indicates deposited SiC matrix around white fiber cross-sections.

uniformity. In this work, a model was developed to simulate the chemical vapor infiltration process for the fabrication of SiC-SiC composites under both isobaric and forced flow conditions. This model uses a direct simulation Monte Carlo approach and accounts for MTS deposition, depletion, and the inhibition of this reaction due to the HCl byproducts.

The effects of different fabrication parameters were simulated to investigate ways to optimize forced flow CVI. Increasing reactant flow through the sample increased both the densification rate (reducing the required processing time) and the final composite density. However, very high reactant flow rates were found to reduce uniformity in the simulation, which could be due to insufficient reactant residence time. Very high reactant velocities are also associated with larger pressure gradients across the sample, and in the supporting experimental work, high pressures were found to lead to non-uniform, nonstoichiometric deposition on the sample. The trends of reactant velocity were similar between the model developed in this work and the experimental results and were also consistent with simulations reported in the literature. The concentration of the MTS precursor (and the corresponding partial pressure) was also found to influence the infiltration process, although the effect was most pronounced

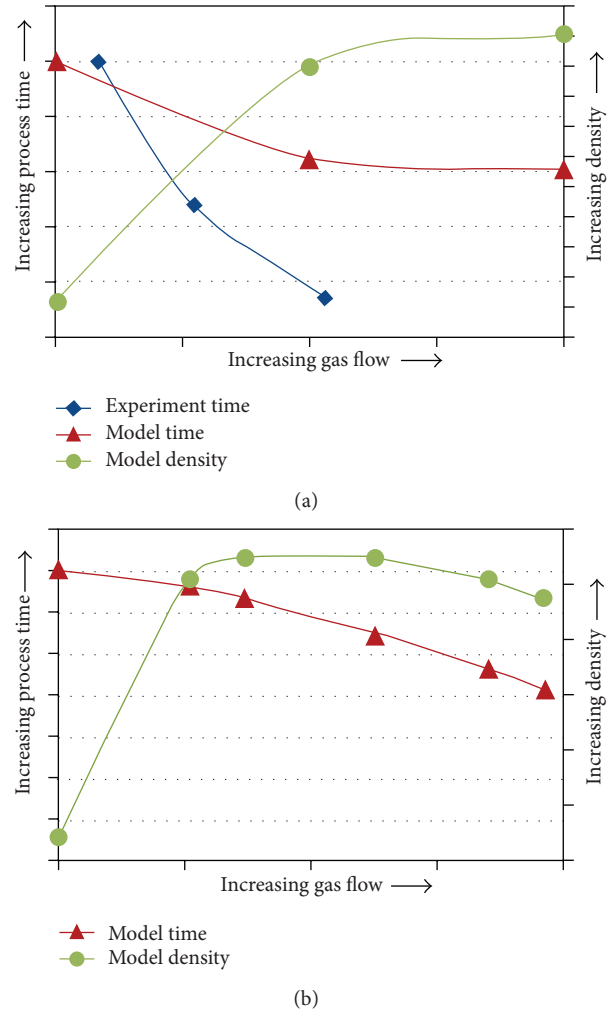


FIGURE 9: (a) Simulation and experimental results from the current work, showing effects of reactant velocity and (b) simulation results from Roman et al., [15] showing similar trends with increasing gas flow.

at lower concentrations. Finally, an increase in the average spacing between fibers led to a composite with a higher final density, but it increased the required processing time as well. Any infiltration improvements achieved by a modification to the fiber architecture would need to be carefully balanced with any impacts the altered structure had on the mechanical performance of the composite.

Further improvements to the model could allow simulation of reactant transport through larger intertow porosity and also account for randomized fiber positioning and the more complex two- or three-dimensional structure found in woven preforms. The model provides means to explore the effects of different microstructures and infiltration process parameters on the composite densification process. Using this model, these effects can be simulated in far less time than would be required to complete a corresponding experimental test matrix. This allows for a much faster approach towards optimization of the fabrication process, but it needs to be coupled with, and confirmed by, experimental results. More efficient composite fabrication can lead to improved

consistency and reduced fabrication cost and time, which will bring SiC-SiC composites closer to the deployment in actual advanced nuclear reactor applications.

Acknowledgments

The authors would like to acknowledge the contributions of the EM² lab personnel to the operation of the SiC composite fabrication facility at General Atomics. The work presented here was supported by General Atomics internal funding.

References

- [1] L. L. Snead, T. Nozawa, Y. Katoh, T. S. Byun, S. Kondo, and D. A. Petti, "Handbook of SiC properties for fuel performance modeling," *Journal of Nuclear Materials*, vol. 371, no. 1-3, pp. 329-377, 2007.
- [2] Y. Katoh, T. Nozawa, L. L. Snead, K. Ozawa, and H. Tanigawa, "Stability of SiC and its composites at high neutron fluence," *Journal of Nuclear Materials*, vol. 417, no. 1-3, pp. 400-405, 2011.
- [3] K. Hironaka, T. Nozawa, T. Hinoki et al., "High-temperature tensile strength of near-stoichiometric SiC/SiC composites," *Journal of Nuclear Materials*, vol. 307-311, no. 2, pp. 1093-1097, 2002.
- [4] M. Kotani, A. Kohyama, and Y. Katoh, "Development of SiC/SiC composites by PIP in combination with RS," *Journal of Nuclear Materials*, vol. 289, no. 1-2, pp. 37-41, 2001.
- [5] R. Naslain, "Design, preparation and properties of non-oxide CMCs for application in engines and nuclear reactors: an overview," *Composites Science and Technology*, vol. 64, no. 2, pp. 155-170, 2004.
- [6] K. Shimoda, J. S. Park, T. Hinoki, and A. Kohyama, "Microstructural optimization of high-temperature SiC/SiC composites by NITE process," *Journal of Nuclear Materials*, vol. 386-388, pp. 634-638, 2009.
- [7] W. G. Zhang and K. J. Hüttinger, "CVD of SiC from methyltrichlorosilane—part II: composition of the gas phase and the deposit," *Chemical Vapor Deposition*, vol. 7, no. 4, pp. 173-181, 2001.
- [8] G. Y. Chung and B. J. McCoy, "Modeling of chemical vapor infiltration for ceramic composites reinforced with layered, woven fabrics," *Journal of the American Ceramic Society*, vol. 74, no. 4, pp. 746-751, 1991.
- [9] X. Wei, L. Cheng, L. Zhang, Y. Xu, and Q. Zeng, "Numerical simulation of effect of methyltrichlorosilane flux on isothermal chemical vapor infiltration process of C/SiC composites," *Journal of the American Ceramic Society*, vol. 89, no. 9, pp. 2762-2768, 2006.
- [10] C. P. Deck, H. E. Khalifa, B. Sammulu, T. Hilsabeck, and C. A. Back, "Fabrication of SiC-SiC composites for fuel cladding in advanced reactor designs," *Progress in Nuclear Energy*, vol. 57, pp. 38-45, 2012.
- [11] T. M. Besmann, B. W. Sheldon, T. S. Moss III, and M. D. Kaster, "Depletion effects of silicon carbide deposition from methyltrichlorosilane," *Journal of the American Ceramic Society*, vol. 75, no. 10, pp. 2899-2903, 1992.
- [12] C. Lu, L. Cheng, C. Zhao, L. Zhang, and Y. Xu, "Kinetics of chemical vapor deposition of SiC from methyltrichlorosilane and hydrogen," *Applied Surface Science*, vol. 255, no. 17, pp. 7495-7499, 2009.
- [13] M. T. Schulberg, M. D. Allendorf, and D. A. Outka, "The adsorption of hydrogen chloride on polycrystalline β -silicon carbide," *Surface Science*, vol. 341, no. 3, pp. 262-272, 1995.
- [14] H. C. Chang, T. F. Morse, and B. W. Sheldon, "Minimizing infiltration times during isothermal chemical vapor infiltration with methyltrichlorosilane," *Journal of the American Ceramic Society*, vol. 80, no. 7, pp. 1805-1811, 1997.
- [15] Y. G. Roman, J. F. A. K. Kotte, and M. H. J. M. de Croon, "Analysis of the isothermal forced flow chemical vapour infiltration process—part I: theoretical aspects," *Journal of the European Ceramic Society*, vol. 15, pp. 875-886, 1995.
- [16] Y. G. Roman, M. H. J. M. de Croon, and R. Metselaar, "Analysis of the isothermal forced flow chemical vapour infiltration process—part II: experimental study," *Journal of the European Ceramic Society*, vol. 15, no. 9, pp. 887-898, 1995.

Research Article

A Compact Gas-Cooled Fast Reactor with an Ultra-Long Fuel Cycle

Hangbok Choi, Robert W. Schleicher, and Puja Gupta

General Atomics, P.O. Box 85608, San Diego, CA 92186-5608, USA

Correspondence should be addressed to Hangbok Choi; h.choi@ga.com

Received 24 October 2012; Accepted 14 March 2013

Academic Editor: Wei Shen

Copyright © 2013 Hangbok Choi et al. This is an open access article distributed under the Creative Commons Attribution License, which permits unrestricted use, distribution, and reproduction in any medium, provided the original work is properly cited.

In an attempt to allow nuclear power to reach its full economic potential, General Atomics is developing the Energy Multiplier Module (EM²), which is a compact gas-cooled fast reactor (GFR). The EM² augments its fissile fuel load with fertile materials to enhance an ultra-long fuel cycle based on a “convert-and-burn” core design which converts fertile material to fissile fuel and burns it in situ over a 30-year core life without fuel supplementation or shuffling. A series of reactor physics trade studies were conducted and a baseline core was developed under the specific physics design requirements of the long-life small reactor. The EM² core performance was assessed for operation time, fuel burnup, excess reactivity, peak power density, uranium utilization, etc., and it was confirmed that an ultra-long fuel cycle core is feasible if the conversion is enough to produce fissile material and maintain criticality, the amount of matrix material is minimized not to soften the neutron spectrum, and the reactor core size is optimized to minimize the neutron loss. This study has shown the feasibility, from the reactor physics standpoint, of a compact GFR that can meet the objectives of ultra-long fuel cycle, factory-fabrication, and excellent fuel utilization.

1. Introduction

Nuclear power has much to offer in addressing the nation's energy security needs in an environmentally acceptable manner. However, today's nuclear power has its own challenges in the management of nuclear waste from both the front end and back end of the fuel cycle, along with huge upfront financial investment and competing against other energy resources—electricity generation cost. Currently, the most prevailing commercial reactor type is the Light Water Reactor (LWR), and it is expected that the advanced LWR will be introduced in the very near future based on proven technologies [1]. However, the International Atomic Energy Agency (IAEA) predicts that for the longer term the focus will be on innovative designs to provide increased benefits in terms of safety and security, nonproliferation, waste management, resource utilization, and economics, as well as to offer a variety of energy products and flexibility in design, siting, and fuel cycle options [2].

Small reactors are defined as reactors with an equivalent electric output of less than 300 MW. The small modular

reactor has been developed since the 1950s when the United States (US) Army and Navy initiated research programs for the design and test of various small nuclear reactors [3]. The Army was interested in producing electricity in remote area, which included a transportable reactor by tractor trailer without dismantlement and a barge reactor transportable by sea. The Navy focused on development and deployment of nuclear power sources for warships and submarines. In 2008, more than 45 small- and medium-sized reactor concepts and designs were developed under the national or international Research and Development (R & D) programs [4].

Though it is difficult for small reactors to compete economically under the same paradigm as large commercial reactors, the market situation of the small reactors will be different from those of large-capacity nuclear power plants. In other words, it will depend on demand for a better distributed electricity supply, better match between the capacity increment and investment, and flexibility in site selection or diversity of the products [5, 6]. The IAEA addressed attractive features of innovative small reactors that might facilitate their

progress in certain energy markets as follows:

- (i) factory fabrication that reduces cost, shortens construction time, and improves quality control; reduced design complexity, impact of human factors, and operation and maintenance requirements;
- (ii) lower absolute capital costs, as compared to large capacity plants; incremental capacity increase with sequential construction; reduced financial risk for the incremental increase of demand;
- (iii) suitability for small electricity grids, including an option of autonomous operation; feasible nonelectric applications such as seawater desalination, district heating, and process heat;
- (iv) improved safety due to smaller core size.

In addition, small reactors with a longer fuel cycle can further improve the plant economy and energy security. The potential incentives of long-life small reactors will be the reduced obligations for spent fuel and waste management and greater or easier nonproliferation assurances to the international community [7]. Many countries such as the USA, the Russian Federation, Japan, India, and Brazil have performed design studies of small reactors without refueling, which include water, sodium, lead-bismuth and gas-cooled reactors [8–14]. The liquid metal reactors have shown good performance of long-life operation because of a high conversion ratio and neutron yield owing to hardened neutron spectrum and transuranic fuel, respectively [15–17]. It is also possible to design a traveling wave type sodium-cooled fast reactor with a capacity of 1000 MW electric, which can last more than 30 years with a single initial fuel loading [18].

General Atomics launched an innovative new gas-cooled fast reactor (GFR) program in 2009, named Energy Multiplier Module (EM²). The reactor system is designed to have dual applications: electricity generation and high temperature heat source. The reactor is small and transportable and can be deployed in an established grid or as a stand-alone power source for an isolated area or a military base. The reactor will be operated for decades without refueling. The reactor core is designed to use nonradioactive nuclear waste, that is, depleted uranium (DU), along with low enriched uranium (LEU). This paper describes the physics design approaches and fuel cycle characteristics of the EM².

2. Design Approach and Tools

2.1. Design Choices. The design choices and their linkage to cost factor are schematically shown in Figure 1. For the high temperature operation and high quality heat source, a gas coolant such as helium is most feasible. When compared to other coolants such as sodium, the helium coolant is inert, single phase, nonradioactive, and chemically stable against water, and no intermediate loop is required for thermal-to-electric energy conversion [19]. High temperature operation improves the thermal efficiency of the plant, which has a direct effect on the electricity generation cost; however, it requires use of high temperature material for the fuel and core structure.

Both the thermal and fast neutron spectrum reactors are feasible for the gas coolant. From the physics design viewpoint, it is recommended to maximize the fuel burnup to improve the fuel cycle economics with a reasonable amount of fissile material in the core. From this perspective, a fast neutron spectrum was chosen, under which fertile fuel can be converted into fissile fuel and burned in situ. All the actinides are effectively burned or transformed under the fast neutron spectrum, while fissile nuclides are mostly burned under the thermal neutron spectrum. To accommodate high fuel burnup, the fuel design should consider high irradiation swelling of the fuel, internal pressure buildup of the fuel rod due to fission gas release, material damage due to high energy neutrons, and so forth.

Both the small and large reactor options are feasible for the gas-cooled fast reactor, while the gas-cooled thermal reactor in general requires large moderator volume which results in a low power density of the core. From the economics viewpoint, small reactors mitigate financial risk owing to low upfront capital investment, and economic competitiveness can be achieved through a modular construction approach, moving a large portion of the construction work from site to factory, shortened site construction period, design simplification, and so forth. In order to achieve an ultra-long fuel cycle in the small reactor, high quality reflector materials are required to minimize the neutron loss and the core configuration needs to be optimized to maximize the fuel utilization.

2.2. Convert and Burn. The excess reactivity of the EM² core is driven by the balance of fissile isotopes and fission product poisoning. Initially, the core is loaded with only uranium fuel, and therefore, fissile uranium produces most of the reactor power and burns quickly until fissile plutonium builds up. Under a very hard neutron spectrum, fertile uranium can also burn as shown in Figure 2. In fact, the amount of fertile fission is around 20% in the GFR which is a nonnegligible contribution to the excess reactivity of the core [20]. However, this also indicates that neutron spectrum softening significantly affects the fertile uranium fission contribution because of its high fission cross-section threshold around 1 MeV. Figure 3 compares the production-to-absorption cross section ratios ($\nu\sigma_f/\sigma_a$) of major nuclides. It can be seen that the nuclear properties of fissile plutonium are strongly dependent on neutron energy. A harder neutron spectrum will lead to higher excess reactivity; this excess reactivity decreases as fission products build up during long-life operation.

2.3. Physics Tools and Models. For the physics design calculations, a lattice code MICROX is used to generate multi-group cross-sections of the fuel and structural materials [21]. MICROX is an integral transport theory flux spectrum code which solves the neutron slowing-down and thermalization equations for a two-region (particle and moderator) lattice cell. The nuclear data of MICROX consists of GAM data (99 groups between 14.9 MeV and 0.414 eV) and GATHER data (101 energy mesh points below 2.38 eV) for the fast and thermal energy ranges, respectively [22, 23]. For the

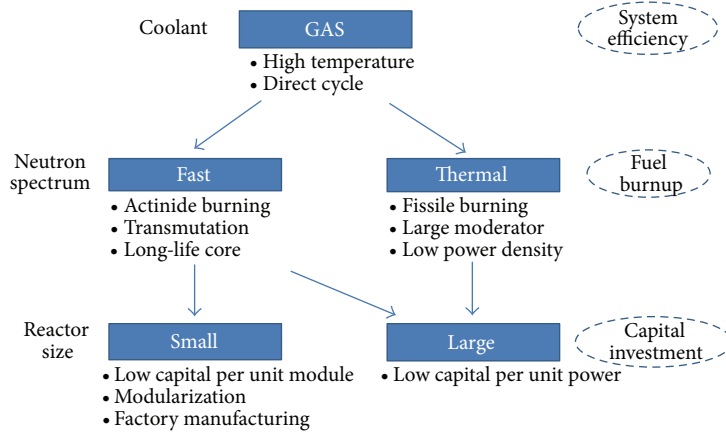


FIGURE 1: Design choices and economic factors.

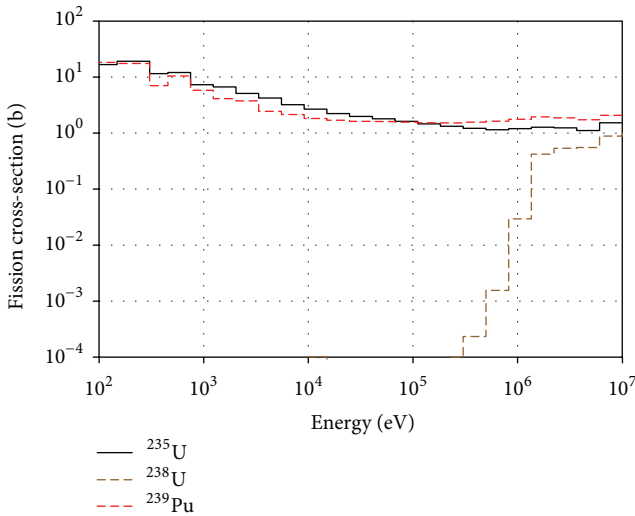


FIGURE 2: Fission cross-sections.

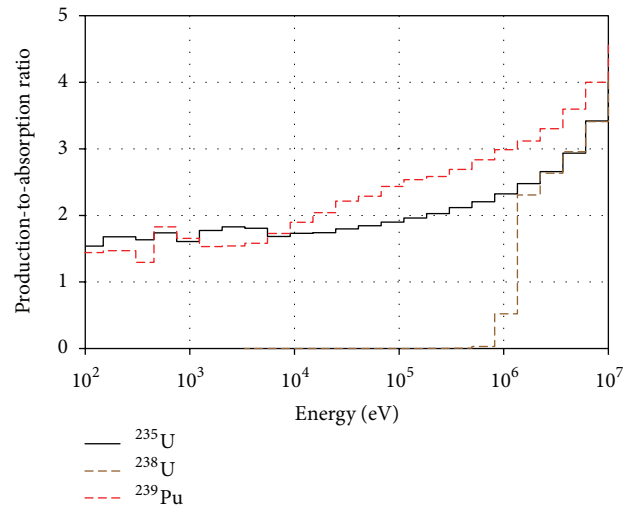


FIGURE 3: Production-to-absorption ratio.

epithermal resolved energy range, the spectrum calculation uses GAR data with temperature-dependent cross sections [24].

The reactor core is analyzed by DIF3D and BURP for the static and depletion calculations, respectively [25, 26]. DIF3D is a multigroup steady-state neutron diffusion and transport code, which is used to calculate the eigenvalue (criticality) and power distribution of the core and to generate the neutron flux distribution to be used for the depletion calculation. The BURP code is also used to produce macroscopic cross sections of each core region using the microscopic cross sections and nuclide number densities, which are used by DIF3D for static diffusion calculations.

The actinide depletion chain used in the calculations is based on 20 nuclides and includes neutron capture, $(n, 2n)$ reaction, and decay chains. Fission product yields have been generated for the fast reactor system based on JENDLE3.3 [27]. These yield data are available for ^{232}Th , ^{233}U , ^{235}U ,

^{236}U , ^{238}U , ^{237}Np , ^{239}Pu , ^{240}Pu , ^{241}Pu , ^{242}Pu , ^{241}Am , and ^{243}Am . For example, direct yield data are provided for 1227 isotopes for 1 MeV neutron fission of ^{235}U . In order to obtain cumulative fission product yield, the decay chain has been prepared for ~ 800 isotopes for which the direct yield is greater than 10^{-10} . The cumulative fission product yield has also been generated for 61 nonsaturating fission products (NSFP), and pseudofission products (PFP) were introduced to minimize the loss of fission products due to the truncated burn-up chain. The properties of PFP were obtained from an ORIGEN2.2 calculation [28].

The EM² core is designed to release gaseous fission products in order to achieve a very high fuel burnup. Considering that the operating temperature of the reactor is high, it was assumed that not only the noble gases (Krypton and Xenon) but also other nuclides with a relatively low boiling temperature ($< 450^\circ\text{C}$) are released during normal operation. For the physics design study, it was assumed that 70% of

gaseous fission products are removed. The NSFP also contains gaseous fission products; the effective number densities for these materials were calculated by considering the reduction of absorption rate due to fission gas removal. The amount of gaseous fission products in the NSFP is 6%–8%. If the removal rate of gaseous fission products is 70%, for example, the inventory of saturating fission products and NSFP is reduced by 9.0% and 6.5%, respectively, at the end-of-cycle, resulting in a 7.2% reduction of total fission product inventory [29].

The adequacy of using the legacy code system for the EM² core depletion calculation was assessed in the earlier study especially for the prediction of peak excess reactivity and fuel cycle length [29] by the Monte Carlo code MCNPX with ENDF/B-VII.0 cross sections [30]. In general, the core excess reactivity is well predicted by the diffusion-based depletion model except for the initial core state where the maximum difference is 0.5% δk . The differences of the peak excess reactivity and cycle length are less than 0.2% δk and 2 years, respectively. Currently the legacy code system is being updated for its cross section library and solution methods [31, 32].

3. Physics Design Requirements

A particular feature of EM² physics design is that it aims for an ultra-long fuel cycle and a very high fuel burnup with a small reactor core size so that the fuel utilization is dramatically increased when compared to a commercial LWR. The principal requirements that guided the initial nuclear design studies are as follows.

- (i) The nuclear reactor system shall have a design life of more than 20 years to enhance a high uranium utilization and fuel cycle economics.
- (ii) There will be no refueling and fuel shuffling during the core life, and therefore, there will be no movement of either fresh or spent nuclear fuel materials to/from the reactor core.

Scoping analyses indicated that a heterogeneous core configuration is more favorable to obtain a longer fuel cycle when using fertile fuel. Therefore, the core will be composed of two distinctive fuel materials: the fissile starter (LEU) and fertile converter (DU). In order to fulfill the principal design requirements, the fissile enrichment, location, and size of the starter have been optimized under the physics design requirements given below.

3.1. Reactor Size. The reactor core size shall be limited by the maximum size of the reactor vessel that can be manufactured by competitive US fabricators and transported through special overspecified routes by special permit. The reactor vessel shall be sized to allow truck transport from the factory to the designated site. The reactor vessel shall be sized to include reactor core, reflector material, radiation shield, thermal shield, instrumentation, and control system. A guideline for maximum vessel size is 250 tons for component mass, 4.8 m

for component diameter, and 30 m for component length, respectively.

3.2. Reactor Power. The reactor produces high temperature heat through controlled fission reactions in the fuel and regulates the rate of heat production to maintain a constant coolant outlet temperature in response to changes in coolant mass flow rate. The total reactor power is 500 MW thermal, and the core outlet temperature shall be 850°C. The power profile shall be flattened to reduce the peak fuel temperature. The fuel assembly peak power density shall be less than 200 W/cm³ throughout the core life.

3.3. Fuel Management. The reactor operation time shall be maximized to enhance maximum overall fuel burnup. During the core life, the magnitude of excess reactivity shall be within the reactivity worth of the reactor control system with a sufficient margin, and the peak power density shall be kept below the 200 W/cm³ design limit. The initial fissile enrichment averaged over the whole core including both the starter and converter fuel assemblies shall be minimized with a goal of overall enrichment close to that of the conventional LWR fuel. The plant life shall be at least 60 years and the fuel life shall be greater than 20 years at rated power without refueling or reshuffling.

3.4. Reactor Control System. The reactor core includes reactivity control systems that consist of multiple control drums strategically located in the reflector region and operating in banks. The reactor control system provides overall reactor power level and excess reactivity control. The reactor control system shall be designed to provide enough negative reactivity to maintain the controlled criticality of the core.

3.5. Reactor Shutdown System. The reactor core includes shutdown systems that are independently and adequately activated to rapidly shut down the reactor core under postulated accident conditions. The static and dynamic reactivity worth of the shutdown system shall be sufficient to terminate the reactivity and power transient following a reactor trip in response to a reactivity excursion accident such as a loss of coolant.

4. EM² Physics Performance

The baseline core was selected through a series of parametric calculations of key design parameters: reactor size, fuel material type, matrix material type, fuel volume fraction, starter size and enrichment, reflector material and thickness, and so forth. The physics design calculations also incorporated some of the fuel and thermal-fluid design features such as fuel material chemical reaction, compatibility of the fuel material with clad, and cooling capability of the fuel. The baseline core model provides fundamental physics design values of EM² so that follow-up calculations are performed for the fuel performance, reactor safety, and economics analyses.

4.1. Baseline Core Model. The major components of the reactor system and coolant flow are shown in Figure 4. The reactor vessel is an internally insulated 4.7 m diameter, 10.6 m high structure constructed from standard SA533-Grade B plate steel. This vessel is of a size that can be manufactured by many vendors and is small enough to be shipped by truck to the construction site.

The EM² baseline core, schematically illustrated in Figure 5, has a cycle length greater than 30 years without refueling, which means that the characteristics of the operating core simply depend on initial fuel loading. The baseline core is divided into three sections: starter, fertile, and reflector. The starter is the “critical” section of the reactor at beginning of life. It contains LEU to initiate criticality and provide excess neutrons for converting fertile to fissile materials in the fertile section. The core contains 85 fuel assemblies arranged in a hexagonal prism. Seventy-nine assemblies contain 91 fuel rods, each 2.7 m long by 20.5 mm in diameter. Six assemblies contain central voids for shutdown rod insertion. The clad is 1 mm thick β -SiC composite, which is highly resistant to both temperature excursions and neutron damage [33, 34]. The fuel is uranium carbide (UC) in the form of porous pellets. The interstitial pores allow room for fuel swelling and pathways for volatile fission products. The pellets are annular with a central hole that provides a means for volatile fission products to escape to a fission product collection system. This vented fuel in principle alleviates the pressure buildup and accommodates fuel swelling over the long core life.

The reflector consists of an inner section of canned Be₂C and an outer section of graphite. These reflector materials are highly neutron economic and keep the neutron leakage from the core under 2%. Due to power peaking around the core periphery, the starter fuel adjacent to the reflector has a reduced enrichment, leading to a radially flattened power profile that results in relatively uniform irradiation rates during the fuel cycle; this precludes the need for shuffling. Six rotatable drums are embedded in the reflector to provide reactivity control during normal operation.

4.2. Core Performance. The average fuel enrichment of the starter region is 11.4%, which results in an average fissile content of 6.1% over the whole core. The k_{eff} is shown in Figure 6, where the k_{eff} initially increases up to 1.023 due to ²³⁹Pu buildup in the starter region, and subsequently decreases due to ²³⁵U depletion and fission product buildup. As ²³⁹Pu also builds up in the converter region, k_{eff} decreases slowly after ~15 years.

The core performance is summarized in Table 1. The average discharge burnup is 145 GWd/t heavy metal (HM). The peak fuel burnup is 298 GWd/tHM for the starter fuel while the lowest fuel burnup is 48 GWd/tHM for the converter fuel located at the core edge region. The average fuel burnup of the starter and converter fuel is 192 and 95 GWd/tHM, respectively. The inlet temperature is 500°C and the temperature rise in the core is ~350°C. Under this condition, the peak fuel temperature is estimated to be 1490°C.

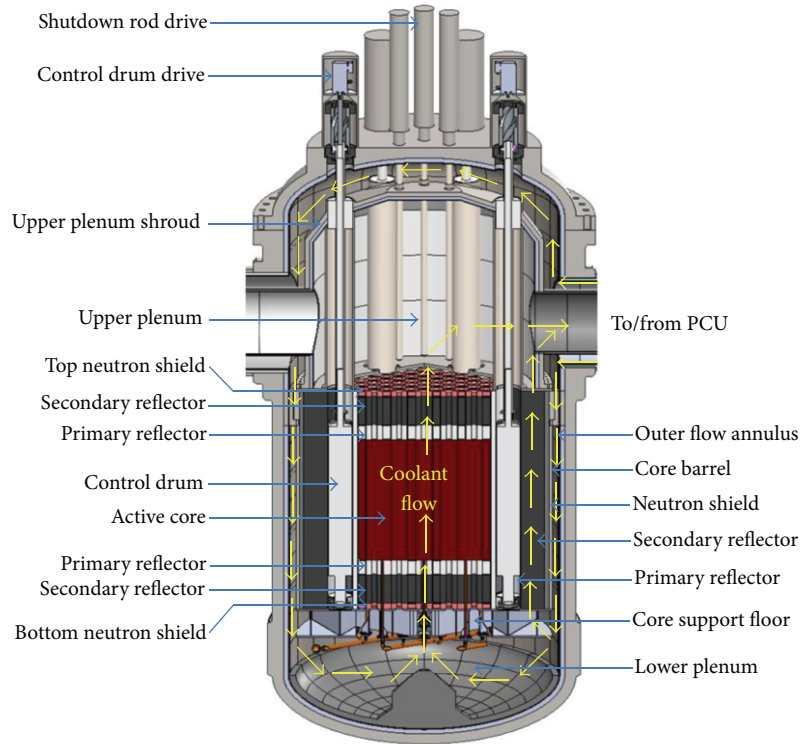
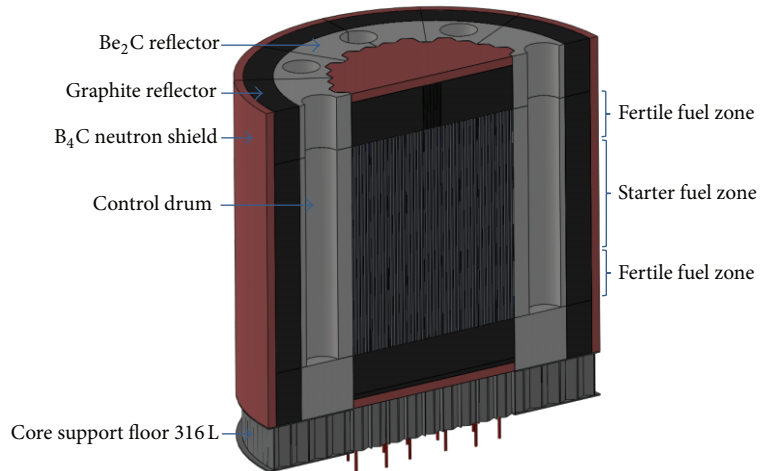
TABLE 1: Summary of EM² baseline core performance.

Reactor power	500 MW thermal
Fuel material	Uranium carbide
Clad/structure material	Silicon carbide
Coolant material	Helium
Cycle length	32 years
Average fissile content	6.1 wt%
Fuel loading	
Uranium	42.8 t
²³⁵ U	2.6 t
Fuel discharged	
Heavy metal	36.7 t
Uranium consumed	23%
Excess reactivity	2.0% δk
Peak/average burnup	285/135 GWd/t
Peak/average power density	165/58 W/cm ³
Peak/average fast fluence (>0.1 MeV)	7.9/3.7 $\times 10^{23}$ n/cm ²
System pressure	13.3 MPa
System pressure (depressurized)	0.45 MPa
Core pressure drop	25 kPa
Core inlet temperature	549°C
Core outlet temperature	850°C

TABLE 2: Isotopic inventory (kg) of EM² baseline core.

	Charge	10 years	20 years	30 years	Discharge
²³⁵ U	2,611	1,335	719	401	317
²³⁶ U	0	250	334	349	345
²³⁸ U	40,235	37,589	35,129	32,839	31,939
²³⁷ Np	0	27	57	77	83
²³⁹ Np	0	2	2	2	2
²³⁸ Pu	0	6	20	36	41
²³⁹ Pu	0	1,592	2,402	2,807	2,901
²⁴⁰ Pu	0	81	225	372	428
²⁴¹ Pu	0	50	94	127	138
²⁴² Pu	0	3	10	19	22
²⁴¹ Am	0	6	17	31	37
^{242m} Am	0	0	1	2	2
²⁴³ Am	0	0	1	2	2
²⁴² Cm	0	1	1	2	2
²⁴³ Cm	0	0	0	0	0
²⁴⁴ Cm	0	1	3	7	9
HM	42,846	40,942	39,016	37,073	36,271
Fuel	42,846	42,589	42,304	41,992	41,856

The fuel inventory as a function of time is summarized in Table 2. Fissile material burning and production are shown in Figure 7 for ²³⁵U and ²³⁹Pu. One of the design targets of the EM² is to promote much higher uranium utilization than that of the conventional power reactors. In the case of EM² once-through fuel cycle, the fissile uranium (²³⁵U)

FIGURE 4: EM² reactor system.FIGURE 5: EM² baseline core region.

is appreciably burned at the end of cycle (EOC) with an average consumption rate of 88%, which was calculated based on initial loading and residual mass. The uranium was most effectively transmuted in the inner layer of the starter, resulting in the maximum consumption rate of 43% locally. The average uranium consumption over the whole core is 25%. Figure 8 compares the fission rates of uranium with those of other nuclides and shows that the fertile uranium (²³⁸U) contributes to the total fission rate by 18%.

The EM² core was designed to breed fissile plutonium and burn it. However, not all the fissile plutonium is burned at EOC and must be discharged. At EOC, the average fissile content (a fraction of ²³⁵U, ²³⁹Pu, and ²⁴¹Pu out of total heavy metal) is 9.4%. The amount of residual plutonium is 3.5 t, of which the fissile plutonium purity (a fraction of fissile plutonium out of total plutonium content) is 87%. This has a high fuel value and will be recycled in the subsequent fuel cycles without conventional reprocessing [35].

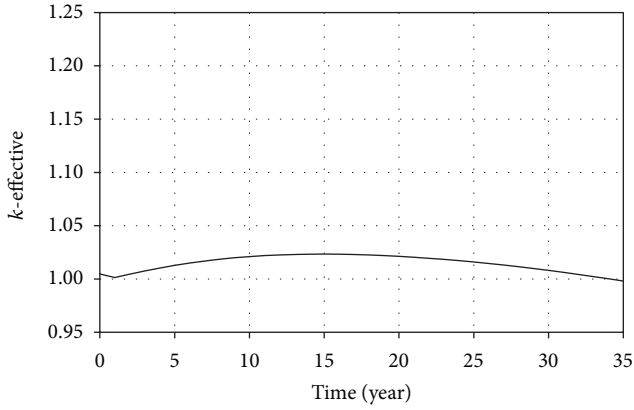


FIGURE 6: k_{eff} of EM² baseline core.

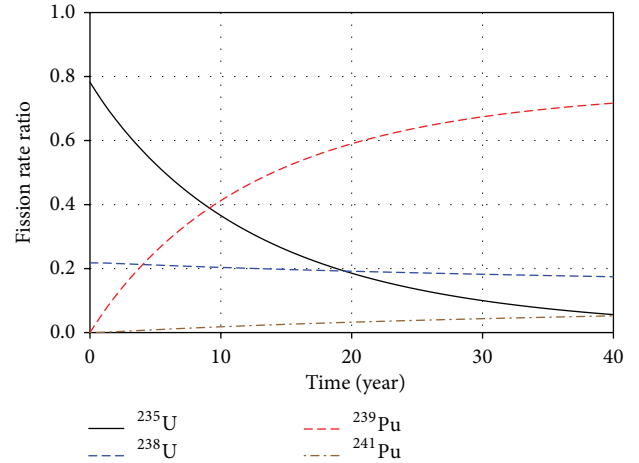


FIGURE 8: Fission rates of major nuclides.

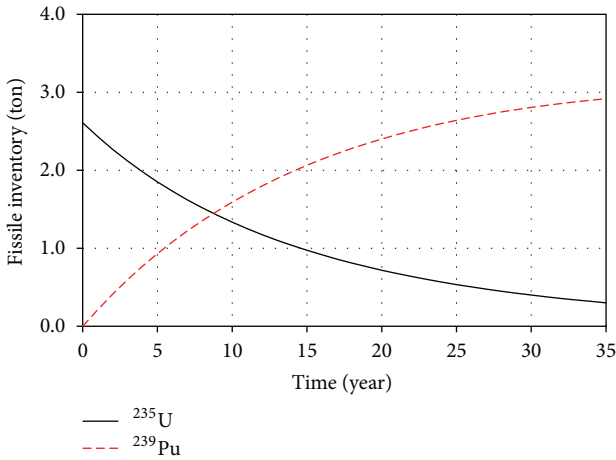


FIGURE 7: Fissile inventory change of EM² baseline core.

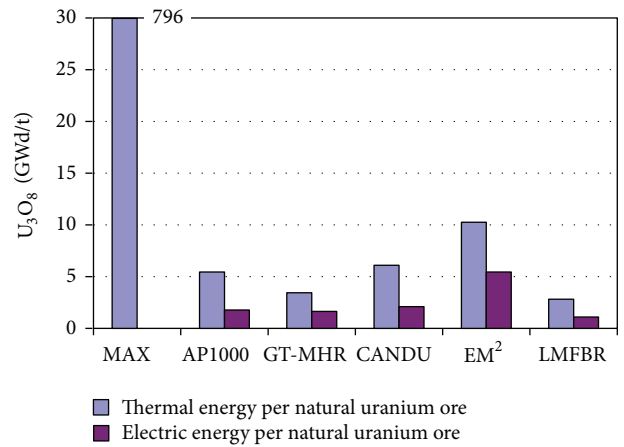


FIGURE 9: Comparison of energy per natural uranium ore.

TABLE 3: Comparison of mass flow for once-through fuel cycle.

	ALWR	EM ²
Comparative power output, MWe	1117	1117
Number of units	1	4.2
Refueling period, year	1.5	34
Number of batches	2.3	1
Fuel burnup, GWd/tHM	60	145
60-year operation		
(i) Heavy metal loading, ton	1522	318
(ii) Heavy metal discharge, ton	1425	270

4.3. Fuel Cycle Characteristics. The mass flow of the EM² baseline core is compared to that of an advanced LWR (ALWR) based on fuel management parameters summarized in Table 3 [36, 37]. The total electricity generation of EM² was normalized to 1117 MW, which requires 4.2 units of EM². For an operation period of 60 years, the amount of heavy metal loading and discharge is reduced by ~80% in the ultra-long EM² once-through fuel cycle when compared to ALWR once-through fuel cycle.

The energy production per natural uranium ore is shown in Figure 9 for various reactor types including ALWR, gas turbine modular helium reactor (GT-MHR), Canadian deuterium uranium (CANDU) reactor, and liquid metal fast breeder reactor (LMFBR) [38–40]. The maximum energy obtainable from 1 ton of natural uranium (U_3O_8) is estimated to be 796 GWd, if all uranium atoms fission and release 200 MeV per fission. The amount of thermal energy produced per ton of natural uranium is 10.3 GWd for the EM², while it is 5.4 GWd for the ALWR under the assumption that the fuel enrichment and fuel burnup are 4.8 wt% and 60 GWd/tHM, respectively.

The amount of high level waste (used nuclear fuel) generated per energy production is shown in Figure 10 for EM² and other reactors. The waste generation is the largest in the CANDU reactor due to the use of natural uranium fuel under a fully thermalized neutron spectrum. For the EM², the waste generation is 5.8 kgHM/GWd, while it is 15.6 kgHM/GWd for the ALWR.

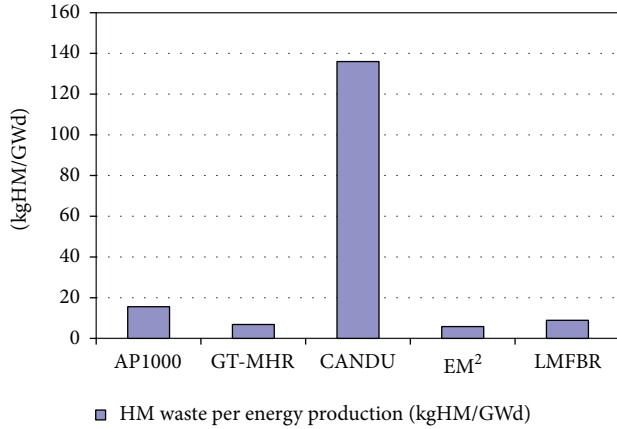


FIGURE 10: Comparison of waste per energy production.

TABLE 4: Comparison of unlevelized electricity costs.

	ALWR	EM ²
Number of cycles	20	1
Total electricity	270 TWh	66 TWh
Unit cost of fuel	~2,400\$/kgHM	~4,760\$/kgHM
Total fuel cost	1,600 M\$	200 M\$
Unlevelized average	~6\$/MWh	~3\$/MWh

4.4. Cost Estimation. Table 4 compares unlevelized electricity costs of EM² and ALWR. The fuel cost of EM² baseline core loading is estimated to be ~200 M\$ which includes uranium ore, conversion, enrichment, assembly structures, and fabrication costs. This fuel generates 66 TWh electricity over 30 years at a capacity factor of 95%. For the ALWR, total fuel cost is expected to be ~1600 M\$ for 30-year operation, including initial core loading. The corresponding total electricity generation will be 270 TWh over 30 years. Therefore, the EM² cycle yields a reduced fuel cycle cost when compared to the ALWR fuel cycle even though the unit fuel cost is expected to be higher for the EM² (~4,760 \$/kgHM on average) when compared to the ALWR fuel (~2,400 \$/kgHM) [41]. It is also worth noting that the fuel is an upfront capital charge in EM² as opposed to an operational charge in case of the ALWR.

A preliminary estimation of the electricity generation cost was made for EM² and other power plants such as ALWR, coal, and natural gas plants, and the results are shown in Figure 11. The assumptions and methodology used for the cost estimation are consistent with the Department of Energy (DOE) GEN IV International Forum cost estimating guidelines [42], and the cash flow methodology is from Du and Parsons [41]. Specifically, the pertinent assumptions used for cost calculations of the EM² and other technologies are as follows:

- (i) the EM² plant consists of 4 reactor modules, each with thermal rating of 500 MW, with a net plant efficiency of 53% and a capacity factor of 95%;

- (ii) ALWR plant consists of a 1,117 MWe net electric rating with a capacity factor of 92% averaged over the life of the plant;
- (iii) the costs are levelized over 60 years for the n th-of-a-kind plant;
- (iv) major financial parameters for nuclear and fossil fired plants include
 - (a) 50% debt at an 8% interest rate,
 - (b) 50% equity at a rate of 12%,
 - (c) general inflation of 2.5% per year;
- (v) enriched uranium cost is based on 95 \$/kg-U₃O₈ feed, 6 \$/kg-U₃O₈ conversion, and 165 \$/Separation Work Unit (SWU) enrichment.

It can be seen that EM² has a significant cost advantage over a comparable ALWR. It would break even with natural gas combined cycle plants at a natural gas price of 6-7 \$/MMBtu. The EM² cost advantage primarily comes from the compact equipment sizes, fewer components, significantly higher net plant efficiency, factory fabrication, and shorter field construction time. The EM² overnight capital cost is 3,800 \$/kWe versus 5,000–6,600 \$/kWe for ALWR plants. A single unit capacity addition is ~1 B\$ versus ~5 B\$ for ALWR. With the ability to add EM² units as power demand grows, the financial risk associated with an EM² plant substantially lower than a large ALWR can be achieved.

It should be noted that the uncertainty of the cost estimation is relatively large for the EM² when compared to the commercial power plant, because the materials and manufacturing technologies are still being developed for the fuel, clad, structural components, and auxiliary systems of the EM² while the market prices are well established for the commercial power plants.

5. Summary and Recommendations

The EM² is a 500 MW thermal GFR loaded with uranium carbide fuels, which satisfies physics design requirements of an ultra-long fuel cycle, high burnup, and compact reactor size, and is also economically competitive to large-scale commercial nuclear plants. These features offer new possibilities for fuel cycles to greatly improve fuel utilization and waste reduction, when compared to large-scale nuclear plants and other power sources. Nevertheless, there are many technical issues, which should be addressed and resolved through R & D activities as follows.

In particular, it is required to resolve uncertainties associated with fission product buildup during the ultra-long fuel cycle with low excess reactivity.

Transient and safety analyses are required to confirm the controllability of excess reactivity and local power peaking throughout the fuel cycle.

Experimental verifications are required for the core criticality and fuel irradiation along with thermal-fluid and mechanical integrity tests.

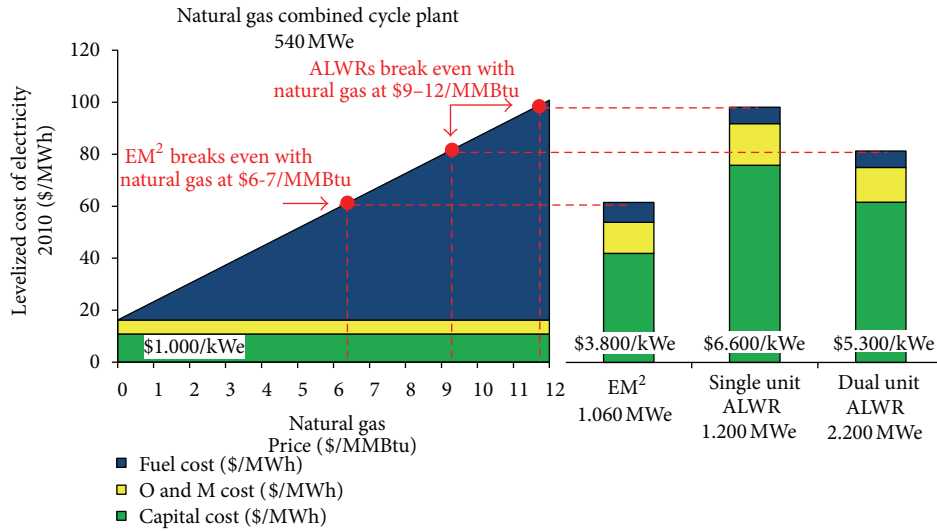


FIGURE 11: Comparison of EM² power cost versus other generating options.

Acknowledgment

This work was supported by General Atomics internal funding.

References

- [1] C. K. Paulson, "Westinghouse AP1000 electrical generation costs—meeting marketplace requirements," in *Proceedings of the International Congress on Advances in Nuclear Power Plants (ICAPP '02)*, Hollywood, Fla, USA, 2002.
- [2] "Innovative small and medium sized reactors: design features, safety approaches, and R&D trends," IAEA-TECDOC-1451, International Atomic Energy Agency, 2005.
- [3] *Report to Congress on Small Modular Nuclear Reactors*, U.S. Department of Energy, 2001.
- [4] *Design Features to Achieve Defense in Depth in Small and Medium Sized Reactors*, Nuclear Energy Series no. NP-T-2.2, International Atomic Energy Agency, 2009.
- [5] *Status of Innovative Small and Medium Sized Reactor Designs 2005: Reactors with Conventional Refuelling Schemes*, IAEA-TECDOC Series no. 1485, International Atomic Energy Agency, 2006.
- [6] R. L. Black, "Small modular reactor U.S. market and licensing possibilities," in *Proceedings of the American Nuclear Society Annual Meeting*, Atlanta, Ga, USA, June 2009.
- [7] *Status of Small Reactor Designs without On-Site Refuelling*, IAEA-TECDOC Series no. 1536, International Atomic Energy Agency, 2007.
- [8] D. J. Senior, C. L. Painter, K. J. Geelhood et al., "A new innovative spherical cermet nuclear fuel element to achieve an ultra-long core life for use in grid-appropriate LWRs," PNNL-16647, Pacific Northwest National Laboratory, 2007.
- [9] A. A. Belyaev, A. V. Kurachenkov, Y. K. Panov, and O. B. Samoilov, "Nuclear energy sources on the basis of integral reactors," *Nuclear Engineering and Design*, vol. 173, no. 1-3, pp. 131-141, 1997.
- [10] K. Hibi, H. Takimoto, M. Chaki, M. Matsuura, and K. Moriya, "Development of the package-reactor (1) -reactor for pioneering new nuclear markets," *Progress in Nuclear Energy*, vol. 47, no. 1-4, pp. 115-122, 2005.
- [11] M. Kambe, H. Tsunoda, K. Mishima, and T. Iwamura, "RAPID-L operator-free fast reactor concept without any control rods," *Nuclear Technology*, vol. 143, no. 1, pp. 11-21, 2003.
- [12] F. Sefidvash, "Status of the small modular fluidized bed light water nuclear reactor concept," *Nuclear Engineering and Design*, vol. 167, no. 2, pp. 203-214, 1996.
- [13] I. V. Dulera, A. Basak, P. P. Kelkar, and R. K. Sinha, "Compact high temperature reactor (CHTR)," in *Proceedings of the 16th Annual Conference of Indian Nuclear Society (INSAC '05)*, Mumbai, India, November 2005.
- [14] Z. Su'ud, "Advanced SPINNORs concept and the prospect of their deployment in remote area," in *Proceedings of the International Conference on Advances in Nuclear Science and Engineering (ICANSE '07)*, Bandung, Indonesia, November 2007.
- [15] Z. Su'ud and H. Sekimoto, "Preliminary design study of the ultra long life fast reactor," *Nuclear Engineering and Design*, vol. 140, no. 2, pp. 251-260, 1993.
- [16] M. Kawashima, K. Aoki, K. Arie, and Y. Tsuboi, "Neutronic feasibility of an LMFBR super long-life core (SLLC)," *Nuclear Engineering and Design*, vol. 106, no. 3, pp. 357-373, 1988.
- [17] T. K. Kim and T. A. Taiwo, "Feasibility study of ultra-long life fast reactor core concept," in *Proceedings of the Advances in Reactor Physics to Power the Nuclear Renaissance (PHYSOR '10)*, pp. 1756-1766, Pittsburgh, Pa, USA, May 2010.
- [18] J. Gilleland, C. Ahlfeld, D. Dadiomov et al., "Novel reactor designs to burn non-fissile fuels," in *Proceedings of the International Congress on Advances in Nuclear Power Plants (ICAPP '08)*, Anaheim, Calif, USA, June 2008.
- [19] A. E. Waltar and A. B. Reynolds, *Fast Breeder Reactors*, Pergamon Press, New York, NY, USA, 1981.
- [20] P. Yarsky, *Core design and reactor physics of a breed and burn gas-cooled fast reactor [Ph.D. thesis]*, Massachusetts Institute of Technology, 2005.

- [21] P. Wälti and P. Koch, "MICROX: a two-region flux spectrum code for the efficient calculation of group cross sections," General Atomic Report GA-A10827, Gulf General Atomic Company, 1972.
- [22] G. D. Joanou and J. S. Dudek, "GAM II, a B3 code for the calculation of fast neutron spectra and associated multigroup constants," General Atomic Report GA-4265, Gulf General Atomic Company, 1963.
- [23] G. D. Joanou, C. V. Smith, and H. A. Vieweg, "GATHER-II, an IBM-7090 code for the calculation of thermal neutron spectra and associated multigroup constants," General Atomic Report GA-4132, Gulf General Atomic Company, 1963.
- [24] C. A. Stevens and C. V. Smith, "GAROL: a computer program for evaluating resonance absorption including resonance overlap," Tech. Rep. GA-6637, Gulf General Atomic Company, 1965.
- [25] K. L. Derstine, "DIF3D: a code to solve one-, two-, and three-dimensional finite difference diffusion theory problems," Tech. Rep. ANL-82-64, Argonne National Laboratory, 1984.
- [26] R. Sherman, "PCBURP: a macroscopic cross section generation and nuclide depletion program for use with DIF3D," 21C024, General Atomics, 1996.
- [27] T. Nakagawa, H. D. Lemmel, and P. K. McLaughlin, "The JENDLE-3.3 fission-product data library," IAEA-NDS-138, International Atomic Energy Agency, 2003.
- [28] A. G. Croff, "A user's manual for the ORIGEN2 computer code," Tech. Rep. ORNL/TM-7175, Oak Ridge National Laboratory, 1980.
- [29] H. Choi, "Physics model of a gas-cooled fast reactor: review and assessment," in *Proceedings of the International Topical Meeting on Advances in Reactor Physics (PHYSOR '12)*, Knoxville, Tenn, USA, April 2012.
- [30] D. B. Pelowitz, Ed., "MCNPXTM user's manual," Tech. Rep. LA-CP-05-0369, Los Alamos National Laboratory, 2005.
- [31] J. Hou, K. Ivanov, and H. Choi, "MICROX-2 cross section library based on ENDF/B-VII," in *Proceedings of the International Topical Meeting on Advances in Reactor Physics (PHYSOR '12)*, Knoxville, Tenn, USA, April 2012.
- [32] J. Hou, K. Ivanov, and H. Choi, "Self-shielding models of MICROX-2 code," in *Proceedings of the International Conference on Mathematics and Computational Methods Applied to Nuclear Science & Engineering (M&C '13)*, Sun Valley, Idaho, USA, May 2013.
- [33] L. L. Snead, T. Nozawa, Y. Katoh, T. S. Byun, S. Kondo, and D. A. Petti, "Handbook of SiC properties for fuel performance modeling," *Journal of Nuclear Materials*, vol. 371, no. 1-3, pp. 329-377, 2007.
- [34] A. Kohyama, Y. Katoh, L. L. Snead, and R. H. Jones, "Development of SiC/SiC composite for fusion application," in *Proceedings of the 18th International Atomic Energy Agency Fusion Energy Conference*, Sorrento, Italy, October 2000.
- [35] H. Choi, D. W. McEachern, and R. W. Schleicher, "Energy Multiplier Module (EM²) recycling fuel cycles," in *Proceedings of the 1st Annual ANS SMR Conference*, Washington, DC, USA, October-November 2011.
- [36] W. E. Cummins, M. M. Corletti, and T. L. Schulz, "Westinghouse AP1000 advanced passive plant," in *Proceedings of the International Congress on Advances in Nuclear Power Plants (ICAPP '03)*, Cordoba, Spain, May 2003.
- [37] "Westinghouse—AP1000," Technology Fact Sheet, Westinghouse, 2008.
- [38] C. Ellis, A. Baxter, and A. Shenoy, "Modular helium reactor fuel cycle concepts and sustainability," in *Proceedings of the 2nd International Topical Meeting on High Temperature Reactor Technology (HTR '04)*, Beijing, China, September 2004.
- [39] "Design manual: CANDU 6 generating station physics design manual," Wolsong NPP 2 3 4, 86-03310-DM-000 Rev. 1, Korea Atomic Energy Research Institute/Atomic Energy of Canada Limited, 1995.
- [40] J. J. Duderstadt and L. J. Hamilton, *Nuclear Reactor Analysis*, John Wiley & Sons, New York, NY, USA, 1976.
- [41] Y. Du and J. E. Parsons, "Update on the cost of nuclear power," 09-004, Center for Energy and Environmental Policy Research, 2009.
- [42] "Cost estimating guidelines for Generation IV nuclear energy systems, Revision 4.2," GIF/EMWG/2007/004, Generation IV International Forum, 2007.

Research Article

Multiphysics Model Development and the Core Analysis for In Situ Breeding and Burning Reactor

Shengyi Si

Shanghai Nuclear Engineering Research & Design Institute, 29 Hongcao Road, Shanghai 200233, China

Correspondence should be addressed to Shengyi Si; jacksil68@gmail.com

Received 13 November 2012; Accepted 19 February 2013

Academic Editor: Wei Shen

Copyright © 2013 Shengyi Si. This is an open access article distributed under the Creative Commons Attribution License, which permits unrestricted use, distribution, and reproduction in any medium, provided the original work is properly cited.

The in situ breeding and burning reactor (ISBBR), which makes use of the outstanding breeding capability of metallic pellet and the excellent irradiation-resistant performance of SiC_f/SiC ceramic composites cladding, can approach the design purpose of ultralong cycle and ultrahigh burnup and maintain stable radial power distribution during the cycle life without refueling and shuffling. Since the characteristics of the fuel pellet and cladding are different from the traditional fuel rod of ceramic pellet and metallic cladding, the multiphysics behaviors in ISBBR are also quite different. A computer code, named TANG, to model the specific multiphysics behaviors in ISBBR has been developed. The primary calculation results provided by TANG demonstrate that ISBBR has an excellent comprehensive performance of GEN-IV and a great development potential.

1. Introduction

After 60 years of development and deployment, nuclear energy has become one of the three main energy sources supporting human society. Although it happened to three major nuclear accidents during past decades and projected a big shadow on the nuclear energy development, especially the Fukushima Nuclear Event, occurred in March, 2011, significantly twisted people's understanding to nuclear safety, but, people still could not stop the prospects on nuclear energy, as the fossil energy on earth is gradually drying up and increasingly expensive, and the other renewable energy is not enough stable and reliable. By now, except for a few European countries, who claim to terminate their nuclear power projects, the main energy consumers of the world, including China and the United States, have clearly declared their positive position to their established nuclear power route, and several new projects just have been approved during the past recent years.

However, it should be pointed out that the existing nuclear power technology could not support the sustainable nuclear energy development for long-term prospects. The reason is that the existing nuclear power technology is mainly based on water-cooled reactor. It is well known that the fuel

utilization of water-cooled reactor is less than 1%, which means that the existing water-cooled reactors are quickly consuming the limited natural uranium resource and producing the huge volume of depleted uranium in front end and the high radioactive spent fuel in back end. According to the 2009 edition of the IAEA red book [1], the natural uranium reserves (including proven and inference) on the earth are about 3.7 million tons (development costs < \$80/kgU) or 4.5 million tons (development costs < \$130/kgU), and the global natural uranium consumption in 2011 is about 70000 tons [2]; at this rate, the existing nuclear development way can only maintain around 50 years. Furthermore, along with the gradual expansion of global nuclear energy, natural uranium demand is expected to rise steadily to 100000 tons/year in 2015 year [2]. On the other hand, it is approximately estimated that the nuclear development during past 60 years has consumed around 2.8 million tons of natural uranium and produced about 2.5 million tons of depleted uranium and 0.25 million tons of high radioactive spent fuel. Therefore, it is clear that the existing nuclear power technology cannot guarantee a sustainable nuclear development.

In fact, the international society has long known the limitation of the existing nuclear energy technology and has been actively looking for effective ways to pursue the sustainability

for nuclear development. Among them, a general consensus is that fuel breeding and closed fuel cycle are the crucial options to realize sustainable nuclear energy development. As is well known, fast reactor or harden spectrum is the necessary condition to achieve fuel breeding for current uranium-plutonium fuel cycle, whereas it seems a little optimistic if we think that the existing fast reactor technology is just the solution to the sustainable issue. Taking the existing sodium-cooled fast reactor (SFR) adopting oxide fuel as an example, the one year or so of the refueling cycle brings not only heavy burden of reprocessing and a significant increase in the fuel cycle cost, but also the 20 to 25 years of doubling time seems to give people a choking sense. In recent years, Terra Power LLC, which is founded by Bill Gates, proposed an innovative concept of traveling wave reactor (TWR), which is based on the platform of pool-type sodium-cooled fast reactor by using metallic fuel pellet and HT9 cladding; TWR can approach 30~40 years of ultralong cycle life and around 30 at % of ultrahigh burnup without refueling, but with periodical fuel shuffling during the cycle life. Theoretically, the TWR can well satisfy the need of sustainable nuclear power development, whereas, because the TWR core is composed of igniting region of medium-enriched uranium and blanket region of depleted uranium, the core radial power distribution shall become severely heterogeneous and have significant variation during the cycle life, and also the ultrahigh burnup shall pose a big challenge to the dose limitation of the HT9 cladding. Therefore, there are still a series of questions for TWR's engineering implementation.

Based on the above understanding, this paper proposed an innovative concept of in situ breeding and burning reactor (ISBBR), which is based on the platform of traditional sodium-cooled fast reactor (SFR), and can approach ultralong cycle and ultrahigh burnup and maintain stable radial power distribution during the cycle life without refueling and shuffling. A computer code TANG modeling main multiphysics phenomenon in ISBBR has been developed for the core design balance. The primary calculation results provided by TANG demonstrate that ISBBR has an excellent comprehensive performance of GEN-IV and a great development potential.

2. The In Situ Breeding and Burning Reactor

Obviously, the prerequisites to approach in situ breeding and burning are that the fuel should have great breeding capability and the fuel reactivity should change very slowly during the cycle life. Figures 1 and 2 present the evolution of reactivity and normalized ^{239}Pu versus fuel burnup for several typical fuel materials, which are designed to have similar initial reactivity. It is clear to see that the ternary alloy of Uranium-Plutonium-Zirconium has good attributes matching the demand of ISBBR.

In addition, in order to ensure the integrity of the fuel rod under the conditions of ultralong cycle and ultrahigh burnup, the ISBBR's structure material, especially the fuel cladding material, should have outstanding radiation resistant performance besides the better heat conduction

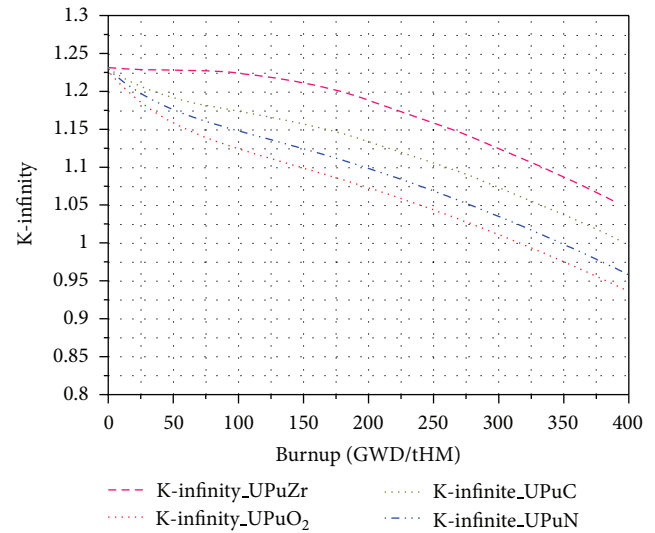


FIGURE 1: Reactivity versus burnup for typical fuel materials.

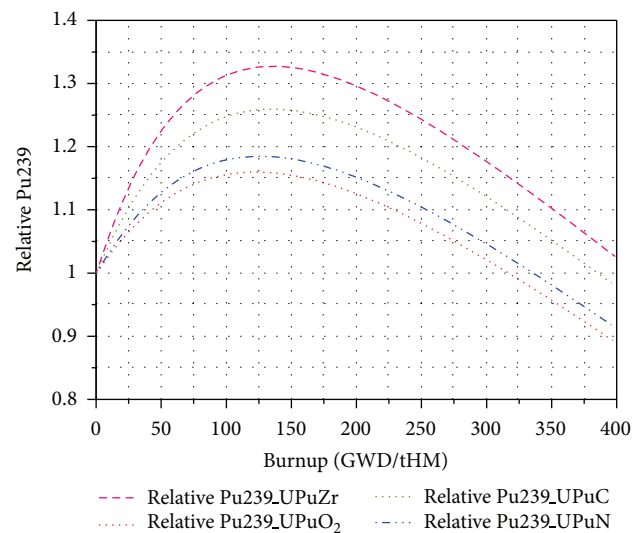
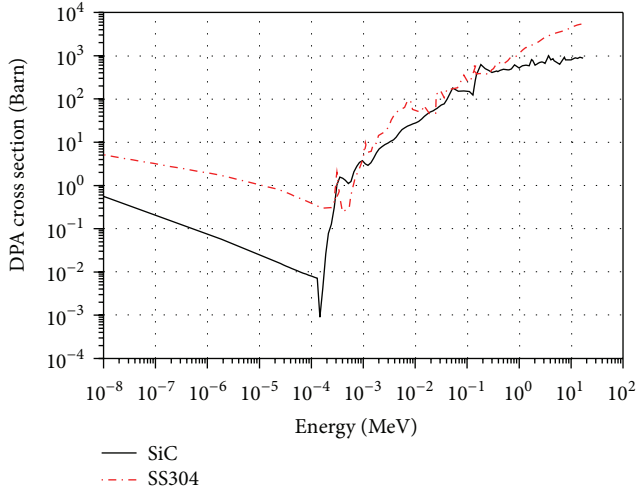
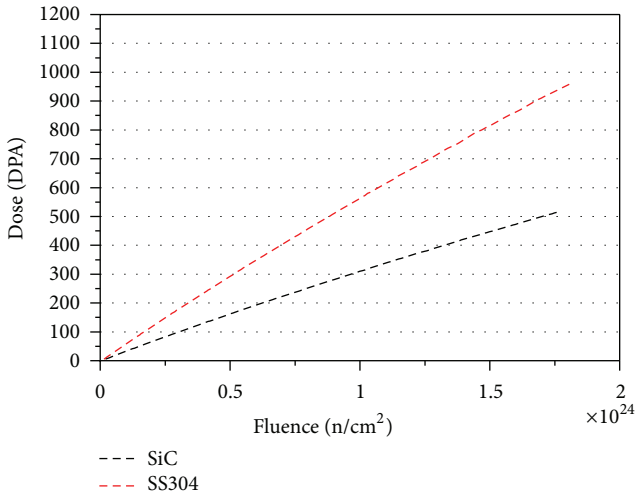


FIGURE 2: Normalized ^{239}Pu versus burnup for typical fuel materials.

capability and mechanical performance. The cladding material of the traditional sodium-cooled fast reactor (SFR) is Austenite or Martensite Stainless Steel, whose radiation-resistant performance is not enough promising. Some new structure materials under developing, such as ODS and HT9, are predicted to have good radiation-resistant capability; however, it is difficult to have a revolutionary solution because these materials are still iron based. Recently, an innovative ceramic composite material SiC_f/SiC has been causing more and more attention from the nuclear field because of its comprehensive performance of heat conduction, mechanical properties, and radiation resistant. It is said that SiC_f/SiC is the most promising for the first wall material in fusion reactor [3]. Figures 3 and 4 present the comparison of DPA cross section and radiation dose for SiC_f/SiC and stainless steel;

FIGURE 3: DPA cross section for stainless steel and SiC_f/SiC.FIGURE 4: DPA dose for stainless steel and SiC_f/SiC.

we can see that the DPA cross section of SiC is much lower than SS304 in lower energy and high energy region, and the accumulated radiation dose of SiC is much lower than SS304 for a given SFR spectrum.

In the view of the above analysis, our proposed in situ breeding and burning reactor (ISBBR) shall select the ternary alloy of Uranium-Plutonium-Zirconium as fuel pellet, SiC_f/SiC as cladding material, and liquid sodium as coolant. Table 1 describes the general design parameters of the reference ISBBR core, and Figure 5 illustrates the schematics of reference core, fuel assembly, and fuel rod.

The reference core is a small modular reactor. The rated thermal power is 800 MWt, the rated mass flow rate is 5000 kg/Sec, and the inlet coolant temperature is 350°C. The core is composed of 222 fuel assemblies, 30 control assemblies, 270 shielding assemblies, and a barrel. The equivalent diameter of active core is about 252 cm and the outer diameter of barrel is about 350 cm. The active core is divided into inner zone (104 assemblies, identified with 1 in Figure 6) and

TABLE 1: General parameters for reference core of ISBBR.

Thermal power, MWt	800
Electricity power, MWe	300
Coolant flow rate, kg/sec	5000
Inlet temperature, °C	350
System pressure, MPa	0.1
Number of fuel assembly	222
Number of control assembly	31
Number of shielding assembly	270
Flat to flat distance of FA, cm	~12.5
Number of fuel pin in a FA	60
Fuel rod pitch, cm	1.50
Fuel rod diameter, cm	1.40
Active fuel height, cm	200
Plenum height, cm	200
Cladding material	SiC _f /SiC
Pellet material	UPuZr
Coolant material	Sodium
Control absorber material	B ₄ C
Detail size	Reference Figure 5
Heavy metal inventory in core, ton	40.4
DU (0.3 w/o ²³⁵ U), ton	35.8
Reactor grade Pu, ton	4.6
Composition of Pu:	
²³⁸ Pu (%)	3.54
²³⁹ Pu (%)	50.94
²⁴⁰ Pu (%)	22.99
²⁴¹ Pu (%)	15.15
²⁴² Pu (%)	7.38

outer zone (104 assemblies, identified with 2 in Figure 6). The unique difference for the fuel assemblies in inner zone and outer zone is the Zirconium contents in the fuel pellet which are 20% and 10%, respectively.

The fuel assembly has an overall length of 460 cm and contains 90 fuel pins arranged in a triangular pitch array within a duct, see Figure 5. The duct thickness is 0.1 cm and the flat-to-flat distance of the duct is around 12.5 cm. Fuel pins are made of sealed SiC_f/SiC cladding containing a metallic fuel pellet column of 200 cm length. Just below the fuel slug is a 60 cm shield segment, with the shield being an integral part of the fuel pin in the form of an extended fuel-pin bottom end cap. Sodium is filled as the initial thermal bond between the fuel column and the cladding. And a 200 cm long fission gas plenum is located above the fuel slug and sodium bond. The fuel pin diameter and cladding thickness are 1.4 cm and 0.1 cm, respectively, and the inner diameter and outer diameter of the annular pellet are 0.4 cm and 1.1 cm, respectively. The fuel smeared density is 80%. The fuel pin is helically wrapped with wire to maintain the pin spacing so that the coolant can flow freely through the pin bundle. The wire-wrap helical pitch is 20.32 cm and the wire diameter is 0.1 cm.

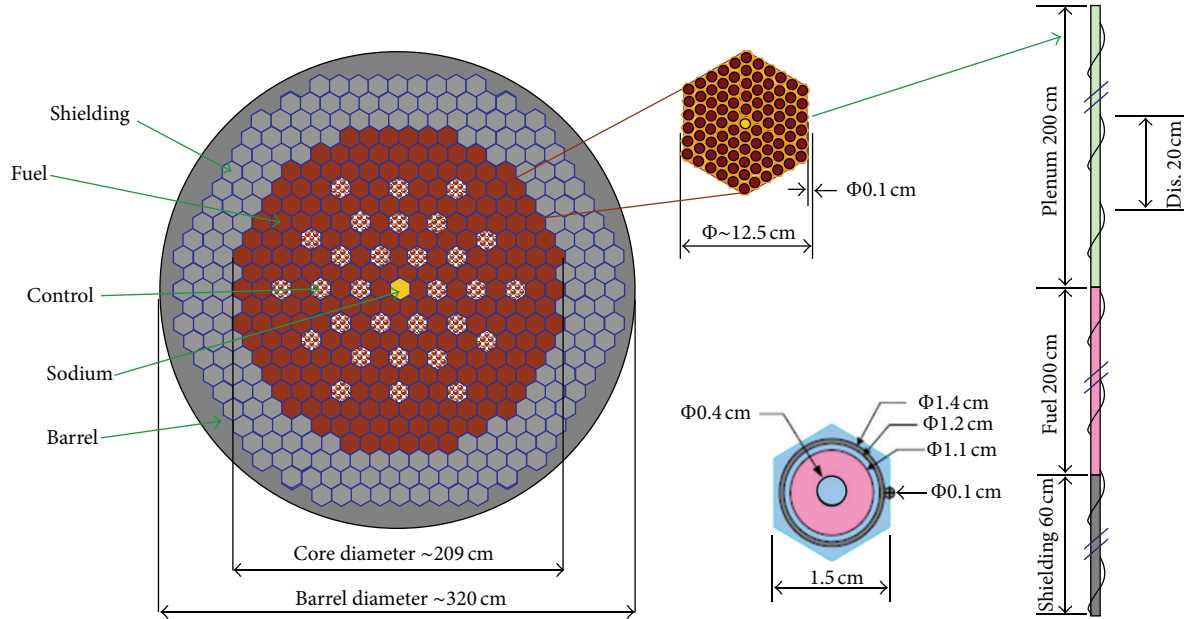


FIGURE 5: Schematic for the reference core of in situ breeding and burning reactor.

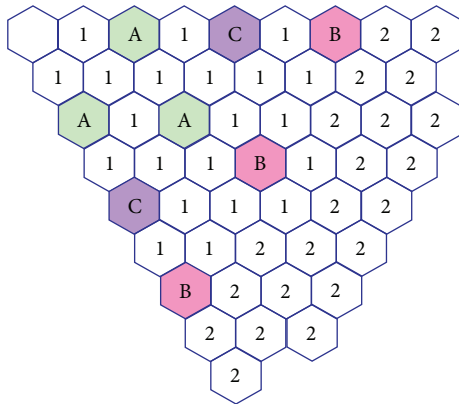


FIGURE 6: Grouping and Layout of Control Assembly.

The control assemblies consist of an absorber bundle contained within a duct. The absorber bundle is a closely packed array of tubes containing compacted boron carbide pellets. The natural boron whose B-10 enrichment is 19.9 a/o is used. Thirty control assemblies are grouped into A, B, and C banks, where bank A is the primary manipulated bank, bank B is the secondary control bank, and bank C is the shutdown bank. The grouping of the control assemblies and its layout are given in Figure 6.

3. The Multiphysics Model Development for ISBRR

Traditionally, nuclear design, thermal-hydraulic analysis, and fuel performance analysis for a reactor core are performed

independently. Actually, the neutronics behavior, thermal-hydraulic behavior, fuel thermodynamics behavior, and fuel irradiation behavior in a reactor core are tightly coupled with each other. In PWR core design, thermal-hydraulic feedback has been considered widely in core analysis code due to the significant spectrum effect of coolant density and Doppler effect of fuel temperature. As for ISBRR, besides the thermal-hydraulic feedback, the reactivity effect of thermal expansion and irradiation swelling also have significant influence on the core reactivity and the cycle life.

Figure 7 illustrates the main physics phenomena in the core using metallic fuel. Basically, the neutronics process (Cross Section Parameter \rightarrow Diffusion/Transport Solution \rightarrow Neutron Flux \rightarrow Reaction Rate \rightarrow Burnup \rightarrow Cross section Parameter, see Figure 7) is the main driving force for the multiphysics phenomena in the core. Generally, the interactions of neutronics with other disciplines can be grouped into instant effect and historical effect. As for the instant coupling effect, power density derived from the reaction rate determines the fuel rod surface heat flux and the coolant flow field (coolant density and temperature), and also, the power density dominates the fuel temperature distribution in pellet. On the other hand, the coolant density and temperature and fuel temperature and the fuel thermal expansion have direct influence on the cross section parameter, neutron flux, and power density. As for the historical accumulation effect, the accumulated neutron irradiation connects to the fuel burnup, deformation (creep and swell) of cladding and pellet, and fission gas release; all these effects will have influence on the local reaction cross section; in addition, the deformation of cladding and pellet affects the free volume of the fuel rod plenum, which has inversely proportional relations with the rod internal pressure.

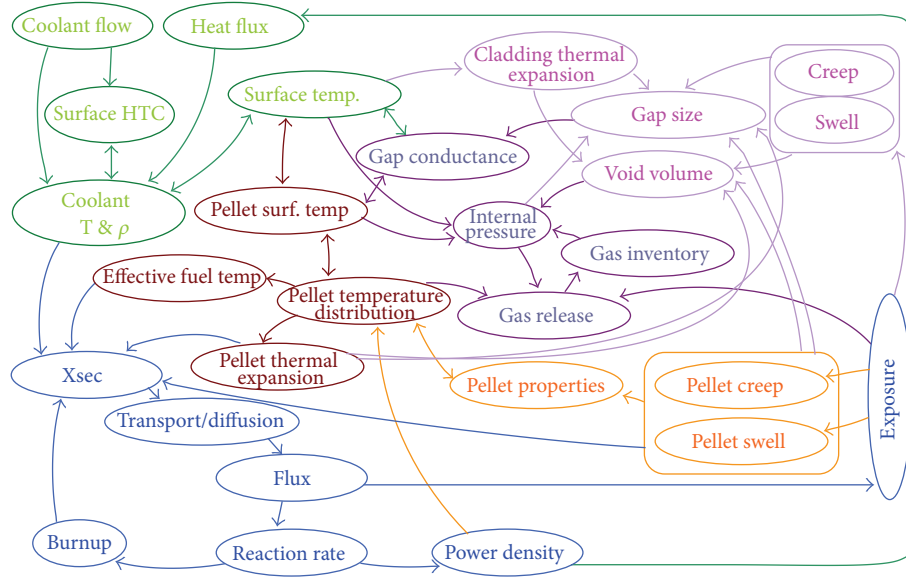


FIGURE 7: Multiphysics behaviors for the core with metallic fuel.

Based on the understanding to the above multiphysics phenomena in the core using metallic fuel and the specific ISBBR fuel design of metallic pellet and ceramic cladding, we developed the specific multiphysics model and the core simulation code TANG for ISBBR. The following sections briefly describe the technical characteristics of the multiphysics model and computer code TANG.

3.1. Neutronics Model. Neutronics model is the kernel of multiphysics model and also the driving force for heat conduction, heat transfer, and deformation of fuel rod. Neutronics model involves depletion model, parameterized cross section model, and multidimension/multigroup neutron diffusion model.

The depletion model solves nonlinear depletion chains by using Matrix Exponential Algorithm and tracks the evolution of nodal-wise number density for major actinides based on the 3D neutron flux and reaction rate during full cycle life. Figure 8 presents the simplified depletion chain for actinides tracked in TANG code.

Parameterized cross section model captures the instant effect and historical effect of various factors on homogenized assembly cross sections. The instant effect is caused by the deviation of instant local conditions from the reference conditions, such as local burnup (bu), local coolant temperature/density (D_c/T_c), local fuel temperature (T_f), and local axial deformation factor (α), and the historical effect is the accumulated effect caused by the long-term deviation of local conditions from the reference conditions since the deviation of local conditions causes the different local neutron spectrum from the reference case, it results in the different depletion rate or production rate for important actinides from the reference case. The local axial deformation factor (α) models the effect of number densities variation caused by axial deformation on homogenized assembly cross

sections. The formula (1) gives the fundamental expression of the parameterized cross section model:

$$\begin{aligned} & \sum (bu, T_f, D_c, \alpha) \\ &= \frac{\sum_{\text{ref}} (bu) + \Delta \sum (bu, T_f, D_c) + \sum_n^N \sigma_n (T_f, D_c) \Delta N_n}{\alpha} \end{aligned} \quad (1)$$

Multidimension/multigroup neutron diffusion model adopts multidimension and multigroup nodal expansion method code MGNEM [4], developed by author previously, to solve multidimension and multigroup neutron diffusion equations for rectangular and hexagonal fuel assembly; also, the universal algorithm of stiffness confinement method (UASCM) [5], which was also developed by author earlier, is coupled with MGNEM to solve multidimension and multigroup time-space kinetic problem. Additional, in order to effectively model the growth of nodal axial mesh caused by thermal expansion and/or irradiation swelling, MGNEM code is using floating mesh in axial direction, so that MGNEM is able to automatically model the axial mesh variation of each node during the iteration process of thermal-hydraulic feedback and finally captures the reactivity effect of axial deformation.

The integration of the above methodologies and technologies endows TANG code abundant calculation functions and flexible simulation ability.

3.2. Fuel Rod Deformation Model. The thermal expansion coefficient of metallic fuel is large (approximately 2 times of ceramic fuel), and the irradiation swelling effect of metallic fuel is also significant (around 30% at high burnup). As a result, the geometrical change of metallic fuel pellet during heating process and/or irradiation process will not only give penalty on the extra reactivity and cycle life of the core, but also will directly affect the transient behavior of the

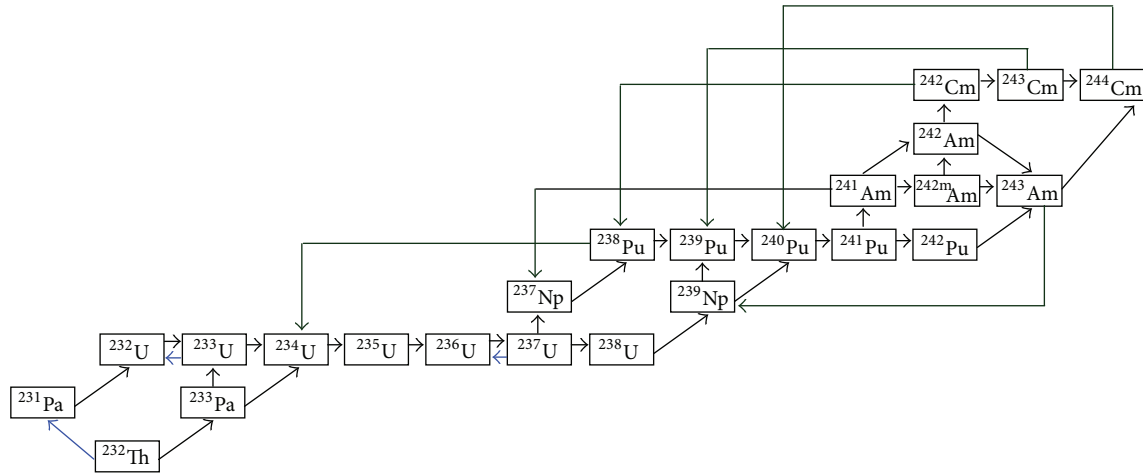


FIGURE 8: Depletion chain for actinides tracked in TANG code.

core, as the negative feedback effect of axial growth can effectively restrain the increase of the reactor core power and automatically bring the reactor to a safe lower power level. The experiments on EBR-II had demonstrated this inherent safety characteristic of the core with metallic fuel [6].

Relative to the metallic pellet, the SiC_f/SiC cladding has very good thermal stability, irradiation stability, and mechanics stability. Firstly, the thermal expansion coefficient of SiC_f/SiC is only about half of the zircaloy; secondly, the existing irradiation experiment (about 43 DPA) shows that the swelling and creeping phenomena are very weak [3]; in addition, since the strength and hardness of SiC_f/SiC are very outstanding, the strain caused by stress for SiC_f/SiC material is also very limited. Table 2 presents the properties of relative materials.

According to the above analysis on the metallic pellet and SiC_f/SiC ceramic cladding, we proposed a “rigid cladding model” to describe the fuel rod deformation behavior in ISBRR, which assumes the following.

- (i) The deformation of SiC_f/SiC ceramic cladding is only due to thermal expansion, irradiation swelling, creeping, and stress/strain are ignored.
- (ii) The deformation of metallic pellet may be caused by thermal expansion, irradiation swelling, and creeping.
- (iii) After the metallic pellet contacts with ceramic cladding, the contact stress shall not cause any strain to ceramic cladding.
- (iv) After the metallic pellet contacts with ceramic cladding, the metallic pellet shall become yielded consequently due to the contact stress, and according to the Prandtl-Reuss flow rule, the expansion shall develop to the inner hole of the annular pellet; once the inner hole is closed, the expansion shall switch to axial direction.

Thermal expansion is recoverable and the irradiation deformation (swelling and creeping) is irrecoverable. Therefore,

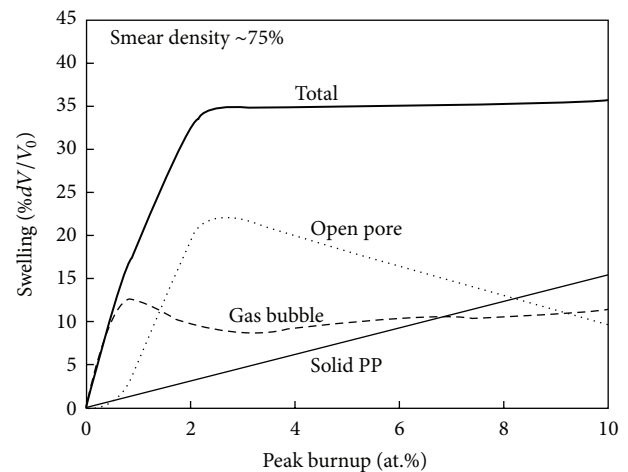


FIGURE 9: Radial swelling versus burnup for metallic fuel.

with the assumption of “rigid cladding model,” the cladding deformation is recoverable, and the pellet deformation involves the recoverable and irrecoverable compositions. The recoverable deformation of metallic pellet can affect the core dynamic parameters and the transient behavior of the core, and the irrecoverable deformation of the metallic pellet has direct penalty on the core extra reactivity and the cycle life.

Metallic fuel had significant irrecoverable deformation (swelling and creeping). Figures 9 and 10 present the radial deformation and axial deformation behavior of metallic fuel versus the fuel burnup, respectively, which are based on the experimental results of EBR-II. It can be seen from Figures 9 and 10 that the irradiation deformation of metallic fuel is anisotropic in radial and axial direction; the radial deformation is much more significant than the axial deformation, and the radial deformation grows quickly before 2 at% burnup, and thereafter it maintains around 35% of volume change rate. The irradiation deformation models used in TANG code are just taken from Figures 9 and 10 [7].

TABLE 2: Properties of several typical fuel materials.

	Thermal expansion coefficient ppm/°C	Brinell hardness kg/mm ²	Young's modular (E) GPa	Poisson's ratio (ν)
UO ₂ (ceramic)	~9	~2000	~96	~0.3
UPuZr (alloy)	~18	~260	~85	~0.3
Zircaloy	~10	~120	~100	~0.3
Stainless steel	~17	~100	~196	~0.3
SiC _r /SiC (ceramic) [3]	~4	~2800	~300	~0.14

3.3. *Fuel Rods Heat Conduction/Transfer Model.* Each fuel assembly in ISBBR is contained within a duct, which directs the coolant flow to fuel rods of the fuel assembly, and there is no exchange of coolant mass and momentum among the assemblies. Therefore, it is reasonable for TANG code to adopt the “single channel model” to simulate the heat conduction within fuel rod and heat transfer between rod surface and coolant; TANG code has a “single channel model” for each fuel assembly modeled in the core to calculate the averaged effect of coolant density/temperature, cladding temperature, and fuel temperature in each elevation of the fuel assembly, and then, the 3D nodal-wise coolant density/temperature, cladding temperature, and fuel temperature are passed to 3D neutronics model, rod deformation model, and other models, so that all models are tightly coupled into a multiphysics model.

The “single channel model” in TANG code uses finite difference method to solve time-dependent heat conduction equation in cylindrical R-Z geometry for steady-state and transient solution, which shall be coupled with steady-state or transient 3D neutronics model. The heat conduction along z-direction is considered due to the high heat conductivity of metallic pellet.

The discrete of heat conduction equation is based on the nominal rod sizes so as to maintain the stability during equation solution, but the deformed rod sizes are used for the gap conductance calculation.

3.4. *Fuel Rod Internal Pressure Model.* The fuel rod in ISBBR might endure extra high internal pressure and even endanger the fuel rod integrity due to the fission gas release and accumulation under ultralong cycle and ultrahigh burnup. Therefore, the fuel rod internal pressure in ISBBR is an important design constraint. Based on the “single channel model” and 3D burnup distribution of the core, TANG code tracks the fission gas release fraction for 3D nodes and calculates assembly-averaged fuel rod internal pressure at each burnup step.

The main components of fission gas are Xe and Kr, and the total fission yield of Xe and Kr is about 0.25 (totally 2.0). Fission gas is gathered in the grain boundary in earlier stage; with the burnup accumulation, the fission gas gradually gathers into bubble; bubbles grow along with the increased inner pressure and connected mutually; finally, it forms a coherent tunnel. Eventually, fission gas is driven by the temperature and the pressure and release to the gap between pellet and cladding and then the plenum of the rod. The coherent tunnel in metallic fuel is formed at around 2~3 at%

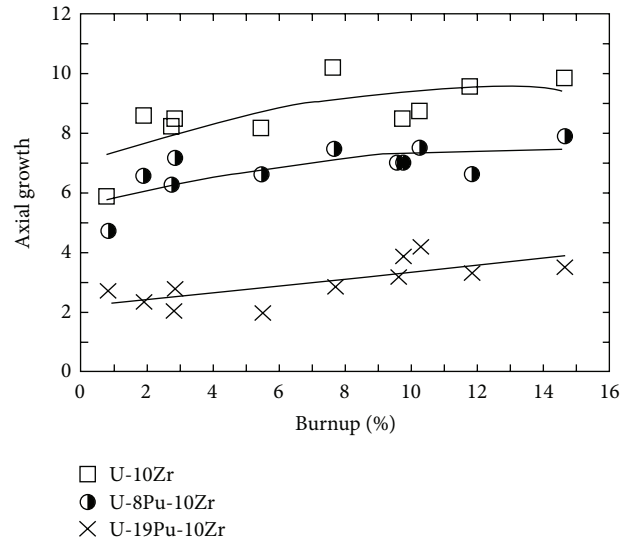


FIGURE 10: Axial swelling versus burnup for metallic fuel.

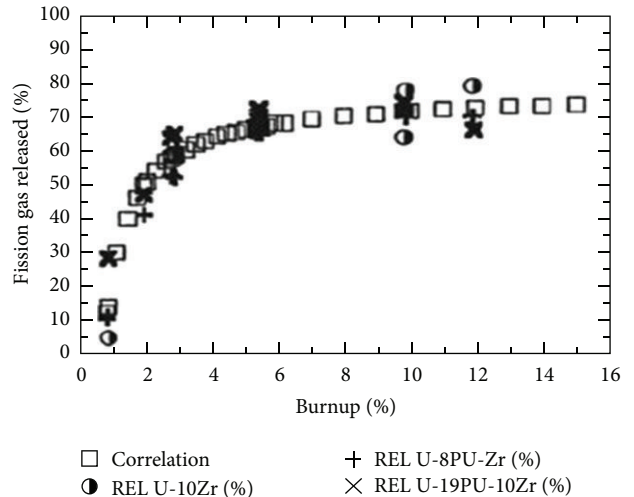


FIGURE 11: Fission gas releases fraction for metallic fuel.

of burnup, the release fraction of fission gas increases quickly prior to 3 at% of burnup; thereafter, the release fraction maintains at around 70%. Figure 11 presents the fission gas release fraction of metallic fuel versus the fuel burnup, which is based on the experimental results of EBR-II. The fission gas release model used in TANG code is just taken from Figure 11 [7].

The fuel rods internal pressure is calculated by using the free gas state equation $PV = MRT$, in which, P is the fuel rods internal pressure; V is the volume of free space in fuel rods, involving the comprehensive effect of the ceramic cladding deformation, metallic pellet thermal expansion, metallic pellet swelling, and the liquid sodium surface rise squeezed by the deformed cladding and pellet; M is the fuel rods internal gas mole number, including the fission gas and the initial fill gas; R is a universal gas constant ($R = 8.34 \text{ J/Mole-K}$); T is the average temperature of the fuel plenum.

3.5. Fuel Rod Exposure Dose Model. The structure material, especially the cladding material, in ISBBR might endure severe radiation damage due to ultralong time exposure of fast neutron spectrum. The radiation damage to material usually is measured by displacement per atom (DPA), which means the accumulative displacement number of each medium atom. TANG code equips a fuel rod exposure dose model, so that the maximum cladding dose can be monitored during core design process.

The multigroup DPA cross sections (σ_g^{DPA}) are stored in the parameterized cross section library as the same as other cross sections expressed in formula (1); TANG code shall evaluate the accumulated cladding dose for each node of core based on the 3D flux solution (ϕ_g) and the depletion time increment (ΔT , Sec) with the following formula:

$$\text{DPA}^{n+1} = \text{DPA}^n + \Delta T \sum_g \sigma_g^{\text{DPA}} \phi_g. \quad (2)$$

4. Calculation Results

The reference ISBBR core was analyzed with TANG code, and the calculation results are introduced in following sections.

4.1. Steady-State Results Analysis. Figure 12 shows the relation of atom burnup and energy burnup for reference ISBBR core during 25 effective full power years (EFPYs); it can be seen that 1 at% burnup is equivalent to about 10 GWD/tHM for the reference core; the slight deviation at end of life is due to the fission energy of minor actinide (MA) which is a little higher than plutonium.

Figure 13 presents the critical position of control assembly and the evolution of the peaking power factors during the cycle life. It can be seen from Figure 13 that ISBBR can achieve stable and flat power distribution during the 25 EFPYs of cycle life; Figure 14 further shows the radial power distribution of reference core at different burnup steps and demonstrates that the radial power distribution of reference core is well maintained without shuffling and refueling within an ultralong cycle life. Therefore, ISBBR can avoid the significant distortion and variation of the power distribution existing in other conceptual breeding and burning reactors [8–11]. It is beneficial to core design and power distribution control in engineering sense.

Figure 15 presents the assembly-wise distribution for key design parameters at EOL (25 EFPYs) tracked by the multiphysics models in TANG code. Maximum dose is the

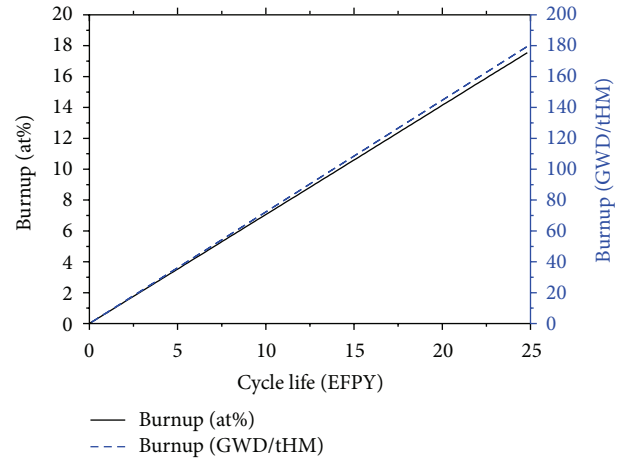


FIGURE 12: Burnup versus cycle length for reference core.

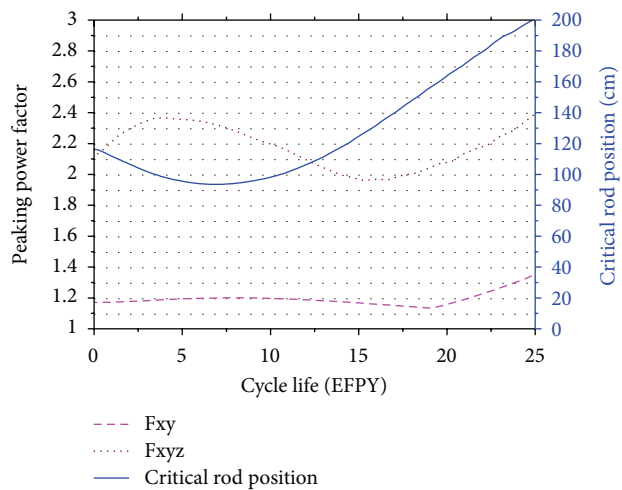
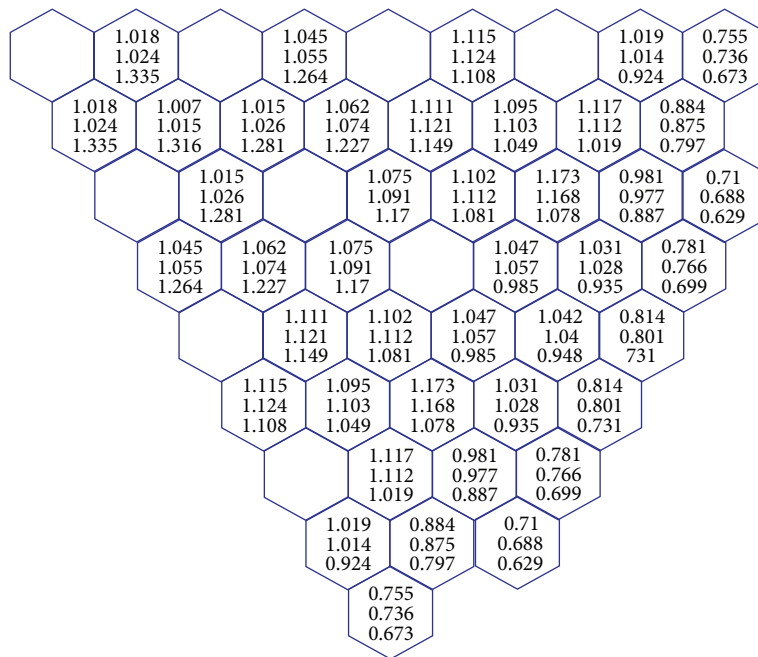


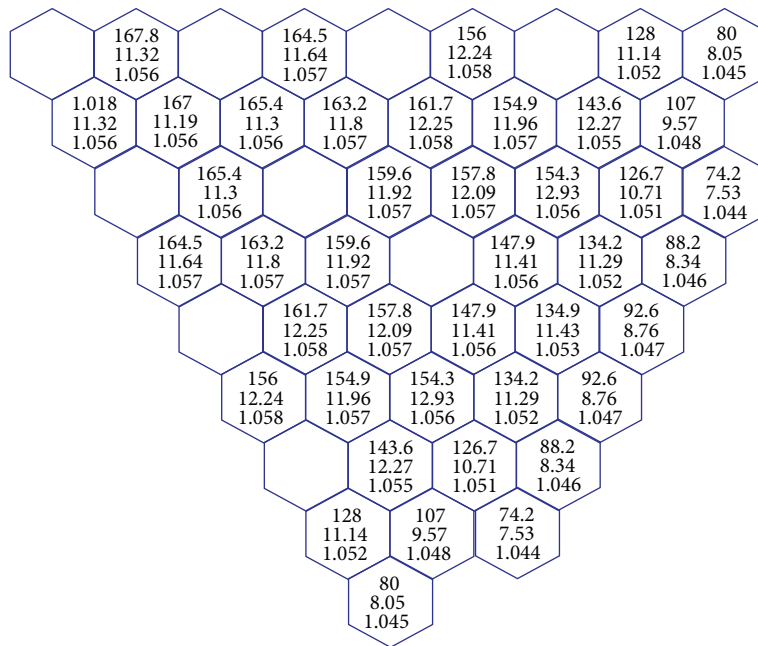
FIGURE 13: Critical rod position and power peaking factor versus cycle lifetime.

peaking irradiation dose for each assembly, and the results show that the maximum irradiation dose at EOL for the SiC_f/SiC ceramic cladding in ISBBR core is about 167.8 DPA, which is far smaller than that using stainless steel cladding (e.g., for TWR, the peaking irradiation dose may be as high as 500 DPA); internal pressure is an assembly-averaged rod internal pressure, and the tracked results demonstrate that the maximum internal pressure of fuel rod at EOL in reference core is about 13 MPa, which is thought to be safe to the rod integrity according to the experience of PWR rod performance analysis; the axial deformation factor is an assembly-averaged axial deformation factor, and the calculation results show that the axial deformation of the reference core is more balanced among the full core, which means that the annular pellet has accommodated the radial pellet swelling and the axial deformation is mainly composed of thermal expansion and axial swelling. Figure 16 illustrates the influence of axial thermal expansion and swelling on the core reactivity.



- 0 EFPY
- 15 EFPY
- 25 EFPY

FIGURE 14: Assembly-wise power distribution at 0 EFPY/15 EFPY/25 EFPY.



- Maximum dose (DPA)
- Internal pressure (MPa)
- Axial deformation factor

FIGURE 15: Assembly-wise maximum cladding dose, rod internal pressure, and average axial deformation factor at EOL.

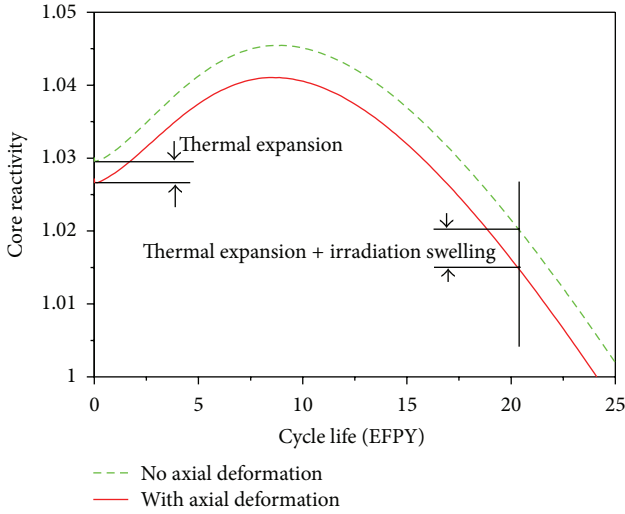


FIGURE 16: Influence of axial expansion on cycle lifetime.

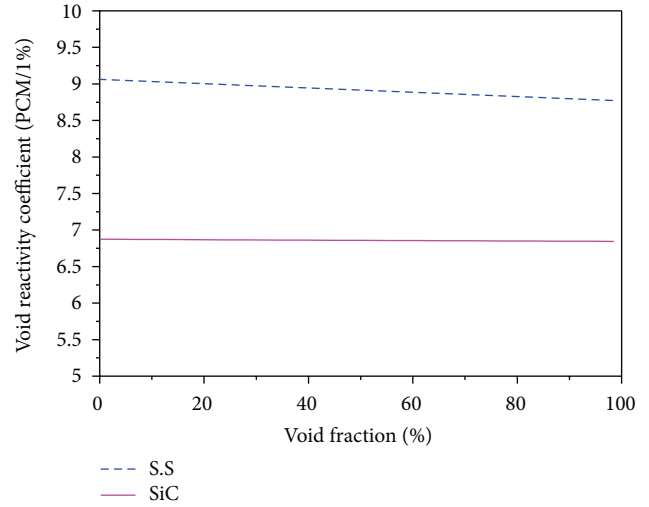


FIGURE 18: Influence of SiC_f/SiC on void reactivity.

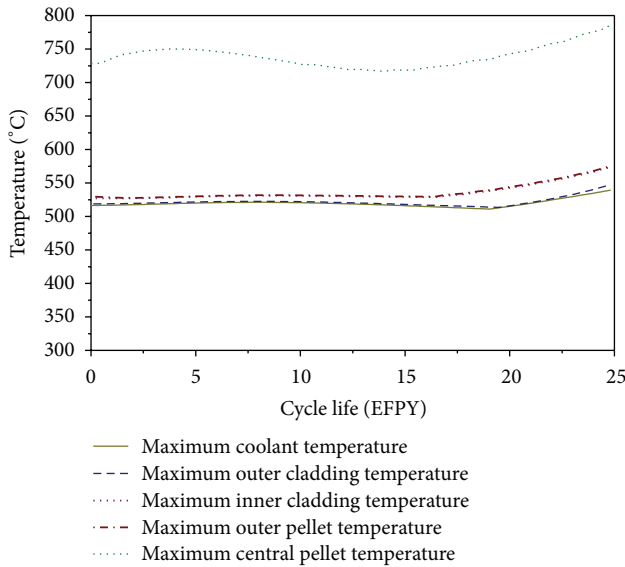


FIGURE 17: Rod peaking temperatures versus cycle lifetime.

Figure 17 shows evolution of the peaking coolant temperature and the peaking fuel rod temperatures versus the cycle life of the reference core. It can be seen from Figure 17 that each indicator has undergone an even history and maintains enough margin to their corresponding design limit, for example, the boiling point of sodium coolant is around 892°C, while the peaking coolant temperature within the reference core cycle life is around 550°C; the maximum operating temperature for SiC_f/SiC ceramic cladding is 1600°C, while the peaking cladding temperature during cycle life of the reference core is only around 550°C, and the molten point of metallic pellet (ternary alloy of Uranium-Plutonium-Zirconium) is about 1200°C, but the peaking fuel central temperature during the cycle life is lower than 800°C. Therefore, the reference core of ISBFR has enough thermal margins during the whole cycle life for steady-state operation.

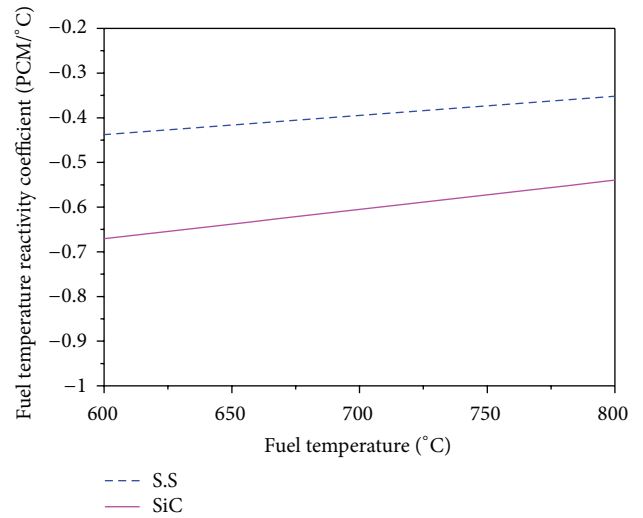


FIGURE 19: Influence of SiC_f/SiC on Doppler effect.

4.2. *Transient Results Analysis.* The positive Void Reactivity Coefficient and smaller Fuel Doppler Temperature Coefficient are the main characteristics of the sodium-cooled fast reactor and also the main concerns of people to the safety of the sodium-cooled fast reactor. Some studies in [12] show that the positive Void Reactivity Coefficient and smaller Fuel Doppler Temperature Coefficient may be improved if some moderator is introduced into the sodium-cooled fast reactor. Actually, SiC is also a kind of good moderator. Therefore, the Void Reactivity Coefficient and Fuel Doppler Temperature Coefficient of the reference ISBFR core can have significant improvement compared with the traditional SFR using stainless steel cladding, see Figures 18 and 19.

The early demonstration experiments on EBR-II had proved that the SFR using metallic fuel could safely approach lower power level during the anticipated transient without

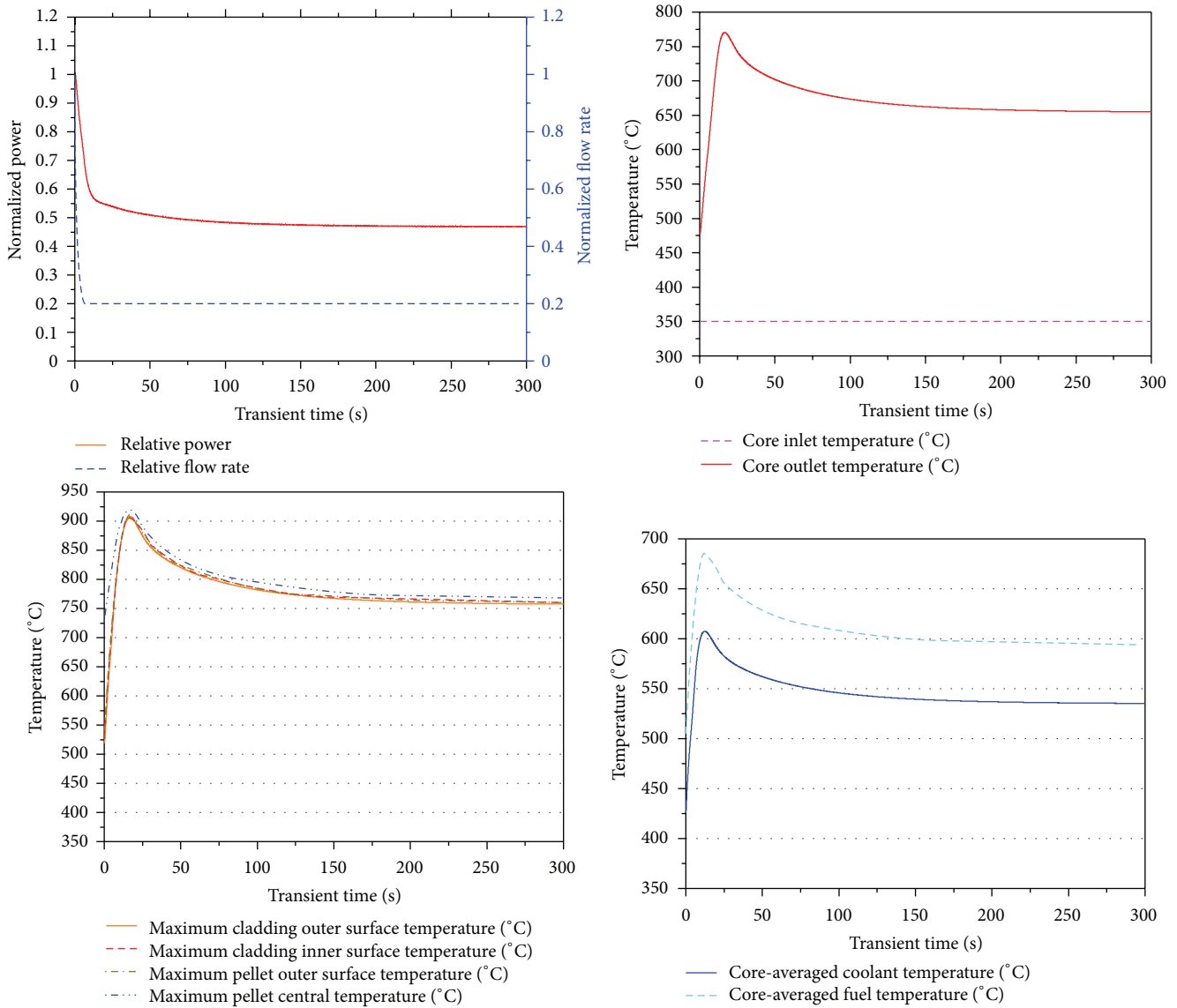


FIGURE 20: Core key parameters response during ULOFA.

scram (ATWS) [6]. The demonstration experiments on EBR-II included unprotected loss of flow (ULOFA) and unprotected loss of heat sink (ULOHSA). In these two events, the initial state of the reactor was full power operation; after the transients were triggered, the reactor power was gradually decreased to lower level due to the inherent safety characteristics of neutronics and thermal-hydraulic and thermal dynamics of metallic fuel, and no damaged consequence happened, such as coolant boiling, cladding defect, or pellet molten.

TANG code is used to simulate the transient response for ULOFA and ULOHSA of reference ISBRR core. The calculated results are given in Figures 20 and 21 for ULOFA and ULOHSA, respectively. It can be seen from Figure 20 that the reactor power shall automatically decrease to 50% or so without any control assembly inserted after the flow rate rapidly reduced to 20% of the nominal value, and the peaking

coolant temperature, the peaking cladding temperature, and the peaking pellet central temperature are far lower than their corresponding operation limits; similarly in Figure 21, after loss of heat sink, the core inlet temperature is rapidly increased from 350°C to 520°C, and at the same time, the power level is gradually decreased to 45% or so without any protective action, and all crucial design parameters are in safe state. These analysis results demonstrate that the reference ISBRR core has inherent passive safety during typical transient processes.

4.3. Fuel Cycle Analysis. ISBRR makes use of the outstanding breeding capability of metallic fuel, produces more fissile material as consuming existing fissile material, and finally achieves ultralong cycle life and ultrahigh burnup.

Figure 22 shows the core-averaged breeding ratio of the reference ISBRR versus cycle life, and it is clear that the

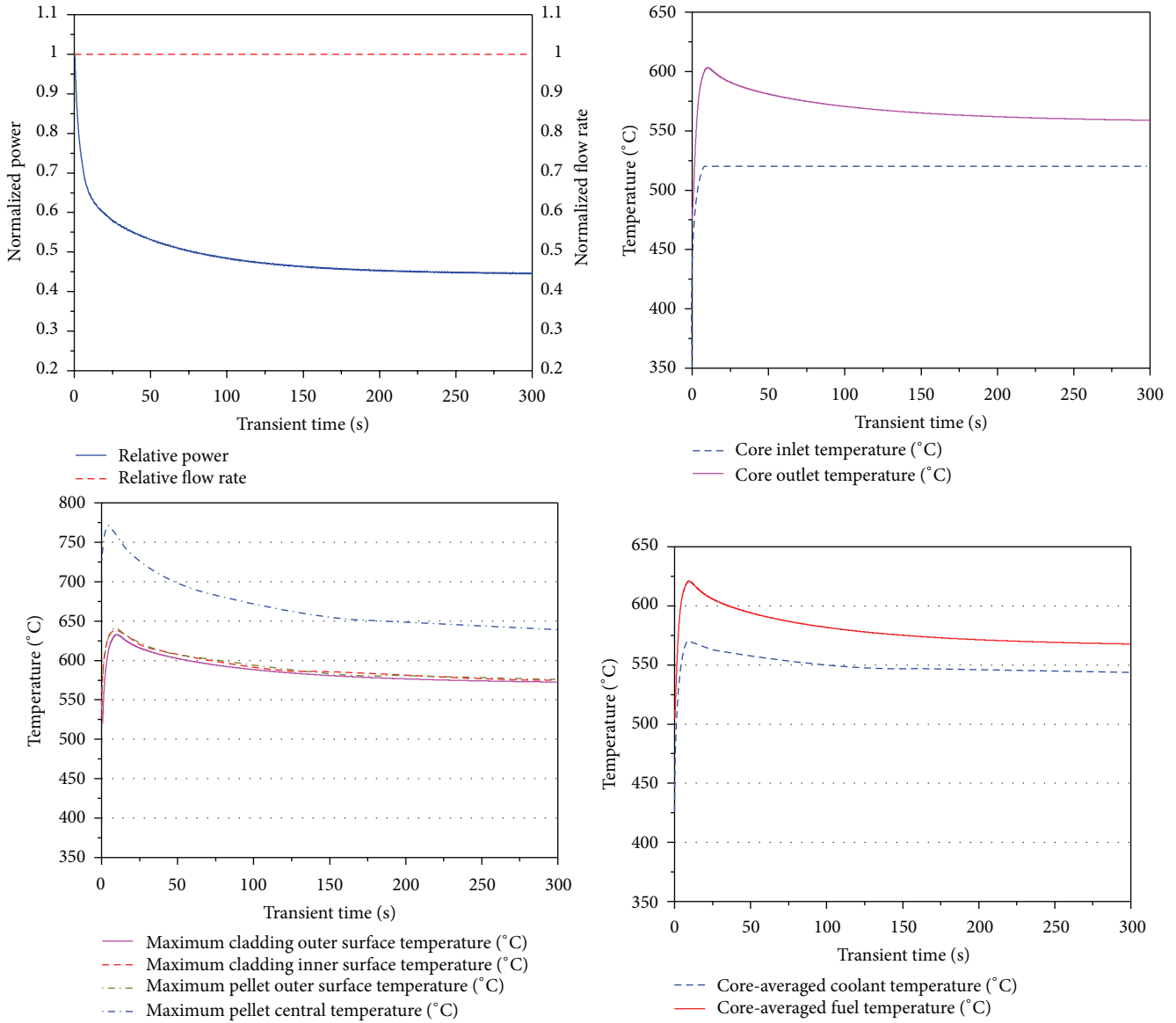


FIGURE 21: Core key parameters response during ULOHSA.

core is always breeding; the heavy metal inventory of the reference core versus cycle life is also given in Figure 22. The initial inventory of heavy metal is about 40.4 tons (including 35.8 tons of depleted uranium and 4.6 tons of Reactor Grade Plutonium), and the final inventory of heavy metal at EOL is around 33 tons, so totally there are about 7.4 tons of heavy metal burnt out, and the fuel utilization rate is about 18%. Therefore, the fuel cycle economy of ISBRR is significantly improved compared with current water-cooled reactor, where the typical utilization is only 0.5~0.6 at%.

The motivation to propose ISBRR is not only to pursue safe and economical energy, but also for the following strategic prospects:

- (1) continuously consume the huge volume of the depleted uranium and spent fuel accumulated by the development and deployment of water-cooled

reactor, and finally achieve the minimization of the waste volume;

- (2) Support sustainable development and deployment of fission energy and provide abundant and reliable energy for the peace and development of human society.

The precondition to achieve the above strategic goals is that ISBRR should implement closed fuel cycle. Fortunately, the low molten point (around 1200°C) property of metallic fuel has provided a very favorable condition for economical reprocessing of spent fuel. And then, the prerequisite to achieve sustainable closed fuel cycle for ISBRR is the quantity and quality of the fission material in the spent fuel which has no degradation compared with the initial inventory. Figure 23 illustrates the evolution of plutonium inventory versus the cycle life; it can be seen that the plutonium inventory is

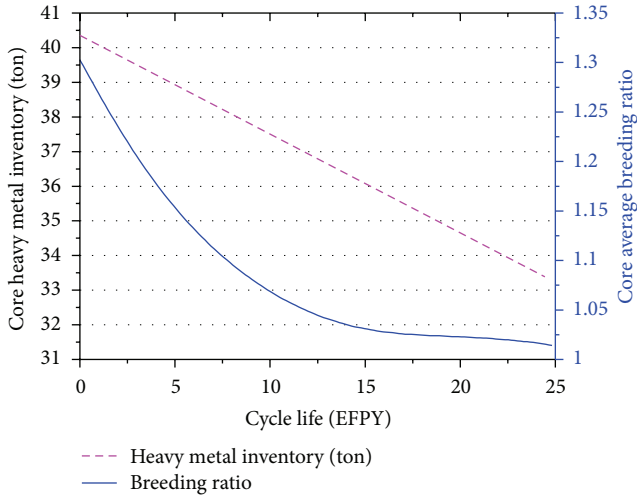


FIGURE 22: Core heavy metal inventory and breeding ratio versus cycle lifetime.

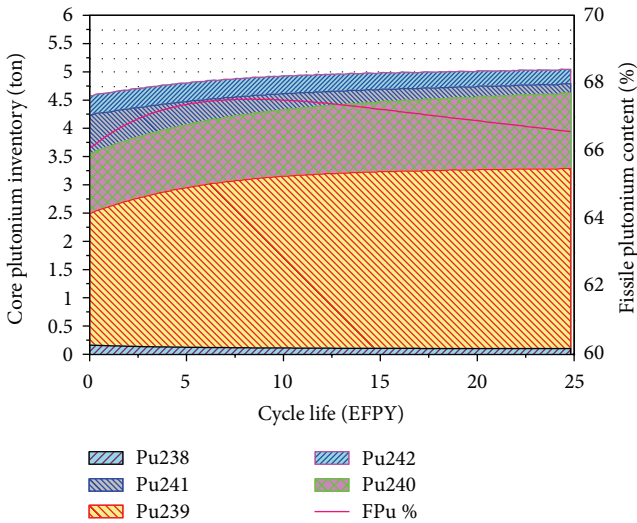


FIGURE 23: Core plutonium inventory and fissile plutonium fraction versus cycle lifetime.

increased from initial 4.3 tons to final 5.1 tons during the cycle life, the incremental is about 10%, and the content of fissile plutonium (^{239}Pu and ^{241}Pu) in total plutonium also has been increased compared with the initial 65%. Therefore, both the quantity and quality of the fission material in ISBBR spent fuel satisfy the prerequisite to maintain sustainable closed fuel cycle.

ISBBR does not pursue the accumulation or doubling of the extra plutonium, but the synchronized breeding and burning of fissile isotopes within an ultralong cycle life; therefore, it naturally satisfies the requirement of nonproliferation.

And also, only relying on the huge amount of depleted uranium and spent fuel accumulated by water-cooled reactor, ISBBR can achieve sustainable fission energy supply for long term and finally achieve the minimization of the waste volume. Let us assume that all the natural Uranium resource

on the earth shall be utilized by PWR, it means that there will be about 6 million tons of depleted uranium and about 0.6 million tons of spent fuel accumulated finally; usually, the content of Reactor Grade Plutonium in the PWR spent fuel is nearly 1%, so the accumulated Reactor Grade Plutonium shall be 6000 tons; taking the reference ISBBR core as an example, where the initial plutonium inventory is 4.6 tons, then, the accumulated Reactor Grade Plutonium is enough to equip $6000/4.6 \approx 1300$ units of reference ISBBR and provides approximate $300 \text{ MWe} \times 1300 = 390 \text{ GWe}$ of power supply (a little higher than the current nuclear power installed capacity 377 GWe in the world); now, the 1300 units of ISBBR shall be loaded with $1300 \times 35.8 \text{ tons} \approx 47,000$ tons of depleted uranium and $1300 \times 4.6 \text{ tons} \approx 6,000$ tons of Reactor Grade Plutonium for a fuel cycle, in which $1300 \times 7.4 \text{ ton} \approx 9600$ tons of heavy metal shall be burnt out; taking another assumption, let us ignore the 10% increment of the Reactor Grade Plutonium in spent fuel and think it is used to compensate for the loss during spent fuel reprocessing and the new fuel fabrication, then, the time for these 1300 units of ISBBR to consume the accumulated 6 million tons of depleted uranium can be approximately estimated as follows:

$$\frac{6000000 + (600000 - 6000) - (47000 + 6000)}{9600} \times 25 \text{ year} \approx 17000 \text{ years.} \tag{3}$$

Humans, of course, may not need 17,000 years of fission energy supply; in turn, they may want to have much more installed capacity. In this case, people can have some breeder reactors in earlier stage and produce Reactor Grade Plutonium, and then, they can get their wanted installed capacity by building enough units of ISBBR. Even if the number of ISBBR unit was increased to 13,000 units, the accumulated 6 million tons of Depleted Uranium still can support over 1000 years of nuclear power supply.

5. Conclusion

Based on the platform of traditional sodium-cooled fast reactor, making use of the innovative fuel design and core design, ISBBR can achieve ultralong cycle and ultrahigh burnup and maintain stable radial power distribution during the cycle life without refueling and shuffling.

Primary calculation results, provided by specifically developed computer code TANG, demonstrate that the ISBBR core has enough thermal margins during steady-state operation and inherent passive safety during anticipated transients.

The fuel cycle analysis indicates that the fuel utilization rate of ISBBR can approach 18% and have significant fuel cycle economy compared with the current water-cooled reactors, where fuel utilization is about 0.5~0.6%.

In addition, the features of ultralong cycle, no extra plutonium accumulation, and sustainable closed fuel cycle demonstrate that ISBBR can realize the minimization of waste volume, nonproliferation, and sustainable nuclear power supply.

In conclusion, ISBRR can well satisfy the requirements of Gen-IV nuclear energy system, such as sustainability, economy, safety, and nonproliferation and has a great development potential.

References

- [1] IAEA/NEA/OECD, *Uranium2009: Resources, Production and Demand*, IAEA/NEA/OECD, 2010.
- [2] World Nuclear Association, *The Global Nuclear Fuel Market: Supply and Demand 2011–2030*, World Nuclear Association, London, UK, 2011.
- [3] R. H. Jones, D. Steiner, H. L. Heinisch, G. A. Newsome, and H. M. Kerch, “Radiation resistant ceramic matrix composites,” *Journal of Nuclear Materials*, vol. 245, no. 2-3, pp. 87–107, 1997.
- [4] S. Si, “3D coarse mesh NEM embedded with 2D fine mesh NDOM for PWR core analysis,” in *Proceedings of the Advances in Reactor Physics to Power the Nuclear Renaissance Conference (PHYSOR '10)*, pp. 257–268, Pittsburgh, Penn, USA, May 2010.
- [5] S. Si, “Algorithm development and verification of UASCM for multi-dimension and multi-group neutron kinetics model,” in *Proceedings of the Advances in Reactor Physics Conference—Linking Research, Industry, and Education (PHYSOR '12)*, Knoxville, Tenn, USA, April 2012.
- [6] S. H. Fistedis, Ed., *The Experimental Breeder Reactor II Inherent Safety Demonstration*, vol. 101 of *Nuclear Engineering and Design No. 1*, North-Holland, New York, NY, USA, 1987.
- [7] R. G. Pahl, D. L. Porter, D. C. Crawford, and L. C. Walters, “Irradiation behavior of metallic fast reactor fuels,” *Journal of Nuclear Materials*, vol. 188, pp. 3–9, 1992.
- [8] T. Ellis, R. Petroski, P. Hejzlar et al., “Traveling-wave reactors: a truly sustainable and full-scale resource for global energy needs,” in *Proceedings of the International Congress on Advances in Nuclear Power Plants (ICAPP '10)*, Paper 10189, pp. 13–17, San Diego, Calif, USA, June 2010.
- [9] G. J. van Tuyle, G. C. Slovik, B. C. Chan, K. J. Kennett et al., “Summary of advanced LMR evaluation-PRISM and SAFR,” Tech. Rep. NUREG/CR-5464, 1989.
- [10] Y. I. Chang, P. J. Finck, C. Grandy et al., “Advanced burner test reactor preconceptual design report,” Tech. Rep. ANL-ABR-1, 2006.
- [11] T. K. Kim and T. A. Taiwo, “Feasibility study of ultra-long life fast reactor core concept,” in *Proceedings of the Advances in Reactor Physics to Power the Nuclear Renaissance Conference (PHYSOR '10)*, pp. 1756–1766, Pittsburgh, Penn, USA, May 2010.
- [12] B. Merk, “On the effect of different placing ZrH moderator material on the performance of a SFR core,” *Annual of Nuclear Energy*, vol. 38, pp. 2374–2385, 2011.

Research Article

Moderating Material to Compensate the Drawback of High Minor Actinide Containing Transmutation Fuel on the Feedback Effects in SFR Cores

Bruno Merk

Department of Reactor Safety, Institute of Resource Ecology, Helmholtz-Zentrum Dresden-Rossendorf, Postfach 51 01 19, 01314 Dresden, Germany

Correspondence should be addressed to Bruno Merk; b.merk@hzdr.de

Received 4 September 2012; Accepted 4 February 2013

Academic Editor: Wei Shen

Copyright © 2013 Bruno Merk. This is an open access article distributed under the Creative Commons Attribution License, which permits unrestricted use, distribution, and reproduction in any medium, provided the original work is properly cited.

The use of fine distributed moderating material to enhance the feedback effects and to reduce the sodium void effecting SFRs is described. The drawback on the feedback effects due to the introduction of minor actinides into SFR fuel is analyzed. The possibility of compensation of the effect of the minor actinides on the feedback effects by the use of fine distributed moderating material is demonstrated. The consequences of the introduction of fine distributed moderating material into fuel assemblies with fuel configurations foreseen for minor actinide transmutation are analyzed, and the positive effects on the transmutation efficiency are shown. Finally, the possible increase of the Americium content to improve the transmutation efficiency is discussed, the limit value of Americium is determined, and the possibilities given by an increase of the hydrogen content are analyzed.

1. Introduction

The positive coolant density feedback coefficient is inherent to the system in sodium-cooled fast reactors (SFRs). This effect is the basis for the sodium void effect, which is the maximal reduction of the sodium density. The reduction of the positive feedback effects as well as the enhancement of the negative ones is an important point in the design of future sodium-cooled fast reactors. The relevance of the topic has been highlighted in the last year in the IAEA TM on Innovative Fast Reactor Designs with Enhanced Negative Reactivity Feedback Features in Vienna [1].

The nature of feedback effects in fast reactors as well as the sodium void effect itself and the different contributions to the effect are well known since the 1960s. Detailed descriptions have already been given in “Reactivity Coefficients in Large Fast Power Reactors” in 1970 [2]. Already in the 1970s numerical studies were performed with the aim to reduce the sodium void effect [3]. These studies were mostly performed on the basis of full core calculations for the optimization of the core geometry to reduce the sodium void effect.

One important outcome of the full core calculations was the development of high leakage cores with their big core diameter (~5 meters) in combination with a very small core height (≤ 1 meter). Another method for the enhancement of the leakage in the case of sodium voiding is the replacement of the reflector above the core with a sodium plenum which enhances the leakage significantly in the case of a sodium voiding event in the upper core region. Current publications mostly concentrate on the design of sodium-cooled fast reactor cores [4], on advanced safety concepts for SFR [5], and on basic or detailed discussions on the different influencing parameters on the sodium void coefficient [6, 7] and the limited possibilities for enhancing the feedback effects in traditional designs.

Recently, a new proposal has been published. The positive void effect is reduced here in combination with a significant enhancement of the negative fuel temperature effect and a decrease of the positive coolant effect by adding fine distributed moderating material. The study has been focused in the first step on the choice of the ideal moderating material [8, 9] and in a second step on the optimization of the placing

of the zirconium hydride to obtain the optimal effect in power distribution and burnup [10, 11] to limit the required changes in the fuel assembly and in the core design.

The calculations are performed with the lattice transport code HELIOS and based detailed full fuel assembly geometry representation. These possibilities are given due to the rapid development of the spectral codes for LWR analysis which solve the integral transport equation in two dimensions on unstructured mesh [12, 13]. These codes offer the chance to investigate the feedback effects on fuel assembly level for different designs in full detail including multigroup visualization of integral and resolved neutron flux and cross sections. The verification of the results for the enhanced feedback effects calculated with HELIOS has been performed by a comparison calculation using MCNP 5 [8, 9].

The insertion of moderating material softens the neutron spectrum of the fast reactor. Nevertheless, for the burning of minor actinides, a hard neutron spectrum is essential due to the fission threshold of these isotopes. Following this knowledge, the effect of the use of a small, fine distributed amount of moderating material on the efficiency of minor actinide burning will be investigated in this publication.

2. Reference System

For the beginning of the study, a reference case based on the European Fast Reactor is defined (see Figure 1). The data is mostly given in the IAEA Fast Reactor Database—2006 Update [14]. Additional data is taken from Waltar, Reynolds: Fast Breeder Reactors [15] and from European fast reactor (EFR) fuel element design [16]. The following major parameters are used: outer pin diameter 8.5 mm, cladding thickness 0.52 mm, pitch to diameter 1.2, can wall thickness 4.5 mm, wire spacers, and 271 fuel rods per element.

Materials. MOX Fuel with 22.4% Pu fissile and Pu vector from 4% enriched LWR fuel with 50 GWd/tHM burnup. 5-year storage is estimated before reprocessing and 2 years until reuse in the reactor. The Pu-Vektor is (2.6/54.5/23.7/11.3/6.8) and 1.1% Am-241 in depleted uranium (0.3% U-235 content). The smeared fuel density is 9.26 g/cm^3 , and the fuel temperature is 900°C . Cladding, wire spacers, and can wall are made from stainless steel 304 along the HELIOS 1.9 definition. The temperatures are 635°C for the cladding and 545°C for wire spacer and can wall. Sodium density is 0.821 g/cm^3 along the formula for liquid saturated sodium at 545°C given in Waltar and Reynolds [15]. The geometric arrangement of the reference system with 10 rings is shown in Figure 1 for 1/6 part of one fuel element. The used power density is 118.8 W/g corresponding to the maximum power density in the EFR. For the calculation HELIOS is used. The internal I12 group fast reactor cross-section library of Studsvik Scandpower is used for the investigation. Only for the calculations of the neutron spectrum the 190 energy group library is used to have a refined energy structure in the thermal range for a better depiction.

Three different minor actinide loadings will be investigated (3% Am, 5% Am, and 2% Np—2% Am) [17]. The Am

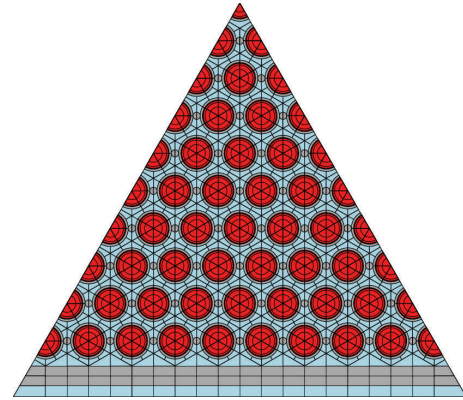


FIGURE 1: 1/6 of the reference fuel element geometry corresponding EFR.

vector is following the same basic definitions as described for the Pu vector mentioned previously. This definition gives 62% Am-241 and 38% Am-243. The data for the used moderators ZrH1.6 and YH is taken from [18].

3. System with Moderating Material

The basic idea to shift a small portion of the neutron spectrum to lower energies is achieved by the introduction of moderating material inside the wire wrapper as is shown in Figure 2. For the visualization purpose, only one unit cell is extracted from the calculated 1/6 of a fuel assembly. The purpose of the moderating material is to force up the absolute value of the negative fuel temperature feedback and to reduce of the positive coolant feedback (consisting of coolant density and temperature effect) coinciding with a reduction of the sodium void effect. The fine distributed placing of the moderating material in each unit cell offers the possibility to keep the original fuel assembly design as well as the power density and the uniform power distribution typical for a homogeneous fast reactor fuel assembly. These three facts ensure that the flow conditions in the fuel assembly can be kept like in the reference design. Thus the flow conditions can still be optimized to keep or improve the safety-related coolability.

The proposed moderating material hydrogen can be inserted in the form of stable metal-hydrogen compounds like zirconium hydride or yttrium hydride; the latter is preferable due to the higher thermal stability. For the manufacturing, it is more suitable to hydride the already produced wire, since it is much easier to handle. Hydride alloys provide a range of hydrogen concentrations in combination with considerable variation in nuclear and mechanical properties. Thus the hydrogen content can be adapted to the special requests. This makes the amount of hydrogen addition into the fuel assembly very flexible; only the maximal values are limited due to the deterioration of the material performance and the solubility limits which decrease with increasing temperatures. “It should not be inferred that the presence of hydrogen in metals is always deleterious. When present

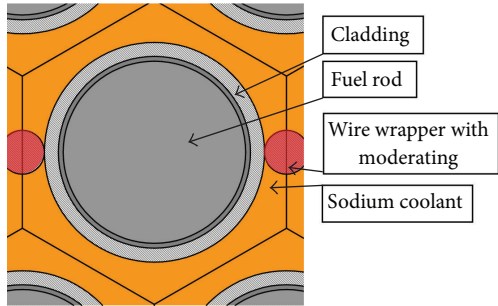


FIGURE 2: Unit cell out of a fuel element based on the European fast reactor (EFR) design with introduced moderation layer.

in amounts less than necessary for embrittlement, hydrogen can cause a noticeable increase in strength so long it can be retained in solution. The important point, again, is that hydrogen presents serious problems only when it is not retained in solution or when its concentration exceeds the solubility limits of the alloy so that hydride precipitates or segregation can occur. Otherwise, hydrogen reacts similarly to other alloying elements in most respects” [18].

Figure 3 gives a general overview on the changes in the neutron flux spectrum due to the insertion of moderating material compared to the reference neutron spectrum. The 190 group HELIOS library is used for these spectral curves to get a sufficiently fine resolution in the thermal groups. The figure shows a significant difference in energy distribution of the neutron flux after the insertion of the moderating material. In the case with the zirconium hydride as wire wrapper, a comparably strong low-energy tail is formed due to the strong moderation effect of the hydrogen atoms in the metallic compound. This low-energy tail has to be seen in conjunction with the radiative capture cross section of U-238 which is added to the figure in green. The insertion of hydrogen causes a significant increase of the share of neutrons in the energies where major capture resonances for the U-238 isotopes appear, especially at energies around 6.67502 eV, 20.8715 eV, 36.6821 eV, 66.0312 eV, 102.559 eV, and 116.8923 eV. Further on, the effectiveness of moderation for the creation of the low-energy tail is compared for a compound based on zirconium and a compound based on yttrium. Both compounds contain exactly the identical amount of hydrogen.

The assembly burnup distribution after 100 GWd/tHM for the reference case and the case with the moderator inside the wire wrapper is given in Figure 4 and compared to the old fashioned solution suggesting pin containing the moderating material. The burnup in the reference fuel assembly (Figure 4(a)) is characterized by a very flat distribution (~1% difference between minimum and maximum) over the fuel assembly as well as over the fuel rods. The reason for this flat burnup distribution can be found in the flat power and neutron flux distribution and in the comparably low total cross sections at the dominating neutron energies. The flat power distribution in the fuel assembly is very favorable, since it disburdens the heat removal. The flat power distribution results in a uniform heat up of the sodium coolant. No hot

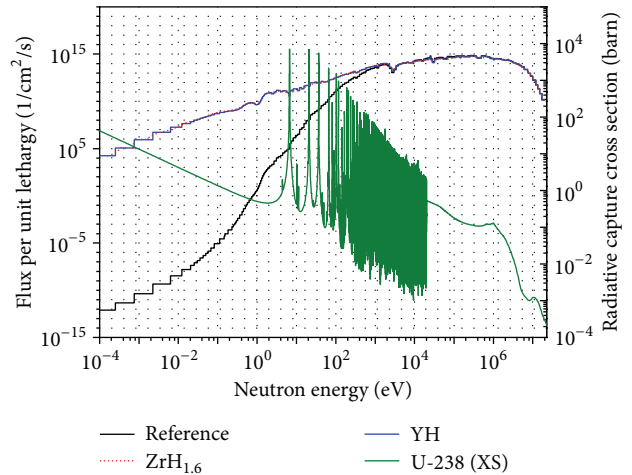


FIGURE 3: Neutron spectrum for the reference fuel assembly and for the fuel assemblies with moderating material based on different hydrogen carrying materials calculated with the 190 group library of HELIOS 1.9.

spots are created and thus all fuel rods can be operated close to the limit power and until the limit burnup defined in the operating permission.

The burnup distribution for case with fine distributed moderating material (Figure 4(b)) is rather uniform over the fuel assembly, too. A small rim effect appears due to the resonance self-shielding in the U-238 and the increased number of neutrons in the resonance region of the U-238 due to the use of the moderating material (compare Figure 3). A very limited burnup increase occurs at the pins close to the can wall. Nevertheless, the insertion of the moderating material in fine distribution, in layers, and in the wire wrapper does not create any severe deterioration in the power and burnup distribution in the fuel assembly. The evaluation of the pinwise values indicates even a more flat distribution than for the reference case, since the power and burnup at the periphery of the fuel assembly are slightly increased [10]. Only the burnup distribution inside the pin is slightly worsened due to the increased rim effect. This behavior is in strong contrast to the results for the use of moderating material in pins as discussed in several publications [18–20]. A locally concentrated introduction of moderating material like moderator pins causes a significant power and burnup increase in the pins around the moderator pins and a lower burnup in the pins far from the moderator pins (see Figure 4(c)). This uneven power and burnup distributions cause limitations to the obtainable maximal average burnup of the fuel assembly, since comparably low burnt fuel rods appear in areas far from the moderation pins. Additionally, a very strong power increase and a rim effect with all followup problems like hot spots and fuel pellet irritations due to the high burnup appear at the pins next to the moderating pins [10, 11].

The use of fine distributed moderating material offers the possibility to enhance the safety characteristics without changing the major operational and design parameters.

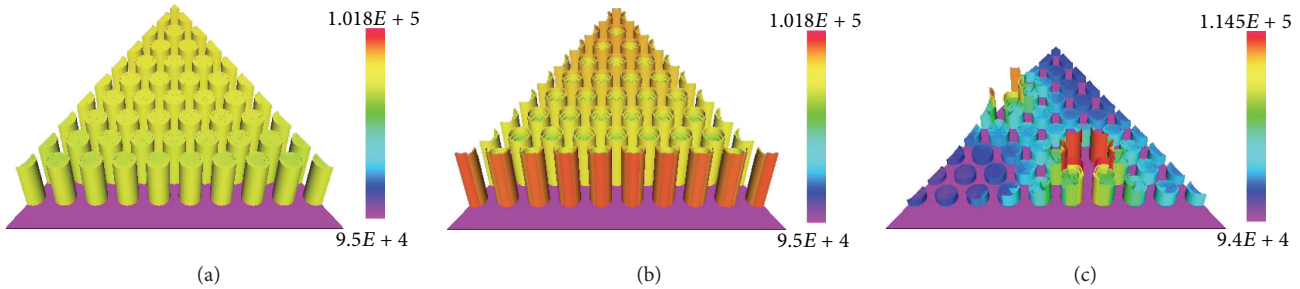


FIGURE 4: Burnup distribution at 100 GWd/tHM for the reference case (a), the case with the moderating material in the wire wrapper (b), and the case with moderating material arranged in pins (c).

Power density and distribution, fuel configuration and density, fuel assembly geometry, and coolant streaming paths are not changed at all. Only the fissile enrichment has to be increased due to the slightly reduced volume available for the fuel, and the loss of criticality caused by the moderating material has to be compensated.

The idea offers new degrees of freedom for the optimization of the design of the sodium cooled fast reactor core, the cycle strategies, and the transmutation potential. The fine distributed moderating material increases the inherent system stability significantly by reducing the positive feedback effects and enhancing the negative ones. Thus it reduces the probability of reaching sodium voiding in a transient. The interesting point is the possibility of tailoring the feedback coefficients to an ideal value simply by adapting the hydrogen content in the compound. The ideal amount has to be determined from system-specific transient and accident analysis, since strong negative feedback is not desired in all accidental scenarios.

On the suggested moderating materials some comments have to be given. For ZrH, on the one hand, the material is a very efficient moderator, due to the extremely high slowing down power of 1.54 ($ZrH_{1.94}$), a value in the same range as for light water [18]. On the other hand, zirconium hydride of δ or ϵ phases does not change the associated volume up to well above 1000°C, since these phases are in the single phase region [18]. Thus zirconium hydride does not show the unpleasant swelling behavior of UZrH fuel, which Olander et al. describe as swelling due to void formation around the uranium particles and due to fission gas production [21]. These described processes should not appear in pure zirconium hydride moderator, since both effects are in conjunction with the Uranium component. The equilibrium hydrogen pressure in ZrH increases at high temperatures, especially above 900°C; this is above the sodium voiding temperature [18]. To suppress Hydrogen release, Mueller et al. suggest to use Kanigen nickel which shows promise as a barrier coating for zirconium hydride with low hydrogen content on the basis of hydrogen loss for times up to 100 h at 1300°F in argon [18].

For YH, the slowing down power is comparable, but the thermal stability is significantly higher, up to ~1300°C for yttrium-mono-hydride [18]. Some limited, but very positive, operational experience on the material is available too, since YH has been used in a test assembly for tailoring the neutron

spectrum for tests for possible radioisotope production in the FFTF [22].

For the verification of the very significant results of the influence of moderating material on the feedback effects in general, a basic cross comparison with MCNP for the fuel temperature and moderator effect on k_{inf} has been performed on simplified basis of a unit cell for the reference cases at the beginning of the investigation of the influence of fine distributed moderating materials in SFR cores to assure that the HELIOS results are reliable. Very good agreement for the moderator temperature and density and for the fuel temperature change has been achieved. The deviation between the MCNP perturbation calculation and the HELIOS 1.9 calculation of the coolant effect on k_{inf} was ~2 pcm which indicates that the sodium void effect calculations are reliable too [8, 9].

An investigation of the transferability of the reduction of the sodium void effect from the infinite to the finite system has been carried out based on the basis of an EFR-like core configuration [23]. To avoid any irritations created by group condensation, the same number of groups has been used in DYN3D. The full core calculations have been performed with the nodal code DYN3D [24, 25]. The calculation is based on 47 energy group cross-section sets calculated with HELIOS 1.10 using the given geometry models (compare Figure 1). To avoid any irritations created by group condensation, the same number of groups has been used in DYN3D. The full core calculations have shown that the full gain in sodium void reduction demonstrated in the infinite system can be expected to be reached in the finite system too [8]. Thus, a superposition of the findings in the infinite system and the traditional methods for the sodium void reduction like the pancake core shape or a sodium plenum is possible. Additionally, it has to be mentioned that the influence of sodium void reduction inside the fuel assembly using fine distributed moderating material already comes into action when the first sodium bubble appears. In contrast, the traditional methods to reduce the sodium void by increasing the neutron leakage do not have influence until a significant amount of sodium is voided.

4. Consequences on Minor Actinide Transmutation

Figure 5 shows the influence of an insertion of the minor actinides as well as the moderating material on the infinite

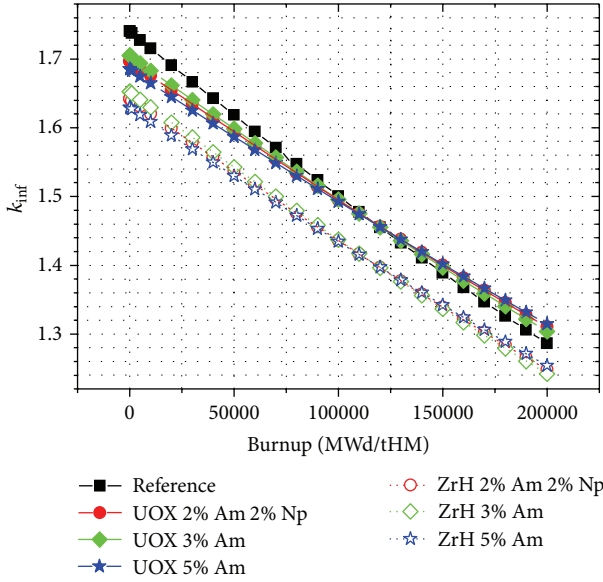


FIGURE 5: Change in the infinite multiplication factor over the burnup for the three different material configurations.

multiplication factor of a fuel assembly over burnup. Three different effects are appearing. On the one hand, the insertion of minor actinides decreases the initial k_{inf} of the fuel assembly, since they cause increased neutron absorption. On the other hand, the insertion of the minor actinides reduces the loss of criticality over burnup, due to the change in the fertile material configuration caused by adding minor actinides as efficient fertile material, replacing the corresponding amount of U-238. The insertion of the moderating material (ZrH1.6) causes in all cases a reduction in the k_{inf} throughout the whole observed burnup period. This reduction of the multiplication factor reduces the possible cycle time. A comparable effect appears for all other, “traditional” methods leading to sodium void reduction too, since they are based on increased neutron leakage. Thus, the breeding is reduced due to the reduced number of available excess neutrons.

The transmutation of Np-237 is shown in Figure 6 over the burnup of the reference fuel assembly. The nuclide density of Np-237 is reduced in both cases, without moderating material as well as with moderating material. In contrast to the reduction of Np-237, in the reference case, a very small amount of Np-237 is formed. The burning of Np-237 in the case with a given begin of life (BOL) Np-237 concentration and the built-up of Np-237 when there is no initial concentration would lead to a comparable asymptotic value for infinitely high burnup. It is visible that the use of the distributed moderating material even enhances the transmutation of Np-237 slightly.

Figure 7 shows the Americium transmutation over burnup for the isotope Am-241 (a) and for Am-243 (b). The Am-241 content in the reference case starts with a finite value, since the defined MOX fuel contains a small fraction of Am-241 as long as Pu-241 appears. The Am-241 is a decay product of Pu-241 and appears already after short storage time of

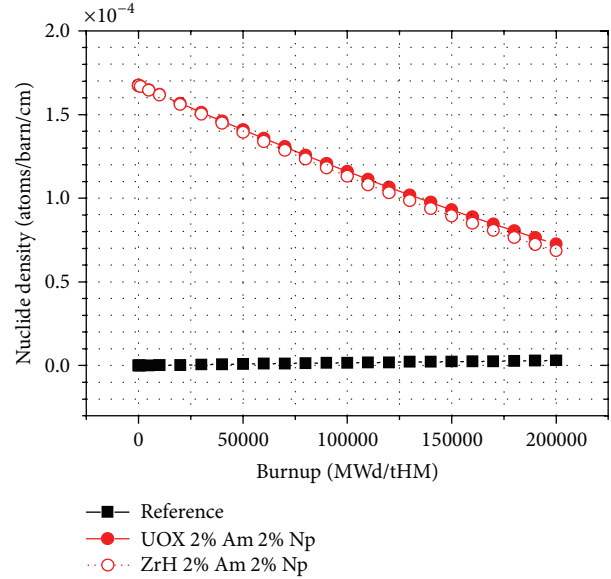


FIGURE 6: Change in the Neptunium-237 content over burnup for the case with and without moderation.

the separated plutonium used for the production of MOX fuel due to the short half-life of Pu-241 (14 years). In the reference case (full black squares), the initial concentration of Am-241 rises slowly to a maximum around 100 GWd/tHM and decreases after this maximum slightly. In all three cases with an added, higher initial Am-241 content, Am-241 is transmuted. The more efficient the transmutation is, the higher the initial Am-241 content is. An interesting fact is the slightly more efficient transmutation in the cases with distributed moderating material, even with the appearing slightly softer neutron spectrum (see Figure 3). This result is very surprising and it has to be investigated, if there is really more Am-241 burnt, or if the Am-241 is only shifted to the higher element Curium due to absorption processes. All cases, independently of the initial concentration of Am-241, tend to a comparable asymptotic limit for infinite burnup. The transmutation of Am-243 shows a comparable behavior (Figure 7(b)). No Am-243 is in the BOL fuel composition in the reference case; thus there is only the production which occurs during the burnup. In all cases with a BOL Am-243 content higher than 0.75% ($\hat{=}$ 2% Am content) Am-243 is reduced. The Am-243 transmutation is not significantly influenced by the use of distributed moderating material.

The change in the Curium content during burnup in the minor actinide containing fuel is shown in Figure 8. The Curium isotopes are built up from Americium in all fuel configurations by neutron capture and decay processes. The Cm-242 content (Figure 8(a)) rises in all cases in dependence of the initial Am-241 content to a maximum value. The more the Am-241 is available, the more the Cm-242 is built in the initial phase, but with decreasing Am-241 content, the Cm-242 content starts to be reduced too after reaching the maximum at about 100 GWd/tHM. The insertion of the moderating material leads in all cases to a slightly increased

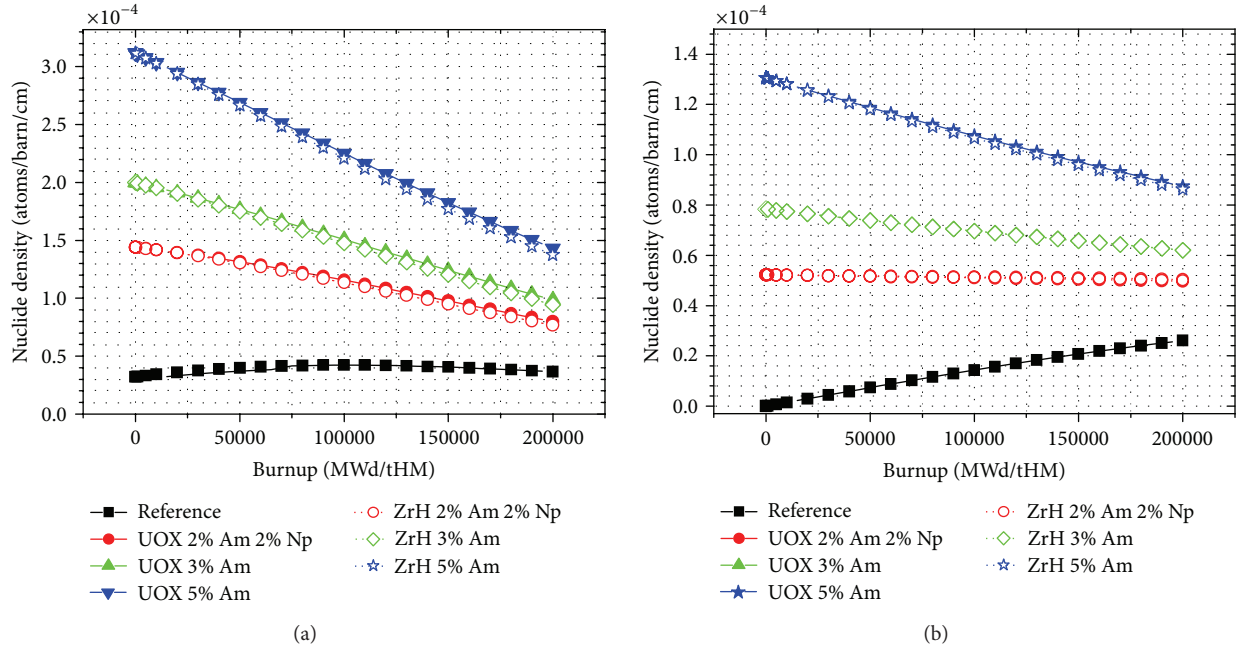


FIGURE 7: Change in the Americium-241 (a) and the Americium-243 (b) content over burnup for the case with and without moderation.

built-up and a slightly higher EOL concentration of Cm-242. The case with the highest Am content (5%) leads after reaching a maximum at ~ 100 GWd/tHM already to a significant reduction of the Cm-242 content. The Cm-244 content (Figure 8(b)) rises for all cases over the full observed burnup period. The overall Cm-244 content is strongly dependent on the initial Americium content in the fuel. The Cm-244 accumulation is slightly higher for all cases with moderating material.

A more detailed insight into the influence of the fine distributed moderating material on transmutation is given in Tables 1 and 2. The comparison of the transmutation efficiency provides information on which fuel assembly provides a lower content of minor actinides at the end of life (EOL). A positive value indicates an advantageous behavior of the fuel assembly with moderating material; a negative value indicates a better transmutation performance for the assembly without moderating material. The comparison of the transmutation efficiency (see Table 1)

Transmutation efficiency [%]

$$= \left(1 - \frac{\text{isotope number density with moderating material}}{\text{isotope number density without moderating material}} \right) \cdot 100 \quad (1)$$

shows that the Am-241 transmutation is roughly 4% more efficient in the fuel assemblies with moderating material for all configurations of transmutation fuel. The Transmutation of Am-243 is slightly less efficient (-1.28%) for a low Americium content and slightly more efficient (1.42%) for high Americium content. In the cases with moderating material,

$\sim 2.5\%$ more Cm-242 is produced than that in the reference cases without moderating material. The use of moderating material increases the production of Cm-244 by 7 to 9%. The transmutation of Np-239 is more efficient in the fuel assembly with moderating material. 5.5% more Np-239 is burnt than in the reference case.

The detailed comparison of the differences in the number densities

Transm. efficiency [number density]

= isotope number density with moderating material

– isotope number density without moderating material (2)

is given in the lower part of Table 1. A positive number indicates more efficient transmutation in the assembly with moderating material and a negative number more efficient transmutation in the assembly without moderating material. A detailed comparison of the numbers shows that the amount of the Am-241 reduction is higher than the increase in the number densities of the higher isotopes (Am-243, Cm-242, Cm-244) in all cases with moderating material. Thus there is really more Am-241 burnt in the fuel assemblies with fine distributed material than that in the “clean” transmutation fuel assemblies. The effect rises with increasing Americium concentration at BOL. Over all it can be stated that the insertion of the fine distributed moderating material in the wire wrapper does at least not have a negative influence on the transmutation efficiency.

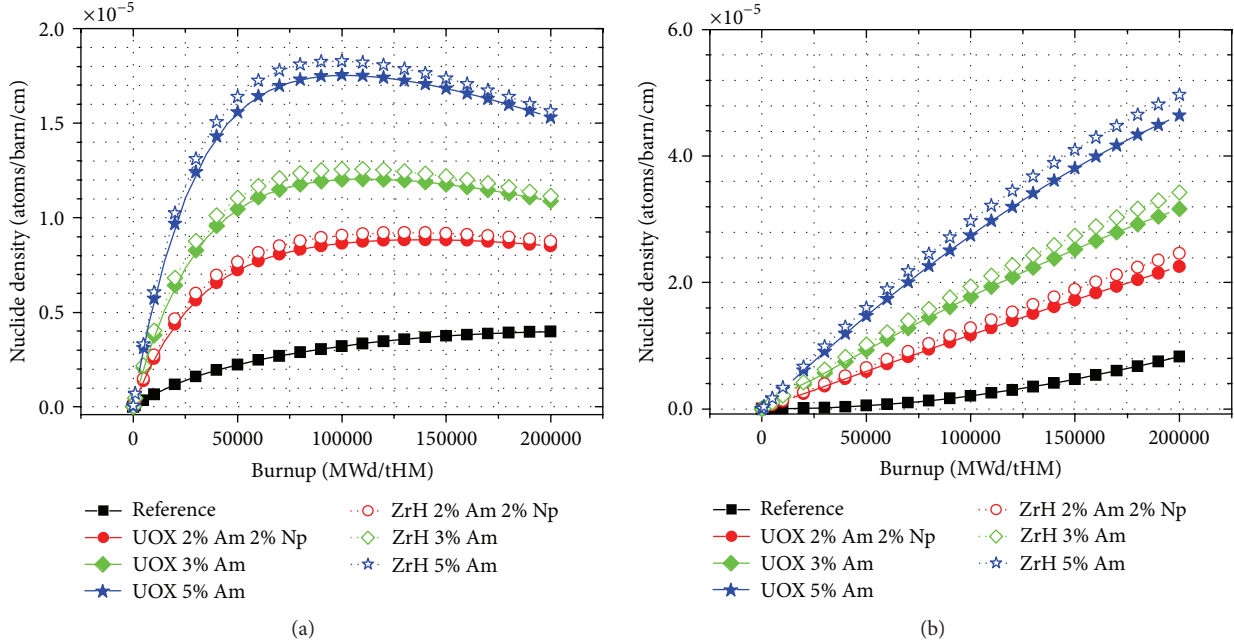


FIGURE 8: Change in the Curium-242 (a) and the Curium-244 (b) content over burnup for the case with and without moderation.

TABLE 1: Comparison of the transmutation efficiency between the reference cases without and the cases with moderating material for the different transmutation fuels.

Transmutation eff. (comparison)	Am-241	Am-243	Cm-242	Cm-244	Np-239
2% Np 2% Am EOL	3.87%	-1.28%	-2.68%	-9.18%	5.65%
3% Am EOL	4.27%	0.02%	-2.43%	-8.24%	
5% Am EOL	4.04%	1.42%	-2.15%	-7.05%	
8% Am EOL	3.59%	2.20%	-1.93%	-6.30%	
2% Np 2% Am EOL	$-2.9466E-06$	$6.0580E-07$	$2.1653E-07$	$2.0270E-06$	$-3.9219E-06$
3% Am EOL	$-4.2160E-06$	$-1.4000E-08$	$2.6400E-07$	$2.6060E-06$	
5% Am EOL	$-5.7900E-06$	$-1.2410E-06$	$3.2900E-07$	$3.2740E-06$	
8% Am EOL	$-7.6950E-06$	$-2.8100E-06$	$4.1970E-07$	$4.2524E-06$	

The analysis of the Americium and Neptunium transmutation rate is given in Table 2. Consider

$$\text{Transmutation rate [\%]} = \left(1 - \frac{\text{isotope number density at EOL}}{\text{isotope number density at BOL}} \right) \cdot 100. \quad (3)$$

The transmutation rate provides the information on how much of the initially inserted material is transmuted at the end of the lifetime of the fuel assembly. A higher number indicates a better transmutation performance for the corresponding isotope. After a burnup of 200 GWd/tHM, the Am-241 concentration is roughly halved and the transmutation rate is increased with increasing initial Americium content. The transmutation of Am-243 becomes only efficient for high Americium content, at least 3% even better 5%. The transmutation of Np-237 remains nearly constant at a low content of 2% efficient.

The conclusion of this evaluation of the transmutation rate is that transmutation especially of Americium becomes significantly more efficient with increasing initial Americium content. Unfortunately, the permissible Americium content is limited due to the negative influence of the Americium on the feedback effects in the reactor core and due to the negative influence on the fuel behavior caused by the high fission gas release in Americium containing fuel.

The consequence of the insertion of minor actinides on different feedback effects and other safety-related values is given in Table 3. A positive value in the negative Doppler feedback indicates the desired stronger feedback. For the positive coolant effect and void effect, a positive value is desired, since the positive feedback should be reduced to stabilize the reactor. The absorber worth reflects the negative reactivity which is inserted by the addition of a given amount of absorbing material; a value close to zero indicates an unchanged efficiency of the absorber rods; a negative value signs a demand of a higher number of absorber rods; a

TABLE 2: Comparison of the transmutation rate for the reference cases and the cases with moderating material for the different transmutation fuels.

Transmutation rate	Reference			With moderator		
	Am-241	Am-243	Np-237	Am-241	Am-243	Np-237
2% Np 2% Am EOL	-47.0%	-9.1%	-58.5%	-49.1%	-8.0%	-60.9%
3% Am EOL	-50.6%	-20.8%		-52.7%	-20.8%	
5% Am EOL	-54.1%	-33.0%		-55.9%	-34.0%	
8% Am EOL	-55.3%	-38.9%		-56.9%	-40.2%	

TABLE 3: Feedback effects and absorber worth for the cases with different transmutation fuels.

	UMOX		+ZrH		UMOX		+ZrH		+ZrH 8% Am	1.2*ZrH 8% Am
	2% Am	2% Np	2% Am	2% Np	3% Am	3% Am	5% Am	5% Am		
Doppler effect $T_f + 100$ K										
BOL	-30.2%		59.7%		-23.0%	73.8%	-36.4%	49.4%	18.9%	31.9%
EOL	-26.9%		52.2%		-20.2%	65.2%	-30.9%	46.8%	18.7%	32.3%
Coolant effect $T_c + 50$ K										
BOL	4.9%		-8.1%		5.7%	-11.7%	12.2%	-4.6%	2.1%	-0.2%
EOL	0.9%		-12.0%		2.1%	-11.3%	1.2%	-14.2%	-13.3%	-15.0%
void effect										
BOL	9.2%		-5.3%		6.9%	-8.1%	10.7%	-3.2%	2.7%	0.9%
EOL	-0.2%		-11.8%		-0.4%	-12.5%	-0.6%	-12.3%	-11.9%	-13.9%
Absorber rod worth										
BOL	-7.8%		-3.6%		-6.0%	-1.6%	-9.6%	-5.6%	-11.1%	-10.6%
EOL	-9.5%		-5.0%		-6.9%	-2.0%	-11.1%	-6.8%	-13.3%	-12.9%

positive value would allow reducing the number of absorber rods.

The insertion of the minor actinides into the fuel has a strong influence on the safety-related effects of the fuel assembly. The negative Doppler effect is reduced in all cases due to the influence of the minor actinides. The already positive coolant effect (the combination of the coolant temperature and the coolant density effect) becomes more positive with increasing Americium fraction. The positive sodium void effect at BOL increases compared to the reference case in all configurations and the absorber rod worth of the shutdown rods decreases compared to the reference case in all configurations, which requires more shutdown elements for the safe shutdown in hot condition compared to the reference case in all configurations. The parallel insertion of minor actinides and distributed moderating material relaxes the situation significantly. The effect of the moderating material on the Doppler effect is even strong enough to overcompensate the influence of the minor actinides in all cases; thus the Doppler effect is still significantly stronger—more negative—than in the reference case without minor actinides and moderating material. The same behavior can be observed for the coolant effect as well as for the sodium void effect. The influence of the minor actinides is overcompensated in all cases by the insertion of the fine distributed moderating material. Finally, the absorber worth, the reduction of the absorber rod worth is only partly compensated due to the insertion of the moderating material, but the situation is relaxed in all cases due to the insertion of moderating material.

One drawback of the moderating material should not be forgotten; due to the significantly stronger Doppler effect, more shutdown rods are required for reaching a defined cold subcriticality status. The amount of moderating material to be used is sure to be optimized from the point of view of system safety and transient behavior and the thermal stability of the ZrH moderator has to be investigated thoroughly or a more stable material like YH has to be envisaged.

An independent evaluation for the maximum possible amount of minor actinides in combination with the use of fine distributed moderating material closes the study. The strong influence of the minor actinides on the safety relevant feedback effects limits the possible amount of minor actinide insertion. For the given amount of hydrogen insertion, the limit has been found for 8% Americium content where the coolant feedback and the sodium void at BOL become slightly positive (see Table 3 first bold column), but this is still compensated by the enhancement of the Doppler feedback by more than 18%. The consequences of this Americium content can be compensated once more by a slight increase of the hydrogen content. This is studied by a test for 8% Americium content and by a 20% increased $ZrH_{1.6}$ content. The insertion of 20% more hydrogen leads once more to at least balanced or even enhanced feedbacks and thus to a more stable system (see Table 3 second bold column). From the transmutation point of view, the by 3% increased Americium amount (relative 60% more Americium) leads to an increased Am-241 burning by 1% (relative increase $\sim 2\%$) and an increased Am-243 burning by roughly 6% (relative

increase ~18%) (see Table 2 bold row). Thus the expected increase of transmutation efficiency can be found mainly for Am-243 which is more problematic to be transmuted.

Nevertheless, the increase of Americium content cannot be continued ad infinitum, since the acceptable Americium content is limited by the swelling behavior of transmutation fuel too. Experiments have demonstrated that target pellets containing 10–12 wt% ^{241}Am already show swelling of the target pellets by the order of 15%. This is attributed to accumulation of helium, produced by alpha decay of ^{242}Cm that occurs in the transmutation scheme of ^{241}Am [26].

5. Conclusions

The effect of the insertion of fine distributed moderating material on the feedback effects and the void effect in a sodium cooled fast reactor has been investigated in several publications [8–11]. The strong improvement in the fuel temperature and coolant feedback effect and in the sodium void effect has already been demonstrated, but negative consequences to the transmutation efficiency have been assumed due to the softer neutron spectrum.

The effect of fine distributed moderating material on fuel assemblies with a high minor actinide concentration like those foreseen for minor actinide transmutation has been investigated for 3 different fuel compositions: fuel with 2% Np and 2% Am, fuel with 3% Am, and fuel with 5% Am. It is demonstrated that the influence of the minor actinides on the feedback effects can be easily compensated by the insertion of fine distributed moderating material into the wire wrapper. The investigation of the transmutation efficiency has shown that there is only a very limited influence due to the moderating material. On the one hand, the Americium transmutation rate is even slightly higher for the fuel assembly containing moderating material. On the other hand, the Curium production increases slightly. Nevertheless, a detailed comparison of the data shows that the higher Americium efficiency rate is not only because breeding reactions lead to more Curium but also a higher fission rate of Americium is reached. Further, it is shown that the Americium transmutation rate depends strongly on the initial Americium amount in the fuel assembly.

Using fine distributed moderating materials, for example, inside the wire wrapper has the potential to improve the safety of a dedicated core for minor actinide transmutation. Additionally, it is shown that the transmutation rate can be improved since it is possible to increase the BOL amount of minor actinides in the core. This can be reached, since it is possible to eliminate the negative effect of the minor actinides on core stability and transient behaviour up to an Americium content of ~8%. Additionally, it is shown that an increase of the hydrogen content by 20% can even improve all feedback effects in this case with 8% Americium content. Using this configuration allows a relative increase of the Am-243 transmutation rate by nearly 20% which is an important improvement for an isotope which is hard to transmute. Thus the concept of fine distributed moderating material offers the possibility of increased transmutation

efficiency in conjunction with an elimination of the negative consequences of transmutation fuel.

The use of fine distributed moderating material can influence the safety of fast reactors strongly—it opens the stage for designable feedback coefficients; thus it creates a new degree of freedom for the optimization of important inherent safety-related parameters in the design of sodium-cooled fast reactor cores.

References

- [1] “IAEA TM on Innovative Fast Reactor Designs with Enhanced Negative Reactivity Feedback Features,” IAEA Headquarters, Vienna, Austria, 2012, accessed March 11, 2013, <http://www.iaea.org/NuclearPower/Meetings/2012/2012-02-27-02-29-TM-NPTD.html>.
- [2] H. Hummel and D. Okrent, *Reactivity Coefficients in Large Fast Power Reactors*, ANS, 1970.
- [3] R. N. Hill and H. Khalil, “Evaluation of LMR design options for reduction of sodium void worth,” in *Proceedings of International Conference on the Physics of Reactors*, vol. 1, pp. 11–19, Marseille, France, 1980.
- [4] G. Rimpault, L. Buiron, P. Sciora, and F. Varaine, “Towards GEN IV SFR design: promising ideas for large advanced SFR core designs,” in *International Conference on the Physics of Reactors (PHYSOR '08)*, pp. 2394–2400, Interlaken, Switzerland, September 2008.
- [5] B. Carlucci and P. L. Pinto, “Lessons learned from Fukushima accident as regards the safety approach of the ASTRID project at conceptual design stage,” in *Proceedings of the IAEA Technical Meeting on Impact of the Fukushima Event on Current and Future Fast Reactor Design*, Helmholtz-Zentrum Dresden-Rossendorf, Dresden, Germany, March 2012, accessed March 11, 2013, <http://www.iaea.org/NuclearPower/Meetings/2012/2012-03-19-03-23-TM-NPTD.html>.
- [6] L. Buiron et al., “Innovative core design for generation IV sodium-cooled fast reactors,” in *Proceedings of the International Congress on Advances in Nuclear Power Plants (ICAPP '10)*, Nice, France, 2007.
- [7] K. Sun et al., “Void reactivity decomposition for the sodium cooled fast reactor in equilibrium closed fuel cycle,” in *Proceedings of the Advances in Reactor Physics to Power the Nuclear Renaissance (PHYSOR '10)*, Pittsburgh, Pa, USA, 2010.
- [8] B. Merk, E. Fridman, and F. P. Weiß, “On the use of zirconium based moderators to enhance the feedback coefficients in a MOX fuelled sodium cooled fast reactor,” *Nuclear Science and Engineering*, vol. 171, 2, pp. 136–149, 2012.
- [9] B. Merk, E. Fridman, and F. P. Weiß, “On the use of a moderation layer to improve the safety behavior in sodium cooled fast reactors,” *Annals of Nuclear Energy*, vol. 38, no. 5, pp. 921–929, 2011.
- [10] B. Merk and F. P. Weiß, “Analysis of the influence of different arrangements for ZrH moderator material on the performance of a SFR core,” *Annals of Nuclear Energy*, vol. 38, pp. 2374–2385, 2011.
- [11] B. Merk and F. P. Weiß, “On the effect of different placing ZrH moderator material on the performance of a SFR core,” in *Advances in Reactor Physics—Linking Research, Industry, and Education (PHYSOR '12)*, Knoxville, Tenn, USA, 2012.
- [12] E. A. Villarino, R. J. J. Stammler, A. A. Ferri, and J. J. Casal, “HELIOS: angularly dependent collision probabilities,” *Nuclear Science and Engineering*, vol. 112, pp. 16–31, 1992.

- [13] R. Sanchez et al., "APOLLO II: a user-oriented, portable, modular code for multigroup transport assembly calculations," *Nuclear Science and Engineering*, vol. 100, article 352, 1988.
- [14] IAEA Fast Reactor Database, 2006, <http://www.iaea.org/inis/nkm/nkm/aws/frdb/auxiliary/generalInformation.html>.
- [15] A. E. Waltar and A. B. Reynolds, *Fast Breeder Reactors*, Pergamon Press, New York, NY, USA, 1981.
- [16] A. Pay, E. Francillon, B. Steinmetz, D. Barnes, and N. Meda, "European Fast Reactor (EFR) fuel element design," in *Proceedings of the 10th International Conference on Structural Mechanics in Reactor Technology*, Anaheim, Calif, USA, 1989, http://www.iasmirt.org/iasmirt-3/SMiRT10/DC_250515.
- [17] J. Carmack and K. O. Pasamehmetoglu, "Review of transmutation fuel studies," in *INL/EXT-08-13779, or GNEP-FUEL-TD-RT-2008-000050*, U.S. Department of Energy, Transmutation Fuel Campaign, 2008, <http://www.inl.gov/technicalpublications/Documents/3901056.pdf>.
- [18] W. M. Mueller, J. P. Blackledge, and G. G. Libowitz, *Metal Hydrides*, Academic Press, New York, NY, USA, 1968.
- [19] K. Tuček, J. Carlsson, and H. Wider, "Comparison of sodium and lead-cooled fast reactors regarding reactor physics aspects, severe safety and economical issues," *Nuclear Engineering and Design*, vol. 236, no. 14–16, pp. 1589–1598, 2006.
- [20] S. E. Bays, H. Zhang, and H. Zhao, "The industrial sodium cooled fast reactor," in *ANFM, INL/CON-09-15519 PREPRINT*, 2009, <http://www.inl.gov/technicalpublications/Documents/4363828.pdf>.
- [21] D. Olander, E. Greenspan, H. D. Garkisch, and B. Petrovic, "Uranium-zirconium hydride fuel properties," *Nuclear Engineering and Design*, vol. 239, pp. 1406–1424, 2009.
- [22] D. W. Wootan, J. A. Rawlins, L. L. Carter, H. R. Brager, and R. E. Schenter, "Analysis and results of a hydrogen-moderated isotope production assembly in the fast flux test facility," *Nuclear Science and Engineering*, vol. 103, no. 2, pp. 150–156, 1989.
- [23] J. C. Lefèvre, C. H. Mitchell, and G. Hubert, "European fast reactor design," *Nuclear Engineering and Design*, vol. 162, pp. 133–143, 1996.
- [24] U. Rohde, U. Grundmann, and S. Kliem, "DYN3D - advanced reactor simulations in 3D," *Nuclear Energy Review*, vol. 2, pp. 28–30, 2007.
- [25] C. Beckert and U. Grundmann, "A nodal expansion method for solving the multigroup SP3 equations in the reactor code DYN3D," in *Proceedings of the Joint International Topical Meeting on Mathematics and Computations and Supercomputing in Nuclear Applications (M&C+SNA '07)*, Monterey, Calif, USA, April 2007.
- [26] R. J. M. Konings et al., "The EFTTRA-T4 experiment on americium transmutation," *Journal of Nuclear Materials*, vol. 282, no. 2-3, pp. 159–170, 2000.

Research Article

Current Status of Pyroprocessing Development at KAERI

Hansoo Lee,¹ Geun-IL Park,² Jae-Won Lee,¹ Kweon-Ho Kang,² Jin-Mok Hur,¹
Jeong-Guk Kim,¹ Seungwoo Paek,¹ In-Tae Kim,¹ and IL-Je Cho¹

¹ Nuclear Fuel Cycle Process Development Division, Korea Atomic Energy Research Institute, 1045 Daedukdaero, Yuseong, Daejeon 305-353, Republic of Korea

² Nuclear Fuel Cycle Waste Treatment Research Division, Korea Atomic Energy Research Institute, 1045 Daedukdaero, Yuseong, Daejeon 305-353, Republic of Korea

Correspondence should be addressed to Hansoo Lee; hslee5@kaeri.re.kr

Received 10 October 2012; Accepted 5 February 2013

Academic Editor: Hangbok Choi

Copyright © 2013 Hansoo Lee et al. This is an open access article distributed under the Creative Commons Attribution License, which permits unrestricted use, distribution, and reproduction in any medium, provided the original work is properly cited.

Pyroprocessing technology has been actively developed at Korea Atomic Energy Research Institute (KAERI) to meet the necessity of addressing spent fuel management issue. This technology has advantages over aqueous process such as less proliferation risk, treatment of spent fuel with relatively high heat and radioactivity, and compact equipments. This paper describes the pyroprocessing technology development at KAERI from head-end process to waste treatment. The unit process with various scales has been tested to produce the design data associated with scale-up. Pyroprocess integrated inactive demonstration facility (PRIDE) was constructed at KAERI and it began test operation in 2012. The purpose of PRIDE is to test the process regarding unit process performance, remote operation of equipments, integration of unit processes, scale-up of process, process monitoring, argon environment system operation, and safeguards-related activities. The test of PRIDE will be promising for further pyroprocessing technology development.

1. Introduction

Pyroprocessing treatment can reduced the volume, radioactivity, and heat load of the light water reactor (LWR) spent fuels [1]. In addition, pyroprocessing based on the group recovery of transuranic element (TRU) can provide metal fuels for the sodium-cooled fast reactor while keeping higher intrinsic proliferation resistance. Therefore, successful development of pyroprocessing can save disposal space, reduce the radiotoxicity of spent fuels, and increase uranium utilization efficiency.

Korea Atomic Energy Research Institute (KAERI) has been developing pyroprocessing since 1997. The concept development, bench scale testing, and demonstration of laboratory scale key unit process had been carried out since 2006. From 2007 to 2011, the focus moved to the design and construction of engineering-scale integrated system. Pyroprocess integrated inactive demonstration facility (PRIDE) was constructed in 2011 and it began test operation in 2012.

Process flow diagram consists of head-end processes (decladding, voloxidation, oxide feed preparation), electro-

chemical processes (electrolytic reduction, electrorefining, electrowinning), and waste treatment processes as shown in Figure 1.

2. Unit Process of Pyroprocessing

2.1. Head-End Process. The head-end process in pyroprocessing is to convert spent fuel assembly into a suitable feed material which is supplied to the electrolytic reduction process.

The first step of head-end process is to disassemble spent pressurized water reactor (PWR) fuel assembly and to extract fuel rods followed by cutting fuel rods of about 4 m into rod-cuts in proper size for decladding process. Disassembling, extraction, and cutting operations of actual spent PWR fuel assembly have been conducted in a laboratory scale for postirradiation examination (PIE) and "Direct Use of PWR spent fuel In CANDU reactors" (DUPIC) experiment in postirradiation examination facility (PIEF).

In order to enhance the decladding efficiency for high burn-up spent fuel, the oxidative decladding efficiency

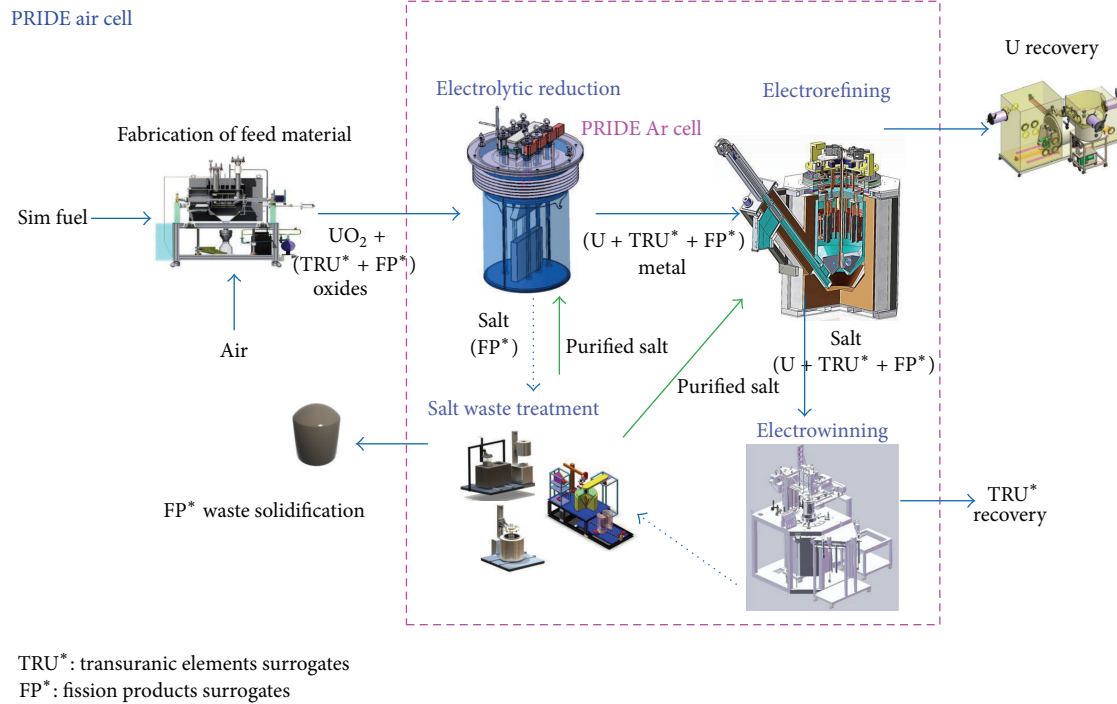


FIGURE 1: Flow diagram of pyroprocessing (PRIDE at KAERI).

without rotation mode was tested. The decladding efficiency was close to 100% for spent fuel with a burn-up less than 40,000 MWd/tU when the oxidative decladding with rod-cuts less than 30 mm was performed at 500°C for 10 h. On the other hand, spent fuel with a burn-up higher than 50,000 MWd/tU showed the low decladding efficiency of about 15% due to small fuel-to-clad gap and low oxidation rate. An improved decladding efficiency higher than 99% for the high burn-up spent fuel required an oxidation time longer than 20 h at 700°C. Therefore, oxidative decladding equipment with rotational device would be required to reduce an oxidative decladding time and obtain the very high decladding efficiency.

Feed material forms such as granule and porous pellet were considered to enhance the current efficiency of electrochemical processes. The particles of U_3O_8 powder were bonded together during thermal pretreatment and transformed into aggregates above 1000°C. In 2009, a laboratory scale rotary voloxidizer (max. 1.5 kg U_3O_8 powder/batch) as shown in Figure 2 was designed and manufactured to investigate particle size controllability for U_3O_8 powder. The fabrication characteristics of granule from 200 g U_3O_8 powder was investigated under the conditions of thermal pretreatment temperature of 1150 to 1200°C in argon atmosphere, treatment time of 5 to 15 h, and rotational velocity of 1 to 3 rpm using a rotary voloxidizer. Recovery rate of granule higher than 1 mm with UO_{2+x} ($0.25 < x < 0.67$) composition (Figure 2) significantly increased with increasing temperature, rotation velocity, and time of up to 10 h. Typical recovery rate of granule showed about 89% (>1 mm) and 98% (>0.5 mm). The UO_2 granule with density of 4.38 g/cm³ (40% theoretical density (TD)) was fabricated by reduction of UO_{2+x} at 1000°C

for 5 h in 4% H_2 -Ar atmosphere. The porous UO_2 pellets with density of 6.78–7.67 g/cm³ (60–70% TD) were fabricated by traditional sequential process of compaction and pretreatment (sintering) using the U_3O_8 powder obtained by oxidation of UO_2 pellets.

Engineering-scale rotary voloxidizer for feed form fabrication was installed at air cell in PRIDE facility in July 2012. Feed form fabrication technology will be demonstrated using simulated fuel pellet from 2013.

An off-gas treatment system for trapping fission products released from oxide feed fabrication process is very important for protecting release of nuclides to environment. In the middle of 1990s, research on the trapping of cesium released from the “Oxidation, REDuction of enriched OXide fuel” (OREOX) and sintering processes has started in fabricating DUPIC fuel [2]. Off-gas treatment system for trapping both volatile fission gases such as H-3 and I in OREOX process and Cs in sintering process has been established at “DUPIC Fuel Development Facility” (DFDF) as shown in Figure 3(a). It was demonstrated that released Cs from sintering process was completely trapped by fly ash filters. Figure 3(b) shows that approximately 100% of each cesium isotope released was trapped by using fly ash filter.

2.2. Electrolytic Reduction. The electrolytic reduction process based on the electrochemical reduction in a $LiCl-Li_2O$ electrolyte has been developed for the volume reduction of PWR spent fuels and for the supply of metal feeds for the electrorefining process. During the electrolytic reduction process, high heat load fission products dissolve into the chloride molten salt resulting in the decrease of heat load of spent fuels. Additionally, the metallization of oxides to more



FIGURE 2: A rotary voloxidizer (a) and UO_{2+x} granules (b).

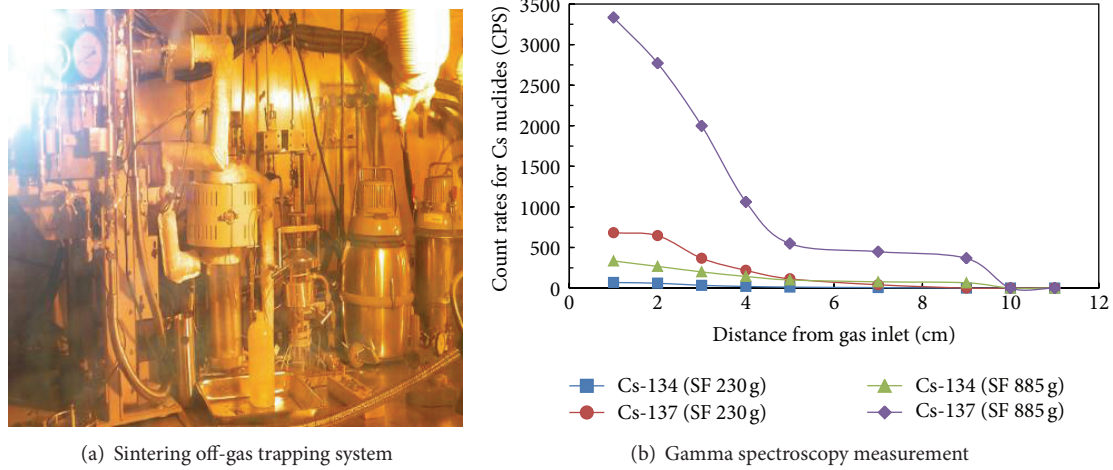


FIGURE 3: Off-gas treatment system for DUPIC sintering furnace in DDFD and gamma spectroscopy measurement results of the fly ash filter.

dense metals enables the volume reduction of spent fuels. The metal products produced by the electrolytic reduction process can be directly transferred to the electrorefining process as feed materials. One of the concerning points is the concomitant transfer of residual salts in the metal products to the electrorefining process. The residual salts from electrolytic reduction process, $LiCl-Li_2O$, would cause the formation UO_2 and the breaking of the eutectic composition in the electrorefining salt, $LiCl-KCl$. To address this incompatibility of salts between electrolytic reduction and electrorefining, electrolytic reduction cathode processing was devised for the removal of residual salts in the metal products of the electrolytic reduction process as shown in Figure 4.

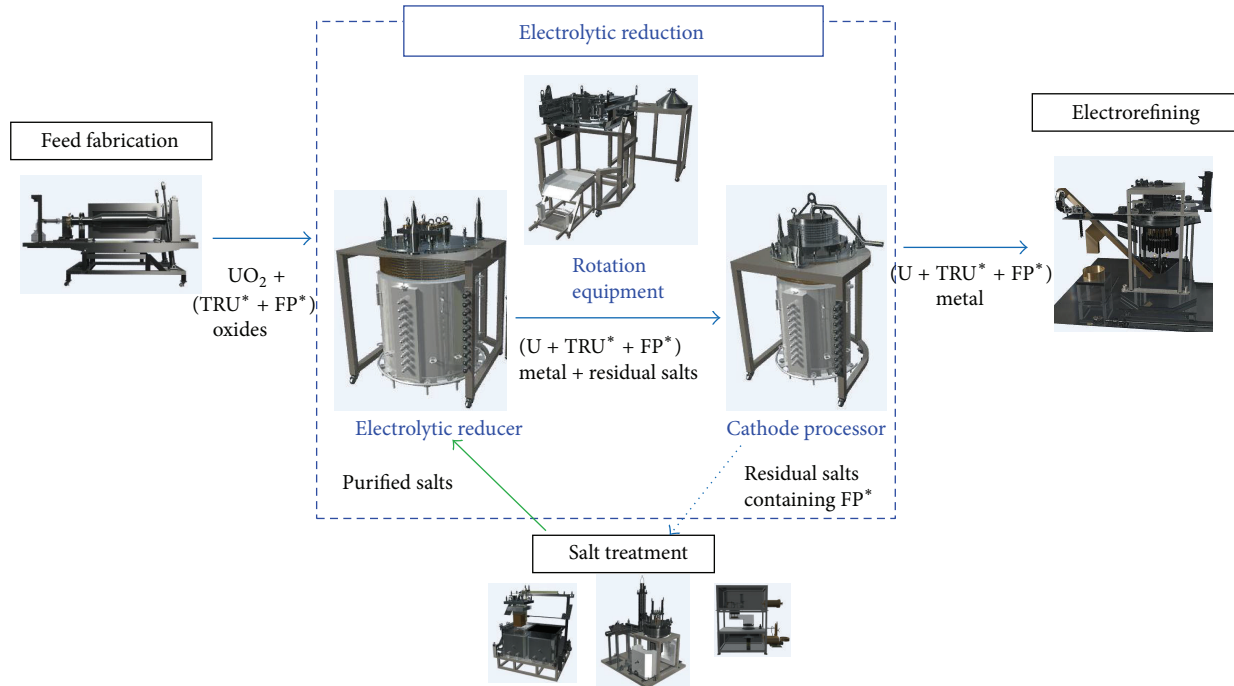
2.2.1. Development of Electrolytic Reduction Process. With the progress of electrolytic reduction reaction, the oxide ion from the oxide spent fuel contained in the cathode basket is evolved as gas on the anode leaving the metal spent fuel in the cathode basket, and alkali and alkali earth elements are dissolved into the molten salt. Lanthanides except Eu and metallic fission products remain in the cathode. Consequently, electrolytic reduction process can supply metal feed to electrorefining

process and separate selectively the high heat load fission products such as Sr and Ba from the spent fuel.

The construction of a newly designed laboratory scale electrolytic reduction system (20 kg UO_2 /batch) was completed at KAERI in 2009 and inactive demonstration has been performed showing high reduction yields up to 99.5%. In 2011, based on the laboratory scale demonstration results, the electrolytic reducer for PRIDE was designed and fabricated to treat 50 kg-U per day, which includes a cathode basket with a capacity of 50 kg-U loading and 6 anodes (Figure 5).

2.2.2. Development of Electrolytic Reduction Cathode Processor. After the electrolytic reduction process, the residual salt in the cathode basket amounts to about 20 wt% of the metal products. The cathode process for the removal of residual salts in the cathode basket of the electrolytic reducer can ease the burden of the electrorefining process. The recovered salt in the cathode processor will be treated in the waste salt regeneration process and then recycled to the electrolytic reduction process. The operation of cathode processor is based on the vaporization under vacuum condition.

In 2010, a laboratory scale cathode processor (4 kg $LiCl$ /batch) was installed. This equipment is characterized



TRU*: transuranic elements surrogates
 FP*: fission products surrogates

FIGURE 4: Electrolytic reduction system.



FIGURE 5: PRIDE electrolytic reducer with a capacity of 50 kg-U/batch.

by the maximization of temperature difference between a heating crucible and a receiving crucible. The salt recovered in the receiving crucible is in a powder form, which is easy to handle in a remote operation condition excluding the necessity of hot molten salt transfer. The principle is the condensing of LiCl vapor as a solid in the cold region of the cathode processor. In an experiment of reduced pressure (100 mtorr) at 900°C, more than 99% of the salts were evaporated and recovered nearly 100% in the receiving crucible.

Based on the laboratory scale demonstration results, the electrolytic reduction cathode processor for PRIDE was designed and fabricated, which can contain two cathode baskets from electrolytic reducer with a capacity of 100 kg-U loading (Figure 6).

2.3. Electrorefining Process. Electrorefining, an electrochemical process to recover pure uranium from a metallic or oxide spent fuel, is an essential process in pyroprocessing, because it handles the uranium which is about 93% of spent fuel. During the electrorefining, the reduced metal from forgoing process, which is composed of uranium, TRU, and rare earth element (RE), is dissolved into a LiCl-KCl eutectic salt, whereas only uranium is deposited as a pure dendritic form on a solid cathode. The used salt containing the accumulated TRU and RE is transferred to electrowinning process.

2.3.1. High-Throughput Electrorefining System. The high-throughput electrorefining system is installed recently in PRIDE. The uranium dendrite is deposited and drawn from the electrorefiner, distilled for salt-removal in salt distiller, and then the salt removed dendrite is consolidated for storage or future use. Uranium trichloride (UCl_3) is prepared separately and supplied to the electrorefiner. The used salt in an ingot form containing U, TRU, and REs is transported to the next process, electrowinning.

2.3.2. Electrorefiner. In order to increase a throughput of electrorefiner, KAERI has developed the advanced



FIGURE 6: PRIDE electrolytic reduction cathode processor with a capacity of 100 kg-U/batch.

high-throughput electrorefiner by employing a graphite cathode. The self-scraping mechanism of graphite cathode increases the efficiency of the electrorefiner due to an elimination of the stripping step [3]. In addition, continuous operation of the advanced electrorefiner can be realized by adding a bucket-type deposit transfer system. The 20 kgU/batch throughput can be achieved when 40 kg of simulated fuel pellets are loaded into anode basket and the UCl_3 concentration is more than 8%. Recently, the high-throughput electrorefiner was manufactured and installed at PRIDE, which is shown in Figure 7. The electrorefiner for PRIDE was designed to treat 50 kg-U per day, which includes 25 graphite cathodes and 4 cathode baskets with a capacity of 100 kg-U loading.

2.3.3. Salt Distiller. The dendritic uranium deposit is drawn out with about 25 wt% of salt in it from the electrorefiner (Figure 8). To remove the salt for following consolidation process, a vacuum evaporation has been developed in laboratory scale to verify the performance. The engineering-scale salt distiller for PRIDE, which has a capacity of 50 kg-U/day, was installed. The salt distiller comprises a distillation tower, a cooler, and a vacuum system. Optimum operation conditions were obtained from the lab-scale experiment at 820°C with a capacity of 20 kg-U/batch, proving that the salt recovery yield was about 97 wt%.

2.3.4. Melting Furnace for Consolidating. The engineering-scale melting furnace for a continuous operation to increase its capacity has been developed. Since the uranium product has a form of dendrite that is difficult to melt by direct heating, a supplemental charge method was developed. The uranium dendrite is gradually added into preexisting molten uranium and tilted toward the molds. The performance of the engineering-scale melting furnace for PRIDE, as shown in Figure 9, was preliminarily evaluated by a melting test of Cu with a capacity of 50 kg-U/batch [4]. An induction heating system with a nonwater cooling coil in an argon gas ambient



FIGURE 7: Engineering-scale high-throughput electrorefiner with a capacity of 50 kg-U/batch.

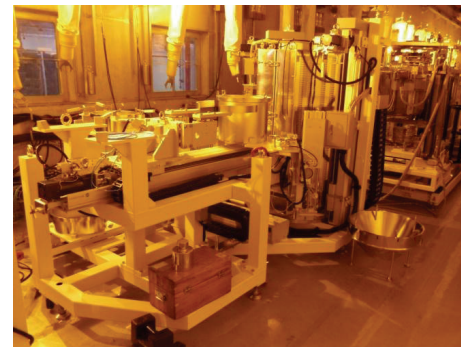


FIGURE 8: Engineering-scale salt distiller with a capacity of 50 kg-U/day.

was also developed to remove the risk from a reaction of the U-dendrite with water in hot cell. The performance of this nonwater cooling coil was confirmed by a melting test of a copper [5]. The temperatures of the melting chamber and the heating coils were maintained below 250°C and 600°C, respectively, during the heating test up to 1050°C.

2.3.5. Uranium Chlorinator. UCl_3 plays the role of electrolyte ions to initiate the reaction. It also removes unreduced lanthanide oxides in the anode basket of the electrorefiner and stabilizes the initial cell voltage between electrodes in the electrorefining reactor. The engineering-scale UCl_3 fabrication apparatus consists of a chlorine gas generator, a uranium chlorinator, a Cd distiller, a pelletizer, and an off-gas and dry gas scrubber. The product UCl_3 in LiCl-KCl is transferred to the Cd distiller to remove Cd in UCl_3 and then transferred to a pelletizer to form a pellet which could be supplied easily to electrorefiner. The engineering-scale uranium chlorinator with a capacity of 30 kg-U/batch, as shown in Figure 10, was installed recently for PRIDE.

2.3.6. Molten Salt Transport System. As the electrorefining operation proceeded, TRU and RE are accumulated in



FIGURE 9: Engineering-scale melting furnace with a capacity of 50 kg-U/batch.

electrolyte LiCl-KCl salt. KAERI has developed the salt transport system by evacuating the used salt for the transfer to the following electrowinning process [6]. The preliminary lab-scale experiments showed 99.5% transport rate (ratio of transported salt to total salt) under vacuum range of 100 mtorr~10 torr at 500°C. An engineering-scale molten salt transport system for PRIDE was installed, as shown in Figure 11.

2.4. Electrowinning System. Electrowinning process is a step of pyroprocessing for the simultaneous recovery of U and TRUs from the remaining salt after electrorefining process using a liquid cadmium cathode (LCC), imposing higher nuclear nonproliferation. The electrowinning process developed at KAERI consists of three steps (Figure 12): (i) LCC electrowinning for simultaneous recovery of U and TRU using an LCC, (ii) residual actinide recovery (RAR) process for recovery of the residual low-concentration U/TRU in the salt after the LCC electrowinning process, and (iii) Cd distillation of the cathode product (i.e., Cd ingot including the U/TRU deposits) produced from the LCC electrowinning and the RAR processes. The essential technologies that include the development of effective LCC structure [7], RAR methods [8], analytical technologies [9], and computational model of electrowinning cell [10] have been developed to enhance the operation efficiency of electrowinning process. In order to demonstrate the developed technologies, the engineering-scale electrowinning system of PRIDE was established.

2.4.1. LCC Electrowinning Process. The electrowinning technique using an LCC is a key step for a nonproliferation because TRU could be codeposited with uranium in liquid cadmium. However, the U ion was known to be deposited in the shape of dendrite on the surface of the liquid cathode [11]. This U dendrite hinders a codeposition of the U and TRU elements. Therefore, the inhibition of the growth of uranium dendrites in the LCC has been considered a critical technique for the electrowinning process. KAERI has developed a mesh-type LCC assembly (i.e., mesh agitator with LCC) to prevent U deposits from growing into dendrites, resulting in the increase of U recovery [7]. The mesh agitator pushes the U



FIGURE 10: Engineering-scale uranium chlorinator (30 kg-U/batch).



FIGURE 11: Engineering-scale molten salt transport system.

deposits generated on the LCC surface into the liquid Cd. Then U deposits sink into the liquid Cd and are gathered at the bottom of the LCC crucible. The performance of the mesh agitator was evaluated in lab-scale LCC experiments. From this experiment, 14 wt% U/Cd was successfully collected without the growth of dendrite out of the LCC crucible.

An engineering-scale PRIDE LCC electrolytic system was designed and constructed based on the lab-scale LCC experiments and the computational simulation results of heat transfer and current distribution [12]. The LCC electrowinning equipment installed in PRIDE and its recovery capacity of heavy metal is 1 kg heavy metal (HM)/batch (Figure 13).

2.4.2. Residual Actinides Recovery Process. RAR process has been developed by combining the electrolysis using an LCC to collect most the residual actinides in a spent salt phase and an oxidation of a part of the rare earth fission products co-deposited onto an LCC by a CdCl_2 oxidant [13]. The same electrowinning equipment using an LCC for a recovery of the fuel material can be used for RAR operation. Therefore, the RAR process has promising merits, such as compact equipment and a simple process to operate in a hot cell [14]. The PRIDE RAR processing equipment was designed and installed in the argon cell of the PRIDE.

2.5. Waste Treatment Process

2.5.1. Metal Waste Treatment Process. Metal wastes generated from the head-end process of spent fuel are mainly composed of cladding hulls and structural parts. A trace of actinides, such as U, Pu, Am, and Cm, and fission products (FPs)

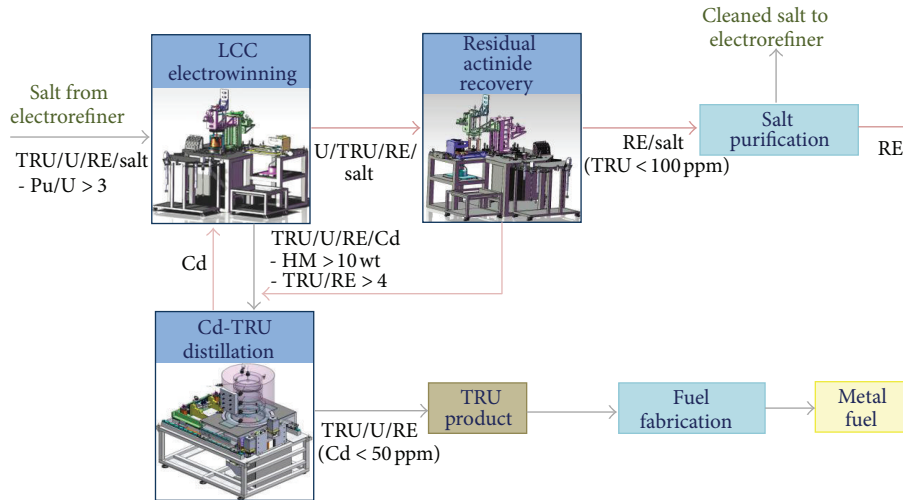


FIGURE 12: Schematic diagram of electrowinning system of KAERI.

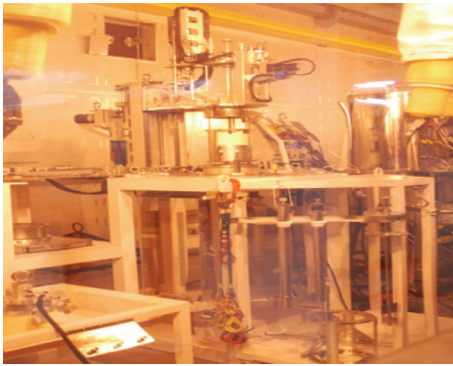


FIGURE 13: PRIDE LCC electrowinning equipment.

penetrate into the inner layer of zircaloy cladding hulls. Structural parts made of various stainless steels, Inconel, and zircalloys are also activated, resulting in the generation of Co-60 by neutrons created during a fuel irradiation process in the reactor. Table 1 shows the amount of metal wastes by volume and mass before and after the treatment. It was assumed that the stacking density of the cladding hull was 980 kg/m³ and actual density of a cladding hull ingot after induction melting was 80% of theoretical density. In addition, the volume reduction of the fuel hardware by 500 ton compaction was assumed to be 1/8.

Two major streams of the metal waste treatment for storage or disposal are the compaction and melting processes. The melting process has a higher volume reduction factor compared to the compaction method while it is a high temperature process that accompanies higher energy and cost. Zr recovery from zircaloy cladding hulls correspond to an alternative technology that can reduce the amount of a high level waste and reuse expensive Zr metal through a recycling process.

2.5.2. Waste Salt Treatment Process. The waste salt treatment process is divided into two parts: LiCl waste salt at 650°C and eutectic (LiCl-KCl) waste salt treatment at around 700°C. In LiCl waste salt treatment process, Groups I and II fission products involved in LiCl waste salt are removed by using a melt crystallization process and then the remaining residual LiCl salts containing high content of Groups I and II fission products, such as Cs, Sr, and Ba, are immobilized by mixing with an inorganic matrix, Si-Al-P (SAP) complex, and sintering at 1,200°C, to the ceramic waste forms. Rare earth fission products bearing eutectic waste salt from the RAR process is treated by successive rare earth removal processes: a combination of oxygen sparging, layer separation, and vacuum distillation/condensation process. Finally, the remaining rare earth oxides (or oxychlorides) are fabricated into the durable ceramic waste forms by mixing with zinc titanate (ZIT) matrix and sintering at 1,200°C. During each waste salt treatment process, pure LiCl and eutectic (LiCl-KCl) salts were recovered for reuse with a high regeneration ratio. Figure 14 shows a brief process diagram of the waste salt treatment process currently being developed by KAERI.

(1) LiCl Waste Salt Regeneration Process. For the reuse of LiCl waste salt, Groups I and II fission products have to be separated from the LiCl waste salt. To separate Groups I and II fission products such as Cs and Sr, chemical agents addition method and ion-exchange method were tested [15–18]. However, the results showed that simultaneous separation of Cs and Sr from the LiCl molten salt via various chemical agents or ion-exchange by zeolite was nearly unlikely [19]. To overcome these difficulties for the separation of both cesium and strontium, a layer crystallization process, which uses the solubility difference of impurities (FPs in this case) between a solid (=crystal) and a melt phase was introduced.

Layer crystallization is a very simple process, which uses cooled plates immersed in a melt for crystal formation, where a crystal grows as a compact crystalline layer on a cooling

TABLE I: Composition of pretreatment process wastes (10 ton/MTU).

	As generated				After treatment			
	Mass (kg)	Composition (%)	Volume (m ³)	Composition (%)	Mass (kg)	Composition (%)	Volume (m ³)	Composition (%)
Cladding hulls	2.454	70.3	2.50	35.7	3.028	74.5	0.46	45.1
Fuel Hardware	1.037	29.7	4.50	64.7	1.037	25.5	0.56	54.9
Sum	3.91	100	7.00	100	4.065	100	1.02	100

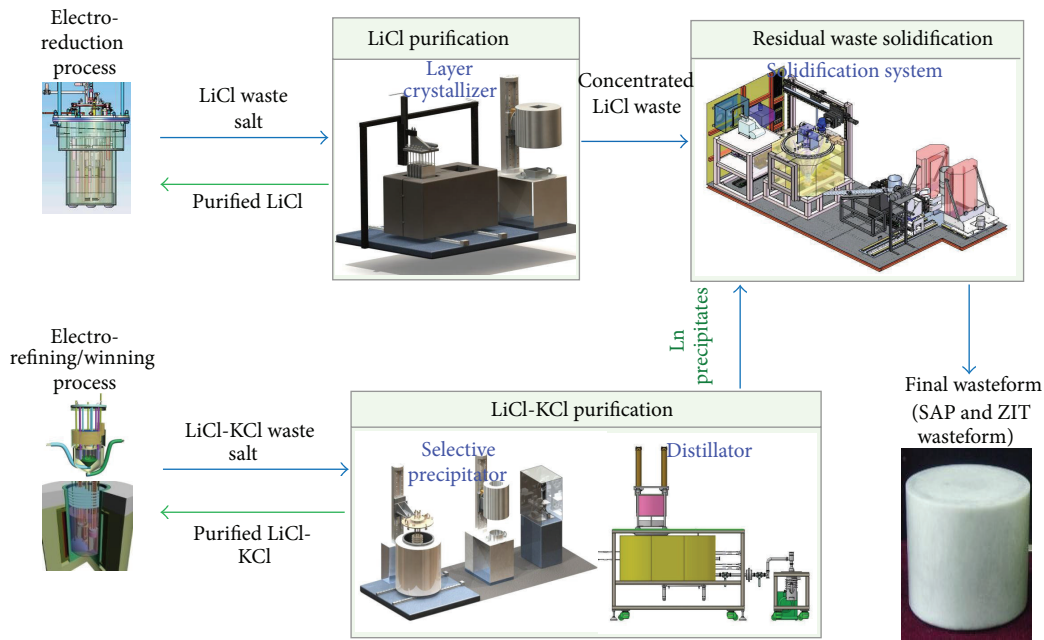


FIGURE 14: Schematic diagram of waste salt treatment process of KAERI.

surface. With the laboratory-scale layer crystallization apparatus (maximum batch size: 4 kg/batch), about 80~90% of LiCl salt containing small amount impurities, Groups I and II fission products can be recovered and the remaining LiCl in the crystallization furnace with most of impurities is transferred to the immobilization process to fabricate the final waste form.

Figure 15 shows the PRIDE engineering-scale LiCl waste salt treatment apparatus of which the maximum capacity is 25 kg-LiCl/batch composed of a layer crystallization and a solid LiCl salt detachment device.

(2) *Eutectic (LiCl-KCl) Waste Salt Regeneration Process.* Rare earth chloride elements involved in LiCl-KCl eutectic waste salt were converted to their molten salt-insoluble precipitates in the oxidative precipitation step by an oxygen gas sparging method. After a full precipitation of these lanthanide precipitates, an eutectic waste salt is separated into two layers: an upper pure (or purified) salt layer and a lower precipitate layer. The upper pure salt layer can be mechanically separated from the precipitate layer, where the separated pure salt layer could be reused (1st pure salt recovery). Then, the adhering eutectic salt involved in the precipitate layer was separated and recovered in the distillation/condensation step (2nd pure

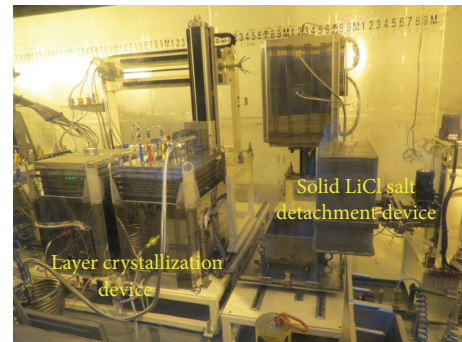


FIGURE 15: Photo of PRIDE engineering-scale LiCl waste salt treatment apparatus.

salt recovery). Finally, all the remaining rare earth oxides or oxychlorides were fabricated as a final waste form in the immobilization step.

The PRIDE engineering-scale rare earth separation apparatus (maximum batch size: 25 kg-eutectic salt/batch) that consists of three devices, a rare earth precipitation, a solid eutectic salt detachment, and a layer separation, is shown in Figure 16.



FIGURE 16: Photo of PRIDE engineering-scale rare earth separation apparatus.

(3) *Residual Waste Solidification Process.* In order to treat waste salt for final disposal, a dechlorination approach was adapted, where metal chloride waste was dechlorinated and thermally stabilized by using the synthetic inorganic composite SAP composed of SiO_2 , Al_2O_3 , and P_2O_5 , and its resultant product was sintered with a conventional borosilicate glass to obtain a monolithic wasteform.

The rare earth precipitates from the eutectic waste salt treatment process must be immobilized to a chemically stable solid wasteform for long-term storage in a geological environment. To immobilize rare earth oxide/oxychlorides, the solidifying matrix, ZIT, composed of Zn_2TiO_4 - CaHPO_4 - SiO_2 - B_2O_3 has been developed.

To realize the immobilization method, the lab-scale solidification process which consists of crushing, pulverizing, mixing/reacting and sintering equipment was used. Up to now, the unit equipments have been developed to obtain a proper performance and their processing conditions have been investigated to abstract the scale-up factors.

Table 2 shows the chemical durability of wasteforms and some physical properties for two wasteforms, SAP and ZIT wasteform. Leach-resistance of radionuclides was comparable to other radioactive wasteforms and the wasteforms had similar physiochemical properties, compared with silicate and phosphate glassy waste form [20].

3. Pyroprocess-Integrated Inactive Demonstration Facility

PRIDE has been constructed and operated as an engineering scale demonstration facility for pyroprocess studies [21]. The objective of PRIDE is to support integrated pyroprocessing demonstration and equipment development which are essential to realize the pyroprocessing. PRIDE is an integrated pyroprocessing system with unit reactor of 50 kgHM/batch capacity. It will use depleted uranium with surrogate materials to show integrated performance and scale-up issues of full-spectrum pyroprocessing technology.

PRIDE is a three-story building and it has a large-scale argon atmosphere cell (40.3 m length, 4.8 m width, 6.4 m height) at the second floor. The argon cell is equipped with cell operation equipments (small and large transfer systems, windows, cell lights, feed-through, etc.) and utilities. All

process equipments are remotely operated and maintained by using remote handling systems such as 34 pairs of mechanical “Master Slave Manipulators” (MSMs), a “Bridge transported Dual arm Servo Manipulator” (BDSM), and an overhead crane [22]. Not only the remote handling systems but also all process equipments and devices for the use in the PRIDE were designed as an assembly of modules considering easy maintenance. The special interface between modules and equipments was devised to assemble and disassemble the modules.

The argon utility system of PRIDE was also developed for maintaining the cell atmosphere within the desired operating parameters (concentration of oxygen and moisture <50 parts per million (ppm), respectively, the pressure (−10 mmAq~−100 mmAq) and the temperature (28~40°C)). The argon utility system consists of argon cell recirculation and cooling system, the purification system, and the relief system. The recirculation and cooling system controls the pressure and temperature of the cell within the above operation conditions, and the purification system removes oxygen and moisture from the cell.

Recently, major process equipments such as electrolytic reducer, cathode processor, electrorefiner, salt transfer system, salt distiller, LCC type electrowinner, residual actinide recovery apparatus, cadmium distiller, and waste molten salt treatment apparatus were installed in the PRIDE argon cell (Figure 17), and voloxidizer, salt waste form fabrication system, UCl_3 fabrication system, and uranium ingot melting furnace were installed at the first floor of PRIDE. The initial operation test of the argon system and evaluation of remote operability of cell equipment are being performed.

4. Conclusion

KAERI has developed an environment-friendly and proliferation resistant pyroprocessing for spent fuel treatment to recover useful materials such as uranium, plutonium, and reduce the volume and radiotoxicity of spent fuel. Through the last decade, R&D, some innovative technologies such as an advanced voloxidation, a high-capacity electrolytic reduction, a high-throughput electrorefining with a graphite cathode, a mesh-type liquid cadmium cathode electrowinning, and waste salt regeneration by crystallization method, have

TABLE 2: Some properties of two wasteforms.

Property	SAP wasteform	ZIT wasteform
Radionuclide leach rate, g/m ² day	10 ⁻⁴ ~ 10 ⁻³ for Cs/Sr	<10 ⁻⁵ for rare earth
Wasteform leach rate, g/m ² day	10 ⁻²	10 ⁻³
Density, g/cm ³	2.35~2.40	3.7~4.2
Thermal conductivity, W/mK	1.1~1.4	1.7
Thermal capacity, J/gK	0.96~1.07	0.65
Glass transition temperature, K	753~800	—
Thermal expansion coefficient, K ⁻¹	3.0 × 10 ⁻⁶	—
Microhardness, GPa	4.76 ± 0.15	5.5



FIGURE 17: Inside view of the PRIDE argon cell.

been tested successfully. PRIDE facility has been constructed at KAERI and advanced technologies in engineering-scale are planned to be demonstrated in PRIDE. The PRIDE will verify the performance of equipments, interaction between units, remote operability, facility management system, and process monitoring. For the commercialization of pyroprocessing, knowledge of a scale-up is essential and PRIDE engineering-scale demonstrations compared to laboratory-scale tests which has been studied to date will give the scale-up information especially on the batch size effects and process yields affected by the equipment size. Therefore, the PRIDE engineering-scale tests will evaluate the technical feasibility, economic feasibility, and nonproliferation acceptability of pyroprocessing.

References

- [1] I. S. Kim, C. S. Seo, H. S. Shin, Y. S. Hwang, and S. W. Park, "Characteristics of reduced metal from spent oxide fuel by lithium," *Journal of the Korean Nuclear Society*, vol. 35, no. 4, pp. 309–317, 2003.
- [2] J. M. Shin and J. J. Park, "Trapping characteristics of cesium in off-gas stream using fly ash filter," *The Korean Journal of Chemical Engineering*, vol. 18, no. 6, pp. 1010–1014, 2001.
- [3] Y. H. Kang, J. H. Lee, S. C. Hwang, J. B. Shim, E. H. Kim, and S. W. Park, "Electrodeposition characteristics of uranium by using a graphite cathode," *Carbon*, vol. 44, no. 14, pp. 3142–3145, 2006.
- [4] J. H. Jang, H. S. Kang, Y. S. Lee, H. S. Lee, and J. G. Kim, "Development of continuous Ingot casting process for uranium dendrites in pyroprocess," *Journal of Radioanalytical and Nuclear Chemistry*, vol. 295, no. 3, pp. 1743–1751, 2013.
- [5] H. S. Kang, J. H. Jang, Y. S. Lee, H. S. Lee, and J. G. Kim, "Development of engineering-scale ingot casting equipment for dendritic uranium deposit," in *Proceedings of the International Conference on Nuclear Chemistry for Sustainable Fuel Cycles (ATALANTE '12)*, Le Corum Montpellier, France, September 2012.
- [6] T. Hijikata and T. Koyama, "Development of high temperature transport technologies for liquid cadmium in pyrometallurgical reprocess," *Journal of Power and Energy Systems*, vol. 3, no. 1, pp. 170–178, 2009.
- [7] S. Paek, S. H. Kim, D. S. Yoon, H. Lee, and D. H. Ahn, "Performance of the mesh-type liquid cadmium cathode structure for the electrodeposition of uranium from the molten salt," *Radiochimica Acta*, vol. 98, no. 12, pp. 779–783, 2010.
- [8] J. B. Shim, Y. J. You, S. W. Kwon et al., "Thermodynamic and experimental approaches for an effective recovery of actinides from a spent LiCl-KCl salt," in *Proceedings of the International Pyroprocessing Research Conference*, Jeju Island, Republic of Korea, August 2008.
- [9] T. J. Kim, Y. Jung, S. H. Kim, S. W. Paek, and D. H. Ahn, "Elucidation of electrode reaction of EuCl₃ in LiCl-KCl eutectic melts through CV curve analysis," *Bulletin of the Korean Chemical Society*, vol. 32, no. 3, pp. 863–866, 2011.
- [10] K. R. Kim, T. J. Kim, S. Paek, D. H. Ahn, J. Y. Park, and I. S. Hwang, "Computational electrochemo-fluid dynamics modeling in a uranium electrowinning cell," in *Proceedings of the 3rd International Nuclear Chemistry Congress (INCC '11)*, Palermo Sicily, Italy, September 2011.
- [11] Argonne National Laboratory, "Chemical technology division annual technical report 1987," Tech. Rep. ANL-88/19, 1988.
- [12] D. H. Ahn, J. B. Shim, S. W. Paek et al., "Development of volume reduction technology for PWR spent fuel by pyroprocessing: development of the electrowinning system for TRU recovery," Tech. Rep. KAERI/RR-3400, Atomic Energy Research Institute, Korea, 2011.
- [13] J. B. Shim, K. S. Han, S. H. Kim et al., "Effects of CdCl₂ on the residual actinides recovery (RAR) system of a spent LiCl-KCl salt," in *Proceedings of Global*, Paris, France, September 2009.
- [14] K. Kinoshita, T. Inoue, S. P. Fusselman et al., "Separation of uranium and transuranic elements from rare earth elements by means of multistage extraction in LiCl-KCl/Bi system," *Journal of Nuclear Science and Technology*, vol. 36, no. 2, pp. 189–197, 1999.

- [15] M. F. Simpson and M. L. D. Gougar, "Two-site equilibrium model for ion exchange between monovalent cations and zeolite-A in a molten salt," *Industrial and Engineering Chemistry Research*, vol. 42, no. 18, pp. 4208–4212, 2003.
- [16] R. K. Ahluwalia, H. K. Geyer, C. Pereira, and J. P. Ackerman, "Modeling of a zeolite from molten salt," *Industrial and Engineering Chemistry Research*, vol. 37, pp. 145–153, 1998.
- [17] S. Phongikaroon and M. F. Simpson, "Equilibrium model for ion exchange between multivalent cations and zeolite-A in a molten salt," *AIChE Journal*, vol. 52, no. 5, pp. 1736–1743, 2006.
- [18] D. Lexa, "Occlusion and ion exchange in the molten (lithium chloride + potassium chloride + alkaline-earth chloride) salt + zeolite 4A system with alkaline-earth chlorides of calcium and strontium and in the molten (lithium chloride + potassium chloride + actinide chloride) salt + zeolite 4A system with the actinide chloride of uranium," *Metallurgical and Materials Transactions B*, vol. 34, no. 2, pp. 201–208, 2003.
- [19] H. S. Park, I. T. Kim, Y. J. Cho, M. S. Son, and H. C. Eun, "Removal behavior of Cs from molten salt by using zeolitic materials," *Journal of Radioanalytical and Nuclear Chemistry*, vol. 283, no. 2, pp. 267–272, 2010.
- [20] W. E. Lee, M. I. Ojovan, M. C. Stennett, and N. C. Hyatt, "Immobilisation of radioactive waste in glasses, glass composite materials and ceramics," *Advances in Applied Ceramics*, vol. 105, no. 1, pp. 3–12, 2006.
- [21] G.-S. You, I.-J. Cho, W.-M. Choung et al., "Concept and safety studies of an integrated pyroprocess facility," *Nuclear Engineering and Design*, vol. 241, no. 1, pp. 415–424, 2011.
- [22] J. K. Lee, H. J. Lee, B. S. Park, and K. Kim, "Bridge-transported bilateral master-slave servo manipulator system for remote manipulation in spent nuclear fuel processing plant," *Journal of Field Robotics*, vol. 29, no. 1, pp. 138–160, 2012.

Research Article

Improvement of Core Performance by Introduction of Moderators in a Blanket Region of Fast Reactors

Toshio Wakabayashi

Department of Quantum Science and Energy Engineering, Tohoku University, 6-6-01-2 Aramaki Aoba, Aoba-ku, Sendai 980-8579, Japan

Correspondence should be addressed to Toshio Wakabayashi; toshio.wakabayashi@qse.tohoku.ac.jp

Received 4 September 2012; Accepted 4 February 2013

Academic Editor: Wei Shen

Copyright © 2013 Toshio Wakabayashi. This is an open access article distributed under the Creative Commons Attribution License, which permits unrestricted use, distribution, and reproduction in any medium, provided the original work is properly cited.

An application of deuteride moderator for fast reactor cores is proposed for power flattening that can mitigate thermal spikes and alleviate the decrease in breeding ratio, which sometimes occurs when hydrogen moderator is applied as a moderator. Zirconium deuteride is employed in a form of pin arrays at the inner most rows of radial blanket fuel assemblies, which works as a reflector in order to flatten the radial power distribution in the outer core region of MONJU. The power flattening can be utilized to increase core average burn-up by increasing operational time. The core characteristics have been evaluated with a continuous-energy model Monte Carlo code MVP and the JENDL-3.3 cross-section library. The result indicates that the discharged fuel burn-up can be increased by about 7% relative to that of no moderator in the blanket region due to the power flattening when the number of deuteride moderator pins is 61. The core characteristics and core safety such as void reactivity, Doppler coefficient, and reactivity insertion that occurred at dissolution of deuteron were evaluated. It was clear that the serious drawback did not appear from the viewpoints of the core characteristics and core safety.

1. Introduction

In order to flatten radial power distribution in fast reactors, ordinary fast reactor cores employ two enrichment zones where outer zone has higher plutonium enrichment. Even in such design the power is dropped at the outer zone of the outer core due to the neutron leakage at the peripheral regions. Zirconium hydride has advantages of high moderation ratio as well as the stability to neutron irradiation as no gas emission occurs at neutron absorption. On the other side, it sometimes induces thermal spikes at the fuel pins adjacent to the moderator zones and reduces breeding ratios due to the large absorption cross section of hydrogen contained even in the fast reactor hard spectrum. However, such features of generating thermal spikes will be useful to increase the power at low power region such as core peripherals if the moderator is appropriately arranged, and it can provide the flattening in power distributions in fast reactors.

There are many studies [1–8] for the application of moderator in fast reactors. When the moderator material is mixed with absorber or long-life fission products (LLFPs)

in the fast reactor core, it will offer many advantages in core performances such as an increase in control rod worth or transmutation rate of LLFP [1–5]. The most promising moderator applicable to the fast reactor has been considered to be zirconium hydride for a long time. It has many experiences in fast reactor plant applications and designs including the shield of KNK-2 [9] in Germany and that of large fast reactor designs in Japan. An application of a hydride absorber as a control rod material in a fast reactor has been studied [7, 8].

The author proposes zirconium deuteride instead of zirconium hydride for flattening power distributions because it has a relatively high moderation ratio and very small neutron absorption cross sections. In this paper, an application of deuteride moderator for fast reactor cores is proposed for power flattening that can mitigate thermal spikes and alleviate the decrease in breeding ratio, which sometimes occurs when hydrogen moderator is applied as a moderator. The power flattening can be utilized to increase core average burn-up by increasing operational time or reducing fuel inventory which can be achieved by the reduction of core height, for example,

under the same restriction of the maximum linear heat rate. In this study, the power flattening and the increase in the core average burn-up were evaluated under the above assumptions for MONJU core. The influences of core characteristics, such as sodium void reactivity, Doppler coefficient, and control rod worth by the introduction of deuteride moderator were evaluated. In the safety aspect, reactivity insertion occurred at dissolution of deuterium was also evaluated.

2. Moderator Design and Monju Core

2.1. Moderator Assembly Design. The evaluated moderators include three types of zirconium compound. One is zirconium deuteride, another is ordinary zirconium hydride and the other is zirconium hydride of 25% smear density, where the effective volume ratio of the zirconium hydride is diluted to 25% of the inside cross sectional area of the pin. Such low smear density pins are usually fabricated by employing hollow pellets or pore rich materials.

The reason to select this arrangement is the mitigation of thermal spike, which sometimes occurs even in the fast reactor core including hydride materials. If the moderator is located at core peripherals, thermal spike is not important because linear heat rates of fuel pins are relatively low. This thermal spike can be utilized to enhance the flattening of power distribution if it occurs at low-power regions such as core peripherals.

The moderator pin arrangements in the moderator assembly are selected as parameters. The pin arrangements are shown in Figure 1. For example, the 9-pin moderator assembly contains 9 moderator pins facing the outer core assemblies and 52 depleted uranium oxide pins facing the second row of radial blanket assemblies. In no moderator core case, the moderator pins are replaced to depleted uranium oxide pins.

2.2. MONJU Core. The specifications of the MONJU core [10–12] are listed in Table 1. The core thermal power is 714 MWt and the fuel material is MOX. The core size is 93 cm in core height and about 180 cm in core diameter. The radial blanket zone is composed of 3 rows of blanket assemblies. The moderator assemblies are located at the inner most row of the radial blanket zone.

3. Analysis Method

The nuclear analysis method is listed in Table 2. A three-dimensional continuous energy Monte Carlo Code MVP [13, 14] is used with the Japanese cross-section library JENDL-3.3 [15] processed adjusted to MVP code.

Typical neutron history number employed is 1000000 divided to 100 batches and other 20 batches are used for generating the initial source distribution. The statistical error of pin power is about 2% in 1 σ level.

MVP-BURN (burn-up routine for MVP) [16] has been used to evaluate burn-up characteristics including breeding ratios. The burn-up chain employed is basically an FBR chain preinstalled in MVP-BURN (burn-up routine for MVP).

TABLE 1: Specification of MONJU core.

Items	Unit	Spec.
Reactor thermal power	MWt	714
Core configuration	—	Homogeneous 2 region core reactor
Operation cycle length	days	123
Core height	mm	930
Number of fuel assemblies (IC/OC/total)	—	108/90/198
Number of moderator assemblies	—	54
Total number of pins in the moderator assembly		61
Number of Moderator pins		9 or 24 or 61
Number of radial blanket pins		52 or 37 or 0
Pin diameter	mm	10.6
Diameter of moderator	mm	9.5
Moderator material		Zr deuteride Zr hydride

Figure 2 illustrates core maps and moderator assemblies in MONJU core. The inner core zone consists of 6 rows of assemblies and the outer core zone consists of 2 rows of assemblies where each assembly has 169 fuel pins. The pin power is integrated in axial direction over the core height. The radial blanket zone has 3 rows of assemblies containing 61 pins, where the first row consists of moderator assemblies. The moderator assemblies are replaced to normal radial blanket assembly for the no moderator core. The moderator assembly consists of moderator pins facing outer core fuels, which contains zirconium hydride or deuteride in a stainless steel cladding and depleted uranium oxide pins.

For pin-wise power distribution in the second row of the outer core has been evaluated for each pin row as shown in Figure 3. The powers of all pins belonging to each row have been summarized and divided by the number of the pins.

4. Results and Discussions

Figure 4 presents the result of pin-wise power peaking factor in the 2-row assembly of the outer core. The radial power peaking of no moderator case shows a monotone decrease while that of other cases produces thermal spike at the pins near to the moderator.

The zirconium hydride (ZrH_{1.7}) case shows the largest spike at the outer pins which peak power is about 3 times of that of the inner most row pins. On the other hand, the peak of the ZrD_{1.7} case does not exceed the power of the inner pins, and the power distribution over the assembly is flattened relative to that of no moderator case. The 25% smeared zirconium hydride (25% ZrH_{1.7}) case has small peak at the outer pins but it has a dip behind the peak.

Figure 5 shows the assembly power peaking factor in radial direction of the core. The power at the second row of the outer core (row no. 8) in the ZrD_{1.7} case is about the same

TABLE 2: Analytical method.

Items	Methods	Notes
Computation method	Three-dimensional continuation energy Monte Carlo analysis code MVP (Burn-up routine is MVP-BURN)	1,200,000 neutron histories with 120 Batches, Initial 20 batches are run to establish the initial neutron source distribution.
Nuclear data	JENDL-3.3 library	
Calculation model	Pin heterogeneous model	

TABLE 3: (a) Dependence of core performances on the number of ZrD_{1.7} moderator pins. (b) Dependence of core performances on the number of ZrH_{1.7} moderator pins.

(a)				
Number of moderator Pins	Power peaking factor in core	Power peaking factor of 2nd row assembly in outer core	Power peaking factor in blanket assembly	Increase of core average burn-up (%)
0	1.233	1.173	1.420	—
9	1.253	1.130	1.703	0.9
18	1.231	1.095	1.251	2.9
24	1.230	1.141	1.927	1.2
61	1.202	1.312	—	7.0
(b)				
Number of moderator pins	Power peaking factor in core	Power peaking factor of 2nd row assembly in outer core	Power peaking factor in blanket assembly	Increase of core average burn-up (%)
0	1.233	1.173	1.420	—
9	1.236	1.373	2.223	4.7
18	1.204	1.890	1.649	7.4
24	1.223	1.379	2.035	4.9
61	1.264	2.748	—	8.2

TABLE 4: Comparison of breeding ratio between cores with and without moderator.

Core	Cycle	Breeding ratio
Core with 61 deuteride moderator pins	Equilibrium cycle	1.02
Core without moderator pins	Equilibrium cycle	1.11

as that of the inner core (row no. 6), It is considered that the power distribution in the assembly of the 2nd row of the outer core for the ZrD_{1.7} case is the most flattened.

Tables 3(a) and 3(b) show the dependence of the power peaking factors and the discharged fuel burn-ups on the number of moderator pins of the ZrD_{1.7} and ZrH_{1.7} moderator assemblies located at the first row of radial blanket region in MONJU, respectively. In cases of 18 and 61 pins of ZrH_{1.7} moderator, it was recognized that these linear heat powers exceed the limit of the maximum liner power because of the large power peaking factors at 2nd row assembly in the outer core. These results indicate the power peaking factor in the

core is the smallest when the number of deuteride moderator pins are 61, and the core average burn-up can be increased by about 7% relative to that of no moderator core due to the power flattening.

Comparison of breeding ratio between cores with and without deuteride moderator pins in Table 4, The breeding ratio of the ZrD_{1.7} case is about 10% smaller than that of no moderator case. The breeding ratio is closely related to the burn-up reactivity loss, thus the result indicates ZrD_{1.7} is the most favorable moderator for fast breeder cores among the candidate moderators.

The influences of core characteristics, such as sodium void reactivity, Doppler coefficient, and control rod worth by the introduction of deuteride moderator pins were evaluated.

Comparison of Doppler coefficient between the cores with and without ZrD_{1.7} moderator pins is shown in Table 5. The absolute value of Doppler coefficient in the core with 61 deuteride moderator pins is about 50% larger than that in the core without moderator pins because of softening of neutron spectra in fuel region by moderator.

Comparison of sodium void reactivity between the cores with and without ZrD_{1.7} moderator pins is shown in Table 6.

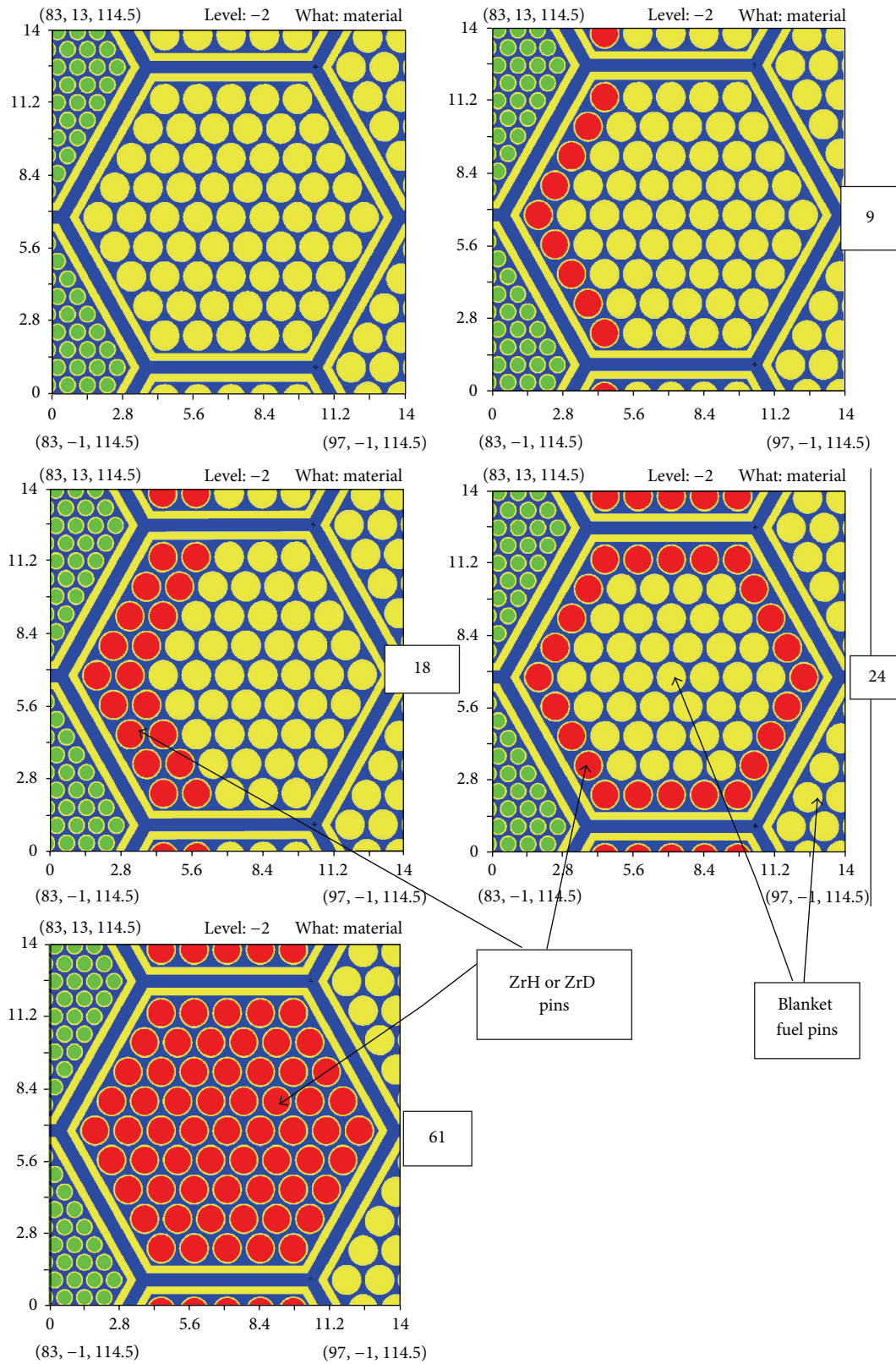


FIGURE I: Pin arrangements in moderator assembly.

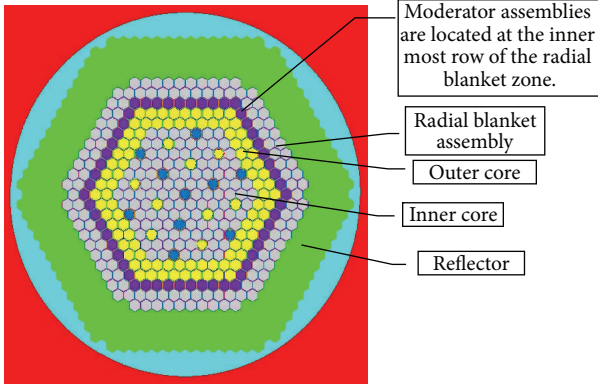


FIGURE 2: Core arrangement of MONJU.

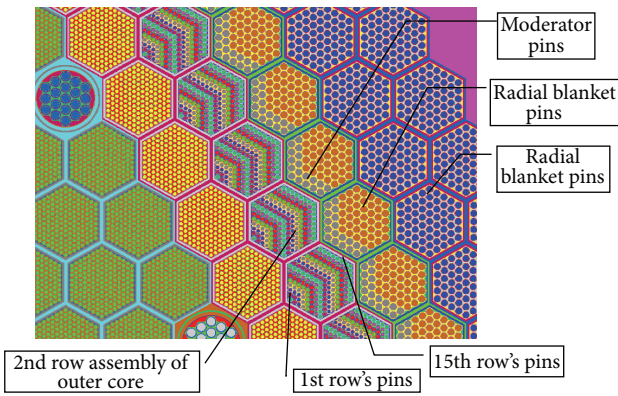


FIGURE 3: Details of pin arrangement at outer core region.

Sodium void reactivity at equilibrium cycle in the core with 61 deuteride moderator pins is a little smaller than that in the core without $ZrD_{1.7}$ moderator pins. It is considered that the reason of reducing positive sodium void reactivity is softening of neutron spectra in fuel region by moderator. This feature is important from the viewpoint of FBR safety.

Comparison of control rod worth between the cores with and without $ZrD_{1.7}$ moderator pins is shown in Table 7. The main control rod worth and backup control rod worth in the core with 61 deuteride moderator pins are, respectively, 5 and 9% smaller than those in the core without $ZrD_{1.7}$ moderator pins. It is considered that the neutron flux in the outer core is larger than that of inner core by the introduction of moderator. But, the control rod worth is satisfied with the design requirement.

Figure 6 presents the neutron spectra of outer row pins of the outer most assembly (the outer core second row assembly) for each moderator cases. The spectra of the outer pins show large differences at low-energy regions among different moderator cases.

The linear power of the moderator was two orders below that of the fuel pins around them because the main energy source is gamma deposition generated at the core fuel. The neutrons by gamma-n reactions in $ZrD_{1.7}$ are roughly estimated five orders below those of neutron generations of MONJU at the normal operation.

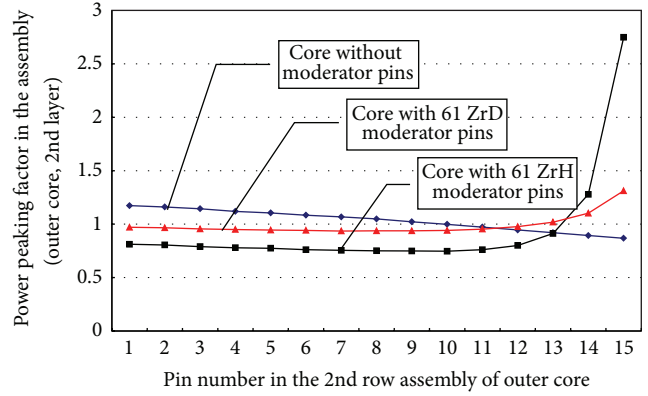


FIGURE 4: Pin wise power peaking factor in the 2 row assembly of the outer core.

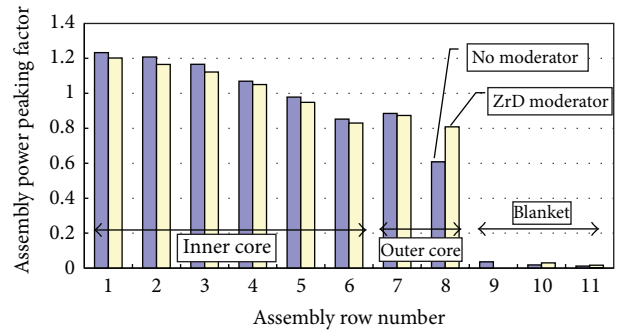


FIGURE 5: Assembly averaged pin power distribution in radial direction.

TABLE 5: Comparison of Doppler coefficient between cores with and without moderator.

Core	Cycle	Doppler coefficient ($\Delta k/kk'/dT/T$)
Core with 61 deuteride moderator pins	Equilibrium cycle	$-9.86E - 3$
Core without moderator pins	Equilibrium cycle	$-6.70E - 3$

TABLE 6: Comparison of sodium void reactivity between cores with and without moderator.

Core	Cycle	Sodium void reactivity ($\% \Delta k/kk'$)
Core with 61 deuteride moderator pins	Equilibrium cycle	1.05
Core without moderator pins	Equilibrium cycle	1.14

One problem of the hydride use in fast reactor is positive reactivity insertion that occurred at the dissolution of hydrogen. The dissolution of the deuterium will also occur in zirconium deuteride, though the penetration rate of the deuterium across the cladding is considered to be smaller than that of hydrogen due to the larger atomic

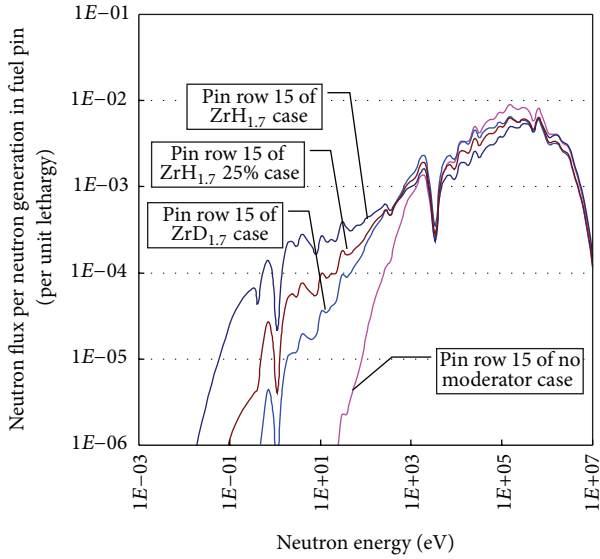


FIGURE 6: Neutron spectra of outer row pins of outer core 2nd row fuel assembly.

TABLE 7: Comparison of control rod worth between cores with and without moderator.

Type of control rods	Core	Control rod worth (% $\Delta k/k'$)
Main control rods (13 rods)	Core with 61 deuteride moderator pins	8.13
	Core without moderator pins	8.51
Back-up control rods (6 rods)	Core with 61 deuteride moderator pins	6.08
	Core without moderator pins	6.65

TABLE 8: Reactivity insertion occurred at dissolution of deuterium.

Ratio of deuterium in moderator pin	Reactivity (% $\Delta\rho$)
1.0	—
0.9	0.029
0.7	0.103
0	0.255

mass. The reactivity insertion by the dissolution of deuterium was evaluated. The reactivity insertion by the dissolution of deuterium is about $+0.255\%\Delta\rho$ as shown in Table 8. It is considered that the reason of positive reactivity is hardening of neutron spectra in moderator region by the dissolution of deuterium. The values of reactivity insertion are below 1 \$.

Deuterium will be transmuted to Tritium by neutron absorption where the generation rate of Tritium is estimated to be about 2 decades smaller than that generated from B-10 (n, α) T reaction in the boron carbide of the control rods.

5. Conclusions

An application of deuteride moderator for fast reactor cores is proposed for power flattening that can mitigate thermal spikes and alleviate the decrease in breeding ratio, which sometimes occurs when hydrogen moderator is applied as a moderator. Zirconium deuteride is employed in a form of pin arrays at the inner most rows of radial blanket fuel assemblies, which works as a reflector in order to flatten the radial power distribution in the outer core region of MONJU. The power flattening can be utilized to increase core average burn-up by increasing operational time. The core neutronics has been evaluated with a continuous-energy model Monte Carlo code MVP and the JENDL-3.3 cross-section library. The result indicates that the power peaking factor in the core is the smallest when the number of deuteride moderator pins is 61, and the core average burn-up can be increased by about 7% relative to that of no moderator core due to the power flattening. Major core characteristics and core safety including sodium void reactivity, Doppler coefficient, control rod worth and reactivity insertion that occurred at dissolution of deuterium were also evaluated. The breeding ratio of the deuteride case is a little less than that of no moderator case. It is also clear that the influence of major core characteristics and safety aspect by the introduction of deuteride moderator is small.

The present study indicates that the use of deuteride moderators in the blanket region has a large potential to improve performances of FBR cores.

Acknowledgments

The author deeply appreciates Dr. T. Yokoyama of Toshiba Nuclear Engineering Services Corporation, Mr. Akira Nagata and Mr. Y. Tsuboi of Toshiba Corporation, and Mr. S. Aoyagi of ISA Corporation for their cooperation and advices. Present study includes the results of “Study on Optimization of Core Arrangement of Core Fuel and Blanket Fuel on FBR” entrusted to “Tohoku University” by the Ministry of Education, Culture, Science and Technology of Japan (MEXT).

References

- [1] T. Wakabayashi, “Transmutation characteristics of MA and LLFP in a fast reactor,” *Progress in Nuclear Energy*, vol. 40, no. 3-4, pp. 457-463, 2002.
- [2] Y. Tachi, T. Wakabayashi, and T. Yokoyama, “Study on target fabrication for LLFP transmutation by fast reactors,” in *Proceedings of the International Conference on the Nuclear Fuel Cycle*, 2009.
- [3] T. Yokoyama, T. Wakabayashi, Y. Tachi, N. Takaki, and S. Matsuyama, “New target concepts for increase in transmutation rate of LLFP in FBR recycle system,” in *Proceedings of International Conference on the Nuclear Fuel Cycle*, 2009.
- [4] Y. Tachi and T. Wakabayashi, “Candidate Iodides for LLFP transmutation in FR core,” *Transactions of the American Nuclear Society*, vol. 103, pp. 268-269, 2010.
- [5] T. Yokoyama, T. Wakabayashi, Y. Tachi, and A. Nagata, “Increase in transmutation rate of long-life FP by employing deuteride moderator in fast reactors,” in *Proceedings of the International*

- Congress on Advances in Nuclear Power Plants*, pp. 536–543, 2011.
- [6] D. R. Olander and M. Ng, “Hydride fuel behavior in LWRs,” *Journal of Nuclear Materials*, vol. 346, no. 2-3, pp. 98–108, 2005.
- [7] T. Yokoyama, K. Konashi, T. Iwasaki, T. Terai, and M. Yamawaki, “Local-spectrum-modified fast reactor cores with hydrides,” in *Proceedings of the International Congress on Advances in Nuclear Power Plants (ICAPP '06)*, pp. 2492–2498, June 2006.
- [8] T. Iwasaki and K. Konashi, “Development of hydride absorber for fast reactor—application of hafnium hydride to control rod of large fast reactor,” *Journal of Nuclear Science and Technology*, vol. 46, no. 8, pp. 874–882, 2009.
- [9] W. Marth, *The History of the Construction and Operation of the German KNK II Fast Breeder Power Plant*, vol. 5456 of KfK, 1994.
- [10] S. Sawada, T. Suzuki, Y. Okimoto, K. Sasaki, T. Deshimaru, and F. Nakashima, “Reactivity characteristics evaluations of the initial core of Monju,” in *International Conference on the Physics of Reactors (PHYSOR '96)*, vol. 2, p. E-76, Mito, Japan, September 1996.
- [11] K. Sugino and T. Iwai, “MONJU experimental data analysis and its feasibility evaluation to build up the standard data base for large FBR nuclear core design,” in *Proceedings of the American Nuclear Society Topical Meeting on Physics of Reactors (PHYSOR '06)*, American Nuclear Society, Vancouver, Canada, September 2006.
- [12] K. Ito and T. Yanagisawa, “Last twenty years experiences with fast reactors in Japan,” in *Proceedings of the International Conference on Fast Reactors and Related Fuel Cycles: Challenges and Opportunities (FR '09)*, pp. 7–11, Kyoto, Japan, December 2009.
- [13] T. Mouri, W. Sato, M. Uematsu, T. Hazama, and T. Suzuki, “Monju core physics test analysis with various nuclear data libraries,” in *International Conference on Fast Reactors and Related Fuel Cycles: Challenges and Opportunities (FR '09)*, Kyoto, Japan, December 2009.
- [14] Y. Nagaya, K. Okumura, T. Mori, and M. Nakagawa, “MVP/GMVP-II: general purpose Monte Carlo codes for neutron and photon transport calculations based on continuous energy and multi-group methods,” JAERI-Report 1348, Japan Atomic Energy Research Institute, 2005.
- [15] K. Shibata, T. Kawano, T. Nakagawa et al., “Japanese evaluated nuclear data library version 3 revision-3: JENDL-3.3,” *Journal of Nuclear Science and Technology*, vol. 39, no. 11, pp. 1125–1136, 2002.
- [16] K. Okumura, T. Mori, M. Nakagawa, and K. Kaneko, “Validation of a continuous-energy Monte Carlo burn-up code MVP-BURN and its application to analysis of post irradiation experiment,” *Journal of Nuclear Science and Technology*, vol. 37, no. 2, pp. 128–138, 2000.

Research Article

Simulation Strategy for the Evaluation of Neutronic Properties of a Canadian SCWR Fuel Channel

G. Harrisson and G. Marleau

Institut de Génie Nucléaire, École Polytechnique de Montréal, P.O. Box 6079, Stn. CV, Montréal, QC, Canada H3C 3A7

Correspondence should be addressed to G. Harrisson; genevieve.harrisson@polymtl.ca

Received 20 November 2012; Accepted 8 January 2013

Academic Editor: Hangbok Choi

Copyright © 2013 G. Harrisson and G. Marleau. This is an open access article distributed under the Creative Commons Attribution License, which permits unrestricted use, distribution, and reproduction in any medium, provided the original work is properly cited.

The Canadian Supercritical-Water-Cooled Reactor (SCWR) is a vertical pressure tube reactor cooled with supercritical light water and moderated with heavy water. For normal operation, the local conditions of the coolant (density and temperature) and fuel (temperature) vary substantially along the channel. This means that to simulate adequately the behavior of the core under operating conditions or for anticipated accident scenario, expensive 3D transport calculations for a complete fuel channel are required. Here, we propose a simulation strategy that takes into account axial variations of the local conditions and avoids 3D transport calculations. This strategy consists in replacing the 3D simulation by a series of isolated 2D calculations followed by a single 1D simulation. It is shown that this strategy is efficient because the axial coupling along the fuel channel is relatively weak. In addition, the neutronic properties of a channel with axial reflector can be modeled using a simplified 3D transport calculation.

1. Introduction

The Canadian Supercritical-Water-Cooled Reactor (SCWR) is a pressure-tube type generation-IV reactor [1] based on CANada Deuterium Uranium (CANDU) reactors [2]. The preliminary concept uses a calandria vessel containing the low-pressure moderator and the five meters long fuel channels [3]. This concept uses off-power batch refueling, and to simplify the fuelling process, the reactor core is oriented vertically. Another feature of this concept is that the coolant is forced vertically downwards; that is, the coolant enters the fuel channels at the top and exits at the bottom of the core.

According to the pressure-temperature phase diagram for water, most of the current reactors operate in the liquid phase or on the saturation line. However, the main characteristic of the Canadian SCWR is that the coolant (light water) operates at pseudocritical and supercritical conditions, that is, at pressures and temperatures above the critical point of water (22.064 MPa and 373.95°C). The preliminary concept has a pressure of 25 MPa, a reactor inlet temperature of 350°C and a reactor outlet temperature of 625°C. Figure ?? shows the expected coolant conditions along a fuel channel.

Light water has an impact on neutron slowing down and on neutron absorption. The importance of this impact

depends on the temperature and on the density of this water [4]. The effect of the large variation of the coolant conditions along a fuel channel on the global neutronic properties should be studied in details, as done recently in some studies [5, 6].

During the optimization phase of the lattice cell of a new reactor, several neutronic transport calculations are done. Usually, these calculations are performed using deterministic codes such as WIMS-AECL [7] and DRAGON [8] for a single 2D lattice cell with average core conditions or with the average conditions in the region of the core that produces the highest power. However, in the case of the Canadian SCWR, this methodology is not directly applicable because the metrics (such as the exit burnup and the reactivity coefficients) used to perform the optimization depend strongly on the set of conditions found along a fuel channel. For example, Figure 2 shows the coolant void reactivity (CVR) along a fuel channel as obtained from a series of 2D infinite lattice cell calculations using the Monte Carlo code SERPENT [9] (14 independent calculations) where

$$\text{CVR (mk)} = 1000 \times \left(\frac{1}{k_{\text{eff}}^{\text{cooled}}} - \frac{1}{k_{\text{eff}}^{\text{voided}}} \right). \quad (1)$$

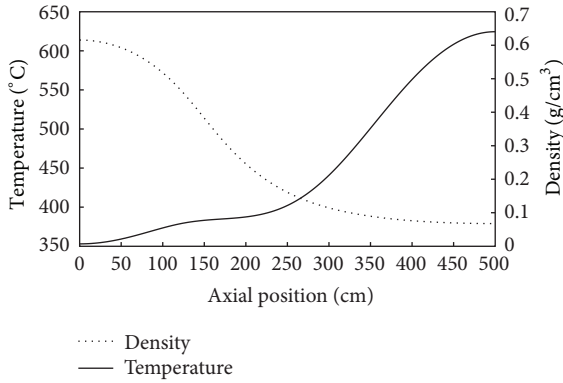


FIGURE 1: Expected coolant conditions along a Canadian SCWR fuel channel.

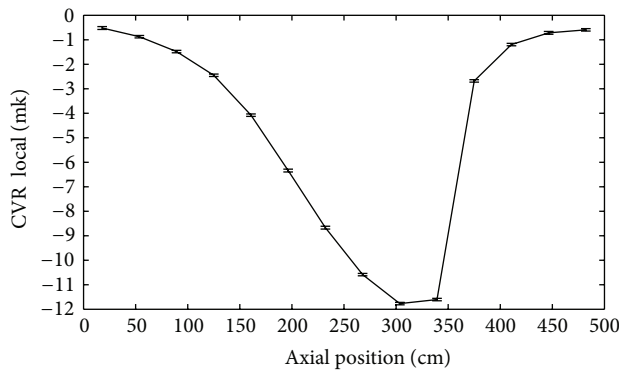


FIGURE 2: CVRs along a fuel channel obtained from independent 2D lattice cell calculations.

Here, $k_{\text{eff}}^{\text{cooled}}$ corresponds to cell calculations performed with the coolant at the expected density and temperature associated with the axial position considered in the channel, and $k_{\text{eff}}^{\text{voided}}$ is for cell calculations with the coolant absent.

The objective of this study is to establish an efficient simulation strategy that will be able to retain the simplicity and efficiency of deterministic 2D lattice cell calculation while correcting the resulting few groups reactor cross sections using a 1D multigroup transport model. As a result, one should be able to avoid the repetitive and computationally intensive 3D calculations that would be required during the optimization and operation of the core. Here we will develop and validate our simulation strategy using SERPENT to perform all 3D and 2D continuous energy simulations and DRAGON for all 1D multigroup simulations. All simulations with SERPENT have been performed with 100 000 neutrons per cycle, 2000 active cycles and 200 inactive cycles. This leads to a total of 200 000 000 histories. The meshing used in DRAGON simulations is mentioned where appropriate in the paper.

In Sections 2 and 3, respectively, we describe and then validate the new simulation strategy proposed for fuel cells

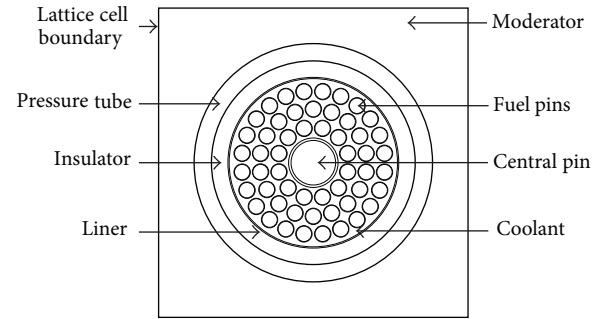


FIGURE 3: Canadian SCWR 54 elements fuel bundle and high efficiency fuel channel.

that are not in direct contact with an axial reflector cell. In Section 4, we extend the strategy to axial reflector cells and fuel cells in contact with that reflector. Finally, in Section 5 we conclude.

2. Simulation Strategy Model for Fuel Channels without Axial Reflector Cells

The lattice cell considered here consists of a 54 elements fuel bundle inserted in a high efficiency fuel channel [10] as shown in Figure 3.

In this design, the channel is composed of a stainless steel liner followed by an insulator of zirconia and of a pressure tube made of a zirconium alloy. The fuel is a mixture of thorium and plutonium. The central pin is filled with light water. Light water is used as coolant and heavy water as moderator. The lattice pitch is set to 25 cm.

Even if alternative fuel bundle designs have been proposed recently [11], the specifications used in this study are based on those used in previous publications [4, 12] in order to facilitate comparisons with other related studies [13, 14].

2.1. Simulation Strategy Model. The simulation strategy proposed is based on the following hypothesis: A 3D calculation is equivalent to a series of independent 2D calculations followed by a single 1D calculation.

As shown in Figure 4, the first step of the simulation strategy proposed consists in performing a series of independent 2D infinite lattice cell calculations at strategic positions along the fuel channel.

The various levels of gray indicate that each lattice cell has a unique set of temperatures (fuel and coolant) and densities (coolant) according to the conditions expected along a fuel channel. In the next subsection, it will be shown that 14 2D infinite lattice cell calculations must be performed in this first step in order to meet the convergence criteria. For each 2D cell, the objective here is to determine the flux distribution ϕ in the $x-y$ plane and then to perform a spatial homogenization over the entire lattice cell containing N regions and an energy condensation into the desired number of energy groups (the group g contains the neutrons having energies between E_g and E_{g-1}) to obtain the multigroup

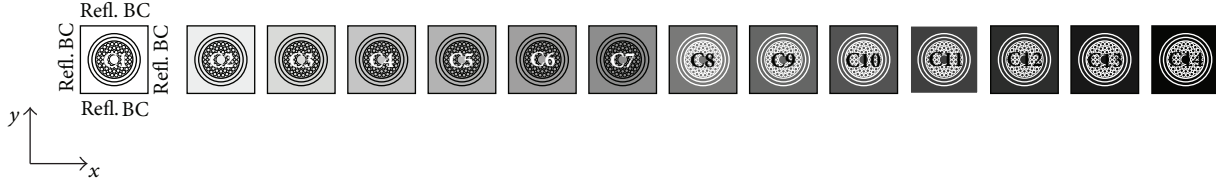


FIGURE 4: First step of the simulation strategy: 2D infinite lattice cell calculations.



FIGURE 5: Second step of the simulation strategy: 1D slab geometry calculation.

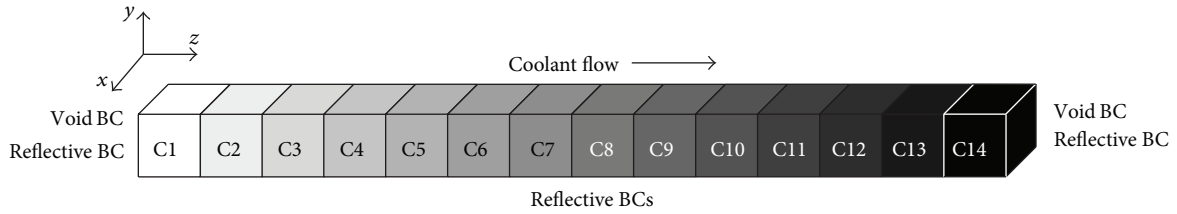


FIGURE 6: 3D reference model without axial reflector cells.

macroscopic cell averaged cross sections at each strategic position as follows:

$$\phi_g = \frac{1}{V} \int_{E_g}^{E_{g-1}} \sum_{i=1}^N \phi_i(E) V_i dE, \quad (2)$$

$$\Sigma_g = \frac{1}{V\phi_g} \int_{E_g}^{E_{g-1}} \sum_{i=1}^N \phi_i(E) V_i \Sigma_i(E) dE,$$

where V is the volume of the lattice cell. Reflective boundary conditions (BCs) have been applied on all outer surfaces. Here for consistency with the 3D reference model presented in Section 2.2, our 2D calculations have been performed with SERPENT.

As shown in Figure 5, the second step of the simulation strategy proposed is to perform a 1D slab geometry calculation using the multigroup cell averaged cross sections calculated in the first step. This time, the objective is to obtain the flux distribution along the fuel channel. Void or reflective BCs can be applied along the axial direction, depending on the case studied. The 1D calculations were performed with DRAGON, since SERPENT cannot perform multigroup calculations. The DRAGON calculations were performed using the collision probability method with a maximum of 10 regions per cell along the z -axis for a maximum of 140 flux calculation regions.

By going through these two simple steps, it is then possible to simulate a 3D fuel channel and to obtain its averaged properties without having to do a complete 3D calculation.

2.2. 3D Reference Model without Axial Reflector Cells. To ensure the validity of the simulation strategy proposed, it has been compared to a complete 3D fuel channel calculation (Figure 6) that takes into account all temperatures and densities axial profiles in a single calculation.

Each 3D cell has a unique set of temperatures and densities according to the expected conditions along the fuel channel. At this point, one can note that the 14 2D cells presented above represent a slice of each 3D cell. The objective here is to calculate the multigroup cross sections associated with the fuel channel in a single calculation. Reflective BCs have been applied in the radial direction, and void or reflective BCs have been applied in the axial direction. All 3D calculations have been performed with SERPENT.

A study, performed with SERPENT, was conducted to optimize the number of 3D cells required to simulate adequately the complete fuel channel. For example, Figure 7 shows the multiplication factor of the 3D channel as a function of the number of 3D cells. A minimum of 2 and a maximum of 64 3D cells have been simulated. Since the results begin to converge at 14 3D cells, there is no need to increase the axial discretization further. This axial discretization leads to a maximum deviation of 0.1 mk from the converged value obtained with 64 3D cells.

2.3. Models Comparison. Table 1 presents a comparison of the multiplication factors and CVRs obtained from the 3D reference model without axial reflector cells (SERPENT 3D) and the simulation strategy model (SERPENT 2D + DRAGON 1D). Here, two situations were considered: (1) reflective axial

TABLE 1: Channel multiplication factors and CVRs for models without axial reflector cells.

Model	$k_{\text{eff}}^{\text{cooled}}$	$k_{\text{eff}}^{\text{voided}}$	CVR (mk)
Reflective axial BCs			
Reference without reflector cells	1.21712 ± 0.00004	1.20923 ± 0.00005	-5.36 ± 0.06
Strategy	1.21711	1.20925	-5.34
Void axial BCs			
Reference without reflector cells	1.21207 ± 0.00004	1.19808 ± 0.00005	-9.63 ± 0.06
Strategy	1.21195	1.19808	-9.55

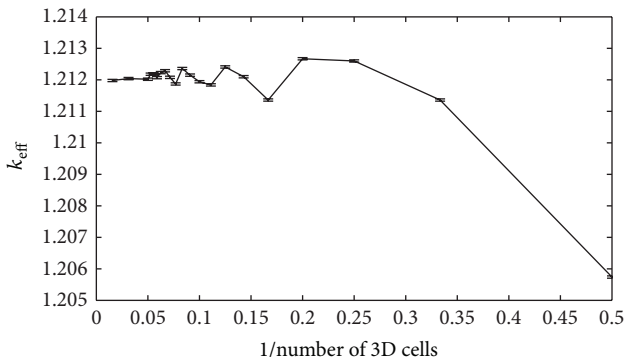


FIGURE 7: Optimization of the number of 3D cells in the channel.

BCs where the neutrons reaching the boundary of cells C1 and C14 are reflected and (2) void axial BCs where the neutrons leaving cells C1 and C14 respectively in the $-z$ and $+z$ directions are lost.

As one can see, the differences between the 3D reference model and the simulation strategy model are very small (maximum of 0.12 mk or 3σ). One can also observe that the CVR is much larger in absolute value for the case where zero incoming flux boundary conditions are considered (void BCs). This may be explained in part by the fact that the effective multiplication constant is reduced. However, the main effect here is that neutron streaming without collisions through the channel along directions nearly parallel to the z -axis will be lost when void BCs are considered, while they will be reflected in the geometry and get a second chance to be slowed down in the moderator when reflective BCs are considered, thereby leading to a smaller absolute value of the CVR.

Overall, the simulation strategy proposed shows good agreement with the 3D reference model because the axial coupling along the fuel channel is relatively small.

3. Assessment of the Axial Coupling

We have assessed the extent of the axial coupling in a previous publication [15]. The main elements of this study

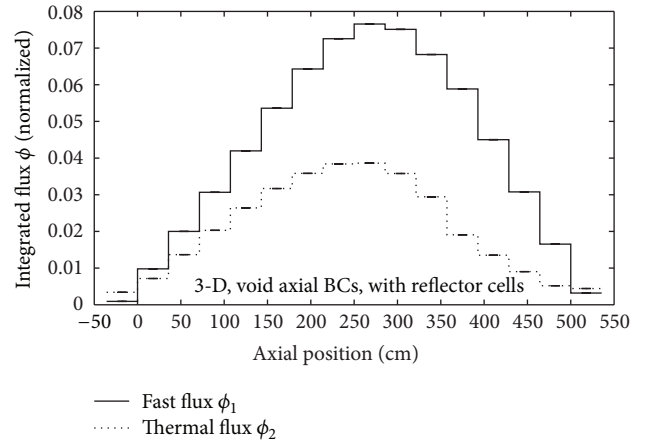


FIGURE 8: Integrated flux for a 3D fuel channel with reflector cells and void axial BC.

are presented here simply to demonstrate why the simulation strategy proposed is effective in the present case.

The physical process behind the axial coupling is described here from a simple example. Imagine two 3D cells. Taken individually, each cell has its own neutron spectrum. This spectrum is defined by the geometry and by the local conditions found in the cell. If these two cells are in direct contact, the neutrons are free to travel from one cell to the other. This exchange of neutrons between the cells can modify the neutron spectrum in them. As can be seen in (2), this shift in spectrum can lead in the end to different multigroup macroscopic cell averaged cross sections because flux levels may be different for a given energy and because the microscopic cross sections depend on the energy. However, if the cells are isolated from each other during the calculation, this exchange of neutrons cannot be taken into account [16].

With the aim to clarify the physical process involved in the axial coupling, it is relevant to take a look at the flux distribution along the fuel channel. Figure 8 presents the SERPENT calculated integrated flux (fast flux ϕ_1 above 0.625 eV and the thermal ϕ_2 flux below this limit) along a 3D fuel channel with reflector cells at both ends (see Figure 9) and void axial BCs.

As one can observe, ϕ_1 is slightly shifted toward the second half of the channel, while ϕ_2 is more shifted toward the first half. Thus, the differences between these fluxes are significantly higher in the second half than in the first half of the channel. This effect is mainly due to the variation of the coolant conditions along the fuel channel. Since the coolant density decreases along the fuel channel, it contributes less to neutrons slowing down (decrease of ϕ_2) leaving them at a higher energy (increase of ϕ_1). Also, an inversion of population is observed in the reflector cells (axial positions <0 cm and >500 cm), since these cells are mainly composed of moderating materials (the reflector cell is similar to a standard cell with the fuel bundle removed (see Section 4.1)).

Figure 10 presents the integrated flux ratio (ϕ_1/ϕ_2) along the fuel channel for four different models studied with SERPENT (models description are given in Section 3.1). The

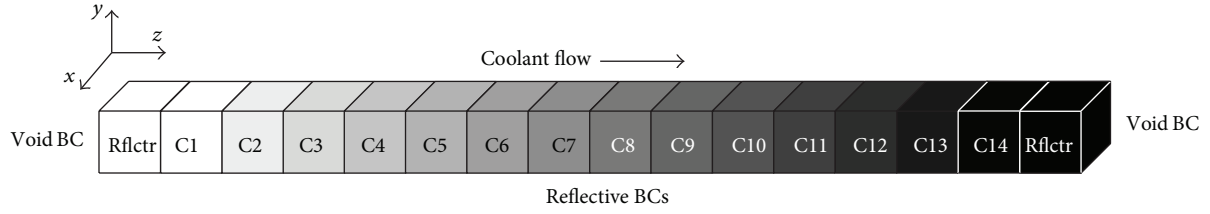


FIGURE 9: 3D fuel channel with axial reflector cells at both ends.

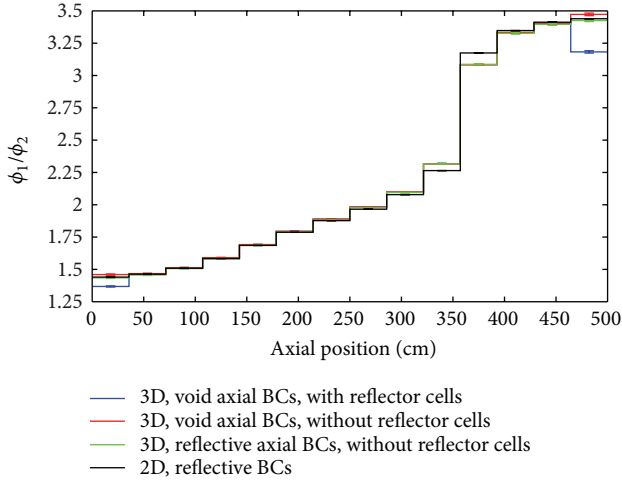


FIGURE 10: Integrated flux ratios for different models.

integrated flux ratio gives an indication on the distribution of the neutrons between the energy groups. Thus, the comparison of integrated flux ratios is in fact a simple comparison of neutron spectra. Here, the ratios obtained from the 3D models must be compared to those obtained from the 2D model. Larger differences between these ratios indicate a higher axial coupling. According to Figure 10, the differences between 3D and 2D ratios remain small for almost the entire length of the channel with a few exceptions, namely, between 325 and 375 cm where the CVR changes abruptly and at both ends of the channel.

While this figure describes the “flux level” component of the axial coupling, Figures 11, 12, 13, 14, 15, and 16 present a more global assessment of the axial coupling because they compare the multigroup macroscopic cell averaged cross sections where the local cell properties are also taken into account.

3.1. Approach Followed. The axial coupling has been evaluated by comparing, along the fuel channel, the multigroup macroscopic cell averaged cross sections obtained from the 3D models to those obtain from the 2D model. The absorption, up and down scattering, and fission neutron production cross sections have been studied. The cross sections have been condensed to two energy groups (fast and thermal) and homogenized over each cell [17]. The models analyzed with SERPENT are as follows.

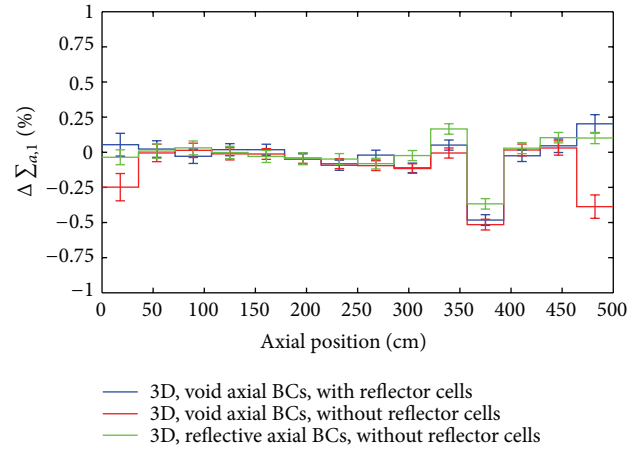


FIGURE 11: Relative differences between absorption cross sections for the fast group.

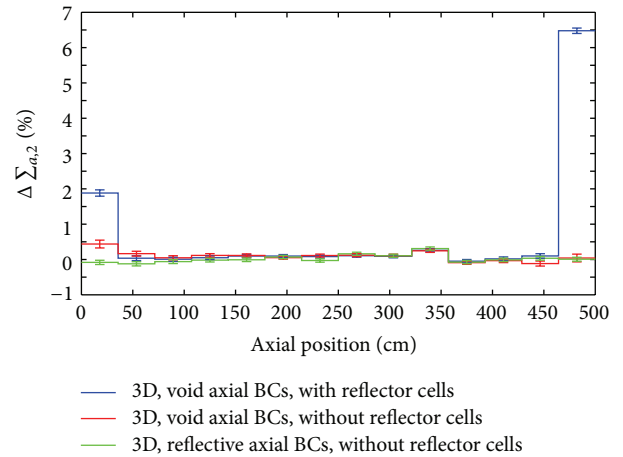


FIGURE 12: Relative differences between absorption cross sections for the thermal group.

- (i) A 3D fuel channel with reflector cells at both ends assuming reflective BCs in the radial direction and void BCs in the axial direction (Figure 9).
- (ii) A 3D fuel channel without reflector cells assuming reflective BCs in the radial direction and void BCs in the axial direction (Figure 6).

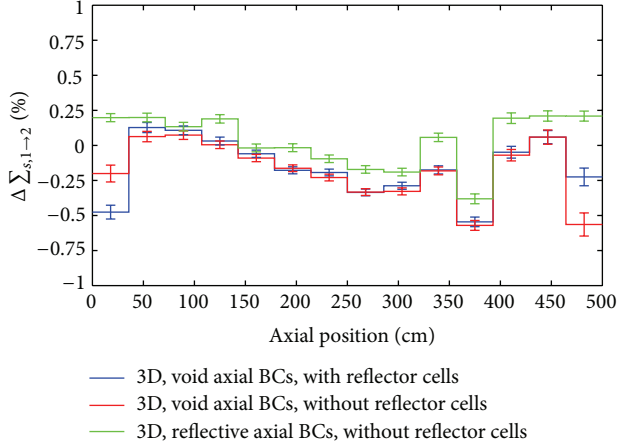


FIGURE 13: Relative differences between down scattering cross sections.

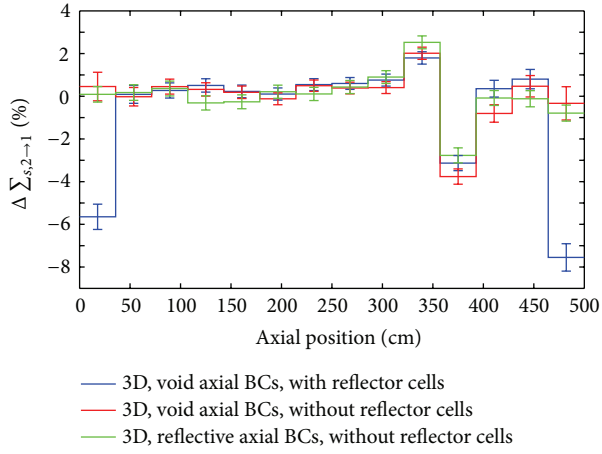


FIGURE 14: Relative differences between up scattering cross sections.

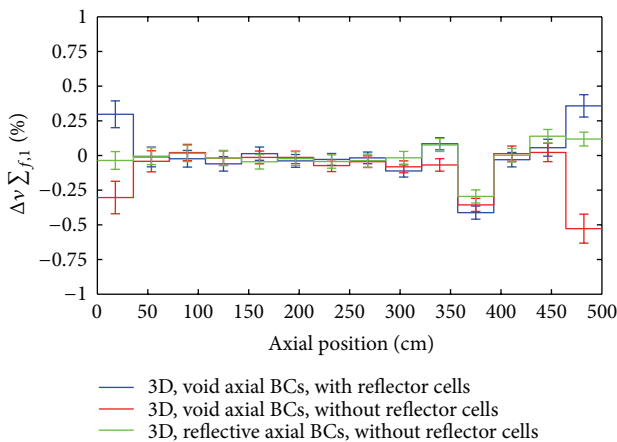


FIGURE 15: Relative differences between fission neutron production cross sections for the fast group.

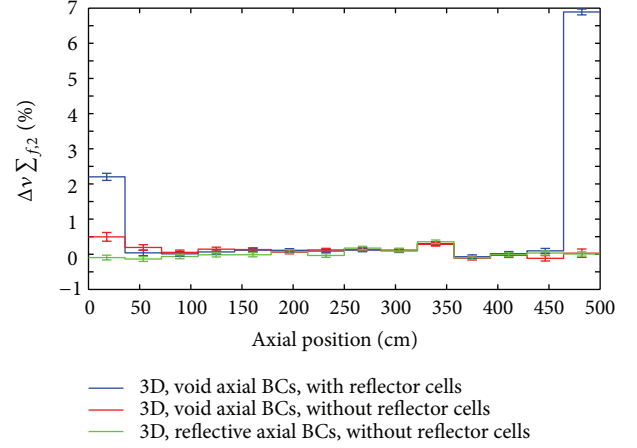


FIGURE 16: Relative differences between fission neutron production cross sections for the thermal group.

- (iii) A 3D fuel channel without reflector cells and with reflective BCs in all directions (Figure 6).
- (iv) 14 2D cells with reflective BCs (Figure 4).

3.2. *Multigroup Macroscopic Cell Averaged Cross Sections Evaluations.* Figures 11–16 present the relative differences between multigroup macroscopic cell averaged cross sections calculated as follows:

$$\Delta\Sigma_{x,g} (\%) = 100 \times \left(\frac{\Sigma_{x,g}^{3D} - \Sigma_{x,g}^{2D}}{\Sigma_{x,g}^{3D}} \right), \quad (3)$$

where the 3D and 2D superscripts refer, respectively, to one of the 3D models and to the 2D model while the subscripts x and g refer, respectively, to the reaction type and the energy group.

Overall, differences below $\pm 0.6\%$ are observed in the central region of the channel. However, differences can rise up to about $\pm 7.5\%$ at channel ends, where the effects of the reflector cells on the multigroup cell averaged cross sections are mainly observed. This investigation demonstrates that the axial coupling along the fuel channel appears to be small compared to the effects of the reflector cells.

4. Extended Simulation Strategy for Fuel Channels with Axial Reflector Cells

Two problems arise when a 3D fuel channel with axial reflector cells has to be reconstructed from a series of independent 2D lattice cell calculations: (1) the multigroup cell averaged cross sections in fuel cells adjacent to the reflector cells are not well approximated by independent 2D lattice cell calculations, as pointed out in the previous section, but more importantly (2) the multigroup cell averaged cross sections in the reflector cells cannot be calculated from a single cell containing only moderator materials because it is not possible to perform a neutron transport calculation without neutron sources and without incoming neutron fluxes.

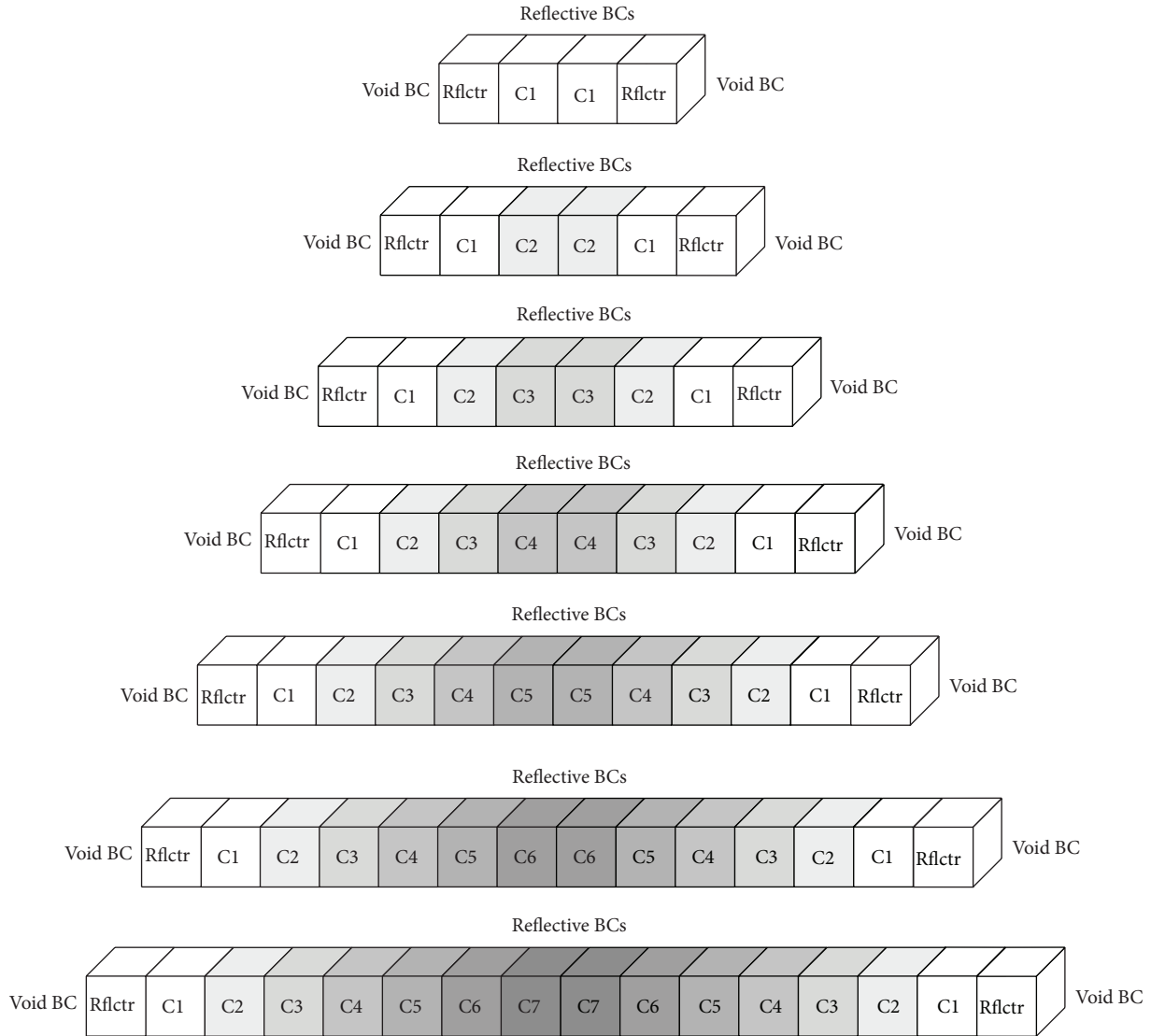


FIGURE 17: Partial 3D fuel channels with axial reflector cells developed for the study of the cells at the inlet.

Due to the geometric nature of the problem, 3D calculations are necessary here. Repetitive time consuming 3D Monte Carlo transport calculations should be avoided as much as possible during the optimization phase of the core. An alternative would be to fall back on the rapidity of deterministic codes, to handle 3D geometries (DRAGON for example). However, a performant deterministic transport calculation deals generally with a restricted number of unknowns (or number of regions in the geometry). Consequently, the objective here is to establish the smallest 3D geometry that is (in terms of number of cells) able to determine the multigroup macroscopic cell averaged cross sections in reflector cells and in fuel cells adjacent to these reflector cells with an acceptable accuracy [18].

4.1. 3D Reference Model with Axial Reflector Cells. Figure 9 illustrates the 3D fuel channel with reflector cells at both ends.

Reflective BCs are applied in the radial direction, and void BCs are applied in the axial direction.

The structure of the high efficiency fuel channel is maintained throughout the reflector cell, but the space normally occupied by the fuel bundle is now completely filled with coolant (or completely voided if the coolant is absent). The local conditions applied in the reflector cells are those found in the inlet and outlet cells, that is, C1 and C14, respectively, since one can assume that there will be no significant variations in temperatures and densities in the reflector cells.

4.2. Extended Simulation Strategy Model. To reduce the size of the 3D geometries, the fuel channel has first been cut into two halves. The first half has been used to study the reflector cell at the inlet and fuel cell C1. The second half has been used to study the reflector cell at the outlet and fuel cell C14.

Figure 17 shows the seven partial 3D fuel channels with axial reflector cells developed in SERPENT for the study of

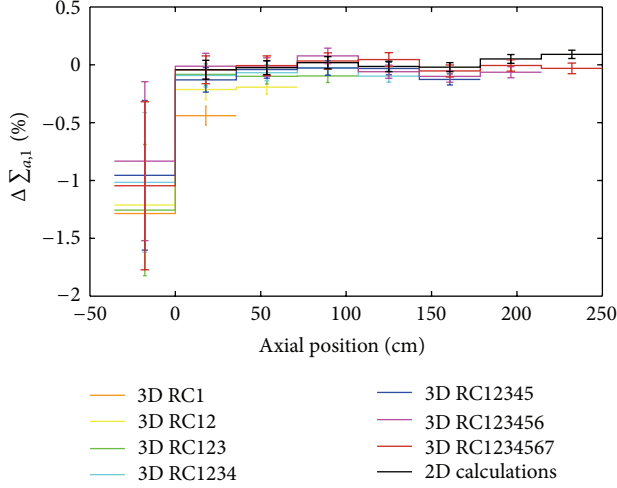


FIGURE 18: Relative differences between absorption cross sections for the fast group.

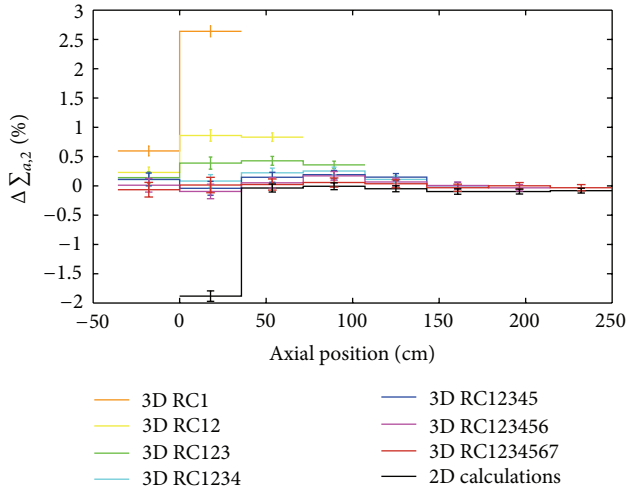


FIGURE 19: Relative differences between absorption cross sections for the thermal group.

the cells at the inlet. To close the geometries, reflective BCs are applied after the last fuel cell (Figure 17 shows the unfolded geometries). The same methodology has been applied for the cells at the outlet.

The accuracy of the partial 3D fuel channels with axial reflector cells has been evaluated by comparing along the fuel channel their multigroup cell averaged cross sections to those obtained from the complete 3D fuel channel with axial reflector cells (Figure 9). As done previously, the absorption, up and down scattering, and fission neutron production cross sections have been studied. The cross sections have been condensed to the same energy groups structure and homogenized over each cell. The accuracy of the independent 2D infinite lattice cell calculations has also been evaluated in the same way.

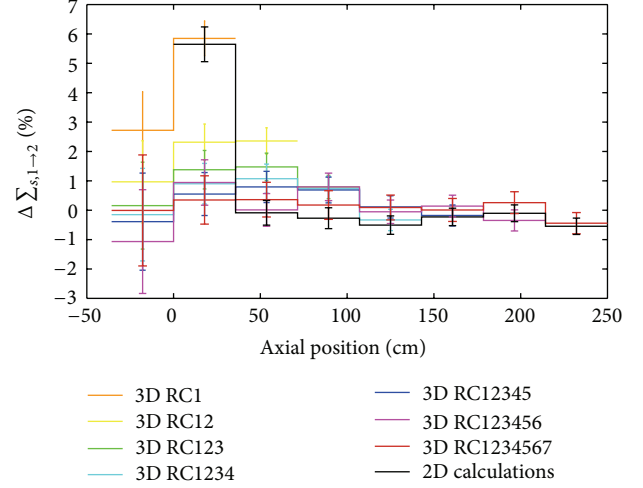


FIGURE 20: Relative differences between down scattering cross sections.

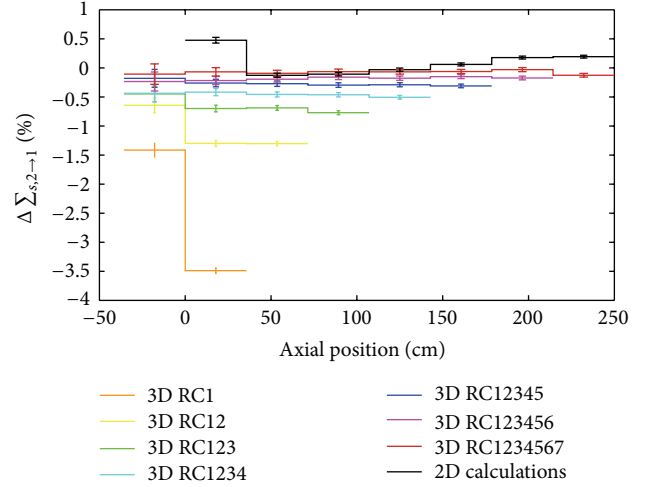


FIGURE 21: Relative differences between up scattering cross sections.

Figures 18, 19, 20, 21, 22, and 23 present the relative differences between the multigroup cell averaged cross sections calculated as follows:

$$\Delta\Sigma_{x,g}(\%) = 100 \times \left(\frac{\Sigma_{x,g}^{\text{Complete}} - \Sigma_{x,g}^{\text{Partial or 2D}}}{\Sigma_{x,g}^{\text{Complete}}} \right), \quad (4)$$

where the Complete superscript refers to the complete 3D fuel channel (Figure 9) and the Partial or 2D refers to one of the partial 3D fuel channels (Figure 17) or to the 2D cells (Figure 4). In each figure, the legend lists the geometries studied. For example, the label “3D RC1” stands for the partial 3D fuel channel containing a reflector cell and the fuel cell C1 (top picture in Figure 17). The label “2D calculations” stands for the independent 2D infinite lattice cell calculations. Note that the reflector cell lies in the negative axial positions.

Figures 18–23 must be analyzed as follows. One must focus on one cell at a time and examine the evolution of the curves in that given cell. The objective here is to find the

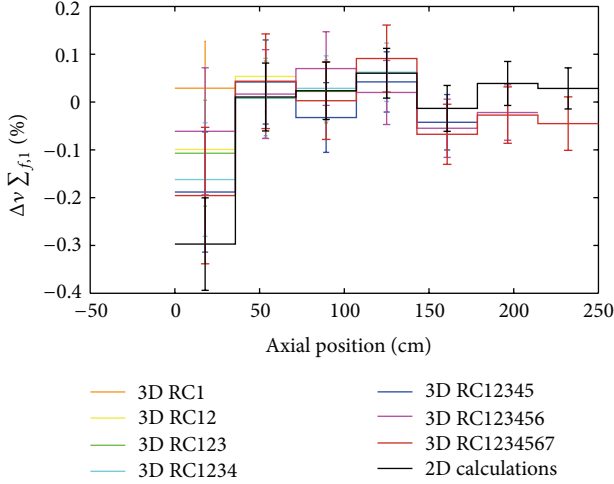


FIGURE 22: Relative differences between fission neutron production cross sections for the fast group.

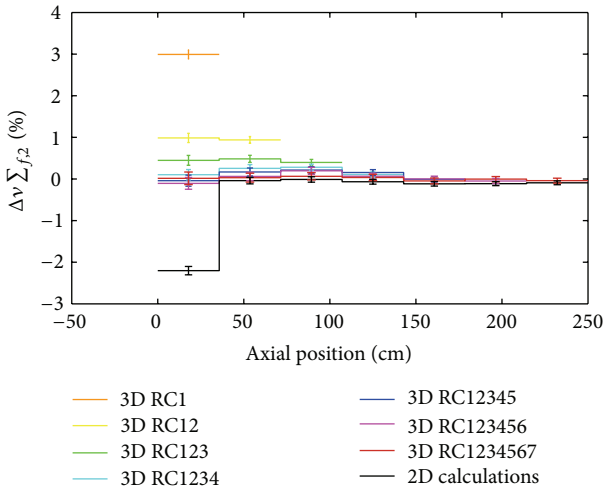


FIGURE 23: Relative differences between fission neutron production cross sections for the thermal group.

appropriate partial 3D fuel channel that reduces (in absolute value) the value of $\Delta\Sigma_{x,g}$ (in the reflector cell and in the fuel cell C1 in particular) to an acceptable level of accuracy considering that the geometry must be as small as possible. Ideally, $\Delta\Sigma_{x,g}$ should be equal to zero.

One can observe that there is no data coming from a 2D calculation in the reflector cell. As mentioned above, this is expected because it is not possible to perform neutron transport calculation without neutrons sources. In addition, it is normal to observe that the partial 3D fuel channels do not show data on all axial positions. For example, the model labeled “RC1” presents only two values located between -35.71 cm and 35.71 cm (for the reflector cell and the fuel cell C1) because the fuel cells C2, C3, C4, C5, C6, and C7 do not exist in this geometry. Also note that for the fission production cross sections, no information is provided for the reflector cell, since it does not contain fissile material.

TABLE 2: Channel multiplication factors and CVRs for models with axial reflector cells.

Model	$k_{\text{eff}}^{\text{cooled}}$	$k_{\text{eff}}^{\text{voided}}$	CVR (mk)
Void axial BCs			
Reference with reflector cells	1.21277 ± 0.00004	1.19960 ± 0.00005	-9.05 ± 0.06
Extended strategy	1.21293	1.19980	-9.02

In general, $\Delta\Sigma_{x,g}$ approaches zero when more fuel cells are added in the partial 3D fuel channel. Also, Figures 18–23 highlight the fact that the independent 2D infinite lattice cell calculations do not provide a good evaluation of the multigroup cell averaged cross sections in the fuel cell C1 located between 0 cm and 35.71 cm. Based on these results, the best compromise between accuracy of the results and simplicity of the 3D geometry consists in selecting the four fuel cells model labeled “RC1234.” The same behavior is also observed at the outlet where only the four last fuel cells are needed.

Following this study, the extended simulation strategy for fuel channels with axial reflector cells is divided into the following three steps.

- (i) Two 3D calculations with SERPENT, one for the channel inlet from a partial 3D fuel channel containing the inlet reflector cell and the four first fuel cells (fourth picture from the top in Figure 17) and the second one for the channel outlet from a partial 3D fuel channel containing the outlet reflector cell and the four last fuel cells in order to generate the multigroup cell averaged cross sections in the two reflector cells and in the fuel cells C1 and C14.
- (ii) Twelve independent 2D infinite lattice cell calculations (Figure 4) with SERPENT in order to generate the multigroup cell averaged cross sections in the fuel cells C2 to C13.
- (iii) Using the cross sections calculated in the two first steps, a single 1D calculation (from a geometry similar to Figure 5 but with a 1D reflector cell at both ends) is performed with DRAGON in order to calculate the global properties of the fuel channel.

4.3. Models Comparison. Table 2 presents a comparison of the multiplication factors and CVRs obtained from the 3D reference model with axial reflector cells (SERPENT 3D) (Figure 9) and the extended simulation strategy model (SERPENT 3D + SERPENT 2D + DRAGON 1D). Here, only the situation with void axial BCs was considered.

By comparing Tables 1 and 2, one can observe that, for void axial BCs, the CVRs obtained from models with axial reflector cells are smaller (in absolute value) than those obtain from models without axial reflector cells. This observation can be explained in part by the fact that the reflector cells reflect some neutrons back in the system, leading therefore to higher multiplication factors.

The extended simulation strategy shows good agreement with the 3D reference model with axial reflector cells.

5. Conclusion

The simulation strategy proposed for the evaluation of the neutronic properties of a Canadian SCWR fuel channel is able to take into account all axial profiles in a single general model. It has been shown, for the cases studied, that a 3D calculation is equivalent to a series of isolated 2D calculations followed by a single 1D calculation. From this fact, most of the calculations can be done very easily. The modeling of the axial reflector still requires 3D calculations. However, the size of these calculations has been reduced considerably.

To conclude, the simulation strategy proposed could reduce the computation time by a factor of about 600. In our case, a 3D Monte Carlo simulation takes approximately 15 hours for one burnup step. For standard deterministic codes, fourteen 2D infinite lattice cell calculations take approximately 1.5 minutes in total, and a 1D calculation takes a few seconds, and this for each burnup step. This deterministic calculation strategy will be investigated in future work.

Acknowledgments

This work was supported in part by the NSERC/NRCan/AECL Generation IV Energy Technologies Program, the Fonds québécois de la recherche sur la nature et les technologies (FQRNT), and the Canadian Nuclear Society (CNS).

References

- [1] "U.S. DOE Nuclear Energy Research Advisory Committee and the Generation IV International Forum, A technology roadmap for Generation IV Nuclear Energy Systems, GenIV International Forum," 2002, <http://www.gen-4.org/Technology/roadmap.htm>.
- [2] D. F. Torgerson, B. A. Shalaby, and S. Pang, "CANDU technology for Generation III+ and IV reactors," *Nuclear Engineering and Design*, vol. 236, no. 14–16, pp. 1565–1572, 2006.
- [3] L. K. H. Leung, "Developing the Canadian SCWR concept for addressing GIF technology goals," in *Proceedings of the 3rd China-Canada Joint Workshop on Supercritical-Water-Cooled Reactors (CCSC '12)*, Shanxi, China, April 2012.
- [4] P. G. Boczar, W. Shen, J. Pencer, B. Hyland, P. S. W. Chan, and R. G. Dworschak, "Reactor physics studies for a pressure tube supercritical water reactor (PT-SCWR)," in *Proceedings of the 2nd Canada-China Joint Workshop on Supercritical Water-Cooled Reactors (CCSC '10)*, Toronto, Ontario, Canada, April 2010.
- [5] J. Shan, W. Chen, B. W. Rhee, and L. K. H. Leung, "Coupled neutronics/thermal-hydraulics analysis of CANDU-SCWR fuel channel," *Annals of Nuclear Energy*, vol. 37, no. 1, pp. 58–65, 2010.
- [6] P. Yang, L. Cao, H. Wu, and C. Wang, "Core design study on CANDU-SCWR with 3D neutronics/thermal-hydraulics coupling," *Nuclear Engineering and Design*, vol. 241, no. 12, pp. 4714–4719, 2011.
- [7] D. Altiparmakov, "New capabilities of the lattice code WIMS-AECL," in *Proceedings of the International Conference on the Physics of Reactors (PHYSOR '08)*, Interlaken, Switzerland, September 2008.
- [8] G. Marleau, R. Roy, and A. Hébert, "A user guide for DRAGON 3.06," Tech. Rep. IGE-174 Rev. 8, Institute of Nuclear Engineering, École Polytechnique de Montréal, Montréal, Québec, Canada, 2009.
- [9] J. Leppänen, *PSG2/SERPENT - A Continuous-Energy Monte Carlo Reactor Physics Burnup Calculation Code*, VTT Technical Research Centre of Finland, Espoo, Finland, 2011.
- [10] C. K. Chow and H. F. Khartabil, "Conceptual fuel channel designs for CANDU-SCWR," *Nuclear Engineering and Technology*, vol. 40, no. 2, pp. 139–146, 2008.
- [11] M. H. McDonald, B. Hyland, H. Hamilton et al., "Pre-conceptual fuel design concepts for the Canadian super critical water-cooled reactor," in *Proceedings of the 5th International Symposium on Supercritical Water-Cooled Reactors (ISSCWR-5)*, Vancouver, British Columbia, Canada, March 2011.
- [12] M. Magill, J. Pencer, R. Pratt, W. Young, G. W. R. Edwards, and B. Hyland, "Thorium fuel cycles in the CANDU supercritical water reactor," in *Proceedings of the 5th International Symposium on Supercritical Water-Cooled Reactors (ISSCWR-5)*, Vancouver, British Columbia, Canada, March 2011.
- [13] W. Shen, "Assessment of the applicability of the traditional neutron-diffusion core-analysis method for the analysis of Super Critical Water Reactor (SCWR)," in *Proceedings of the Advances in Reactor Physics-Linking Research, Industry and Education (PHYSOR '12)*, Knoxville, Tenn, USA, 2012.
- [14] X. Wang and J. Pencer, "Assessment of reactor core simulations using DONJON for a 2-dimensional SCWR Benchmark Core," in *Proceedings of the 20th International Conference on Nuclear Engineering (ICONE-20)*, Anaheim, Calif, USA, July-August 2012.
- [15] G. Harrisson and G. Marleau, "2-D and 3-D evaluation of neutronic properties along a Canadian SCWR fuel channel," in *Proceedings of the 3rd China-Canada Joint Workshop on Supercritical-Water-Cooled Reactors (CCSC '12)*, Shaanxi, China, April 2012.
- [16] M. Varvayanni, P. Savva, and N. Catsaros, "Aspects of cell calculations in deterministic reactor core analysis," *Annals of Nuclear Energy*, vol. 38, no. 2-3, pp. 185–193, 2011.
- [17] E. Fridman and J. Leppänen, "On the use of the Serpent Monte Carlo code for few-group cross section generation," *Annals of Nuclear Energy*, vol. 38, no. 6, pp. 1399–1405, 2011.
- [18] M. Blaise, *Étude de l'interface coeur-réflexeur Application au calcul du réflecteur lourd [Ph.D. thesis]*, Université Paris XI Orsay, Paris, France, 1993.

Research Article

Study of Thorium-Plutonium Fuel for Possible Operating Cycle Extension in PWRs

Klara Insulander Björk,^{1,2} Cheuk Wah Lau,² Henrik Nylén,³ and Urban Sandberg³

¹ Thor Energy AS, Sommerrogaten 13-15, 0255 Oslo, Norway

² Division of Nuclear Engineering, Department of Applied Physics, Chalmers University of Technology, 412 96 Gothenburg, Sweden

³ Ringhals AB, 432 85 Väröbacka, Sweden

Correspondence should be addressed to Klara Insulander Björk; klara.insulander@scatec.no

Received 14 October 2012; Accepted 11 January 2013

Academic Editor: Hangbok Choi

Copyright © 2013 Klara Insulander Björk et al. This is an open access article distributed under the Creative Commons Attribution License, which permits unrestricted use, distribution, and reproduction in any medium, provided the original work is properly cited.

Computer simulations have been carried out to investigate the possibility of extending operating cycle length in the Pressurised Water Reactor Ringhals 3 by the use of thorium-plutonium oxide fuel. The calculations have been carried out using tools and methods that are normally employed for reload design and safety evaluation in Ringhals 3. The 3-batch reload scheme and the power level have been kept unchanged, and a normal uranium oxide fuel assembly designed for a 12-month operating cycle in this reactor is used as a reference. The use of plutonium as the fissile component reduces the worth of control rods and soluble boron, which makes it necessary to modify the control systems. The delayed neutron fraction is low compared with the reference, but simulations and qualitative assessments of relevant transients indicate that the reactor could still be operated safely. Differences in reactivity coefficients are mainly beneficial for the outcome of transient simulations for the thorium based fuel. A 50% extension of the current 12-month operating cycle length should be possible with thorium-plutonium mixed oxide fuel, given an upgrade of the control systems. More detailed simulations have to be carried out for some transients in order to confirm the qualitative reasoning presented.

1. Introduction

The objective of the work described herein is to investigate the possibility of extending operating cycle length in a Pressurized Water Reactor (PWR) by the use of Thorium-Plutonium Mixed Oxide (Th-MOX) fuel.

The general viability of Th-MOX fuel in light water reactors (mainly PWRs) has been confirmed by several recent studies [1–5]. In addition, the neutronic and physical properties of Th-MOX indicate that the fuel is not only viable, but may also improve the economy of a nuclear power plant by allowing for longer operating cycles and hence a higher availability of the reactor. Most importantly, the good material properties [6, 7] of the Thorium-Plutonium Mixed Oxide ceramic indicate that Th-MOX fuel may be capable of sustaining higher burnups than Uranium-Oxide- (UOX-) based fuel types. Secondly, the currently practiced uranium enrichment limit of 5% U-235 does not affect Th-MOX, which

can be loaded with high amounts of plutonium. Finally, the slow change of the multiplication factor with depletion of Th-MOX makes it possible to achieve high burnups without having an excessively high initial multiplication factor [4].

In this paper, we present and discuss the simulation of a standard PWR fuel assembly loaded with Th-MOX fuel and a full Reload Safety Evaluation (RSE) of the Ringhals 3 PWR core when loaded with this fuel assembly. The content of Pu and Burnable Absorbers (BA) in the fuel is adapted for achieving an 18-month cycle, which is an operating cycle extension of 50% compared with the normal cycle length in Ringhals 3. The fuel assembly design is developed using the fuel assembly burnup simulation program CASMO-4E [8], and the RSE is carried out with SIMULATE-3 [9].

The simulated fuel and reactor systems are described in Section 2 and the calculation tools and methods used in this study in Section 3. The results in terms of depletion behaviour

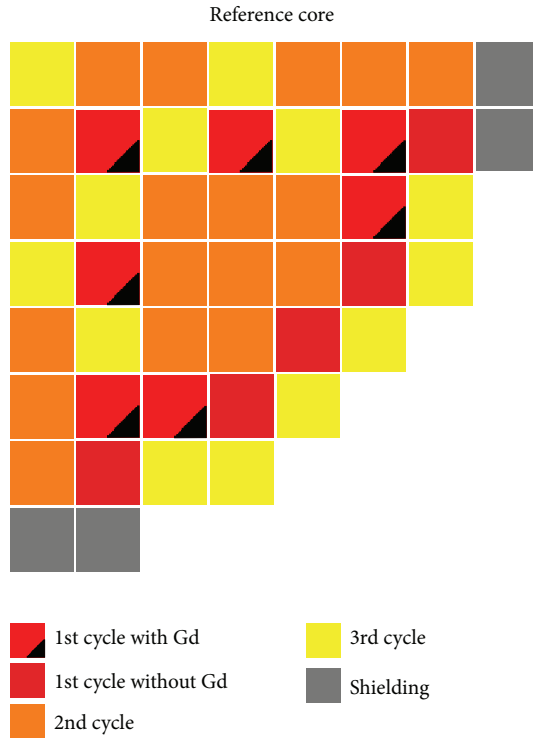


FIGURE 1: The UOX reference core.

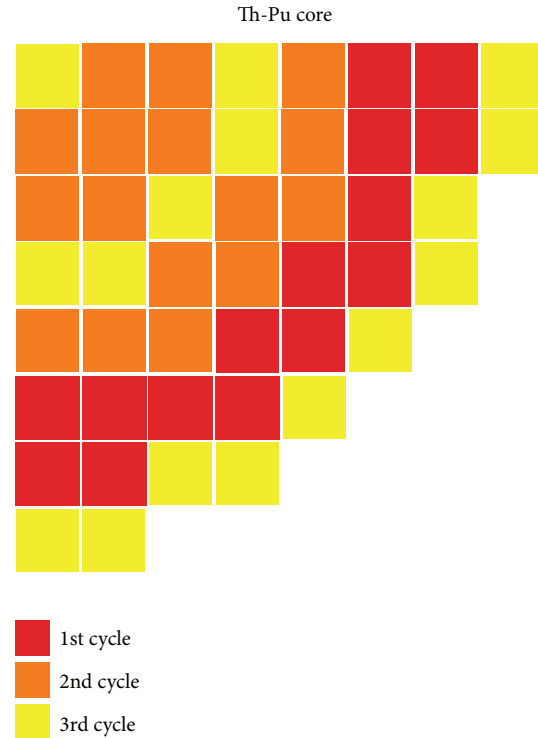


FIGURE 2: The Th-MOX core.

and neutronic safety parameters are presented in Section 4 and conclusions are drawn in Section 5.

2. Description of the Modelled System

2.1. Reactor. The reactor simulated in this study is the Swedish Ringhals 3 reactor, which is a 3135 MW_{th} reactor of Westinghouse design. This reactor operates with a 12-month cycle and a 3-batch reload scheme. In the reference case, which is a typical operation cycle, the Ringhals 3 core is loaded with 28 fuel assemblies containing the BA Gd₂O₃ and 20 fuel assemblies without BA. Such a reload is used as a reference in this work. The core design is shown in Figure 1 and the fuel assemblies will be discussed in more detail in Section 2.2.

The Th-MOX core is designed for an 18-month cycle using a different core layout, designed to reduce the power of the oldest fuel assemblies. Without this change of the layout, the oldest fuel assemblies (having the highest burnup) would run at a power level which would be too high considering the deterioration of the fuel material at high burnup. This core design is shown in Figure 2.

2.2. Fuel Assemblies. The reference fuel is a UOX fuel assembly designed for a standard 12-month cycle in Ringhals 3, which requires an enrichment of 4.4% in most fuel rods. The assembly comprises 264 fuel rods, arranged in a standard 17-by-17 lattice with a central instrumentation thimble and 24 control rod guide tubes. In the assemblies containing Gd₂O₃, this is located in 12 rods. Since the addition of Gd₂O₃ lowers

the thermal conductivity of the fuel, a lower enrichment (2.8%) is used in order to avoid high power in these fuel rods. The reference fuel design with Gd₂O₃ is shown in Figure 3. The reference fuel without BA is identical except that all rods have 4.4% enrichment and no BA. The fuel assembly heavy metal weight is 461 kg.

The Th-MOX fuel design uses the same mechanical structure as the reference fuel, but differs in two important aspects.

Firstly, the uranium oxide fuel is exchanged for a mixture of thorium and plutonium oxides. The Pu isotope vector used in the Th-MOX fuel is 2%²³⁸Pu, 53%²³⁹Pu, 25%²⁴⁰Pu, 15%²⁴¹Pu, and 5%²⁴²Pu. This corresponds to the Pu vector in spent light water reactor fuel burnt to approximately 42 MWd/kgHM, if reprocessed immediately [10].

Secondly, the Integral Fuel Burnable Absorber (IFBA) concept is preferred over the use of Gd₂O₃ as a BA. The reason not to use Gd₂O₃ is that it is normally mixed into the fuel matrix. Since Th-MOX is already a mixed oxide, using Gd₂O₃ would require a ternary mixture of ThO₂, PuO₂, and Gd₂O₃ which is very difficult to fabricate with good homogeneity. The IFBA concept entails a thin layer of zirconium boride applied to the surface of the fuel pellets [11].

In order to achieve an even power profile within the fuel assembly, three different levels of Pu content are used. The rods with the highest Pu content contain 13.7% Pu, the lowest 9% Pu, and the rest 11.7% Pu. The fuel assembly design is shown in Figure 4.

The mixture of ThO₂ and PuO₂ has a slightly lower density than UO₂ due to the lower mass number of Th. Given

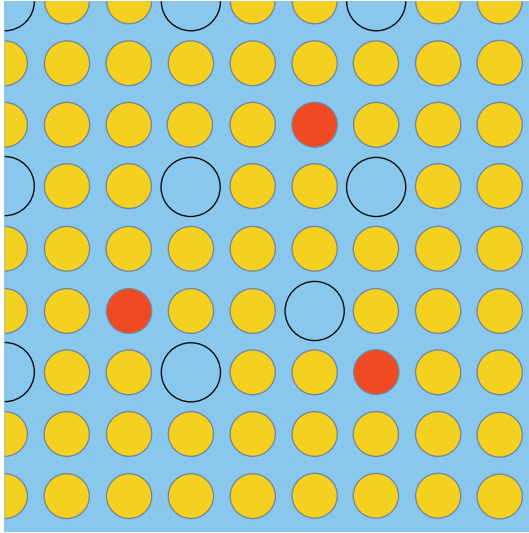


FIGURE 3: The BA-containing UOX reference fuel assembly design (a quarter of the fuel assembly). Yellow rods consist of 4.4% enriched uranium; red rods consist of 2.8% enriched uranium and 6% Gd_2O_3 . The non-BA-containing reference fuel design is identical except that all rods are of the former (yellow) type.

that the same mechanical structure is used, this results in a slightly lower assembly heavy metal weight; 431 kg, assuming the same porosity.

3. Method

3.1. Simulation Tools. The fuel assembly simulations are carried out in two dimensions, using the fuel assembly burnup simulation program CASMO-4E [8] together with the microscopic cross-section library JEF2.2. CASMO-4E generates cross-section data for the subsequent use in core simulations.

The core simulations are carried out in three dimensions, using SIMULATE-3 [9] and the macroscopic cross-section libraries generated by CASMO-4E and converted by the linking program CMS-link (Studsvik Scandpower's Core Management System (CMS) linking program [12]). SIMULATE-3 is a two-group steady-state nodal code. All the used softwares are supplied by Studsvik Scandpower, Inc.

3.2. Reload Safety Evaluation. The Swedish Radiation Safety Authority requires that an RSE is performed for every core reload, in order to ensure that the reactor can be operated safely with the new core design during the whole cycle. The reload safety evaluation employed at Ringhals 3 is based on the Westinghouse reload methodology which is licensed by the United States Nuclear Regulatory Commission (USNRC) as described in the topical report WCAP-9272 [13]. This is a bounding analysis approach, and it is employed in this work in the same way as is usually done when a new reload is designed for Ringhals 3.

In the RSE, a number of key parameters are calculated. These are effective delayed neutron fraction β_{eff} , boron worth,

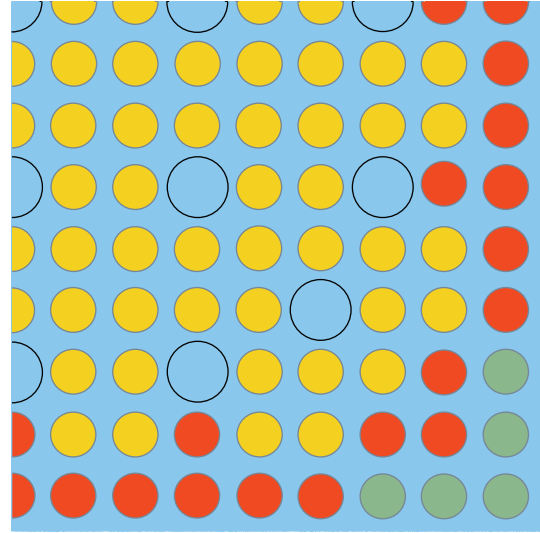


FIGURE 4: The Th-MOX fuel assembly design (a quarter of the fuel assembly). Yellow rods contain 13.7%, red rods 11.7%, and grey rods 9.0% Pu (weight percent of heavy metal content). The zirconium boride layer is too thin to be visible in the figure.

Shut Down Margins (SDM), Moderator Density Coefficient (MDC), Moderator Temperature Coefficient (MTC), Isothermal Temperature Coefficient (ITC), Doppler Temperature Coefficient (DTC), and Doppler Power Coefficient (DPC). For each of these (except for the MTC, in the case of Ringhals 3), there are a lower and/or upper safety limits, specific to the reactor for which the calculations are done. These safety limits take into account the uncertainty in the calculations.

The calculated values of key parameters are then used for checking whether safety conditions are fulfilled for a large number of transients; that is, whether there is departure from nucleate boiling and whether the burnup-dependent limit on the linear heat generation rate (LHGR) is contained.

4. Results

4.1. Depletion Behaviour. The infinite multiplication factor k_{∞} for the different fuel assemblies is shown in Figure 5. One clear difference between the Th-MOX and the reference fuel is that the reactivity decreases more slowly in the Th-MOX case. Another difference is seen during the first cycle (approximately the first 1/3 of the curves), and that is the difference in the rate with which the BA burns out. Whereas the Gd_2O_3 burns out fairly rapidly and almost linearly, the effect of the IFBA in the Th-MOX assembly lingers for a longer time and decays rather exponentially. In both cases, the objective of avoiding an exceedingly high k_{∞} at the Beginning Of Life (BOL) is fulfilled. If BA would not be used, the much higher reactivity of the fresh fuel assemblies compared with the once or twice burnt would cause locally high-power levels where the fresh fuel is located, which would limit the power at which the reactor can be safely operated.

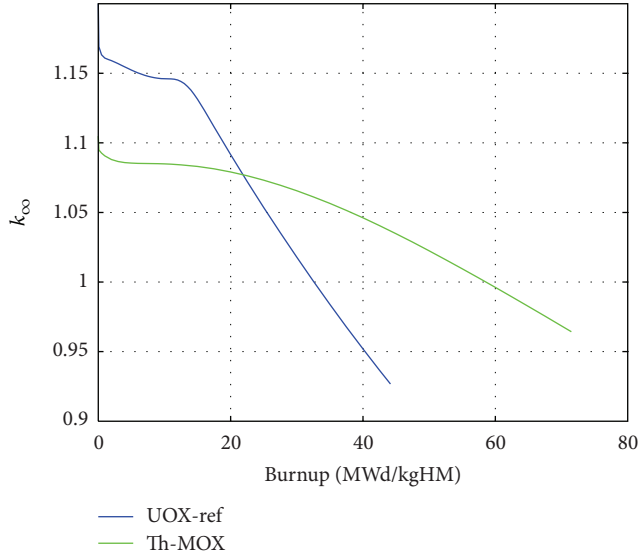


FIGURE 5: Infinite multiplication factor dependence on burnup.

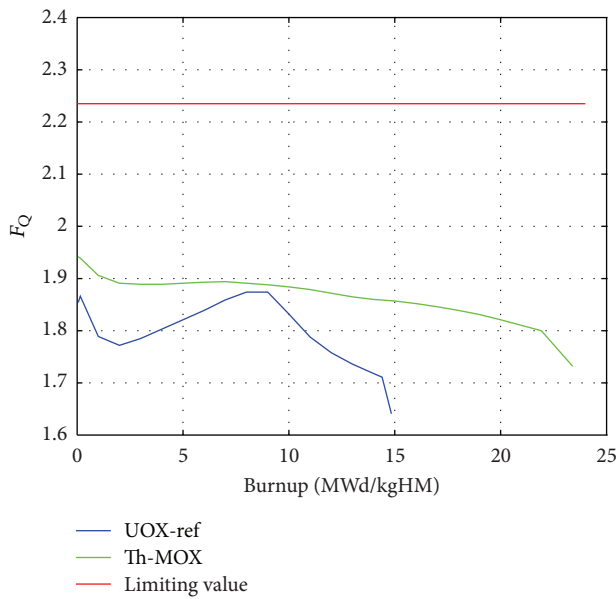


FIGURE 6: F_Q , that is, local power relative to core average power as a function of burnup.

Also, a higher concentration of soluble boron would be needed to keep the reactor critical.

In order to reach the desired operating time of three 18-month cycles, the assembly average discharge burnup is increased to 78 MWd/kgHM in the Th-MOX case. It should be noted that this discharge burnup is considerably higher than the currently employed limits on UOX fuel. There are several reasons to believe that this burnup will in fact be achievable. Firstly, although the burnup is high, the residence time within the reactor is only 4.5 years. Whereas this residence time is quite long for PWR fuel, it is a normal residence time for boiling water reactor fuel, so fuel aging factors related to the residence time should be within acceptable range.

Secondly, it is expected that thorium-based fuel will have a capacity to keep its thermal and mechanical robustness to high burnup, for several reasons. One is that the thermal conductivity of the Thorium-Plutonium Mixed Oxide ceramic is higher than that of a corresponding uranium oxide ceramic, up to about 14% Pu [6]. This means that the fuel temperature will remain lower in the pellet, causing less swelling, less pellet-cladding mechanical interaction, and a larger margin to fuel melting. Another reason is that fission gases have a lower mobility in the thorium oxide matrix, which results in a lower fission gas release. The higher thermal conductivity also has a beneficial effect on the fission gas release, since the lower fuel temperature makes the fission gases diffuse more slowly.

Deterioration of the cladding integrity may constitute an obstacle to safe operation at high burnups. This is partially mitigated by the fact that the residence time is not extremely long, and there are documented cases of cladding operating well up to such burnups [14]. There are also interesting initiatives towards combining thorium fuel with silicon carbide cladding for realizing much higher burnups than the current standard [15].

4.2. Power Distribution. As mentioned, the development of the infinite multiplication factor with burnup is important for maintaining an even power distribution within the core. The parameter F_Q denotes the maximum local fuel rod linear power density divided by the average fuel rod linear power density.

F_Q is calculated for equilibrium xenon at Beginning of Cycle (BOC), Middle Of Cycle (MOC), End Of Gadolinium (EOG), and at End Of Full Power (EOFP). The highest F_Q in the core, for normal operating conditions, is plotted in Figure 6 as a function of burnup. As can be seen, F_Q is higher for the Th-MOX fuel than for the reference fuel but stays comfortably below the limiting value.

Another measure of the evenness of the power distribution is $F_{\Delta H}$, which for each fuel rod denotes the integral rod power of that fuel rod relative to the average integral rod power. This parameter is calculated similarly to F_Q and the highest value, corresponding to the hottest rod, is plotted in Figure 7. In this case, the value for Th-MOX is similar and even a bit lower than that for the reference fuel, and also below the limiting value.

The limits are set by the material properties of the fuel, and the same limits are employed for the Th-MOX core and the reference core. The limits displayed in these plots are the least restrictive ones, which are applicable for fresh fuel. For older fuel, lower limits are applied. A more detailed analysis shows that some of the older fuel assemblies break the applicable age-dependent limits in the Th-MOX case. However, as discussed in Section 4.1, there are reasons to believe that Th-MOX fuel will have better material properties than UOX fuel also at high burnup.

Keeping the power distribution even has two main purposes, one being economical utilization of the fuel and the other one being to allow operation at high power without reaching departure from nucleate boiling anywhere

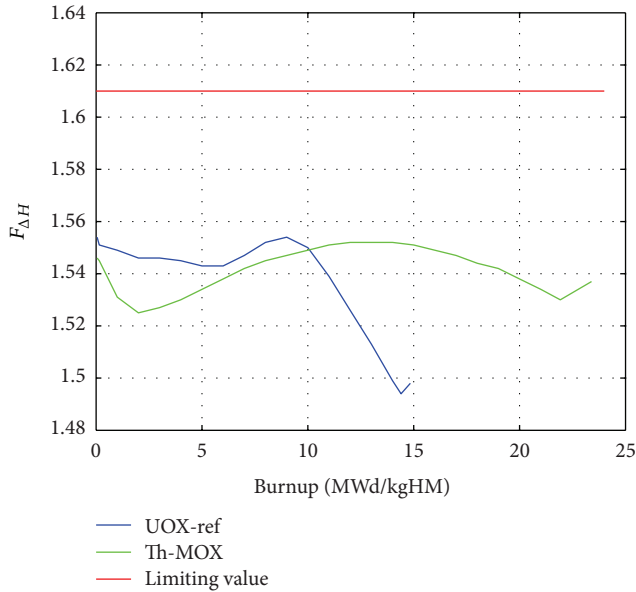


FIGURE 7: $F_{\Delta H}$, that is, maximum rod power relative to core average rod power as a function of burnup.

in the core. A measure of how large the margin is to departure from nucleate boiling is the Departure from Nucleate Boiling Ratio (DNBR). This is the ratio between the heat flux which would cause departure from nucleate boiling and the actual local heat flux at a fuel rod surface and should thus be kept above unity, and preferably above a certain threshold to provide margin to departure from nucleate boiling in the case of transient events. The threshold employed in Ringhals 3 is 1.36. The reference fuel is very slightly above the limit, whereas the Th-MOX fuel has a larger margin with a cycle minimum DNBR of 1.43. This is a very positive feature of the core, which provides extra margin in a large number of transients.

4.3. Control Systems. The boron worth is calculated for boron concentrations between 0 and 2500 ppm and for the whole power range, from Hot Zero Power (HWP) with no xenon to Hot Full Power (HFP) with xenon equilibrium. Usually natural boron is used for reactivity control, that is, with 19.8% ^{10}B , which is the isotope having the largest thermal neutron capture cross section. Using this isotopic composition, the boron worth is significantly reduced (closer to zero) in the Th-MOX case. This is expected, since the presence of large absorption resonances in several of the Pu isotopes causes the flux to decrease at the thermal energies where ^{10}B has its highest absorption cross section. In order to cope with this problem, the Th-MOX cycle is simulated with boron enriched to 60% in ^{10}B . As can be seen in Table 1, this gives a boron worth for the Th-MOX core similar to that in the reference UOX core, and within the safety limits.

The flatter slope of k_{∞} , which allows for a lower initial k_{∞} of the Th-MOX assembly, lowers the boron concentration needed for keeping k_{eff} equal to unity. The use of enriched

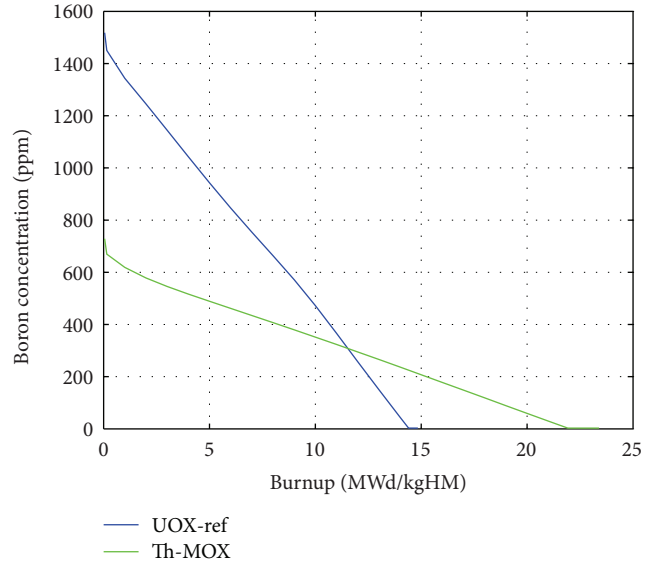


FIGURE 8: Boron concentration as a function of burnup.

TABLE 1: Control rod and boron worth, their limits, and the calculated values for the Th-MOX and the reference UOX core. For the Th-MOX core, the boron used for reactivity control is enriched to 60% in ^{10}B instead of the usual 19.8% (natural isotopic composition), and stronger control rods are used.

Parameter	Limit	UOX-ref	Th-MOX
Min boron worth [pcm/ppm]	-15	-8.3	-8.7
Max boron worth [pcm/ppm]	-5	-6.2	-5.2
Min SDM [pcm]	2000	2559	3895
Max rod worth [pcm]	—	6505	7808

boron enhances this effect significantly, and the result is shown in Figure 8.

The same mechanisms that cause the lower boron worth for Th-MOX fuel also cause a significant lowering of the control rod worth. In order to adhere to the limits on SDM, the normal control rods, containing a silver-indium-cadmium alloy as the neutron absorber, had to be exchanged for stronger ones containing B_4C . This shortens the lifetime of the control rods but improves the shutdown margin significantly. Furthermore, the four extra openings available in the Ringhals 3 pressure vessel have been utilized for inserting four extra control rods in addition to the 48 which are normally used. The values shown in Table 1 show that the minimum SDM with the B_4C control rods is well above the lower limit.

Also the maximum control rod worth is shown in Table 1 and proves to be higher than the reference. This gives a higher value of the Ejected Rod Worth (ERW) in case of a Rod Ejection Accident (REA) when this transient is evaluated at HWP. However, when evaluated at HFP, the ERW is smaller than the reference, as discussed in Section 4.5. This is most likely due to the strong DTC, discussed in Section 4.4. The same tendency can be seen for the Differential Rod Worth

TABLE 2: Key safety parameters, their limits, and the calculated values for the Th-MOX and the reference UOX core. No limit is specified for moderator temperature coefficient in Ringhals 3.

Parameter	Limit	UOX-ref	Th-MOX
Max MDC [($\Delta k/k$)/(g/cm ³)]	0.50	0.41	0.34
Max MTC [pcm/K]	—	-1.3	-4.0
Max ITC [pcm/K]	0.0	-4.4	-7.9
Min DTC [pcm/K]	-4.00	-3.72	-4.53
Max DTC [pcm/K]	-1.70	-2.10	-2.36
Min DPC [pcm/% power]	-21.0	-15.5	-21.5
Max DPC [pcm/% power]	-6.5	-9.8	-14.6
Min β_{eff} EOC [pcm]	430	502	350
Max β_{eff} BOC [pcm]	720	647	370

(DRW) in case of Rod Withdrawal At Power (RWAP), also discussed in Section 4.5.

4.4. Key Safety Parameters. The MDC quantifies the reactivity change caused by a change in moderator density when all other parameters, such as core power, moderator flow, and fuel temperature, are kept constant. The highest and hence most limiting MDC occurs at End Of Cycle (EOC), HFP, All control Rods Inserted (ARI), a boron concentration of 0 ppm, and the highest average moderator temperature, 305.3°C. This is clearly not a set of authentic operating parameters; for example, the core is never operated at HFP with ARI, but it guarantees that the calculated value of MDC is conservative. As can be seen in Table 2 the MDC of the Th-MOX core is smaller than that of the reference core and is well within the safety limits. As will be discussed below, this small value of the MDC is beneficial in many transient scenarios. Many transients involve a cooling of the core, which leads to an increase of the moderator density. The small positive MDC in the Th-MOX core means that the associated reactivity increase is comparatively small.

A high MDC corresponds to a low MTC and vice versa, so the highest MTC occurs at the operating conditions corresponding to the lowest MDC, which are BOC, HZP, All control Rods Out (ARO), no xenon, and critical boron concentration. The MTC is the ratio between the reactivity change caused by a change in moderator temperature, divided by the magnitude of that temperature change. For Ringhals 3, a limit is defined for the ITC instead of the MTC although the MTC is used in many transient simulations and is thus of great interest. The MTC at BOC for Th-MOX fuel is significantly lower than that of the reference, providing a larger margin to becoming positive. Later in the cycle, however, the MTC of the Th-MOX fuelled core is higher than that of the reference core (-75 pcm/K at EOC to be compared with -89 pcm/K for the reference). This means, once again, that many transients are handled in a better way, since the reactivity increase related to a temperature decrease is smaller for Th-MOX fuel than for the reference UOX fuel.

The ITC corresponds to the change in reactivity caused by a simultaneous increase of the temperature of all present

materials while all other parameters are kept constant. The limiting ITC occurs at BOC, HZP, no xenon, and maximum samarium. The ITC for both the Th-MOX and the reference core is well within the safety limits, the ITC for the Th-MOX core being significantly larger in amplitude than that of the reference core.

The MDC, MTC, and ITC all show the same tendency of larger amplitudes for the Th-MOX fuel than for the reference. This is primarily due to the two competing effects of a moderator density increase (associated with a temperature decrease in the MTC and ITC cases). An increase in the moderator density causes an increase in the parasitic neutron absorption by the moderator. This effect is independent on fuel type. However, the density increase also improves the moderation which causes a thermalization of the neutron spectrum. This in turn increases the macroscopic fission cross section to an extent which depends on the specific energy dependence of the microscopic fission cross sections of the fissile nuclei present in the fuel. In the Th-MOX fuel, the dominating fissile isotopes are ²³⁹Pu and ²⁴¹Pu, which have large peaks in their microscopic fission cross sections at about 0.3 eV. The main fissile isotope in the reference UOX fuel is ²³⁵U, which has a smaller peak at 0.3 eV. Pu bearing fuels thus benefit more than UOX fuel from the thermalization of the neutron spectrum caused by a density increase.

The DTC indicates the reactivity response caused by a change in fuel temperature only, due to the Doppler broadening of the absorption resonances of the fuel material. This parameter varies quite irregularly with power and burnup, so it is calculated for several different sets of operating conditions and a minimum and maximum value is sought. Due to the presence of several nuclides in the Th-MOX fuel, the DTC is lower (larger in amplitude, negative) in the Th-MOX core than in the reference UOX core, below the lower safety limit. When the result is outside the safety limits, a closer investigation must be made of the transient simulations where the minimum value of the DTC is used. These are Feed Water Malfunction (FWM), Steam Line Break (SLB), at HFP and HZP, Feed Line Break (FLB), Inadvertent Safety Injection (ISI) and the previously mentioned REA and RWAP transients. These are the same transient simulations that use the minimum value of β_{eff} and will be discussed in the following section.

A closely related parameter is the DPC. It is defined as the reactivity change due to a change in core power, which is related to a corresponding change in fuel and cladding temperatures while the moderator temperature is fixed. The physical principle behind the DPC is thus the same as for the DTC. The DPC is also calculated at a large number of burnup and power levels. For illustration, the DPC at 100% power is listed in Table 2, since most transients start at this power level. As can be seen, the DPC is slightly below the lower safety limit in the Th-MOX fuelled core. The transients where the minimum DPC is used are the following: Loss Of Normal Feedwater/Offsite Power (LONF/LOOP), Partial/Complete Loss of Flow (PLOF/CLOF), Locked Rotor (LR), and Steam Generator Tube Rupture (SGTR) and also some of the same transients that use the minimum DTC: FLB, RWAP, and ISI. Also these transients will be discussed in Section 4.5.

TABLE 3: Calculated safety parameters for the representative transients SLB, REA, and RWAP. For REA, the parameters and limits are for EOC conditions. For SLB and RWAP, the same limits are employed throughout the cycle and the parameters which are listed for the moment in the cycle where they are closest to these limits.

Parameter	Limit	UOX-ref	Th-MOX
SLB at HZP, limiting moment			
Min DNBR [-]	2.93	4.56	5.37
SLB at HFP, limiting moment			
Min DNBR [-]	1.36	1.86	1.93
Max LHGR [W/cm]	545	426	440
REA at HZP, EOC			
Max ERW [\$]	2.55	0.99	1.12
Max F_Q [-]	59.2	15.3	9.48
REA at HFP, EOC			
Max ERW [\$]	0.30	0.056	0.047
Max F_Q [-]	5.75	2.183	2.079
RWAP at HFP, limiting moment			
Max DRW [pcm/cm]	50	11.95	10.88

The effective delayed neutron fraction β_{eff} is calculated at BOC and EOC for HZP, ARO, no xenon, and maximum samarium. β_{eff} is strongly affected by the fissioning isotope. The numbers in Table 2 mainly reflect the fact that the delayed neutron fraction is considerably lower (less than half) in ^{239}Pu and ^{233}U compared with ^{235}U , which leads to a β_{eff} below the lower safety limit. This indicates that the Th-MOX-core will have a smaller margin to prompt criticality compared with the reference. As mentioned, the minimum value of β_{eff} is used in the same transients as the minimum DTC: FWM, SLB at HZP and HFP, FLB, RWAP, ISI, and REA. These transients are discussed below.

4.5. Transient Simulations. A large number of transients have previously been simulated in large detail for the accepted values of the safety parameters, that is, for the values between the upper and lower limits shown in Table 2. As long as the key parameters fall within the safety limits, these general simulations are applicable and the outcome of the transient is known to be acceptable. When any of the key parameters discussed above falls outside the safety limits, the affected transients must be checked in order to determine whether the outcome is acceptable. As noted above, β_{eff} , DPC, and DTC fall outside these safety limits for Th-MOX fuel, which means that the transient simulations which have been carried out for Ringhals 3 have not been carried out for the calculated values for these parameters. A discussion of the affected transients follows, indicating why they are likely to be acceptable even though the simulation results are not exactly applicable. Some representative simulation results are listed in Table 3, showing that the margins are large in all cases, and in many cases larger for Th-MOX than for the reference fuel.

All of the transients where the minimum value of β_{eff} is used, except for REA, are rather slow transients; that is,

they happen over a time scale of a few seconds. Within this time frame, there is time for the comparatively slow feedback process provided by the MTC and the MDC to contribute.

In the cases of FWM, SLB, and FLB, the moderator temperature sinks and the density increases. The generally weaker reactivity feedback provided by the higher MTC and lower MDC in the Th-MOX case makes the consequent reactivity increase smaller compared with the reference case, which causes the Th-MOX core to behave well in these transients despite the lower β_{eff} . DNBR and in the HFP case also LHGR are checked and the calculated values for SLB are listed in Table 3. As previously mentioned, the margins to the limiting values are seen to be large. There are small differences between Th-MOX and the reference, which depend partly on the fuel type and partly on the core design in each case.

An ISI involves an increased flow of borated water to the core. This transient has large margins and the power never increases above 100%, neither for the Th-MOX core nor the reference core, so this transient does not imply any safety concerns.

For the REA transient, the minimum value of β_{eff} is of larger importance, since the transient is fast. However, the results of the analysis show that all investigated parameters (the maximum ejected rod worth and F_Q) were within the employed limits with good margins throughout the transient. The reason for this is that the large negative DPC and DTC of the Th-MOX core provide strong and rapid negative reactivity feedback. In the HFP case, where the fuel temperature is high, the ERW is even lower for the Th-MOX fuel than for the reference. Given the large margins there is good reason to believe that a Th-MOX-fuelled core would cope well with this transient even though the actual value of β_{eff} is smaller than the one used in the simulations.

RWAP is similar to REA but happens more slowly, so the large negative DPC should make also this transient acceptable. The listed value of the maximum differential rod worth for the Th-MOX case, showing an even larger margin to the limit than the reference, strengthens this assumption.

As mentioned above, the transients in which the minimum DPC plays a role also involve the value of β_{eff} , but the maximum value of β_{eff} rather than the minimum value discussed above. The main concern in these cases is the reactivity increase after a SCRAM caused by the low DPC. However, the strong (and added) control rods provide an extra reactivity margin during and after a SCRAM, which makes it very likely that also these transients will turn out well. Also, the small value of the maximum β_{eff} makes the power decrease at SCRAM come faster than in the reference case, which leaves a smaller decay power that needs to be cooled off.

5. Conclusions

The simulations, which have been carried out according to the same routines which are normally employed when designing a new reload, do not show any fundamental obstacles to loading the Ringhals 3 core with Th-MOX fuel with maintained safety margins in normal operation and transient scenarios. However, the condition is that the control

systems are upgraded: Boron enriched to 60% in ^{10}B must be used for reactivity control, and stronger control rods than the current ones must be used for shutdown. In our simulations, control rods with B_4C are used, which fulfil the safety conditions. In addition, it might be necessary to utilize the four currently unused control rod openings for inserting four additional control rods.

Three kinetic parameters, namely, the minimum Doppler power, temperature coefficients, and the minimum effective delayed neutron fraction β_{eff} , have values outside the current safety limits. However, differences in the values of the reactivity coefficients along with the extra margins at SCRAM provided by the use of stronger control rods make it possible to argue that the Th-MOX-fuelled core will behave acceptably also in transients where these parameters are of importance.

What remains to be done is to carry out the transient simulations in detail, using the exact calculated values of the key parameters for Th-MOX fuel. This is a major undertaking, which does not only require a large amount of computing capacity and modelling work, but also that temperature and power limits specific to Th-MOX fuel are determined experimentally. These parameters are assessed in an upcoming experiment which will be carried out in the Halden research reactor [16]. This experiment also aims to experimentally confirm the claims made about Th-MOX fuel being able to withstand higher burnup than UOX fuel while maintaining acceptable thermal and mechanical robustness.

Ringhals 3 is a typical PWR, which started commercial power production as early as 1981. Hence, it has no features which would make it particularly suited for using Th-MOX fuel. Thus, our conclusion, based on this limited set of simulations, is that PWRs in general can be loaded with Th-MOX fuel, given that the control systems are strong enough and that the properties of the Th-MOX fuel material become experimentally determined.

Acknowledgments

The authors would like to thank Ringhals AB for the scientific and technical support and the Norwegian Research Council, Vattenfall AB, Oskarshamn Kraftgrupp AB, and the Swedish Centre for Nuclear Technology for the financial support. The support from the Norwegian Research Council was provided through the industrial Ph.D. program.

References

- [1] H. R. Trelleue, C. G. Bathke, and P. Sadasivan, "Neutronics and material attractiveness for PWR thorium systems using monte carlo techniques," *Progress in Nuclear Energy*, vol. 53, no. 6, pp. 698–707, 2011.
- [2] E. Fridman and S. Kliem, "Pu recycling in a full Th-MOX PWR core—part I: steady state analysis," *Nuclear Engineering and Design*, vol. 241, no. 1, pp. 193–202, 2011.
- [3] H. Tsige-Tamirat, "Neutronics assessment of the use of thorium fuels in current pressurized water reactors," *Progress in Nuclear Energy*, vol. 53, no. 6, pp. 717–721, 2011.
- [4] K. Insulander Björk, V. Fhager, and C. Demazière, "Comparison of thorium-based fuels with different fissile components in existing boiling water reactors," *Progress in Nuclear Energy*, vol. 53, no. 6, pp. 618–625, 2011.
- [5] M. Todosow and G. Raitses, "Thorium based fuel cycle options for PWRs," in *Proceedings of the International Congress on Advances in Nuclear Power Plants (ICAPP '10)*, pp. 1888–1897, San Diego, Calif, USA, June 2010.
- [6] C. Cozzo, D. Staicu, J. Somers, A. Fernandez, and R. Konings, "Thermal diffusivity and conductivity of thorium-plutonium mixed oxides," *Journal of Nuclear Materials*, vol. 416, no. 1-2, pp. 135–141, 2011.
- [7] M. Karam, F. Dimayuga, and J. Montin, "Fission gas release of (Th,Pu) O_2 CANDU fuel," Tech. Rep. CW-124950-CONF-002, Atomic Energy of Canada Limited, 2008.
- [8] J. Rhodes, D. Lee, and K. Smith, *CASMO-4E: Extended Capability CASMO-4—User's Manual*, Studsvik Scandpower, 2009.
- [9] D. W. Dean, *SIMULATE-3 Advanced Three-Dimensional Two-Group Reactor Analysis Code*, Studsvik Scandpower, 2007.
- [10] "Plutonium," World Nuclear Association, 2009, <http://www.world-nuclear.org/info/inf15.html>.
- [11] A. Biancheria and R. J. Allio, "Nuclear fuel elements," US patent 3.427.111, 1969.
- [12] T. Bahadir, *CMS-LINK User's Manual*, Studsvik Scandpower, 1999.
- [13] "Westinghouse reload evaluation methodology," Tech. Rep. WCAP-9272, US Nuclear Regulatory Commission, 1978.
- [14] G. Ledergerber, S. Valizadeh, J. Wright et al., "Fuel performance beyond design—exploring the limits," in *Proceedings of the LWR Fuel Performance Meeting/Top Fuel/WRFPM*, pp. 513–524, Orlando, Fla, USA, September 2010.
- [15] E. Shwageraus and H. Feinroth, "Potential of silicon carbide cladding to extend burnup of Pu-Thmixed oxide fuel," *Transactions of the American Nuclear Society*, vol. 104, pp. 658–660, 2011.
- [16] J. F. Kelly and V. Fhager, "Designing a thorium fuel irradiation experiment," in *Advanced Fuel Pellet Materials and Fuel Rod Design for Water Cooled Reactors*, no. TECDOC 1654, International Atomic Energy Agency, 2010.

Research Article

Economic Evaluation on the MOX Fuel in the Closed Fuel Cycle

Youqi Zheng, Hongchun Wu, Liangzhi Cao, and Shizhuang Jia

School of Nuclear Science and Technology, Xi'an Jiaotong University, Xi'an, Shaanxi 710049, China

Correspondence should be addressed to Youqi Zheng, yqzheng@mail.xjtu.edu.cn

Received 13 September 2012; Accepted 11 December 2012

Academic Editor: Hangbok Choi

Copyright © 2012 Youqi Zheng et al. This is an open access article distributed under the Creative Commons Attribution License, which permits unrestricted use, distribution, and reproduction in any medium, provided the original work is properly cited.

The mixed oxide (MOX) fuel is one of the most important fuels for the advanced reactors in the future. It is flexible to be applied either in the thermal reactor like pressurized water reactor (PWR) or in the fast reactor (FR). This paper compares the two approaches from the view of fuel cost. Two features are involved. (1) The cost of electricity (COE) is investigated based on the simulation of realistic operation of a practical PWR power plant and a typical fast breeder reactor design. (2) A new economic analysis model is established, considering the discount rate and the revenue of the reprocessed plutonium besides the traditional costs in the processes of fuel cycle. The sensitivity of COE to the changing parameters is also analyzed. The results show that, in the closed fuel cycle, the fuel cost of applying MOX fuels in the FBR is about 25% lower than that in the PWR at the current operating and fuel cycle level.

1. Introduction

The closed fuel cycle becomes more and more attractive in the fast development of nuclear industry. Many countries have executed or decided to execute such strategy. Especially in China, the nuclear energy expanded rapidly in the past several years. In the future, it is pointed that the nuclear power installation will be over 75 GWe by 2020. Huge amount of natural uranium is required. Large pressure is withstood for the low efficiency of current resources utilization. The closed fuel cycle strategy becomes the necessary choice.

The fabrication, application, and reprocessing of mixed oxide (MOX) fuel is one of the key technologies in the closed fuel cycle. By using the reprocessed plutonium, the utilization efficiency of uranium, which is defined as the mass of uranium consumed duo to per kilowatt hour electricity production, is significantly increased. The previous studies have shown that the utilizing of MOX fuel in the thermal reactors can increase the utilization efficiency by 20%–30% [1]. If it is applied in the fast reactors (FRs), the efficiency can be increased by 20 times [2]. From 1996, the European union (EU) countries have used over 104 tons of plutonium in the thermal reactors and saved about 10% uranium [3]. Up to now, several fast reactors have

been loaded with the MOX fuel and proved to be feasible [4].

In China, the closed fuel cycle strategy and the reusing of the recycled plutonium have been determined by the government. However, the way to reuse the plutonium is still need to be considered further, especially for the investor of nuclear power plant. The cost must be considered seriously. It sometimes dominates the decision. For the nuclear power plant, the MOX fuel can be used in both thermal and fast reactors. Therefore, it is useful to analyze the composition of cost while using the MOX fuel in different reactors and make the comparisons to suggest a better decision from the view of economics besides the technologies, and so forth.

The economic analysis on the fuel cycle has been paid attention to since years ago. In 1991, the Westinghouse applied the minimum revenue requirement method to analysis the economics of open and closed fuel cycles [5]. Owen and Omberg compared the economics of pressurized water reactor (PWR) and FR. They pointed out that the construction cost and fuel cost are the two main parts [6]. In 2003, Bunn and Fetter studied the economics of open and closed fuel cycles considering the MOX fuel, in which the reliability of economic parameters is specially evaluated [7].

In this study, the fuel costs of using the MOX fuels in PWR and FBR are investigated, considering the current

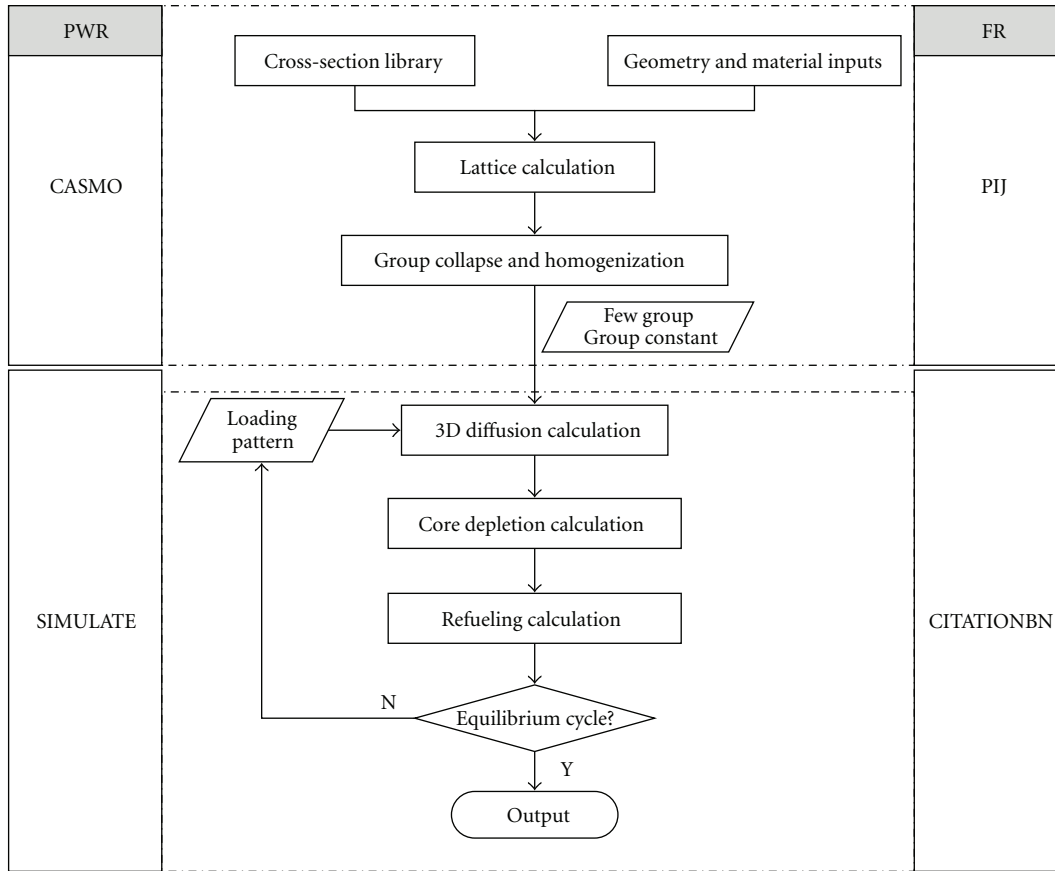


FIGURE 1: The computational flowchart of reactor core simulation.

design of reactors besides the economic parameters only. The operation of power plant is simulated by the reactor core analysis codes. The comparisons in the current or near future situation are analyzed. Also the sensitivity of the costs is predicted. The results show that the fuel cost of electricity (FCOE) in PWR with MOX fuel loaded is 25% higher than that of in FBR. But the situation will be changed with the burnup and discount rate.

2. Evaluation Methods

2.1. Reactor Core Simulation Method. To simulate the operation of PWR with the MOX fuel loaded, the code package CASMO/SIMULATE [8, 9] is applied according to the computational flowchart as in Figure 1. For the fast reactor simulation, the code package PIJ/CITATIONBN is used. This is a home-developed code for fast reactor analysis, which is also based on the computational flowchart as in Figure 1.

2.2. Economic Analysis Method. To avoid the confusion from the differences of reactors, the fuel cost of electricity (FCOE) evaluated by the cost per kilowatt hour electricity production from the fuel cycle is applied in the analysis. The mass flow of heavy metal (including the uranium and plutonium) in the closed fuel cycle is illustrated in Figure 2. The differences between reusing the recycled plutonium in

PWR and FBR arise in two main aspects. (1) Even after loading the plutonium, the fuels in PWR still consist of the MOX fuel and the necessary UO_2 fuel. Therefore, the cost is contributed from both the two kinds of fuels. (2) The plutonium bred in the FBR is valuable for further use. The feed material of FBR is contributed from two sources, that is, the recycled plutonium from PWR spent fuel and the plutonium bred in FBR.

Cash flow as in Figure 3 depicts the main costs of MOX fuel in the fuel cycle. The horizontal axis represents the timeline, and the sizes of bars represent nominal costs associated with the subscripted processes. As in the figures, the values above the horizontal axis denote the cost, while the below ones denote the revenue. Here, the time t_{om} , at which the fuels are consumed for generating the electricity, is appointed as the reference time. P - and F - stand for the variables in the PWR and FBR, respectively. C_u , C_c , C_s , and C_{lf} are the costs of original uranium, chemical conversion of UF_6 , separative work and enriching process, and UO_2 fuel assembly fabrication, respectively. t_u , t_c , t_s , and t_{lf} are the times at which these costs are paid relative to t_{om} . C_r , C_{dh} , C_{DU} , and C_{mf} are the costs of reprocessing the spent UO_2 fuel assemblies, disposal of the high-level waste (HLW), depleted uranium (from the tails in enriching process) purchasing, and MOX fuel assembly fabrication at t_r , t_{dh} , t_{DU} , and t_{mf} , respectively. When the fuels are ready, they will be loaded

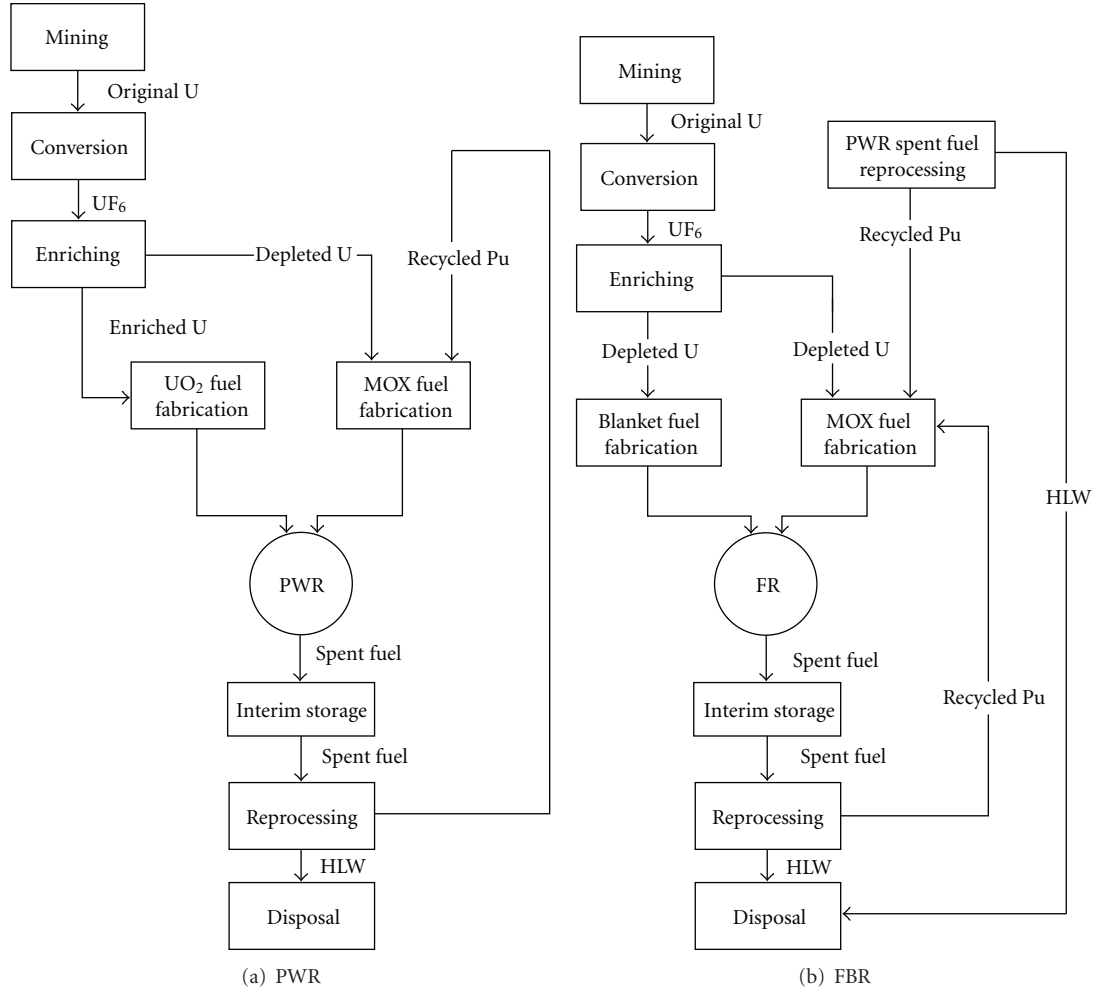


FIGURE 2: The mass flow of heavy metal in the closed fuel cycle.

in reactor. C_{md} and C_{ld} are taken as the total costs of interim storage and disposal of the MOX fuel and UO_2 fuel after discharging, respectively. For the fast breeder reactor, it should be noted that the plutonium from breeding is taken as the revenue. C_{bd} is the total cost of fuels in the blanket of FBR after discharging.

The cost of a power plant consists of the capital cost, fuel cost, annual cost, and so forth. This study focuses only on the fuel costs.

For the PWR, due to the limit of loading fraction, two kinds of fuels should be considered together, that is, the UO_2 fuel and the MOX fuel. The cost is formulated as:

$$C_{PWR} = w \frac{C_{P-MOX} F_{c,MOX}}{24,000 B U_{MOX} \epsilon} + (1-w) \frac{C_{P-UO_2} F_{c,UO_2}}{24,000 B U_{UO_2} \epsilon}, \quad (1)$$

where w is the power fraction of MOX fuel in the reactor core and ϵ is the thermal efficiency of the power plant (kW_e/kW_t). C_{P-MOX} and C_{P-UO_2} are the costs of MOX fuel and UO_2 fuel, respectively. The carrying charge factor, F_c (usually smaller than 1.0), accounts for the fact that the electricity revenue

to pay for the disposal over the time τ as in (2), BU , is the discharging burnup. Then,

$$F_c = \frac{\tau i}{(1+i)^\tau - 1}, \quad (2)$$

where i denotes the discount rate.

The costs of UO_2 fuel and MOX fuel are obtained according to the material flow and cash flow described above. They are represented as follows:

$$C_{P-UO_2} = C'_u + C'_c + C'_s + C'_{lf} + C'_{ld}, \quad (3)$$

$$C_{P-MOX} = C'_r + C'_{dh} + C'_{DU} + C'_{mf} + C'_{md},$$

where P - denotes the variable related to the PWR. C'_u , C'_c , C'_s , C'_{lf} , and C'_{ld} represent the same variables as in Figure 3. The superscript denotes that the losses including the loss of material and capital in these processes are considered.

For the fast breeder reactor, there are also two types of fuel assemblies. The seed assemblies, made from the MOX fuel, produce most of the energy for generating the electricity. The blanket assemblies, which contain only

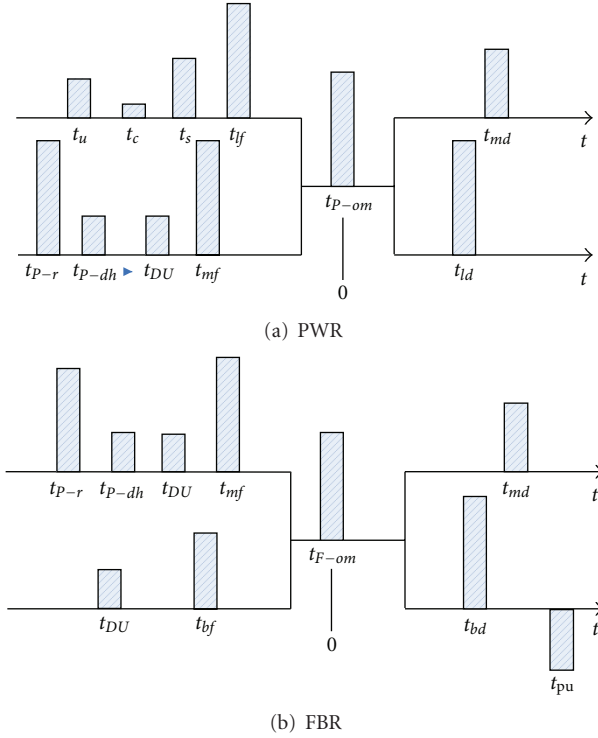


FIGURE 3: The cash flow in the closed fuel cycle.

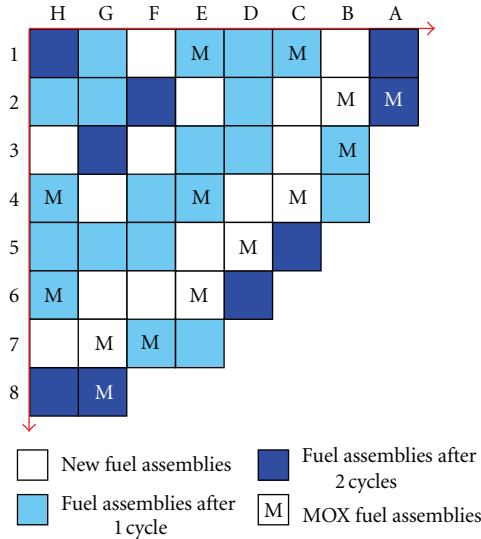


FIGURE 4: The loading pattern of fuel assemblies in the PWR.

depleted uranium, breed the plutonium with small fraction of electricity production. Therefore, the composition of fuel cost is

$$C_{FR} = \frac{(C_c + C_{ab})F_c + C_{rb}F_{rb}}{24,000\text{BU}\epsilon} - \frac{M_{Pu} C_{Pu} F_c}{(1+i)^{t_{pu}} 24,000\text{BU}\epsilon}, \quad (4)$$

where C_c , C_{ab} , and C_{rb} are the cost in seed assemblies, axial blankets, and radial blankets, respectively. They are

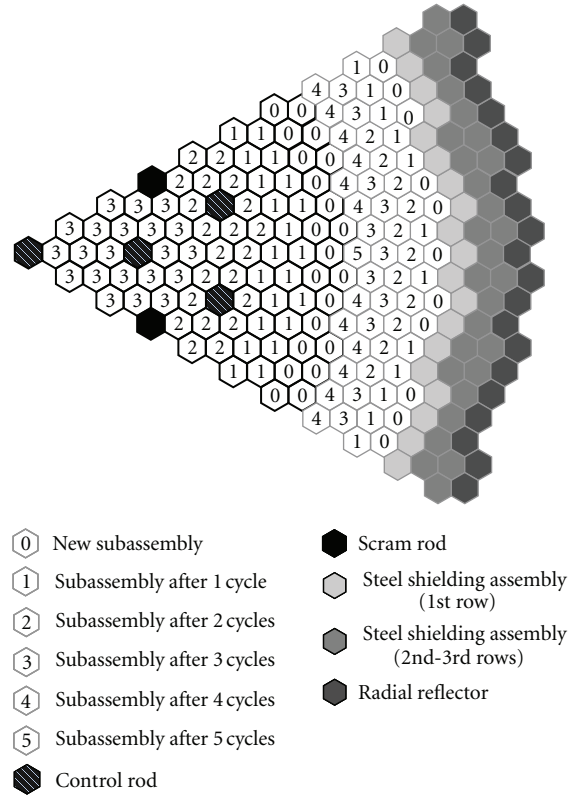


FIGURE 5: The loading pattern of fuel assemblies in the fast reactor.

determined depending on the material and cash flow as follows:

$$\begin{aligned} C_{C-\text{mox}} &= C'_r + C'_{dh} + C'_{DU} + C'_{mf} + C'_{md}, \\ C_{a-b} &= C'_{a-DU} + C'_{a-bf} + C'_{a-md}, \\ C_{r-b} &= C'_{r-DU} + C'_{r-bf} + C'_{r-md}, \end{aligned} \quad (5)$$

where F - denotes the variable related to the FBR.

For the fast breeder reactor, the discharged plutonium from breeding is very important and can be further used in other fast reactors. It is considered as the potential revenue. The benefit is represented as in (4). C_{Pu} is the revenue of recycled plutonium from breeding. M represents the mass.

Additionally, a special issue should be noticed, and the plutonium should be stored for some time before it is fabricated into the new fuel assemblies. However, it is expensive to keep the reprocessed plutonium securely. The additional cost should be involved.

3. Simulation of the PWR and FBR with MOX Fuel Loaded

3.1. Performance of PWR with MOX Fuel Loaded. The M310-type PWR is chosen in the simulation for its common installation. However, limited by the safety factors, the fraction of MOX fuel in the reactor core should not exceed 30% due to the change by the plutonium [1].

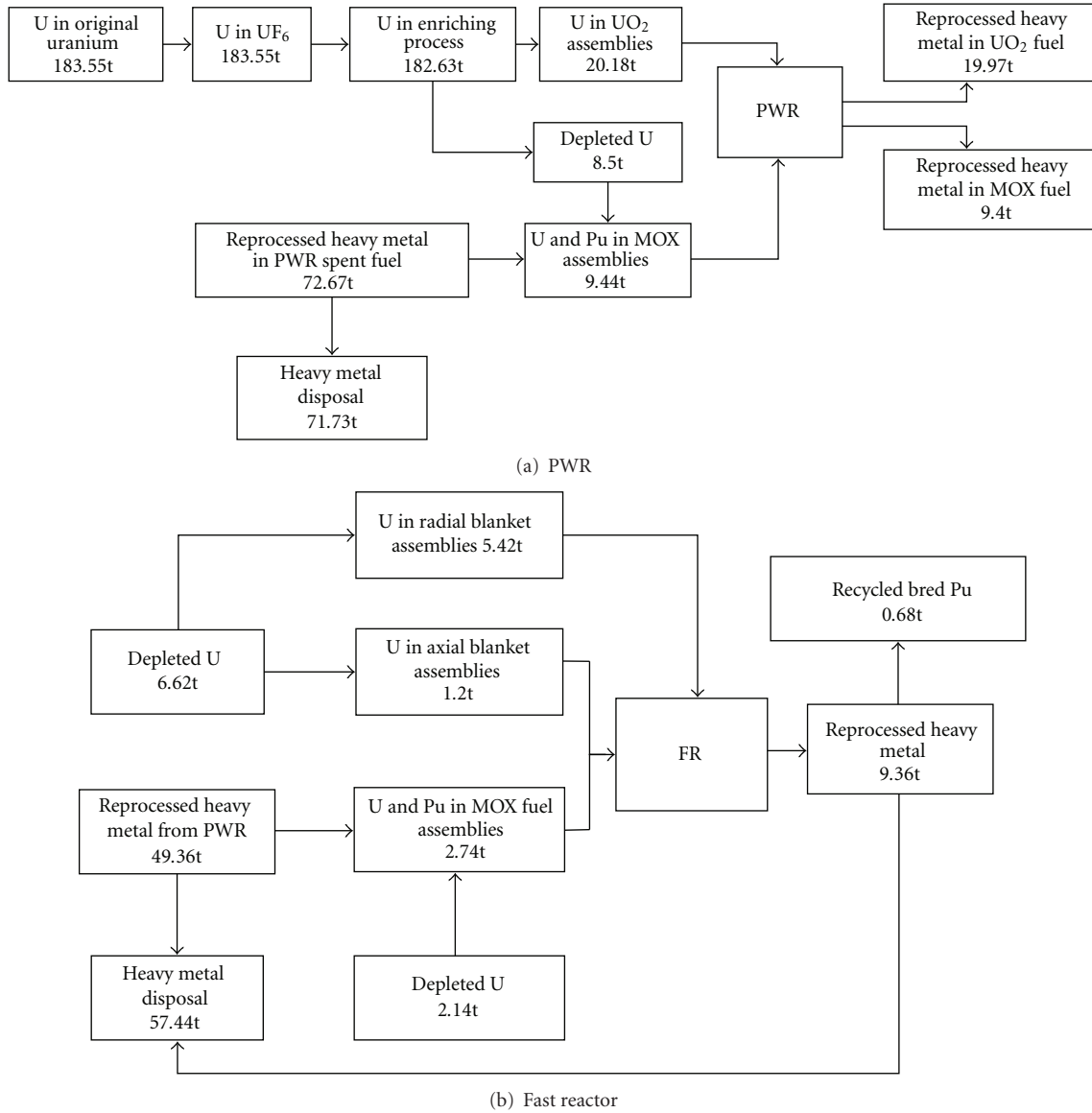


FIGURE 6: The mass balance of heavy metal in the closed fuel cycle.

In the original reactor core, only the UO_2 fuel assemblies are loaded. The MOX fuel assemblies are imported batch by batch. The plutonium in MOX fuel is reprocessed from the current PWR spent fuels. The composition is given as in Table 1.

The refueling scheme is illustrated as in Figure 4. The in-out refueling scheme with low-leakage consideration is adopted. After refueling five times, the new equilibrium cycle is obtained. A total of, 48 MOX fuel assemblies are loaded in the reactor core. The fraction is 30%, similar with the mostly common case in the EU PWR power plants [3]. The reactor performances in the equilibrium cycle are given in Table 2. It indicates that, in this reactor core design, loading MOX fuel does not bring significant changes in the core performance compared with the traditional UO_2 -fueled PWR.

3.2. Performance of FBR with MOX Fuel Loaded. The BN600-type fast reactor is chosen as the basis for its success operation experience [10]. The composition of plutonium in the MOX fuel is the same with the one in PWR, but the weight percent is higher, up to 22.05%.

There are two options in developing a fast reactor, one is called the breeder reactor, and the other is called the burner reactor. In this study, the breeder reactor is investigated only since the economics of the burner is not so meaningful. From this point, the core design is improved from the current BN600's. The radial blanket is added to enhance the breeding and make the conversion ratio bigger than 1.0. The loading pattern is illustrated as in Figure 5, mainly based on the original design, but four rings of blanket assemblies are arranged outside the driver. A total of 474 seed assemblies and 336 blanket assemblies are loaded.

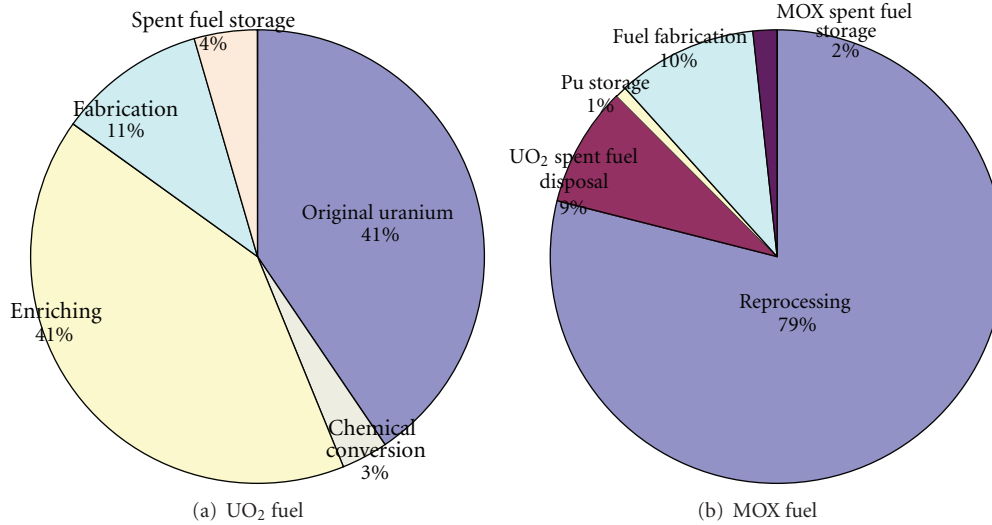
FIGURE 7: The cost compositions of UO_2 and MOX fuels.

TABLE 1: The composition of reprocessed plutonium.

Isotopes	^{238}Pu	^{239}Pu	^{240}Pu	^{241}Pu	^{242}Pu
Mass percent/%	2.85	52.28	23.33	15.20	6.34

TABLE 2: The reactor core performance of PWR with MOX fuel loaded.

Items	Value
Length of cycle (EFPD ¹)	480
Maximum burnup of UO_2 assembly (GWd/tHM ²)	53.02
Maximum burnup of MOX assembly (GWd/tHM)	49.56
Average burnup of UO_2 assembly (GWd/tHM)	46.69
Average burnup of MOX assembly (GWd/tHM)	47.11
Critical concentration of boric solution, BOL (ppm ³)	1773
Enthalpy rising factor, BOL ⁴ /EOL ⁵	1.51/1.34
Axial power peak factor, BOL/EOL	1.47/1.33
Radial power peak factor, BOL/EOL	1.34/1.17

¹Effective full power day. ²Tons of heavy metal. ³Parts per million. ⁴Beginning of life. ⁵End of life.

The out-in refueling scheme is designed. Figure 5 also shows the refueling scheme. In each refueling process, 120 new seed assemblies and 66 blanket assemblies are loaded. The seed assemblies are totally renewed after 4 batches of refueling, and the blanket assemblies are renewed after 5 batches of refueling.

The reactor performances are simulated by using PIJ/CITATION. After 10 batches of refueling, the equilibrium cycle can be obtained. The parameters are obtained as in Table 3. The averaged burnup reaches 105.19 GWd/tHM. The consumption of plutonium in each cycle is 0.6 tons with the conversion ratio bigger than 1.0. It is also consistent with the common core performance of fast breeder reactor.

TABLE 3: The reactor core performance of FBR with MOX fuel loaded.

Items	Value
Length of cycle (EFPD)	225
Reactivity loss ($\Delta k/k\%$)	4.25
Average burnup (GWd/tHM)	105.19
Max. burnup (GWd/tHM)	113.13
Mass of plutonium loading (ton)	0.6
Mass of discharged plutonium from blankets each cycle (ton)	0.192
Power fraction in the seed assemblies, BOC/EOC (%)	96.62/93.78
Axial power peak factor, BOC/EOC	1.239/1.199
Axial power peak factor, BOC/EOC	1.197/1.197
Max. linear power density (kw/m)	38.9
Conversion ratio, BOC/EOC	1.09/1.137

Based on the simulation, the mass balance can be obtained from the following economic analysis. Besides, the discharging parameters are also necessary to analyze the FCOE. Since all the core performances in PWR and FBR do not deviate from the traditional conditions of current UO_2 -fueled reactors, no excess changes should be considered further in operating the reactors due to loading the MOX fuel.

4. Economic Analysis

4.1. Analysis in Current Level. The price in the processes of fuel cycle is the most important economic parameter. The price used in this study is cited from the website <http://www.uxc.com> and the literature [6]. Table 4 summarizes the data, and its reference change interval for sensitivity analysis.

TABLE 4: The price of processing techniques and its change interval in the fuel cycle.

Items	Unit (\$/kgHM)		Time lag (month)	Material loss (%)
	Current level	Reference change interval		
Price of original uranium	109.2	80~300	-18	
Price of chemical conversion	9.23	6.42~12.84	-12	0.5
Price of UO ₂ fuel fabrication	275	200~350	-6	1.0
Price of UO ₂ spent fuel reprocessing	2107	940~3712	-24	0.5
Price of reprocessed uranium (RU)	20	0~100	-24	
Price of plutonium storage/\$/kgy	1200	1000~1300	-24~-6	
Price of tails	12	7~36	-12	
Price of depleted uranium	6	0~100	-12	
Price of MOX fuel fabrication for PWR	2215	838~2754	-6	0.5
Price of MOX fuel fabrication for FBR	2400	1435~3350	-6	0.5
Price of blanket fuel fabrication for FBR	275	200~350	-6	0.5
Price of MOX spent fuel storage	470	360~580	54	
Price of recycled plutonium from FBR	2347	1060~4072	60	
Discount rate	5%	2%~8%		

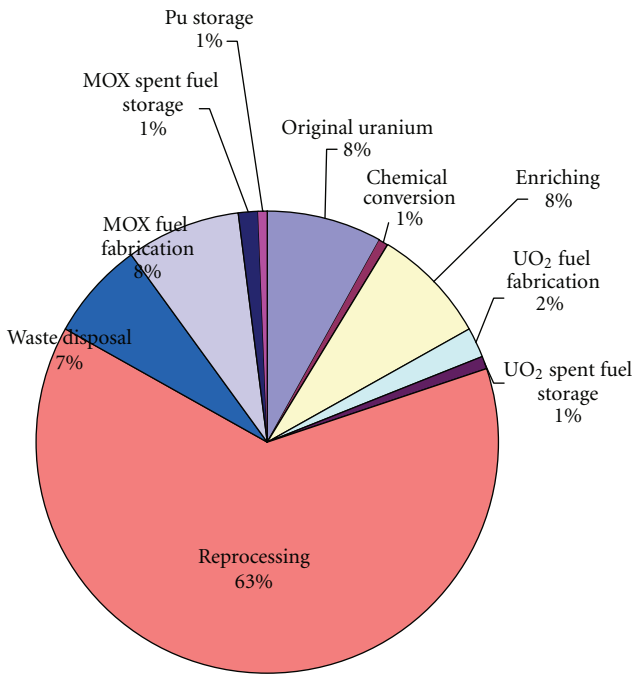


FIGURE 8: The FCOE composition of using MOX fuel in the PWR.

According to the simulation on the M310-type PWR and BN600-like fast breeder reactor, the mass balance based on the mass flow as in Figure 2 is determined. The results are shown in Figure 6, in which the preprocesses for getting the depleted uranium is omitted in the FBR cycle for simplification.

For the PWR loaded with MOX fuel (up to 30%), the amount of required plutonium equals to the reprocessed mass from three PWR in the same scale. In this case, the uranium resources can be saved over 10%. If the currently reserved PWR spent fuels are used, the fraction will be increased to over 30%.

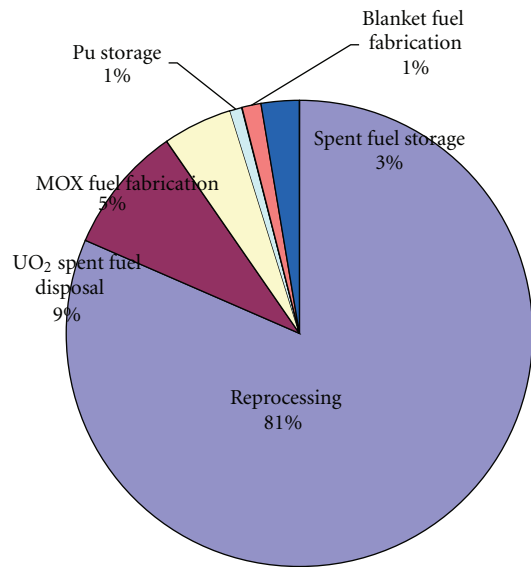


FIGURE 9: The FCOE composition of using MOX fuel in the FBR.

The final price of MOX fuel reaches 22720 dollar per kilogram (\$/kgHM), which is about 8.5 times higher than the one of current UO₂ fuel. Figure 7 illustrates the composition of the price. The reprocessing cost dominates the fuel cost, which is different from the UO₂ fuel, whose main part consists of the cost of original uranium and enriching process.

The final FCOE of PWR is 2.43 ¢/kwh. Figure 8 illustrates the composition. For the PWR, the main cost in the fuel cycle is the one arises in reprocessing. The FCOE of FBR is 1.83 ¢/kwh; it is even lower than the one in PWR. It is contributed from the revenue of plutonium bred in the blankets. Here, the revenue accounts for 55% of the final FCOE (4.10 ¢/kwh), that is, 2.27 ¢/kwh. Figure 9 illustrates the composition excluding the revenue.

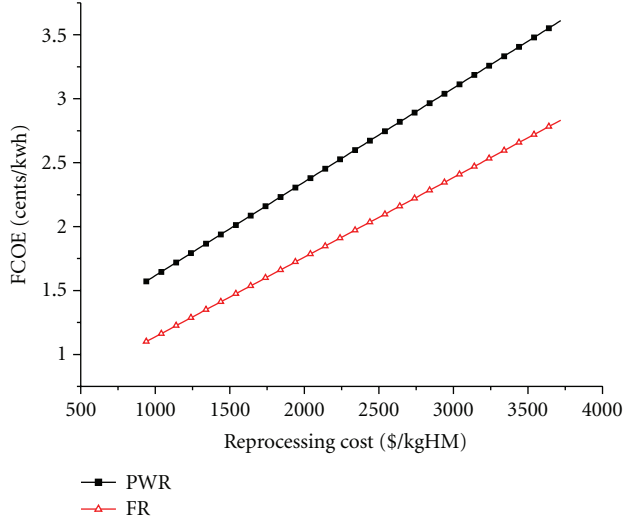


FIGURE 10: The changes of FCOE with reprocessing cost.

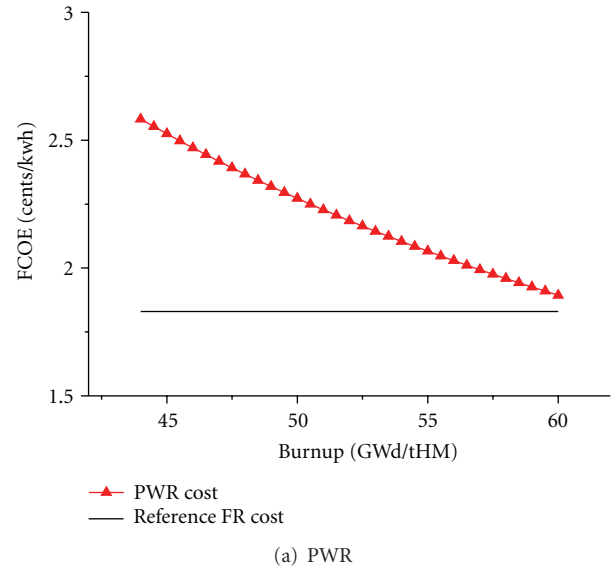
In this study, the typical design of a breeder reactor is investigated. Without considering the revenue in some fast reactors like ABR [11] (advanced burner reactor designed by Argonne National Laboratory), the cost will significantly increase. It will be about twice as much as the one of PWR. However, considering the revenue, the FCOE is 25% lower than the one of PWR with 30% MOX fuel loaded.

4.2. Sensitivity Analysis. For the economic analysis, the uncertainty of parameters is quite important due to many complicated factors. The sensitivity analysis is necessary. In this study, the sensitivity is investigated by defining the coefficient of elasticity as:

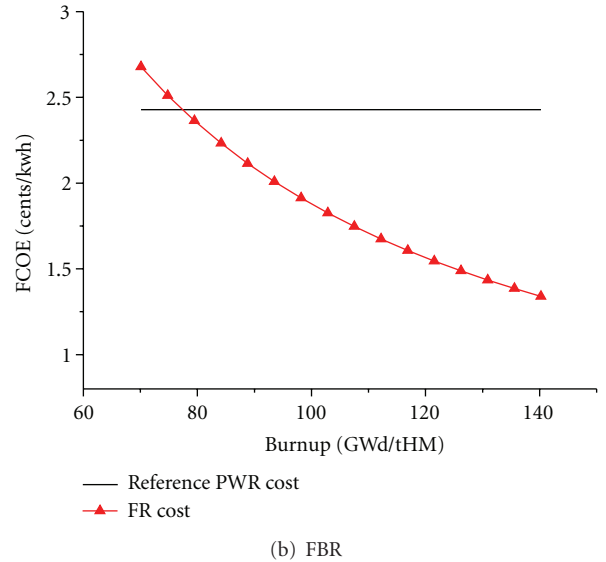
$$\varepsilon_{y,x_0} = \left. \frac{dy/y}{dx/x} \right|_{x=x_0} = \frac{x_0}{y(x_0)} y'(x_0). \quad (6)$$

Among the costs in the fuel cycle, the reprocessing cost accounts for the largest proportion, either in PWR or in FBR. Figure 10 shows the change of FCOE against the reprocessing cost. Linear increase arises with the increase of reprocessing cost. Based on (6), the coefficients of elasticity are 0.64 and 0.72, respectively. It means that if 1% increase of the reprocessing cost happens, the FCOE of PWR will increase by 0.64% and the one of FBR will increase by 0.72%, that is, the FCOE of PWR increases by 0.016 cents, and the one of FBR increases by 0.013 cents.

The practical design and operation of reactors also impact heavily on the costs. For FCOE, the coefficients of elasticity are -0.99 for both PWR and FBR. It means that 1% increase of burnup contributes about 0.99% decrease of the FCOE, which is more attractive in PWR for its higher FCOE at current value. Figure 11 illustrates the change of FCOE against burnup in PWR and FBR, respectively. The reference costs are given, which are the current value of FCOE of FBR



(a) PWR



(b) FBR

FIGURE 11: The changes of FCOE with burnup.

and PWR, respectively. It indicates that if the burnup of PWR can be increased up to 62 GWd/tHM, the FCOE will be smaller than the one of current FBR even if the revenue of plutonium is considered. In another aspect, if the burnup of FBR cannot reach the value as designed in this study, the FCOE of FBR will increase. If the value is lower than 80 GWd/tHM, the FCOE of PWR will be lower, also even if the revenue of plutonium is considered.

The discount rate is very important for the FBR, because the FCOE of FBR is impacted significantly by the revenue of reprocessed plutonium. Unfortunately, the plutonium cannot be immediately applied. The plutonium should be carefully stored as it costs a lot. Due to the effect of time lag, the cost will be increased. The coefficient of elasticity for the FBR is 0.73, which is 10 times larger than the one of PWR.

If the discount rate is greater than 8%, the FCOE of FBR is larger than the one of PWR.

Additionally, the original uranium cost is thought to be sensitive for PWR, since most of the fuels are still the UO_2 fuels. However, the analysis indicates that the coefficient of elasticity is only 0.081 at current price of original uranium. This factor becomes insignificant.

5. Conclusion

In this study, the economics of MOX fuel in the closed fuel cycle is analyzed. Considering the two options of applying the MOX fuel, the cost of PWR and FBR are investigated, respectively. The FCOE is used as the evaluation parameter. To find the valuable conclusion, the operations of a typical PWR and FBR are simulated using the reactor core analysis codes. The economic analysis model is established, considering all the components in the closed fuel cycle, especially the revenue of reprocessed plutonium and capital loss in the time lag.

The FCOE of PWR and of FBR are obtained based on the reactor parameters in the equilibrium cycles. For the PWR, the FCOE is 2.43 ¢/kwh, and for the FBR, the FCOE is 4.10 ¢/kwh. If the value of the reprocessed plutonium from breeding is considered, the cost will be reduced to 1.83 ¢/kwh, which is even lower than the one of PWR. The results are sensitive to the cost of reprocessing. The FCOE linearly increases with the increase of reprocessing cost in both PWR and FBR, where the PWR's FCOE keeps larger. Besides, the FCOE changes sensitively to the burnup and discount rate. With the increase of burnup in PWR or the decrease of burnup in FBR, the FCOE of PWR will become smaller than the one of FBR, even after considering the revenue of breeding. If the discount rate is large, the value of plutonium from breeding will be reduced. Also, the FCOE of PWR will be smaller.

Although it is only a part of the whole costs in constructing and operating a power plant, the FCOE is one of the most important influencing factors in the daily operation. This study gives the comparison of FCOE in different MOX fuel-loaded reactors. It will be useful to analyze the effect of utilizing the MOX fuel in the future closed fuel cycle.

Acknowledgment

This paper was carried out partly under the financial support of the National Natural Science Foundation of China (Approved no. 11105104).

References

- [1] P. Bernard, "French experiences and perspectives on plutonium recycling in the existing power fleet," *AREVA-COGEMA Recycling Business Unit*, vol. 49, no. 8, pp. 583–588, 2007.
- [2] Z. Gu and G. Ye, "Recent developments in studies of advanced nuclear fuel cycle system," *Atomic Energy Science and Technology*, vol. 36, no. 2, pp. 97–104, 2002.
- [3] J. Provost, M. Schrader, and S. Nomura, "MOX fuel fabrication and utilization in LWRs worldwide," in *MOX Fuel Cycle Technologies For Medium and Long Term Deployment*, Vienna, Austria, 1999.
- [4] J. Leclere, Y. Bibilashvili, F. Reshetnikov et al., "MOX fuel fabrication and utilization in fast reactor worldwide," in *MOX Fuel Cycle Technologies For Medium and Long Term Deployment*, Vienna, Austria, 1999.
- [5] J. Zhu, A. Nechaev, and M. Tauched, *Nuclear Fuel Cycle Training*, Westinghouse Proprietary, Pennsylvania, Pa, USA, 1992.
- [6] A. Waltar and A. Reynolds, *Fast Breeder Reactor*, Pergamon Press, Oxford, UK, 1981.
- [7] M. Bunn and S. Fetter, *The Economic of Reprocessing Vs. Direct Disposal of Spent Nuclear Fuel*, Project on Managing the Atom, Cambridge, Mass, USA, 2003.
- [8] "CASMO-4: A Fuel Assembly Burn-up Program User's Manual," *SSP-09/443-U Rev 0*, Studsvik, UK, 2009.
- [9] "SIMULATE-3: Advanced Three-Dimensional Two-Group Reactor Analysis Code," *SSP-09/447-U Rev 0*, Studsvik, UK, 2009.
- [10] P. Nporpammbi, "Updated codes and methods to reduce the calculational uncertainties of the LMFR reactivity effects," in *The 5th Research Co-Ordination Meeting*, Vienna, Austria, November, 2004.
- [11] E. Hoffman, W. Yang, and R. Hill, "Preliminary Core Design Studies for the Advanced Burner Reactor over a Wide Range of Conversion Ratios," *ANL-AFCI-177*, Argonne National Laboratory, 2006.